Transition in a Laminar Separation Bubble and the Effect of Acoustic Excitation

by

John William Kurelek

A thesis
presented to the University of Waterloo
in fulfillment of the
thesis requirement for the degree of
Master of Applied Science
in
Mechanical Engineering

Waterloo, Ontario, Canada, 2016

I hereby declare that I am the sole author of this thesis. This is a true copy of the thesis, including any required final revisions, as accepted by my examiners.

I understand that my thesis may be made electronically available to the public.

Abstract

Flow development within a laminar separation bubble and the effect of controlled acoustic excitation are investigated experimentally for a NACA 0018 airfoil at a chord Reynolds number of 125 000 and an angle of attack of 4°. The investigation is carried out in a series of wind tunnel tests and employs a combination of surface pressure measurements and time-resolved, planar, two-component Particle Image Velocimetry. Both streamwise and spanwise aspects of the flow development are assessed. Three types of acoustic excitation are investigated: (i) harmonic: tonal excitation at the frequency of the most amplified disturbances in the natural flow, (ii) subharmonic: tonal excitation at the subharmonic frequency, and (iii) random: white noise filtered to the naturally unstable frequency band.

For all the cases examined, the results show that strongly periodic shear-layer vortices form in the separation bubble due to the amplification of disturbances in the separated shear layer. The formation of these structures is found to occur when velocity fluctuations reach a critical amplitude equal to approximately 6% of the free-stream velocity. These structures feature strong spanwise coherence at roll-up; however, they deform rapidly upstream of the mean reattachment point. Spanwise undulations in the vortex filaments develop in a non-periodic fashion, with the spanwise wavelength shown to be predominantly two and a half times the characteristic streamwise wavelength of the structures. These spanwise deformations lead to regions of local vortex breakup, which expand rapidly as the vortices approach the mean reattachment point. This is accompanied by a rapid decay of the spanwise coherence length, which reaches a value typical of turbulent boundary layers downstream of mean reattachment.

Harmonic and random excitations are found to decrease the separation bubble in size, with the effect becoming more pronounced with increasing amplitude. The changes in the mean bubble topology are linked to alterations in the features of the shear layer vortices. Specifically, these types of excitation cause earlier shear layer roll-up, which results in the aft portion of the bubble shifting upstream. Harmonic excitation is shown to organize the shedding process and increase the spanwise coherence of the vortices, while random excitation has the opposite effect. It is proposed that mean reattachment in a separation bubble is a result of momentum exchange between the outer-flow and the near wall region, which can be facilitated by either the coherent roll-up vortices or the smaller scale structures that result from their breakdown, with the latter proving to be more effective. Subharmonic excitation is shown to promote periodic and spanwise non-uniform vortex merging, which otherwise occurs randomly in the unperturbed flow. The results demonstrate that the development of shear-layer vortices plays the fundamental role in defining the separation bubble, and the later stages of transition are directly related to the breakdown of these structures in the aft portion of the bubble.

Acknowledgements

I would like to thank my supervisor, Professor Serhiy Yarusevych, for the indispensable guidance and insight provided throughout this endeavour. Your teachings and infallible approach to research have taught me the skills and mindset necessary for a successful career in academia.

I would like to thank all my graduate student colleagues: Chris Morton, Jeff McClure, Manpreet Bansal, Andrew Lambert, Eugene Zivkov, Sahil Mahey, Winston Hu, Ajith Airody, Supun Pieris and Mark Istvan. Thank you for the helpful discussions, eagerness to lend a helping hand, and companionship. Andrew's patient instruction and help in all things related to wind tunnel experimentation and Mark's inexhaustible willingness to discuss ideas and results are particularly appreciated.

I am grateful to technical staff members Jim Merli, Neil Griffett, Rich Gordon, Jason Benninger, and Fred Bakker for the support they provided. I would specifically like to acknowledge the outstanding efforts of Jason and Fred in fabricating and assembling the wind tunnel. The facility is truly world-class.

Finally, I would like to thank my parents, Dianne and Andy, and my best friend and girlfriend, Nicole Kelly Pinto, for their unwavering support in me and my decision to pursue higher education.

Financial support for this work was provided by the Natural Sciences and Engineering Research Council of Canada and the Ontario Graduate Scholarship program.

Table of Contents

List of Tables

List of Figures

Nomenclature

Dimensionless Numbers

Symbol	Description	Definition
Re	chord-based Reynolds number	$\frac{U_0 c}{\nu}$
St	chord-based Strouhal number	$\frac{fc}{U_0}$
St_θ	momentum thickness-based Strouhal number	$\frac{f\theta}{U_0}$
C_P	surface pressure coefficient	$\frac{P - P_0}{\frac{1}{2}\rho {U_0}^2}$
H	boundary layer shape factor	$\frac{\delta^*}{\theta}$
R	shear layer velocity ratio	$\frac{U_1 - U_2}{U_1 + U_2}$
R_{UU}	correlation coefficient function of two $U(t)$ signals, e.g. U_1 and U_2	$\frac{\mathrm{cov}(U_1, U_2)}{\sigma_{U_1}\sigma_{U_2}}$
t^*	dimensionless time	$\frac{tU_0}{c}$

Roman Symbols

Symbol	Description	Units
A	Gaussian curve fitting coefficient	m
a	speed of sound in air	$\mathrm{m\,s^{-1}}$
c	airfoil chord length	m
d	fundamental wavelength of acoustic standing waves in the test section	m
f	frequency	Hz
f_s	sampling frequency	Hz
k_x	streamwise wavenumber of disturbances; $\frac{2\pi}{\lambda_x}$	$\mathrm{m^{-1}}$
l	airfoil leading to trailing edge arc length	m
ℓ_z	spanwise coherence length	m
P	local mean static pressure	Pa
P_0	free-stream static pressure	Pa
P_{dyn}	mean free-stream dynamic pressure	Pa
ΔP_{con}	mean pressure drop across the wind tunnel contraction	Pa
p	fluctuating pressure	Pa
p'	root-mean-square of p	Pa
$\mathbf{S}$	rate-of-strain tensor; refer to Eq. F.1	$\mathrm{s^{-1}}$
t	time	s
Δt	PIV frame separation time	s
U	x-velocity component	$\mathrm{m\,s^{-1}}$
$\overline{U}$	time-average of U	$\mathrm{m\,s^{-1}}$

U_0	free-stream velocity	$\mathrm{m\,s^{-1}}$
U_c	convective velocity of shear layer vortices	$\mathrm{m\,s^{-1}}$
$\overline{U_c}$	average convective velocity	$\mathrm{m\,s^{-1}}$
$\overline{U_{c\mathrm{win}}}$	window-averaged convective velocity	$\mathrm{m\,s^{-1}}$
U_e	local streamwise edge velocity	$\mathrm{m\,s^{-1}}$
u	fluctuating component of U	$\mathrm{m\,s^{-1}}$
u'	root-mean-square of u	$\mathrm{m\,s^{-1}}$
U_i	contraction inlet velocity	$\mathrm{m\,s^{-1}}$
$\overline{uv}$	Reynolds shear stress	$\mathrm{m^2\,s^{-2}}$
V	y-velocity component	$\mathrm{m\,s^{-1}}$
v	fluctuating component of V	$\mathrm{m\,s^{-1}}$
v'	root-mean-square of v	$\mathrm{m\,s^{-1}}$
x	surface-tangent coordinate	m
x_h	time-averaged streamwise point of maximum bubble height	m
x_R	time-averaged streamwise reattachment point	m
x_S	time-averaged streamwise separation point	m
x_T	time-averaged streamwise transition point	m
y	surface-normal coordinate	m
z	spanwise coordinate	m

Greek Symbols

Symbol	Description	Units
α	angle of attack	degrees (°)
β	desired quantity	–
δ	boundary layer thickness; $y\vert_{U(y)=0.99U_e}$	m
δ^*	displacement thickness; $\int_0^\delta \left[1 - \frac{U(y)}{U_e}\right] \mathrm{d}y$	m
ϵ	measured quantity	–
θ	momentum thickness; $\int_0^\delta \frac{U(y)}{U_e} \left[1 - \frac{U(y)}{U_e}\right] \mathrm{d}y$	m
θ_S	momentum thickness at separation	m
λ_2	second eigenvalue of $\mathbf{S}^2 + \mathbf{\Omega}^2$	s^{-2}
λ_x	streamwise wavelength of disturbances	m
$\overline{\lambda_x}$	average streamwise wavelength	m
$\overline{\lambda_x}_{\mathrm{win}}$	window-averaged streamwise wavelength	m
λ_z	spanwise wavelength of disturbances	m
ν	kinematic viscosity	$\mathrm{m\,s}^{-2}$
ρ	density	$\mathrm{kg\,m}^{-3}$
σ_U	standard deviation of U	$\mathrm{m\,s}^{-1}$
Φ_{pp}	auto-spectral density of p	Pa^2
Φ_{uu}	auto-spectral density of u	$\mathrm{m}^2\,\mathrm{s}^{-2}$
Φ_{vv}	auto-spectral density of v	$\mathrm{m}^2\,\mathrm{s}^{-2}$
ψ_β	uncertainty estimate of β	–
$\mathbf{\Omega}$	rate-of-rotation tensor; refer to Eq. F.2	s^{-1}
ω	spanwise vorticity; $\nabla \times \langle U, V \rangle$	s^{-1}

Chapter 1

Introduction

The airfoil is of fundamental technical importance in the field of fluid mechanics, as its use is ubiquitous for a vast range of Reynolds numbers, Re, that spans animal flight, marine and wind turbine propellers, and aviation [1]. When set in motion relative to a fluid stream, satisfactory performance is predicated on maximizing the lift-to-drag ratio of the airfoil. In the past century, humanity has made astounding strides in the field of general aviation, $Re > 10^6$, as one need only consider the pioneering accomplishments of the Wright brothers at the beginning of the twentieth century in contrast to the pervasiveness of commercial air travel today. However, significant challenges remain for applications in the low Reynolds number range, $10^4 < Re < 5 \times 10^5$, which continue to motivate many experimental and computational efforts in the fluid mechanics research community.

The main impediment for applications in the low Reynolds number regime, such as unmanned aerial vehicles and small-to-medium scale wind turbines [1–3], is laminar separation. In contrast to airfoil operation at high Reynolds numbers, the boundary layer on the airfoil's suction side often remains laminar downstream of the point of minimum pressure, where an adverse pressure gradient opposes the flow. As such, boundary layer separation is common, where the formed detached shear layer is unstable and undergoes transition to turbulence. At high angles of attack or low Reynolds numbers, the airfoil is left in a stalled state, resulting in very poor aerodynamic performance [2]. For lower angles of attack or higher Reynolds numbers, the increased entrainment due to the transition of the shear layer can cause reattachment to the airfoil surface and the formation of a closed region of recirculating fluid, referred to as a laminar separation bubble (LSB) [4–6]. This improves performance, but not to levels observed in the absence of laminar separation [2].

Recent research efforts have been focused on the transition process within the separation bubble, so that, ultimately, the process may be controlled and the performance losses

mitigated. The initial stage of transition is characterized by the amplification of small-amplitude disturbances within a band of unstable frequencies, shown to be primarily due to an inviscid Kelvin-Helmholtz instability [7–9]. This results in initial disturbance growth that is exponential and predominantly two-dimensional. The process has been shown to be well modelled by Linear Stability Theory (LST) [9–14], up until non-linear interactions begin to occur between disturbances, marking the later stages of transition. Both experimental [8, 15–20] and numerical studies [7, 11, 21–23] have shown the defining feature of these later stages to be the roll-up of the separated shear layer into spanwise vortices, which dominate the flow development in the aft portion of the bubble. After formation, the development of the vortices is characterized by significant three-dimensional deformations prior to a rapid breakdown to turbulence. Recent Direct Numerical Simulation (DNS) studies describe initially two-dimensional spanwise vortices that break up due to the onset of secondary instabilities [21, 23]. However, in conflict with the DNS observations, recent experimental studies have described the spanwise uniformity of the structures as sporadic [16, 18] or even not present entirely [17, 20]. The later stages of transition in laminar separation bubbles remains an area of active research [24], as unequivocal answers, particularly through experimental means of investigations, have yet to be provided on the development of coherent structures in separation bubbles and the role they play in defining the LSB.

Flow control studies have been successful in exploiting the inherent sensitivities of separation bubble transition to improve the aerodynamic performance of low Reynolds number airfoils. Studies have generally focused on controlling the separated flow region [25, 26], employing various actuators, such as external acoustics [27–30], synthetic jets [31] and plasma-based actuators [32, 33]. In particular, investigations employing controlled acoustic disturbances have shown that excitation at the most amplified frequency of the LSB transition process and of relatively low amplitude can improve performance and delay stall [27–29] through promoting transition. The effect of external acoustics on LSBs is of further interest since it also arises as a consequence of airfoil self-noise. Strong acoustic tones are commonly observed on airfoils that also produce LSBs [34–39], as strong tones are produced when coherent shear layer instability waves pass over the airfoil trailing edge [40, 41]. The presence of an acoustic feedback loop between trailing edge noise emissions and the transition process within the LSB has been shown to exist [37–39, 41, 42]. Recent investigations have shown that trailing edge tonal noise, dictated by either suction or pressure side LSBs, can establish a feedback loop with the shear layer transition process(es), and thus alter LSB characteristics [38, 39]. However, the majority of previous studies, be them flow control or self-noise focused, have concentrated primarily on global flow changes (i.e. lift, drag, far-field acoustic emissions, etc...). The attendant changes in separation bubble dynamics due to acoustic disturbances remain to be investigated in detail.

1.1 Study Objectives

The purpose of this investigation is to experimentally examine the transition process within a separation bubble formed over an airfoil at a low Reynolds number, with the goal of elucidating the role coherent structures play in the process. In addition, the effect of controlled acoustic disturbances on the transition process, and more specifically on the development and breakdown of the structures is of interest, due to the technique's relevance as a means of effective flow control and as a consequence of airfoil self-noise. Accordingly, the specific research objectives of this thesis are as follows:

1) Assess the streamwise and spanwise spatio-temporal flow development in a separation bubble formed on an airfoil, in order to
   a) provide a time-resolved description of the formation, convection and breakdown of the coherent structures,
   b) determine the underlying physical breakdown mechanisms, and
   c) identify similarities and distinctions to the transition processes in attached boundary layers and free shear layers.
2) Examine the effect of controlled acoustic disturbances on flow development and transition in a separation bubble, specifically considering the effect of excitation frequency content and amplitude on
   a) the dynamics of the roll-up vortices, and
   b) the resulting mean topological changes in the separation bubble.

Chapter 2

Background

Our fundamental understanding of airfoil operation at low Reynolds numbers is incomplete, as one need only compare the capabilities of natural and man-made flyers in this regime for evidence. However, the topic has benefited from considerable research effort over the past century, the forefront of which is discussed in this chapter. Particular interest is paid to the laminar separation bubble and the laminar-to-turbulent transition process of its separated shear layer. In addition, literature regarding the transition of attached boundary layers and free shear layers is reviewed so that similarities and distinctions to separated shear layer transition may be identified. The effects of acoustic disturbances on laminar separation bubbles are also discussed, due to the significant practical interests as both a viable flow control technique and as a consequence of airfoil self-noise production.

2.1 Low Reynolds Number Flows over Airfoils and the Laminar Separation Bubble

In fluid flow over an airfoil, the chord-based Reynolds number, Re, quantifies the relative importance of inertial and viscous effects. The range of Reynolds numbers in applications involving airfoils is impressively large, spanning from 10^2 to 10^9. At the lower end of this spectrum, $Re < 10^4$, appreciable airfoil performance is difficult due to dominating viscous forces, while the well-established general aviation finds its home at $Re > 10^6$ [1, 2]. In between these two is the low Reynolds number range ($10^4 < Re < 5 \times 10^5$), where both viscous and inertial effects play important roles. Common engineering applications in this regime include glider and model airplanes, cooling fans, propellers, unmanned aerial vehicles and small-to-medium scale wind turbines, of which the latter two have received

considerable attention in recent years [3, 42].

The main impediment to aerodynamic performance in the low Reynolds number regime is laminar boundary layer separation, as the developing boundary layer on the airfoil's suction surface often remains laminar beyond the point of minimum pressure, and hence is susceptible to separation due to the adverse pressure gradient. In the event of separation, the resulting detached shear layer is unstable and undergoes transition to turbulence, which enhances momentum exchange. Depending on flow conditions, the shear layer may remain separated or reattach to the airfoil surface in a mean sense, with the former leaving the airfoil in a stalled state and the latter forming a closed region of recirculating fluid, referred to as a laminar separation bubble [4–6]. These two flow conditions are illustrated in Fig. 2.1. While aerodynamic performance decreases dramatically for the stalled case (Fig. 2.1a), reattachment (Fig. 2.1b) improves performance, but not to levels experienced in the absence of laminar separation [2, 3].

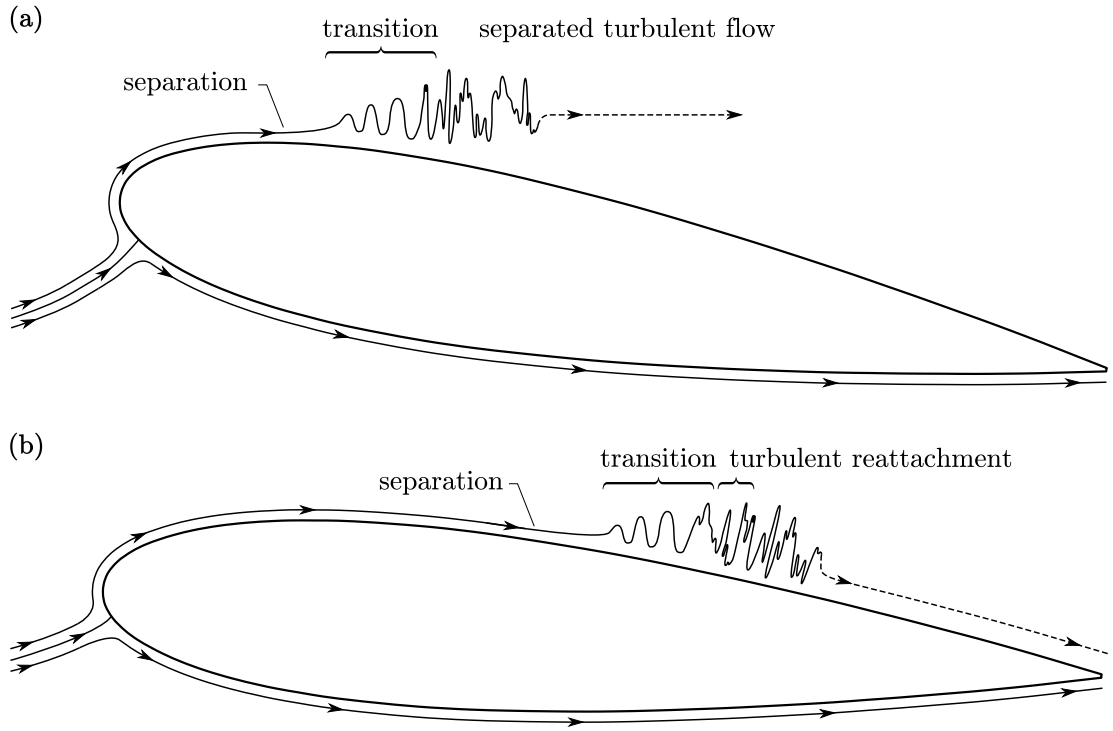

Figure 2.1: Flow over an airfoil at low Reynolds numbers showing laminar separation leading to (a) stall, and (b) separation bubble formation, after Yarusevych *et al.* [19].

Early experimental characterization of the laminar separation bubble focused on identifying the location and extent of the bubble on the airfoil surface. Owen and Klanfer [43] were first to classify bubbles as short or long, while Tani [4] extended this to distinguish short bubbles as those who have a minor effect on the static pressure distribution, while long bubbles have a greater effect by diminishing the suction peak on the airfoil's upper surface. The now generally accepted time-averaged representation of the separation bubble was first proposed by Horton [6] and is shown in Fig. 2.2, which describes a region of recirculating fluid bounded by the airfoil surface and the separated shear layer. A time-averaged dividing streamline can be identified as the locus of zero streamwise velocity [44], whose upstream and downstream intersection points with the surface are the mean separation and reattachment points, respectively. For convenience, a mean transition point is often identified, however it should be noted that transition occurs over a region rather than at a given location. It is important to note that these time-average characteristics of a separation bubble, while useful, do not provide a complete description as the separated shear layer is, by nature, unsteady. The unsteady features of a separation bubble are illustrated in Fig. 2.2 and are discussed in Section 2.2.3.

Mean surface pressure measurements have proven to be reliable in estimating the mean separation, transition and reattachment points [2, 4, 45]. Tani [4] noted the presence of a mean pressure plateau between the separation and transition points, and as such the start and end of this region have been used to estimate these points [45, 46]. The pressure plateau is followed by a region of rapid pressure recovery. Mean reattachment can be estimated as the point where the rate of this pressure recovery decreases [45]. Velocity-based boundary layer parameters have also been used to describe the development of the separation bubble [9, 45, 47]. Boundary layer displacement thickness, δ^*, increases downstream of separation to a maximum approximately at the transition point and then decreases to a local minimum near the reattachment point [9, 47], while momentum thickness, θ, is relatively constant in

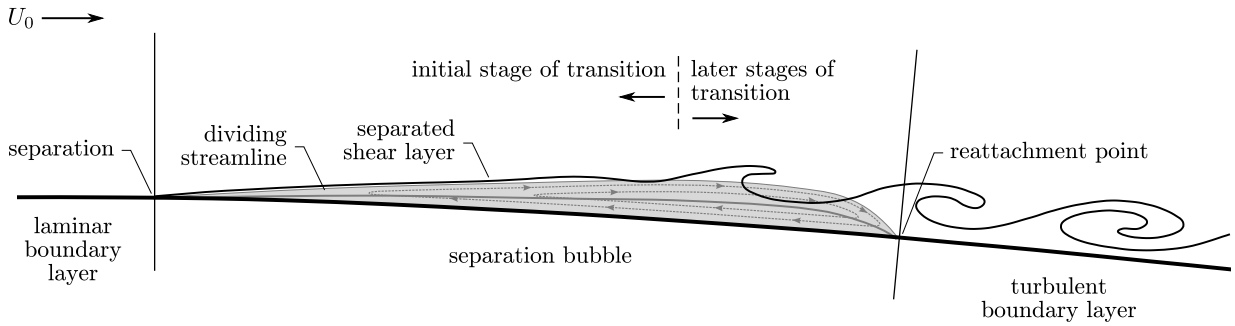

Figure 2.2: Time-averaged (grey lines) and unsteady features of a separation bubble.

the separated region, but then begins to increase near the transition point [45, 47]. This has lead some investigators to use the displacement thickness or shape factor, $H = \delta^*/\theta$, to estimate the transition point [47, 48]. Other, more recent methods employed to estimate the transition location include turbulence intermittency parameters [22, 49], and Reynolds shear stress parameters [15, 16, 18, 50, 51].

Given its importance related to airfoil performance and stall, much experimental effort has gone into detailing separation bubble characteristics on airfoils for a wide range of flow conditions and geometries [2, 4, 46, 52–55], which have been successful in establishing general trends for Reynolds number and angle of attack effects [3]. At low angles of attack and sufficiently high Reynolds numbers, laminar separation is followed by reattachment, thus forming a separation bubble. With the Reynolds number held constant, increasing the angle of attack causes the bubble to move upstream and decrease in length, until some critical angle at which reattachment is not possible and the airfoil stalls. Changes to the Reynolds number at a fixed angle of attack has a less significant effect on the location of the bubble, however, decreasing the Reynolds number causes the bubble to increase in length until a critical value of $Re \approx 50\,000$ [2, 3], at which point the shear layer fails to reattach. This phenomenon is called bubble bursting and is generally attributed to Gaster [5], who noted that small changes at the critical angle of attack or critical Reynolds number can cause the bubble to suddenly increase in length and cause stall.

In addition to the Reynolds number and angle of attack, low Reynolds flows over airfoils are extremely sensitive to factors that are difficult to control or vary systematically, making their study difficult. These factors include model imperfections [52, 56], free-stream turbulence [50, 52, 57–60], acoustic disturbances (treated in Section 2.3), and intrusive experimental techniques [47, 61, 62]. Mueller *et al.* [57] found it difficult to relate the effect of free-stream turbulence intensity to airfoil performance, as they found the accurate measurement of relatively small aerodynamic forces to be further exacerbated by changes to the turbulence intensity. However, Mueller *et al.* [57, 58] and Marchman [52] did show that elevated turbulence intensity levels altered the stall behaviour of airfoils, as lift recovery was promoted when approaching from post-stall angles of attack. Examination of the effects of the experimental setup in separation bubble studies has shown that intrusive probes, e.g. hot-wires, can alter the flow topology when placed near the separation point [47, 61]. Furthermore, Boutilier and Yarusevych [62] showed that end plates and corrections against blockage effects should be employed in two-dimensional airfoil studies in order to avoid errors in estimating separation bubble characteristics and lift forces, respectively, particularly when near the bursting condition. The extreme sensitivity of flows involving separation bubbles is exemplified by the investigation of Ol *et al.* [50], who, in compiling data from three different experimental facilities, found significant discrepancies

in the measured location and flow structure of the separation bubble for nominally identical experiments. Similarly, Olson *et al.* [59] found it difficult to find agreement among experimental and computational results for, again, largely similar flow conditions. The challenges in conducting low Reynolds experiments therefore necessitates the careful documentation of free-stream conditions, as well as the use of carefully manufactured models and minimally-invasive measurement techniques.

2.2 Transition to Turbulence

While the main focus of this thesis is the transition process of a laminar separation bubble's separated shear layer, it is instructive to first review the transition processes of the attached boundary layer (Section 2.2.1) and the free shear layer (Section 2.2.2), since separated shear layer transition (Section 2.2.3) can be viewed as some combination of the two.

2.2.1 Attached Boundary Layer

A brief review of boundary layer transition is provided here. For more comprehensive reviews of this vast topic, the reader is referred to Refs. [63–67].

A boundary layer's transition process may take one of many paths to turbulence [68], the full extent of which is discussed by Saric *et al.* [66]. The process begins with the laminar boundary layer's receptivity to free-stream disturbances [69], such as sound or vorticity, which establish the initial conditions of disturbance amplitude, phase and frequency for the breakdown process. Disturbances within the boundary layer undergo growth, governed by an instability whose nature is dependent on Reynolds number, wall curvature, surface roughness, and initial conditions, among others [66]. If the initial disturbance amplitude is sufficiently small, the processed illustrated in Fig. 2.3 is followed, which involves the growth of an unstable wave packet due to the flow's convective instability [70, 71], followed by three dimensional breakdown. However, it is worth noting that a vast number of flows do not follow this route to turbulence, as the slow convective growth of disturbances can be bypassed [69], leading to the flow quickly becoming turbulent. Such cases have been documented to occur in the presence of surface roughness or high free-stream turbulence [72, 73].

Figure 2.3 shows the idealized progression of boundary-layer transition over a flat plate, which is described in Refs. [64, 67, 74, 75]. The unstable disturbances in the laminar boundary layer are of relatively small amplitude and undergo weak growth that occurs over a relatively long (streamwise) length scale. This initial stage can be successfully described

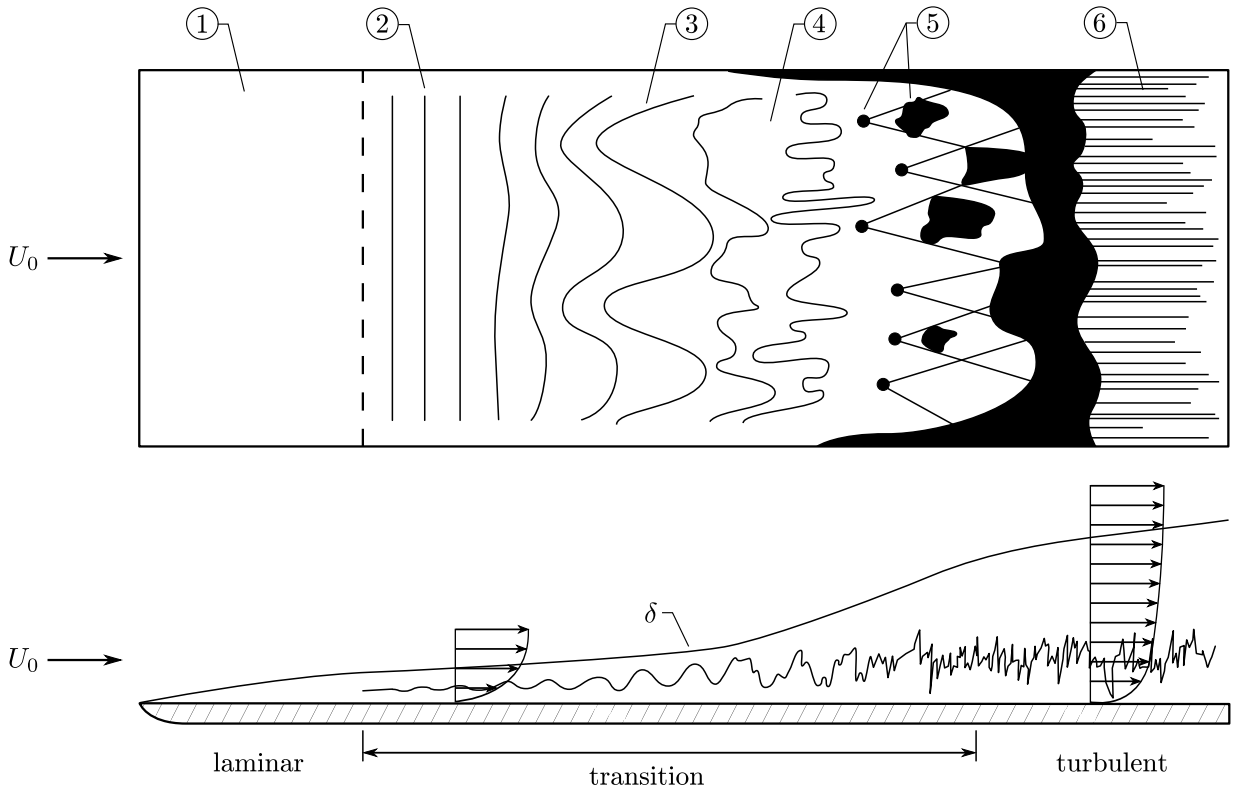

Figure 2.3: Idealized description of flat plate boundary layer transition, after White [74], Schlichting and Gersten [75], and Kachanov [64]. ① Stable laminar flow; ② unstable TS waves; ③ three-dimensional waves and vortex formation (Λ-structures); ④ vortex decay; ⑤ formation of turbulent spots; ⑥ fully turbulent flow.

by LST. As amplitudes grow, three-dimensional and non-linear interactions begin to occur. This leads to the formation of characteristic Λ-structures. Disturbance growth is very rapid in this stage, i.e. over a convective length scale, and the breakdown to turbulence begins to occur as the Λ-vortices decay and are replaced by turbulent spots. These turbulent spots increase in number, continue to spread, and lead to the completion of the transition process. However, the described process is idealized, as in reality numerous waves grow and compete simultaneously, and so subsequent stages do not begin only after the preceding one has ended.

The methods developed by Orr [76] and Sommerfeld [77] serve as the foundation upon which the understanding of boundary layer transition is built. The flow is decomposed into a mean/base flow and unsteady fluctuations, whose amplitude are assumed to be

infinitesimal. Applying such assumptions to the governing equations produces a set of linearized equations, which if accompanied by the parallel flow assumption, give the famous Orr-Sommerfeld equation (OSE). Application of the OSE is commonly referred to as LST, the full breadth of which is treated in the texts of Betchov and Criminale [78], and Drazin and Reid [79]. Understanding the process by which the laminar flow begins to amplify unstable disturbances, as depicted in Fig. 2.3, began with the landmark work of Tollmien [80], who solved the OSE for flat plate boundary layer flow. Through this, Tollmien computed the neutral stability curve, thus identifying the unstable wave frequencies and Reynolds numbers at which they are present. Schlichting [81] extended these results to include growth rates within the curve of neutral stability. The two-dimensional waves modelled in their analyses are now called Tollmien-Schlichting (TS) waves.

Experimental verification of TS waves was achieved by the investigation of Schubauer and Skramstad [82]. In their investigation, the disturbances were made detectable by reducing the free-stream turbulence level and artificially disturbing the boundary layer by means of a thin vibrating ribbon. The presence of TS waves in natural transition has since been experimentally confirmed, e.g. Ref. [83]. The results of Schubauer and Skramstad [82], and others [84, 85], have reported good agreement with LST within the region of disturbances generally responsible for the transition process, i.e. low frequencies, however, disagreement emerges at higher frequencies where disturbance amplification is weak. The discrepancy has been attributed to the high sensitivity of such measurements to experimental conditions [86, 87] and the effect of disturbances produced by an oscillating band [87, 88].

Klebanoff *et al.* [89] were first to clearly show the deformation of amplified TS waves into three-dimensional structures, which when visualized form a streamwise aligned pattern of Λ-structures (e.g. see Fig. 3 in Ref. [63]). Further experiments [90, 91] showed another type of three-dimensional deformation of TS waves, in which the Λ-structures align in a staggered pattern (e.g. see Figs. 2 and 3 in Ref. [90]). Saric and Thomas [90] showed this modification of the transition process occurred by varying the amplitude and frequency of the initial TS wave. Theoretical explanation for the observed phenomena began with the works of Orszag *et al.* [92, 93], who unveiled the linear mechanism responsible for the growth of the three-dimensional mode. Herbert [63] used this observation as the basis to develop secondary instability analysis, where the solutions from LST are used as a new local base flow and three-dimensional perturbations are superposed. The resulting analysis successfully reproduced the experimental results [89–91], showing that, for relatively large initial amplitudes of the primary TS wave, the harmonic and subharmonic perturbations of the secondary instabilities move in phase with the TS waves, thus creating the streamwise peak-to-peak alignment of Λ-structures. For small amplitudes of the TS wave, maximum

amplification of the secondary disturbance occurs at subharmonic frequencies, thus creating the staggered vortex pattern. The aligned and staggered secondary disturbance patterns are now referred to as K- and H-type transition, after Klebanoff *et al.* [89] and Herbert [63], respectively.

The onset of secondary instabilities coincides with rapid disturbance growth and interaction, leading to significant non-linear effects, making the underlying assumptions of the OSE invalid. As such, the scientific community has shifted focus to numerical solutions of the Navier-Stokes equations to elucidate the 'later' stages of boundary layer transition. Early investigations [94–96] were successful in simulating incipient non-linear effects, showing that the onset of disturbance three-dimensionality and spikes in streamwise velocity fluctuations (as shown in Fig. 2.3) coincides with significant growth in local shearing, thus inducing the decay of the Λ-structures and the transition to turbulence. However, due to the computational capabilities of the time, these investigations were limited to a temporal formulation, where a spatially periodic domain travels with the disturbance and the temporal evolution is evaluated. These implementations lack physical integrity and so subsequent studies focused on a full spatial implementation [97–99]. In particular, Rist and Fasel [99] compared their DNS results of K-type transition to experiments [89, 91], finding good quantitative agreement up until the onset of non-linearities, and qualitative agreement on the dynamical behaviour of the Λ-structures. However, due to the slow spatial evolution of the primary TS wave, these DNS investigations employed large streamwise domains, and so suffered from either convergence issues [97] or truncated spanwise domains [98, 99]. These issues still persist today and so the later stages of transition in attached boundary layers remain an open topic in the research community [100].

2.2.2 Free Shear Layer

A free shear layer is formed when two fluid streams with different velocities are brought into contact, traditionally achieved downstream of a thin splitter plate, as shown in Fig. 2.4. The configuration is typically characterized by the velocity ratio of the two streams, $R = (U_1 - U_2) / (U_1 + U_2)$. The velocities are equal when $R = 0$, only one stream is present when $R = 1$, and their directions are opposite when $R > 1$. When $R \neq 0$ the flow is inviscidly unstable, as was first postulated by Helmholtz and then proven by Kelvin [101], and so the associated instability bears their names. The physical progression of a free shear layer's transition process is of interest to this thesis, and so is briefly reviewed. For a more comprehensive review, the reader is referred to Ho [102] and Huerre [103].

The velocity ratio of a shear layer dictates its dynamics, as a bifurcation of the governing instability exists at a critical value of $R = 1.32$, as established by Huerre and Monkewitz

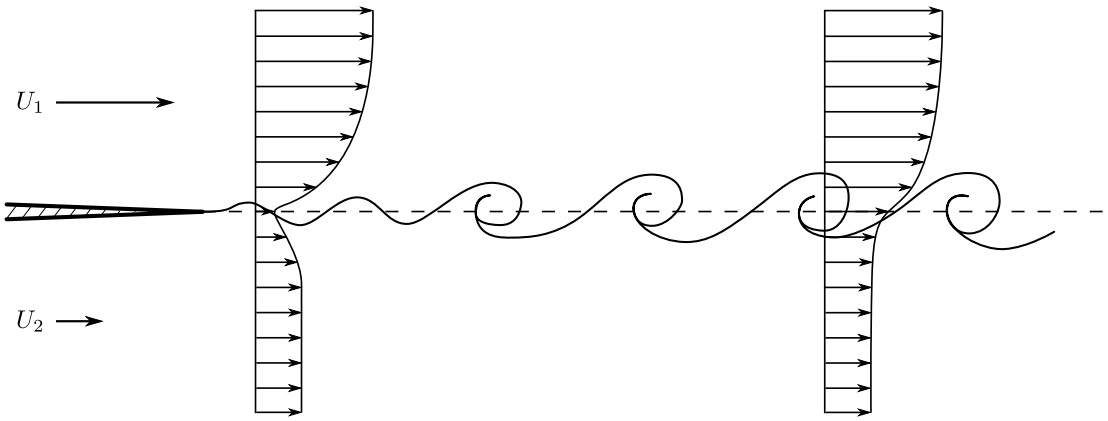

Figure 2.4: The formation of spanwise vortices in a co-flowing shear layer via the Kelvin-Helmholtz instability, after Ho [102].

[104]. For co-flowing streams and those with minor reverse flow ($R < 1.32$), the governing Kelvin-Helmholtz instability is convective in nature and the flow develops as depicted in Fig. 2.4. In the case of strong reverse flow ($R > 1.32$), an absolute or global instability is observed [71, 104]. Such flows are not the focus of this thesis, and therefore are not discussed here, however, the reader may refer to the works of Strykowski and Niccum [105]. In the case of convectively unstable mixing layers, the initial amplitude of the spatially growing wave is small. As a result, LST has been successful in predicting the characteristics of the unstable disturbances in this region, with most investigations assuming mean velocity profiles of a hyperbolic-tangent form [102]. Most notably, Michalke [106] found the most amplified frequency and growth rate of two-dimensional disturbances scale with the shear layer momentum thickness and mean velocity, i.e. with the disturbance Strouhal number, $St_\theta = 2f\theta/(U_1 + U_2)$. In the unforced case, the natural frequency of the mixing layer corresponds to the frequency of the most amplified disturbance, a value which has shown good collapse to $St_\theta \approx 0.03$ throughout literature (e.g. Table 1 in Ref. [107]) and only varies slightly within $0 < R \leq 1$ [108]. Comparisons between calculations [106, 108, 109] and experiments [110–114] have been favourable, showing good agreement between spatial growth rates and phase velocities. Furthermore, the growth rate of three-dimensional disturbances has been shown to be smaller than that of two-dimensional disturbances [115], and so the linear disturbance growth regime is characteristically two-dimensional.

Continued disturbance growth leads to the eventual roll-up of the shear layer at the frequency of the most amplified disturbance and the formation of an array of spanwise vortices, as shown in Fig. 2.4. The vortices are commonly referred to as Kelvin cat's eyes and are connected to each other by thin vorticity braids. Particularly striking flow visual-

izations of the phenomenon are presented in Refs. [116–118]. The structures are primarily two-dimensional at roll-up and are convected at the average velocity of the two streams, while growing proportionally to the difference in the stream velocities [114, 119, 120]. Experimental results has shown the growth of the perturbation energy associated with the shear layer fundamental frequency saturates, reaching a maximum at the approximate roll-up location [114], indicating the end of the linear regime and the onset of non-linearities.

Downstream of roll-up, successive pairings or triplings occur between consecutive vortices, which was first documented by Freymuth [112], followed by Browand [111], Miksad [113], and others. The investigation of Winant and Browand [116] showed the successive merging of vortices is the primary process responsible for the growth of the mixing layer thickness, and thus momentum transfer across the layer. In the case of a naturally developing mixing layer, vortex merging leads to the appearance of spectral peaks at subharmonics of the fundamental frequency [111–114]. Applying external forcing at or near the fundamental frequency synchronizes the roll-up process, creating a well defined maximum in the fundamental perturbation energy at the streamwise roll-up location, at which point the subharmonic component begins to grow, reaching a maximum at a pairing location further downstream, e.g. see Fig. 3 in Ref. [102]. However, forcing in the vicinity of the fundamental frequency inhibits pairing with respect to the natural case [103]. Ho and Huang [114] showed that the process can be manipulated by altering the forcing frequency, as after disturbance growth at the fundamental frequency saturates, a secondary subharmonic resonance mechanism gives rise to subharmonic disturbance growth [108, 121]. Thus forcing applied at the first subharmonic frequency accelerates the growth of the subharmonic mode, which was found to promote vortex pairing and increase the spreading rate of the layer [114]. Similar to the roll-up location coinciding with the peak in the fundamental mode, the pairing location occurs downstream where the subharmonic reaches a maximum [114].

The transition of the Kelvin-Helmholtz rollers to small-scale turbulence begins with the onset of three-dimensionality, which was first observed by Miksad [113]. The experimental observations of Konrad [122], and later in more detail by Bernal and Roshko [123] clearly showed the formation of streamwise oriented vortices, or rib vortices (after Hussain [124]), which consist of a single vortex line that winds back and forth between the high and low-speed sides of consecutive primary rollers [123], i.e. in the braid region. Experimental investigations [123, 125, 126] have found the behaviour of the streamwise vortices largely depends on the disturbance environment present in the facility, while numerical simulations [127–129] must employ specifically designed initial conditions to produce the structures . Mechanisms linking the streamwise vortices to the production of small-scale turbulent structures have been put forward. Huang and Ho [130] observed that small-scale motions

appeared in the vortex core region only after the first vortex pairing, and so concluded the eddies were produced by the interaction of the merging primary rollers and the streamwise structures 'trapped' in-between. However, in the experiments of Nygaard and Glezer [131] small-scale transition was observed to occur without pairing, as the interaction of the primary and secondary vortices created a trough and ridge pattern in the cross-stream direction. These distortions resulted in spanwise-periodic inflection points that served as amplifiers of broadband perturbations present in the base flow and led to the production of turbulent scales. It should be noted that the generation of small-scale erratic flow does not destroy the large-scale coherent structures, as the primary rollers can coexist with the fine-scale motion [119], even at Reynolds numbers as high as 10^7 [132].

Recent progress has been made in identifying the secondary instabilities responsible for the onset of three-dimensionality in free shear layers; the theoretical bases for which began with the stability analysis of a train of Stuart vortices (after Stuart [133]) by Pierrehumbert and Widnall [134]. Most notably, Pierrehumbert and Widnall found a 'translative' instability, most unstable to spanwise wavelengths on the order of the primary streamwise wavelength, that can lead to the generation of streamwise vorticity and coherent ridges. This was later generalized by Pierrehumbert [135] and Bayly [136], showing that a single vortex with elliptical streamlines is linearly unstable to three-dimensional disturbances, with the disturbances becoming concentrated near the centre of the vortex. This instability is now more commonly referred to as an elliptical instability, and is treated in the review of Kerswell [137]. Many of the previously discussed investigations [123, 129, 131] have appealed to an elliptical instability of the primary Kelvin-Helmholtz core, since these structures do take an elliptical form and the observed rib vortices agree well with the description of Pierrehumbert and Widnall [134]. Other investigators have abstained from placing the origin of the instability within the vortex cores, as independent and higher disturbance growths rates have been observed in the braid region [127, 128]. These observations have been supported by the stability analyses of Klaassen and Peltier [138] and Caulfield and Kerswell [139], who found that a three-dimensional instability centred on the stagnation point in the braid region appears to be preferred over any elliptical instability. This instability has been linked to that of stagnating flows with hyperbolic streamlines [140, 141], and so is referred to as a hyperbolic instability.

2.2.3 Separated Shear Layer

Despite Horton's [6] widely accepted time-averaged model of the separation bubble, the true nature of the separated shear layer is unsteady, as shown in Fig. 2.2 and observed in flow visualization experiments [15, 19, 142–144]. Following separation, the formed sep-

arated shear layer is laminar and exhibits no initial unsteadiness. Transition is initiated by the amplification of small-amplitude disturbances, present in the background, within a band of unstable frequencies in the separated region [8, 10, 145]. This initial stage of transition has been examined extensively, both experimentally [8, 9, 14, 15, 146, 147] and through DNS [7, 11–13, 21, 148, 149]. Experiments have been successful in measuring the shear layer disturbances, capturing their frequency content, spatial growth rates and convective velocities by means of hot-wire anemometry [8, 9, 14, 146, 147], fluctuating surface pressure [9, 150], and Particle Image Velocimetry (PIV) [15, 16, 51]. In DNS, the initial disturbances must be artificially generated, and so researchers have used this opportunity to investigate the effect of two- vs. three-dimensional initial disturbance input, concluding that transition is initially driven by the convective amplification of two-dimensional disturbances [13, 149]. This result has been experimentally validated [15] and agrees with the Kelvin-Helmholtz instability's preferred amplification of two-dimensional waves established in free shear layers [115]. This, however, does not obviate the need for fully three-dimensional DNS [11] since, as will be discussed later, the transition process quickly becomes three-dimensional.

The frequencies and growth rates of the unstable disturbances during the initial stage of transition have been shown to be well modelled by LST [7, 9–14]. LST has been used to identify the instabilities responsible for initial disturbance growth, showing that an inviscid, Kelvin-Helmholtz-type instability is primarily responsible [7, 9, 13, 14], while near the wall, the reverse-flow region is susceptible to a viscous instability [9, 12]. Both instabilities are convective in nature, however, Alam and Sandham [11] showed that an absolute instability develops when reverse flow velocities reach more than 15% of the free-stream, similar to the bifurcation observed for free shear layers with significant counter-flow [104]. In their review, Dovgal *et al.* [145], and more recently Boiko *et al.* [151], conclude that the spatial growth rate spectrum of linear disturbances in the separated region is roughly bounded between those of an attached boundary layer and a free shear layer. Therefore, inviscid stability analysis can provide accurate predictions for thick separation bubbles, while viscous effects need to be considered for thinner bubbles [145, 151].

The initial stage of transition is marked by exponential growth, and ends once disturbance amplitudes have increased such that non-linear interactions begin to occur [151], thus beginning the 'later stages' of transition. These interactions are of primary importance to the flow development in the aft portion of the bubble, which has been examined in experimental studies over airfoils [16, 18, 20, 39, 51, 143, 152], and flat plates with an imposed adverse pressure gradient [8, 13, 15], in addition to DNS of airfoils [21, 153–155] and flat plates [7, 11, 13, 22, 23, 49, 148, 149]. The overwhelming observation in experiments and simulations is the formation of large scale vortices through the roll-up of the separated shear layer, as illustrated in Fig. 2.2. Watmuff [8] was first to observe these structures

experimentally through a detailed study of a two-dimensional separation bubble formed over a flat plate. Using stationary and flying hot-wire anemometry, Watmuff [8] linked the detected roll-up structures to the inviscid Kelvin-Helmholtz instability by observing: (i) classic 'cat's-eye' vorticity patterns, (ii) the maximum disturbance amplitude occurring at the velocity profile inflection point, and (iii) good agreement between the observed dominant disturbance frequency and the most amplified frequency found in free shear layer transition [108]. Furthermore, Watmuff [8] found the band of disturbance frequencies to coincide with the vortex shedding frequencies. These observations supported the findings of earlier studies [7, 145], and have been substantiated by the investigations that have followed.

The shedding of shear layer vortices is, however, not ubiquitous [11, 16, 148, 155]. Alam and Sandham [11] found that, with increased levels of reverse flow, the increasing influence of the viscous instability leads to the formation of staggered large-scale Λ-vortices in the transitional region. They likened these structures to those observed in boundary layer K- and H-type transition, discussed in Section 2.2.1. Spalart and Strelets [148] also investigated a separation bubble with significant levels of reverse flows, albeit lower than that required for the onset of an absolute instability [11], finding that Kelvin-Helmholtz rollers did form but instantly became three-dimensional and broke down to turbulence. For flows over airfoils, the amount of reverse flow is directly related to the magnitude of the adverse pressure gradient, which increases with angle of attack. Therefore, larger and more persistent structures are expected at lower angles of attack. Burgmann and Schröder [16] and Balzer and Fasel [155] independently showed this to be true, as they found large vortices were only shed at lower angles of attack, while at higher angles, the vortices were smaller and broke down more rapidly. In addition, Burgmann and Schröder [16] showed the vortex shedding frequencies increased with angle of attack and Reynolds number, thus supporting the link between vortex roll-up and the fundamental disturbance of the shear layer, since the former's frequencies have also been shown to scale with angle of attack and Reynolds number [19, 46].

For convectively unstable flows, the roll-up structures tend to persist and dominate the flow development in the aft portion of the bubble [21, 39, 143, 152], and may be responsible for reattachment in the mean sense. After formation, the development of the vortices is characterized by significant three-dimensional deformations prior to the breakdown to turbulence [16, 18, 21, 23]. As a consequence, only with the recent advances in spatio-temporal measurement techniques and computational capabilities has it become possible to investigate the development of these structures. Several recent DNS studies have observed spanwise-uniform formation of the roll-up vortices [21–23], however, disparate vortex breakup mechanisms have been put forward. Brinkerhoff and Yaras [22]

attributed the breakup of the spanwise rollers to an interaction with streamwise oriented, smaller-scale vortices that originate in the attached boundary layer upstream of transition. This interaction lead to the development of a spanwise non-uniformity, followed by three-dimensional breakdown and the emergence of hairpin-shaped vortex loops in the reattached boundary layer [22]. In contrast, Jones *et al.* [21] ascribed the vortex breakup to the amplification of three-dimensional disturbances due to a combination of instabilities present in the vortex core and braid regions, similar to the elliptic and hyperbolic instabilities of plane mixing layers discussed in Section 2.2.2. Similarly, Marxen *et al.* [23] suggested that initially two-dimensional roll-up vortices undergo significant spanwise deformation due to the presence of an elliptical instability, followed by rapid vortex breakup speculated to occur due to a hyperbolic instability present in the braid region.

Much of the recent experimental progress in the study of separation bubbles is attributed to PIV. Planar PIV has been used to study the streamwise flow development in the bubble, e.g. Serna and Lázaro [143] and Lengani *et al.* [152], who both used phase-averaging techniques to identify the periodic shedding of structures. Performing time-resolved measurements removes the ambiguity associated with phase-averaging a quasi-periodic process, with such measurements performed by Refs. [16–18, 20, 33, 39, 51, 156, 157]. The majority of these investigations also employed techniques to elucidate the three-dimensional evolution of the structures, however, a wide-range of differing descriptions have been put forward. Burgmann *et al.* [51], followed by Burgmann and Schröder [16], used time-resolved and scanning PIV to analyze separation bubble development over an SD7003 airfoil at low angles of attack and Reynolds numbers between 20 000 and 60 000. For these experimental conditions, the observation of spanwise uniform structures was sporadic and in some cases not possible. The structures that formed in the separation bubble underwent rapid three-dimensional deformation into so-called 'C-shaped' vortices, followed by breakdown to turbulence [16, 51]. Zhang *et al.* [17] also performed scanning PIV measurements over an SD7003 airfoil at a similar angle of attack and Reynold numbers, where the roll-up of the separated shear layer was observed in planar streamwise views. However, identification of these structures in the three-dimensional reconstructions was not possible, as only highly three-dimensional structures downstream of reattachment were observed. Hain *et al.* [18] used planar, time-resolved PIV in two separate configurations over the same airfoil and at a Reynolds number of 66 000. In their streamwise assessment of the flow development, periodic shedding of roll-up structures was once again observed, however, no strongly coherent structures were detected in the spanwise velocity field. Instead, sinks and sources were observed, which were speculated to indicate structures of varied spanwise extent, similar to those observed by Burgmann and Schröder [16].

Some investigations have employed fully three-dimensional volumetric measurements

within a separation bubble, rather than reconstructions from planar measurements. Wolf *et al.* [20] employed Volumetric Three-Component Velocimetry (V3V), which is a proprietary derivative of defocused PIV by Willert and Gharib [158] and Pereira *et al.* [159]. Due to the relatively coarse spatial resolution of the measurements and the difficulty in resolving near-wall structures, Wolf *et al.* investigated the flow development downstream of mean reattachment, finding structures consistent with the previously discussed investigations [16–18, 51] that propagated through the redeveloping boundary layer into the airfoil wake. Similar findings were reported by Wahidi *et al.* [156], who also used V3V to investigate the coherent structures of a separation bubble formed over a NACA 4412 airfoil at a Reynolds number of 50 000. Nati *et al.* [157] successfully captured the three-dimensional roll-up and shedding of structures from a separation bubble formed over an SD7003 airfoil at a Reynolds number of approximately 30 000 using time-resolved tomographic PIV. At roll-up, uniformly distributed two-dimensional Kelvin-Helmholtz vortex filaments were observed, which developed a spanwise waviness and deformed into Λ-shaped rollers as they convected downstream. Eventually, further deformations lead to the breakdown of the rollers into three-dimensional hairpin structures.

2.3 Effect of Acoustic Disturbances on Separation Bubble Development

It is the author's hope that the previous sections have made clear and underscored the importance of a transitioning flow's sensitivity to disturbances present in the background. In the case of a separation bubble formed over an airfoil, the effect of external acoustic disturbances is of particular importance since its relevance is twofold: first as an effective flow control technique [25, 26], and second as a consequence of airfoil self-noise production [160]. As such, the topic has generally been investigated from one of these two perspectives, and therefore is reviewed in the same manner here.

2.3.1 As a Flow Control Technique

Collins and Zelenevitz [161] were first to demonstrate improvements in airfoil performance due to acoustic disturbances produced by a remote source, unlike traditional flow control techniques where momentum is directly added to the separated near-wall region [26]. Further studies have gone on to shown that the introduction of periodic acoustic waves, produced either externally [27–30, 162–164] or internally [165–167] at an appropriate frequency and amplitude can improve performance and delay stall. The externally and in-

ternally excited cases differ with respect to the location of the acoustic source, with the former located in the free-stream and the latter located at the airfoil surface. Generally, the two techniques have produced largely similar results, with the exception of the internal case requiring notably lower excitation amplitudes. However, with disturbances supplied internally, the effectiveness depends strongly on the location and orientation of the slot, an issue compounded by the fact that the optimum location and orientation remain unclear [26], and may change based on operating conditions without the possibility of easy *in situ* modification.

Regardless of the location of the acoustic source, investigations have provided similar findings with regards to the optimum excitation frequency. At angles of attack below and close to the stall angle, early investigations [28, 29, 167] suggested that the optimal excitation frequency is the frequency of the most amplified disturbance in the natural separated shear layer. Yarusevych *et al.* [164] established this correlation clearly through detailed flow visualizations and boundary layer measurements over a NACA 0025 airfoil. They showed that the separated region was reduced most effectively when excitation was provided at or near the fundamental instability frequency of the shear layer, the inference being that such excitation promotes the transition process thus leading to earlier reattachment. At post-stall angles of attack, Chang *et al.* [166] and Hsiao *et al.* [167] noted the dominate feature of the flow shifted to large scale vortices shed from the stalled airfoil, and so decreasing the excitation to the frequency of this process was necessary to achieve improvement in lift. The result was consistent with the findings of Zaman [163], who found that relatively high excitation amplitudes at frequencies an order of magnitude lower than the shear layer's fundamental frequency were required to delay stall and increase lift at high angles of attack.

The amplitude of the excitation has also been shown to be strongly linked to the effectiveness of the control technique [166]. Ahuja and Burrin [27] and Yarusevych *et al.* [30] both showed that a minimum threshold, associated with the background noise level, exists, above which excitation must be applied to influence airfoil performance. Yarusevych *et al.* [30] went on to conclude that, for moderately stalled flows, increases to the excitation amplitude narrows the airfoil wake and eventually leads to separation bubble formation, both associated with increases to lift and decreases in drag. Once a separation bubble is formed, the positive effects associated with increasing the amplitude diminishes and a maximum efficient amplitude can be identified for a given application. Further increases to the excitation amplitude, required for airfoils in deep stall [163], have been shown to incite resonant modes in the experimental facilities that influence the flow development [27, 162], thus leaving in doubt the effect of the flow control technique itself [26].

Interesting parallels can be drawn between the effects of flow control via acoustic dis-

turbances and synthetic jets. Synthetic jets effect flow changes by producing a train of vortices from alternating ejection and suction of fluid across an orifice such that the net mass flux is zero [31, 168]. In fact, some variants of synthetic jet designs employ acoustic actuator within the orifice, as high amplitude dynamic pressure fluctuations can produce the desired periodic velocity oscillations [26, 31]. The emphasized control approach for synthetic jets is the use of an actuation frequency high enough such that the jet and cross flow interaction is invariant to the timescales of the flow. This approach then decouples the effected changes in the flow from the operating frequency of the actuator [31]. However, the line between a synthetic jet and internal acoustic excitation is blurred when actuation frequencies are of the same order of those in the flow, thus making the underlying control mechanism the exploitation of a flow instability. For example, in the investigations of Amitay and Glezer [169] and Glezer *et al.* [170], when the actuation frequency approached that of the shear layer instability, aerodynamic performance was recovered by inducing unsteady reattachment through the amplification of the shear layer disturbances.

The fact remains that, regardless of the particular technique employed, in order for flow control techniques to be used successfully in practice, the underlying mechanisms by which they effect changes in the flow must be understood. In low Reynolds number flows over airfoils, this is done through exerting control over the separated shear layer/laminar separation bubble. However, due to the limitations of the experimental techniques of their time, the majority of investigations to-date have been limited to examining global changes (i.e. lift and drag). More recent investigations have shifted focus to the attendant changes in separation bubble dynamics, e.g. Refs. [30, 170], the findings of which urge further investigation.

2.3.2 Airfoil Self-Noise

Airfoil self-noise is the product of unsteady fluctuations present in the flow field interacting with the airfoil to produce noise. Brooks *et al.* [160] (see their Fig. 1) provide a categorization of the noise generation mechanisms possible in airfoil flows, of which the laminar boundary layer instability noise and turbulent boundary layer trailing edge interaction noise are relevant. With the former, common for Reynolds number at which LSBs form [34, 38, 41, 171], the initially laminar boundary layer separates to form a detached shear layer, where instability waves are coherently amplified, as discussed in Section 2.2.3. When in close proximity to the trailing edge, the instability waves scatter [40, 41], generating acoustic tones which can be as high as 40 dB above the background level [35]. In the case where the airfoil boundary layer transitions to turbulence, random fluctuations over a wide range of scales are present at the trailing edge to be scattered. This results

in sound generation over a wide range of frequencies of comparable intensity (broadband), with generally low overall intensity, e.g. Refs. [40, 172].

In the case of tonal noise emissions, the observed acoustic spectrum consists of a broadband hump superposed with a set of discrete tones of frequency f_n [34, 41, 173], where n is the ordinal number of a tone. A tonal frequency of maximum intensity, $f_{n_{\max}}$, exists in close proximity to the central broadband frequency, which follows a scaling behaviour with the free-stream velocity ($\sim U_0^{1.5}$) [34], that is different compared to the individual tones, i.e. $f_n \sim U_0^{0.8}$ [174]. Furthermore, Arbey and Bataille [41] showed that the dominant tone can shift to a neighbouring tone with a change in free-stream velocity. Therefore, the dominant tone follows a dependency on $U_0^{0.8}$ over a finite interval of Reynolds number (constant $n_{\max}$) with sudden jumps between intervals (change in $n_{\max}$), resulting in an overall trend that follows $U_0^{1.5}$. The acoustic emissions spectrum with respect to free-stream velocity is therefore arranged in what's referred to as a 'ladder' structure.

There has been much debate in the aeroacoustics research community regarding the noise generation process and the origin of the ladder structure. Arbey and Bataille [41] attribute the process to the scattering of TS waves at the trailing edge that establish a feedback loop with the upstream receptivity region. Atassi [175] pointed out that boundary layer separation and the formation of a shear layer is a strong indicator that the Kelvin-Helmholtz instability is likely responsible for amplification. This is supported by Nash *et al.* [35], who concluded that a separation bubble or separated shear layer sufficiently close to the trailing edge is a necessary condition for tonal noise production. Furthermore, later studies [36–39] found strong vortical structures, similar to those observed in separation bubbles (Section 2.2.3), that convect past the trailing edge at a shedding frequency equal to that of the primary tone. This is supported by Yarusevych *et al.* [19], who found that the central vortex shedding frequency from a separation bubble varies with U_0^m, with $0.9 \leq m \leq 1.92$, a range that compares remarkably well with the variation of f_n and $f_{n_{\max}}$. Compelling evidence in support of the acoustic feedback mechanism of Arbey and Bataille [41] has been produced both experimentally [39, 176–178] and numerically [21, 37, 42]. However, disagreement exists with respect to the location of the upstream receptivity region, as Arbey and Bataille [41] associated it with location of the maximum edge velocity, while Chong and Joseph [173] and Kingan and Pearse [179] place it where the instability first occurs.

As established in Section 2.3.1, periodic acoustic forcing can significantly change the development of the separated shear layer, and hence influence airfoil performance. Therefore tonal emissions from the trailing edge are expected to share this effect on the flow development, presumably through their acoustic feedback mechanism, however studies of this nature are scarce in literature. Pröbsting *et al.* [38, 171] investigated the noise gener-

ation mechanisms in the presence separation bubbles formed on the suction and pressure sides of a NACA 0012 airfoil, finding that suction side events lead to noise emissions at lower Reynolds numbers, while at higher Reynolds numbers events on the pressure side tend to dominate. The nature of the possible feedback mechanisms between and within the suction and pressure sides was only recently examined by Pröbsting and Yarusevych [39], who found that trailing edge tonal noise emissions, dictated by either suction or pressure side LSBs, establish a feedback with the suction side shear layer transition, and thus alter the overall LSB characteristics.

Chapter 3

Experimental Methodology

In this study, the process of transition within a separation bubble formed over an airfoil at a low Reynolds number is examined, with a focus on the role coherent structures play and the effects of controlled acoustic disturbances. The investigation was carried out using a NACA 0018 airfoil model, which was developed by Gerakopulos [180], and used in the studies of Boutilier [181], Kirk [142], and Lambert [182]. The experimental techniques employed include static and fluctuating surface pressure measurements, and time-resolved, two-component PIV measurements in two separate configurations. The studied flow conditions were selected to produce a separation bubble that: (i) is large enough such that adequate spatial resolution could be achieved with the available imaging equipment, (ii) is located on the aft portion of the airfoil, where the surface curvature is minimal, and (iii) whose principal frequencies are sufficiently removed from any of the test section's resonant frequencies. Based on these criteria, a chord Reynolds number and angle of attack of 125 000 and 4° were selected, respectively.

This chapter describes the experimental facility, model, and measurement techniques employed. Uncertainties associated with the experimental conditions and measured parameters are specified here, while Appendix A details their quantification.

3.1 Experimental Setup

3.1.1 Wind Tunnel

Experiments were performed in the recirculating wind tunnel, shown in Fig. 3.1, at the University of Waterloo. The flow is recirculated by a six blade, vane axial fan coupled to a

variable frequency driven AC motor. The flow is conditioned in the settling chamber by an aluminum honeycomb grid and five wire mesh screens, upstream of a contraction with a 9:1 ratio. The test section is 0.61×0.61 m in cross-section, 2.44 m long and is fabricated from Lexan, thus allowing full optical access. The facility was brought online at the beginning of the year 2015, and therefore required detailed characterization prior to any experimental campaigns, the results of which are presented in Appendix B and summarized here.

The free-stream characteristics were assessed in the empty test section. The uniformity was found to be within $\pm 0.4\%$ in the spanwise and vertical directions by Laser Doppler Velocimetry measurements at multiple streamwise locations. A minor favourable pressure gradient, equal to 0.23% of the free-stream dynamic pressure over the airfoil chord length, was measured in the streamwise direction. The free-stream turbulent characteristics were assessed using a single normal hot-wire probe. A turbulence intensity of 0.1% and an integral length scale of $0.2c$ were found, with signals low-pass filtered at 10 kHz ($St = 208$). Furthermore, the free-stream was verified to have no significant spectral content within the frequency range of interest to this investigation, $100 \leq f \leq 2000$ Hz ($2 \leq St \leq 42$). When band-pass filtered to within this range, the free-stream turbulence level is approximately 0.01%. The free-stream velocity was set based on a calibration between the static pressure drop across the contraction and the free-stream dynamic pressure measured by a pitot-static tube, with the associated uncertainty in the free-stream velocity estimated be less than 2.5%.

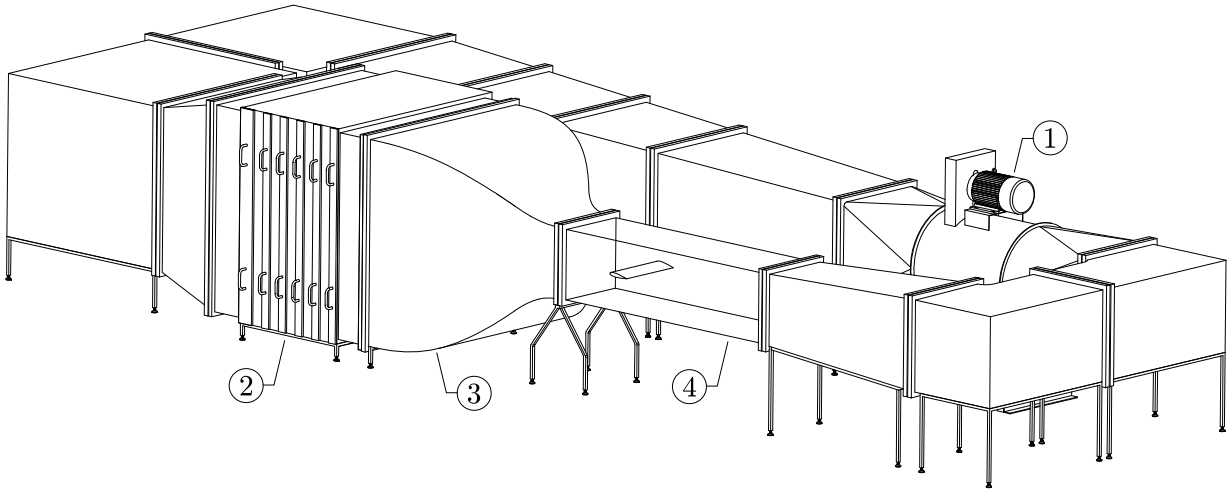

Figure 3.1: University of Waterloo recirculating wind tunnel. ① Fan and motor; ② settling chamber; ③ contraction; ④ test section.

3.1.2 Airfoil Model

All tests were performed using a NACA 0018 airfoil model with a chord length and span of 0.2 and 0.6 m, respectively. A diagram of the model is provided in Fig. 3.2, where the surface-attached coordinate system used throughout is indicated. The origin is located at the airfoil leading edge and mid-span point. The x-coordinate is co-planar with the chordline cross-section and tangent to the airfoil surface for all streamwise positions. The y-coordinate is normal to the x-direction, and the spanwise coordinate, z, is normal to the x-y plane. Traditionally, the airfoil chord length is used to non-dimensionalize the spatial coordinates, however, when employing surface-attached coordinates this results in x/c positions greater than one at or near the trailing edge. Therefore the airfoil leading to trailing edge arc length, $l = 0.206$ m, is used throughout to non-dimensionalize the spatial coordinates.

Shown in Fig. 3.2, the airfoil model has ninety-five static pressure taps of 0.4 mm diameter, sixty-five of which are arranged in a staggered row at the mid-span plane. The remainder are divided into three spanwise rows on the suction surface at chordwise locations of $x/c = 0.15$, 0.30, and 0.60. The model is also equipped with twenty-five Panasonic WM-62C condenser microphones under 0.8 mm diameter ports, twenty-two of which are distributed along the chord in a staggered row at $z/c \approx -0.2$. Further details on the model design, fabrication, and instrumentation are available in Refs. [150, 180]. The angle of attack was set using a digital protractor with an angular resolution of 0.1°. The model axis of rotation was located $0.3c$ downstream of the leading edge and $3c$ downstream of the contraction outlet, as per the recommendation of Barlow *et al.* [183]. The aerodynamic zero angle of attack was determined by measuring lift coefficients via static pressure distributions within $-5° \leq \alpha \leq 5°$ and then determining, via interpolation, the angle that gives a zero lift coefficient. At $\alpha = 4°$, the estimated solid blockage ratio is 6.1%, an amount which has been shown not to have a substantial effect on separation bubble development

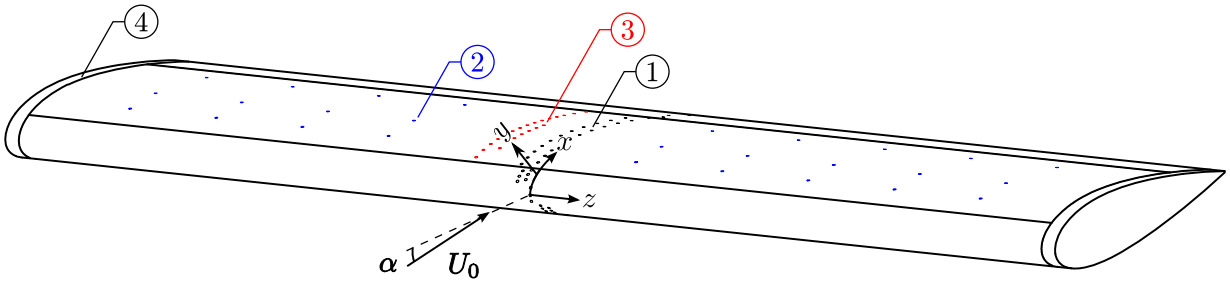

Figure 3.2: Airfoil model. ① Chordwise and ② spanwise rows of static pressure taps; ③ chordwise row of surface embedded microphones; ④ end caps.

[62], and therefore no blockage corrections were applied.

Caps were installed at the ends of the airfoil to fill the 5 mm gaps between the model and side walls. To assess end effects on the flow development over the airfoil suction side, spanwise static surface pressure and fluctuating surface pressure measurements were performed with and without end plates installed. The detailed results are provided in Appendix C, which show that, for the given experimental conditions, installing end plates had no appreciable effect on the spanwise flow uniformity and evolution of shear layer disturbances over more than 40% of the central span of the model. These findings are consistent with those of Boutilier and Yarusevych [62], and therefore end plates were not used in this investigation in order to maintain a low solid blockage ratio and to improve the quality of PIV images.

3.1.3 Acoustic Environment

All characterizing acoustic measurements in the test section were performed using a Brüel and Kjær 4192 free-field condenser microphone. Based on the instrument's precision for a frequency range of 40 to 1000 Hz ($0.8 \leq St \leq 20.8$), the uncertainty in the measured sound pressure levels (SPLs) is estimated to be ± 0.2 dB (± 20.5 µPa). For the selected experimental conditions, separation bubbles form on both the suction and pressure surfaces, with the latter forming close to the trailing edge. As discussed in Section 2.3.2, such a configuration produces tonal noise emissions, which can establish a feedback loop with a separation bubble's transition process [39]. Therefore, to isolate the effect of the controlled acoustic disturbances on the suction side LSB, the pressure side boundary layer was tripped to turbulence by a 10 mm wide strip of randomly distributed three-dimensional roughness elements (carborundum, nominal grain size 0.5 mm) placed on the pressure side at $x/c = 0.4$ (upstream of the laminar separation point). The effectiveness of the trip was assessed by microphone measurements. Similar methodologies have been employed to control airfoil boundary layer development in previous experimental studies [34, 38, 39, 177].

Controlled acoustic disturbances were provided by a Pyramid WH88 sub-woofer placed within the test section on a vibration isolating pad, more than $6c$ downstream of the airfoil trailing edge. The speaker was driven by a TOA P912-A amplifier, with the excitation signal supplied by a National Instruments (NI) USB-6259 data acquisition unit (DAQ). The free-field microphone was used to quantify the SPL on the suction surface at the separation point in quiescent conditions. Three types of acoustic excitation were employed: (1) tonal excitation at the fundamental frequency, (2) tonal excitation at the first subharmonic of the fundamental frequency, and (3) white noise band-pass filtered to the unstable frequency band, with all frequencies taken with respect to the separated shear layer's transition

process. Detailed characterizations of the excitation cases are presented in Chapter 5.

All hard walled test section environments produce acoustic standing waves of frequencies fixed by their cross-stream dimensions, e.g. see Refs. [35, 184–186]. For the wind tunnel employed, the test section is square in cross-section and therefore standing waves of only one fundamental wavelength, $d = 1.22\,\mathrm{m}$ (twice the test section dimension), are expected, in addition to higher harmonics of wavelengths $1/2d$, $1/4d$, etc. These waves travel at the speed of sound, $a = 344.4\,\mathrm{m\,s^{-1}}$ for air at 22 °C, and thus their fundamental frequency is $f = a/d$. Table 3.1 summarizes the expected wavelengths and frequencies for these acoustic waves. Spectra of acoustic pressure measured in the test section for $Re = 125\,000$ (Fig. 3.3) confirm the presence of the standing waves at the expected frequencies. In Fig. 3.3, the spectral peak associated with the fundamental tone, $St = 5.9$, is several orders of magnitude larger than the background noise level, while the higher harmonics are much less significant, particularly with the airfoil model installed. Knowledge of these of environmental acoustic disturbances is imperative, as their presence must not obfuscate the effect of the applied acoustic excitation on the transition process within the LSB.

Table 3.1: Estimated wavelengths and frequencies for acoustic standing waves present in the wind tunnel test section.

Wavelength [m]		Frequency [Hz]	St
d	1.22	282	5.9
$1/2d$	0.61	564	11.8
$1/4d$	0.30	1129	23.6

3.2 Measurement Techniques

Three quantitative measurement techniques were employed in this investigation: static surface pressure measurements using digital differential pressure transducers, fluctuating surface pressure using the airfoil model's surface embedded microphones, and planar, time-resolved velocity in two separate configurations using Particle Image Velocimetry. The procedures followed for each of these techniques are described in this section.

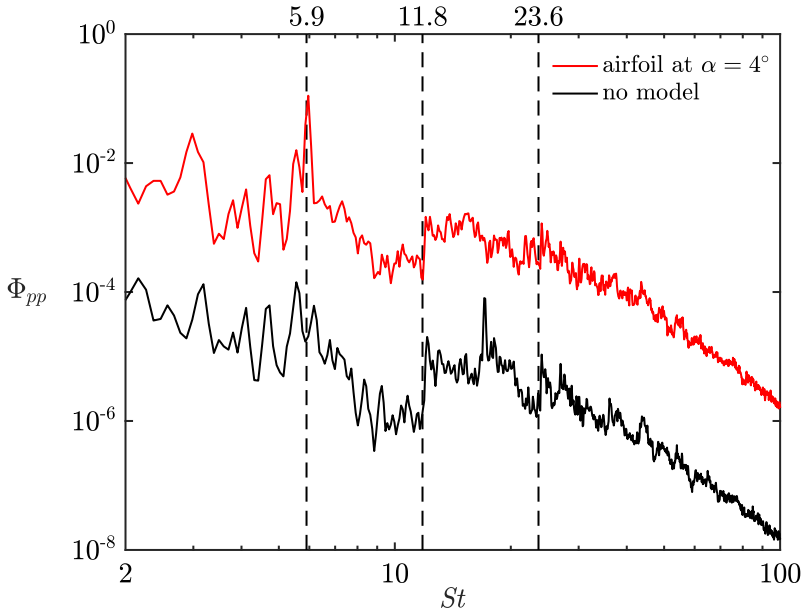

Figure 3.3: Spectra of acoustic pressure measured in the free-stream for $Re = 125\,000$. Dashed lines indicate the harmonic frequencies of the standing wave established between the test section walls. Spectra are separated by two orders of magnitude for clarity.

3.2.1 Static Surface Pressure

All static pressure measurements were performed using Setra Model 239 high accuracy differential pressure transducers with a full range of 500 Pa. The transducers were calibrated using a Druck DPI 610 LP pressure calibrator. The airfoil's ninety-five static pressure taps (Fig. 3.2) were scanned using the multiplexing configuration developed by Boutilier [181]. The taps were connected to a Scanivalve mechanical multiplexer using 0.8 mm diameter PVC tubing, whose outputs were connected to two of the Setra transducers. The reference inputs of the transducers were connected to a 0.4 mm diameter free-stream static pressure tap installed in the floor of the wind tunnel test section, $2c$ upstream of the airfoil leading edge. The ± 2.25 V outputs of the transducers were sampled by the NI USB-6259 DAQ for 4 s at 5 kHz to yield mean voltage measurements. This configuration allowed for sequential measurement of mean surface pressures relative to the free-stream static pressure in simultaneous pairs. Prior to a measurement routine, any drift in the calibrated zero-pressure voltage due to ambient temperature effects [187] was corrected for by zeroing the transducers. A delay of 30 s was employed between measurement pairs to ensure the pressure in the lines had stabilized. Based on the calculations in Appendix A, the uncertainty in all static

pressure measurements is estimated to be $\pm 0.8\%$ of the free-stream dynamic pressure.

3.2.2 Fluctuating Surface Pressure

Fluctuating surface pressures were measured using the array of twenty-five Panasonic WM-62C surface embedded microphones (Fig. 3.2) developed by Gerakopulos [180]. The microphones' outputs were amplified by an Linear Technology LT 1120 low-noise amplifier and then carried to the acquisition unit via 6 m long coaxial cables. Up to eight microphones were sampled simultaneously using a 24 bit NI PCI-4472 acquisition card, with all signals low-pass filtered at the Nyquist limit prior to digitization. All sampling of the microphone signals was performed at 40 kHz for a total of 2^{22} samples. Spectral analysis of the pressure signals is completed using the modified periodogram method [188] with signals divided into segments of 2^{14} samples using Hamming windows with 50% overlap. The resulting spectra are a result of 511 averages and have a frequency resolution of $St = 0.05$ ($f = 2.44$ Hz). The uncertainty in estimating a particular frequency using this technique is therefore $St \pm 0.025$.

The calibration of each microphone was carried out in an anechoic facility by Gerakopulos [180]. The microphones were placed in the same arrangement as that in the airfoil model and calibrated relative to a reference 4189 Brüel and Kjær microphone. A nearly constant voltage response with frequency was found for all microphones in the range $100 \leq f \leq 2000$ Hz ($2 \leq St \leq 42$). The resulting frequency response curves and sensitivity constants are presented in Ref. [180], however, these calibrations were conducted over five years ago, and as a result some drift is expected to have occurred since. Therefore the microphones were re-calibrated. Details on the procedure followed and the results are given in Appendix D, which show that the microphones' responses are still relatively flat (± 1 dB) within the aforementioned frequency range, however, the sensitivities values required, on averaged, a correction of approximately 9%.

3.2.3 Particle Image Velocimetry

Time-resolved, two-component PIV was employed in the two configurations depicted in Fig. 3.4. The flow was seeded using a glycol-water based fog with a mean particle diameter of 4 µm and illuminated by a laser sheet produced by a Photonics DM20-527 high-repetition rate Nd:YLF pulsed laser. For the side-view configuration, Fig. 3.4a, the sheet was oriented normal to the airfoil axis of rotation and passed through the mid-span plane. For the top-view, Fig. 3.4b, the sheet was oriented parallel to the airfoil surface within the investigated field of view (FOV). For both configurations, images were captured by two Photron SA4

high-speed cameras synchronized with the laser via a LaVision timing unit controlled through LaVision's DaVis 8 software.

For the side-view configuration (Fig. 3.4a), the laser beam was conditioned into a sheet using a LaVision focusing optical piece mounted directly to the laser head and sheet optics installed in the test section. The sheet optics were mounted to an adjustable breadboard and consisted of a 90° turning mirror, a 750 mm focal length spherical lens, and a −75 mm focal length cylindrical lens. The breadboard was mounted $3c$ downstream of the airfoil trailing edge. Through mean and fluctuating surface pressure measurements, it was verified that the presence of the breadboard and optics and did not affect the separation bubble. The high-speed cameras were placed on opposites sides of the test section and fitted with Nikon 200 mm fixed focal length macro lenses set to an aperture number ($f\#$) of 4. The cameras' sensors were cropped to 1024×512 pixels (px) and the fields of view were adjusted to maximize the spatial resolution in the aft portion of the separation bubble, while maintaining equal magnification factors of 0.67. The fields of view were overlapped by 10% and images were acquired in double-frame mode at a sampling rate, f_s, of 3.8 kHz and a frame separation time, Δt, of 40 µs. The frame separation time was selected to provide particle displacements of approximately 17 px in the LSB outer flow region.

For the top-view PIV measurements (Fig. 3.4b), the laser sheet was produced using the same LaVision optical piece at the laser head, in addition to a −20 mm focal length cylindrical lens. The cameras were mounted above the test section and fitted with Nikon 105 mm fixed focal length macro lenses set to an $f\#$ of 2.8. The streamwise extent of each cameras' FOV was set to match the same extent of the side-view configuration, resulting in equal magnification factors of 0.33. The full sensor resolution, 1024×1024 px, was used for both cameras. In order to overlap the fields of view by 10%, one camera was titled with respect to the desired imaging plane, and was equipped with a Scheimpflug adapter. Images were acquired in double-frame mode at $f_s = 1.95$ kHz. The detrimental effect of out-of-plane loss of particles due to strong wall-normal velocity components was mitigated through the use of a frame separation time of $\Delta t = 60$ µs, which kept particle displacements less than or equal to 9 px. This approach was deemed acceptable as the maximum random errors for this configuration were verified using the particle disparity method [189, 190] to be comparable to those for the side-view configuration.

All image capturing and processing was done in LaVision's DaVis 8 software. For both PIV configurations, the focus was adjusted to produce particles with an approximate imaged diameter of 2 px. Calibration was completed by imaging a calibration target consisting of marks on a 5×5 mm grid placed precisely within the laser sheet. Third order polynomial functions were fit to the calibration target images, resulting in fits with a standard deviation of 0.4 px or less. The particles images were pre-processed using temporal

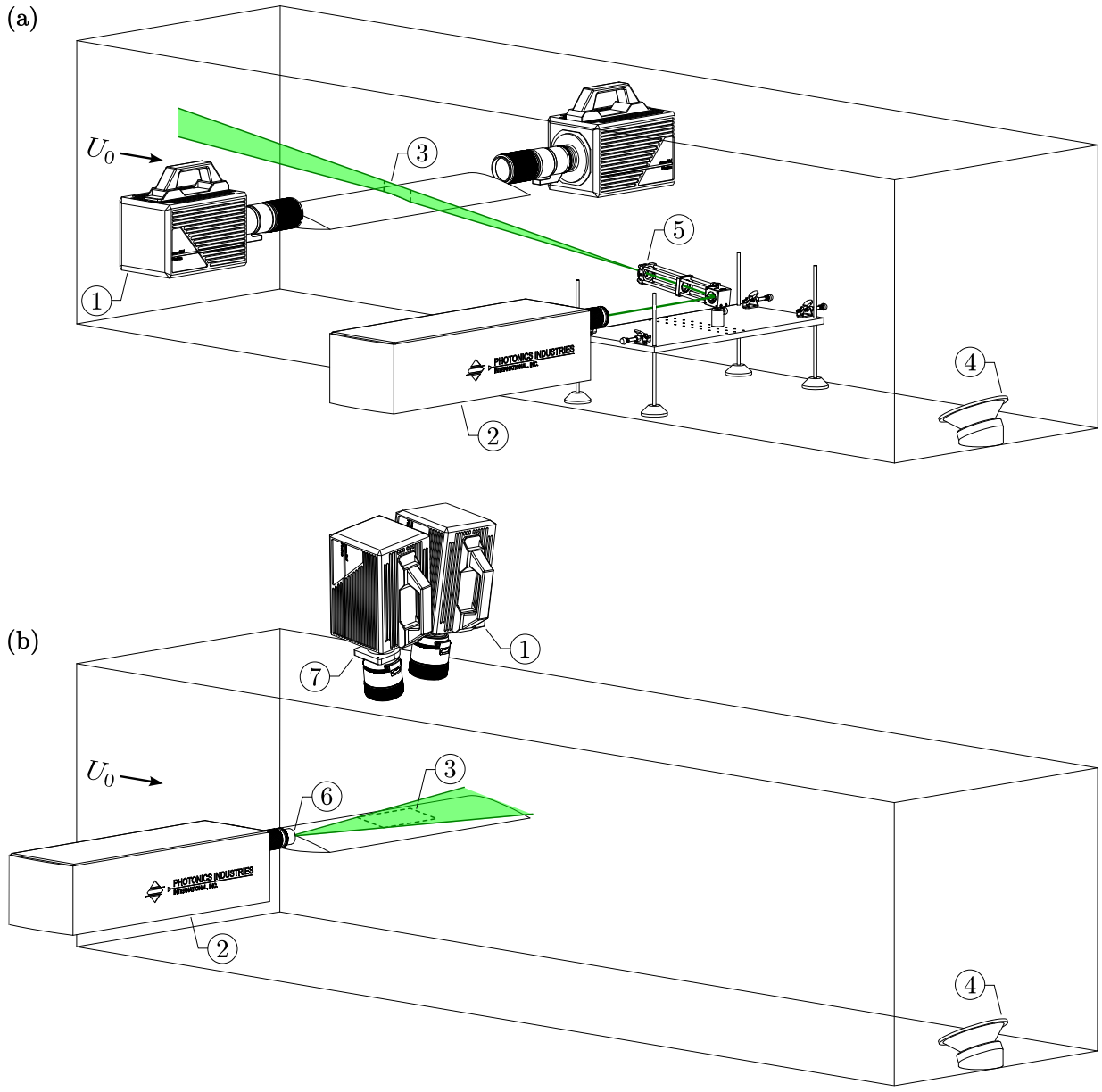

Figure 3.4: (a) Side-view and (b) top-view experimental configurations for PIV measurements. ① High-speed cameras; ② laser with focusing optics; ③ field of view; ④ speaker; ⑤ side-view sheet optics located $3c$ downstream of airfoil trailing edge; ⑥ top-view sheet optics; ⑦ Scheimpflug adapter.

sliding minimum subtraction and intensity normalization. Velocity fields were computed using an iterative, multi-grid cross-correlation scheme with window deformation. A final interrogation window size of 16×16 px with 75% overlap was employed, with each window containing, on average, 14 particles. The resulting velocity vector pitches for the side and top-view configurations are 0.12 mm and 0.24 mm ($0.0006l$ and $0.0012l$), respectively. The results were post-processed using universal outlier detection [191] and removal with vector replacement. Once the respective vector fields were calculated, the mean velocity fields for each camera were cross-correlated in the overlap region to align the FOVs. The vector fields were then interpolated onto the surface attached coordinate system with a cosine weighted blending function employed in the overlap region. Following the methods and discussion provided in Appendix A, the uncertainty in the PIV measurements within the separated shear layer are estimated to be less than 4.0% and 5.0% for the side and top views, respectively. Table 3.2 provides an overview of the pertinent PIV parameters.

Table 3.2: Parameters for PIV experiments.

Parameter	Side-view	Top-view	Unit
Laser	Photonics DM20-527		
Cameras	Photron SA4		
Lens focal length	200	105	mm
Lens $f\#$	4	2.8	
Magnification factor	0.67	0.33	
Sensor resolution	1024×512	1024×1024	px
Total field of view	55×14.5	55×106	mm
	$0.27l \times 0.07l$	$0.27l \times 0.51l$	
PIV mode	Double-frame		
Sampling rate	3.8	1.95	kHz
Frame separation time	40	60	µs
Outer flow displacement	17	9	px
Number of samples	5000	2728	
Window size	16×16		px
	0.48×0.48	0.96×0.96	mm
Vector pitch	0.12	0.24	mm
	$0.6l \times 10^{-3}$	$1.2l \times 10^{-3}$	

Chapter 4

Separation Bubble Flow Development

In this chapter, the flow development and the laminar-to-turbulent transition process in a separation bubble formed on the suction surface of a NACA 0018 airfoil at $Re = 125\,000$ and $\alpha = 4°$ is considered in the presence of natural disturbances, i.e., without controlled acoustic excitations applied. First, the streamwise flow development is evaluated based on measurements performed at the mid-span plane of the airfoil (Fig. 3.4a). Then, the spanwise evolution of coherent structures within the separation bubble is considered based on measurements performed in a spanwise-oriented view (Fig. 3.4b). Throughout, quantitative results are presented with uncertainty intervals and a brief description of how the estimates were made. More detailed information on the uncertainty analysis can be found in Appendix A.

4.1 Streamwise Flow Development

Mean surface pressure distributions, shown in Fig. 4.1, are analyzed to identify the presence and extent of the separation bubble. Following the point of minimum pressure on the airfoil suction side, the region of nearly constant pressure marks the presence of boundary layer separation [4, 45]. Following the technique of Boutilier and Yarusevych [46], the separation point is estimated as the beginning of this pressure plateau, which is estimated at $x_S/l = 0.35 \pm 0.029$. The onset and completion of rapid pressure recovery in the aft portion of the bubble are commonly used to estimate the mean locations of transition and reattachment, respectively [45, 46]. Applying these criteria in evaluating Fig. 4.1 finds these two point as $x_T/l = 0.53 \pm 0.039$ and $x_R/l = 0.60 \pm 0.040$.

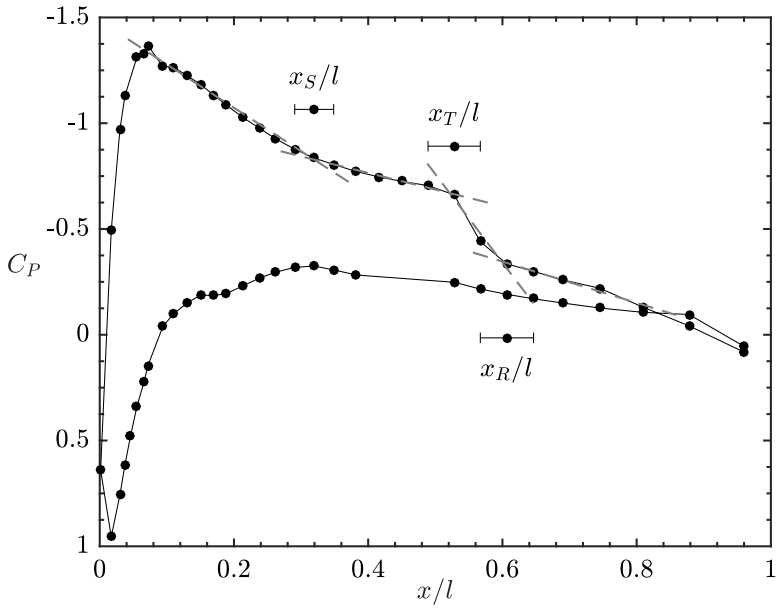

Figure 4.1: Mean surface pressure distribution. Dashed lines indicate linear fits used to estimate the mean separation, transition and reattachment points. Indicated uncertainty bounds are based on the spacing of the pressure taps. C_P values on the pressure side within $0.4 < x/l < 0.5$ are removed due to the taps being covered by the boundary layer trip.

Figure 4.2 illustrates the time-averaged flow-field characteristics of the separation bubble. A dividing streamline is identified by the solid line in each plot, and is defined as the locus of zero streamwise velocity points [44]. Linear and smoothing spline fits are applied to the dividing streamline in the fore and aft portions of the bubble, respectively, whose intersection points with the airfoil surface are used to estimate the separation and reattachment points, respectively. The mean maximum bubble height and its streamwise location, x_h, are estimated from the dividing streamline. The uncertainties in determining x_S, x_h, and x_R from the dividing streamline are indicated by the dotted lines in Fig. 4.2a, which are determined by propagating the random errors in the PIV measurements and the uncertainty in locating the airfoil surface in the PIV images through the estimation of the dividing streamline and its intersection with the surface.

The mean streamwise velocity contours (Fig. 4.2a) show the presence of the bubble extending from $x_S/l = 0.36 \pm 0.027$ to $x_R/l = 0.55 \pm 0.008$, values which agree, within the uncertainty intervals, with those determined from the mean surface pressure distribution. The bubble reaches its maximum height at $x_h/l = 0.50 \pm 0.002$, which is within the vicinity of estimated mean transition point, $x_T/l = 0.53 \pm 0.039$ from the surface pressure

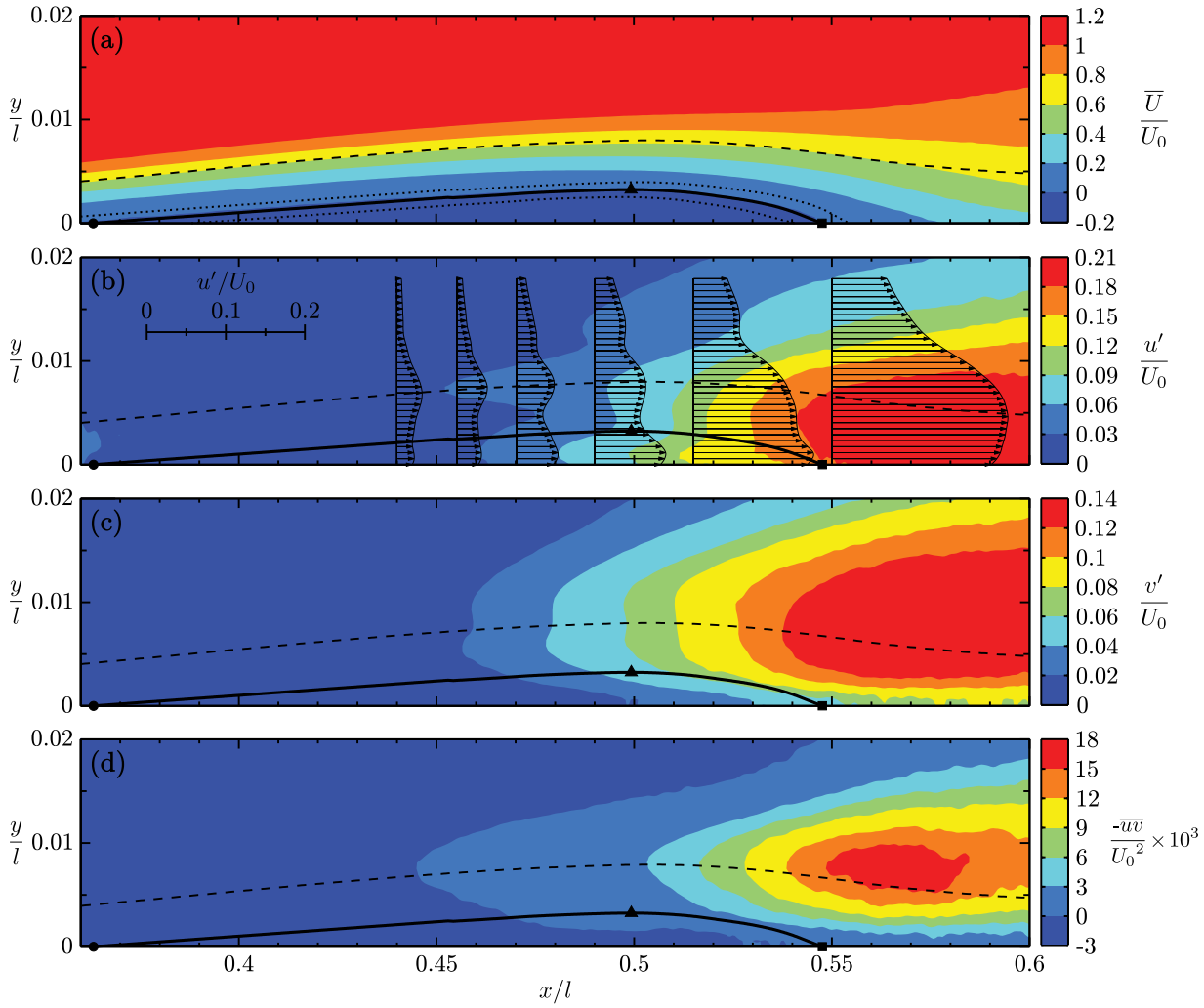

Figure 4.2: (a) Mean streamwise, (b) streamwise rms, and (c) wall-normal rms velocity contours, and (d) Reynolds shear stress contours. Solid lines mark the dividing streamline, whose uncertainty limits are indicated by the dotted lines in (a). Circle, triangle and square markers denote mean separation, maximum bubble height, and reattachment points, respectively. Dashed lines indicate displacement thickness (δ^*/l).

distribution. Within the separation bubble, reverse flow is present near the airfoil surface, with the maximum reverse velocity equal to approximately 10% of U_0, which is less than the critical limit required for the development of an absolute instability in a separation bubble [11].

The root-mean-square (rms) contour plots (Figs. 4.2b and 4.2c) show the spatial amplification of velocity fluctuations in the separation bubble. In particular, Fig. 4.2b shows the streamwise rms velocity profiles develop three distinct peaks, e.g. at $x/l = 0.47$ and 0.49, which are consistent with profiles reported in previous investigations [8, 9, 15, 33]. Upstream of mean reattachment, significant amplification follows the two near-wall peaks, with the first coinciding with the reverse flow area, and the second agreeing well with the streamwise development of the displacement thickness and the separated shear layer (Fig. 4.2a). The latter region is also associated with the strong amplification of wall-normal velocity fluctuations, as seen in Fig. 4.2c, where the rate of disturbance amplification is highest between the maximum bubble height and reattachment points, i.e. in the aft portion of the bubble.

As expected, the streamwise development of the Reynolds shear stress (Fig. 4.2d) is similar to that of the velocity fluctuations (Figs. 4.2b and 4.2c), with the locus of $\overline{uv}$ minima following the displacement thickness closely. Several investigators have relied on the Reynolds shear stress as an indicator of transition onset in the separated shear layer. Specifically, Hain *et al.* [18] and Ol *et al.* [50] identified x_T as the point where $-\overline{uv}$ exceeded an arbitrary threshold of $0.001{U_0}^2$, while Burgmann *et al.* [16, 51] and Lang *et al.* [15] used the points where the growth rate in $\overline{uv}$ sharply increases and deviates from exponential growth, respectively. Other investigators [47, 48] have used the streamwise maximum in shape factor as an estimate for transition onset. A comparison of these methods, validated against the estimate for x_T from the surface pressure measurements, is presented in Fig. 4.3. The approach of Burgmann *et al.* [16, 51] produces an estimate for x_T well outside the range established from the surface pressure measurements and therefore is deemed unsuitable. This is attributed to the method being sensitive to the noise level present in the measurement. Similarly, the thresholding approach [18, 50] produces an estimate that is too far upstream. Coincidentally, this point marks the start of a region where the shear stress undergoes spatial amplification at a fixed exponential growth rate. In this region, the method of Lang *et al.* [15] produces an estimate of $x_T/l \approx 0.54$, which is identified as the point where the Reynolds shear stress first deviates from exponential growth by 10% or more. However, this method is sensitive to both the parameters used to determine the exponential curve fit and the amount by which the shear stress is allowed to deviate. The location of maximum shape factor produces an estimate of $x_T/l = 0.50 \pm 0.010$, where the uncertainty interval is based on the random errors in the PIV measurements and the uncer-

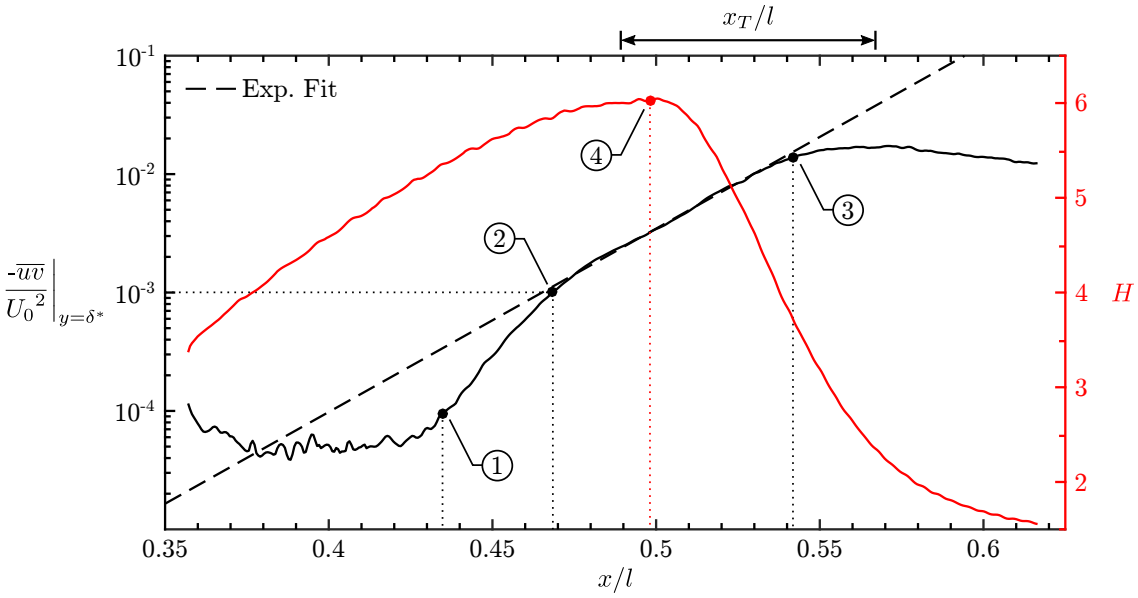

Figure 4.3: Identification of the mean transition point by means of ① sharp increase in Reynolds shear stress growth rate [16, 51], ② threshold of $0.001{U_0}^2$ [18, 50], ③ deviation from exponential growth [15], and ④ shape factor maximum [47, 48]. Range within which x_T must fall established from C_P distribution (Fig. 4.1).

tainty in locating the coordinate system origin. For the given experimental conditions, this method is preferred over the others considered here due to: (i) the estimate agreeing with the mean surface pressure measurements, (ii) the ability to unambiguously and robustly identify the estimated transition point, and (iii) the method sharing a clear link between the identification criteria and the flow physics, rather than rely on ad hoc thresholding.

A summary of the separation bubble's mean streamwise topological characteristics is presented in Table 4.1, where the estimates produced from the pressure and PIV measurements are compared. The results show good agreement between the two methods, as all values for a given location agree within the uncertainty intervals. Furthermore, the velocity-based method produces equal estimates for x_T and x_h; a result which is consistent with the findings of previous investigations [16, 18, 33], as both locations have been independently shown to correspond well with the region in which shear layer roll-up occurs. Also, it is noted that the velocity-based estimates have lower uncertainties than those of the pressure estimates. Therefore all subsequent discussions will only reference the velocity-based estimates of x_S, x_T, x_h, and x_R.

The streamwise growth of disturbances is analyzed via spectra of the wall-normal veloc-

Table 4.1: Comparison of mean separation bubble characteristics estimated from surface pressures (C_P), and streamwise velocity field ($\overline{U}$).

Method	x_S/l	x_T/l	x_h/l	x_R/l
C_P	$0.35 \pm 8.3\%$	$0.53 \pm 7.4\%$	-	$0.60 \pm 6.7\%$
$\overline{U}^*$	$0.36 \pm 7.4\%$	$0.50 \pm 1.8\%$	$0.50 \pm 0.5\%$	$0.55 \pm 1.5\%$

* Estimates for x_S, x_h, and x_R are based on the dividing streamline, while estimate for x_T is based on the shape factor.

ity fluctuations sampled at several streamwise positions within the separated shear layer, which is taken to be where $y = \delta^*$ for all x. The spectra are computed using the modified periodogram approach [188], with the velocity signals divided into equal windows of 2^{10} samples with 75% overlap, resulting in a frequency resolution of $St = 0.08$. The results are shown in Fig. 4.4a, while spectra of the surface pressure fluctuations at the same streamwise locations are shown in Fig. 4.4b for comparison. The results of Fig. 4.4a show amplification of disturbances in the separated shear layer within a wave packet centred on the frequency of the most amplified disturbances, $St = 15.6$ (dashed lines in Fig. 4.4). Initially, the energy content associated with the unstable wave packet broadens, i.e. within $0.36 \leq x/l \leq 0.48$. Further downstream, in the vicinity of the transition point ($x/l = 0.52$), the energy within the unstable band is redistributed over a wide range of frequencies, marking the later stages of transition. This leads to the appearance of broadband spectra indicative of turbulent flow near the reattachment point ($x/l = 0.57$ and 0.60).

Fig. 4.4b indicates that the amplification of the shear layer disturbances is captured by the surface pressure spectra, which has been previously reported in Refs. [9, 150]. However, the pressure spectra show earlier amplification of disturbances within the unstable band, e.g. comparing spectra at $x/l = 0.4$ in Figs. 4.4a and 4.4b. This is a result of the disturbances being of relatively low amplitude in this region and therefore falling within the noise level of the PIV measurements, rather than a reflection of the flow physics. In fact, when more sensitive experimental techniques are employed, e.g. hot-wires, previous investigations [9, 150] have shown that the amplification of vortical disturbances slightly precedes that of the pressure fluctuations, e.g. see Fig. 9 in Ref. [150]. The pressure spectra also indicate significant frequency activity at $St = 5.9$ for all streamwise locations, with the peaks at this frequency being much less significant in the velocity spectra (Fig. 4.4a). This activity is attributed to the acoustic standing wave in the test section (see Table 3.1 in Section 3.1.3), whose frequency band falls well outside the unstable wave packet of the shear layer. Thus, the standing wave does not directly influence the transition process.

The unsteady nature of the laminar separation bubble is illustrated by the sequence of

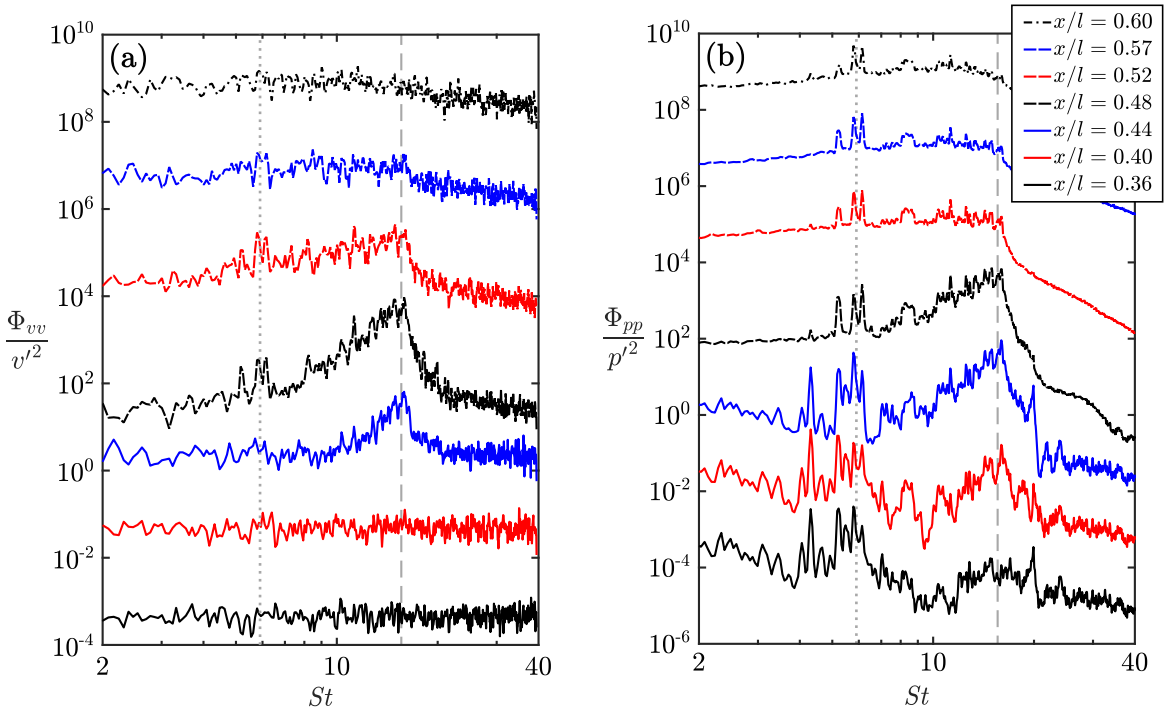

Figure 4.4: Frequency spectra of fluctuating (a) wall-normal velocity in the separated shear layer and (b) surface pressure. Each spectrum is stepped by two orders of magnitude for clarity. Grey dashed lines indicate the frequency of the most amplified disturbances, $St = 15.6$. Grey dotted lines denote the fundamental frequency of the standing wave present in the test section, $St = 5.9$ (Table 3.1).

instantaneous vorticity contours presented in Fig. 4.5. Contours of the λ_2-criterion [192] are added to aid in identifying vortical structures, in addition to dashed lines to assist in tracking individual vortices between frames. The spacing and slope of these lines give an indication of the streamwise spacing and convective velocity of the vortices, respectively. The field of view begins downstream of separation and shows the separated shear layer rolls up into periodic vortices upstream of the mean transition point ($x_T/l = 0.50$). The structures are shed, convect downstream, and undergo deformation within the vicinity of mean reattachment ($x_R/l = 0.55$), which leads to their breakdown to smaller scales further downstream.

Figures 4.5b–d span approximately one vortex shedding cycle, with a time period between consecutively shed vortices of $t^* = 0.074$ giving a shedding frequency of $St = 13.5$. This frequency falls with the unstable band captured in Fig. 4.4. Thus the results indicate

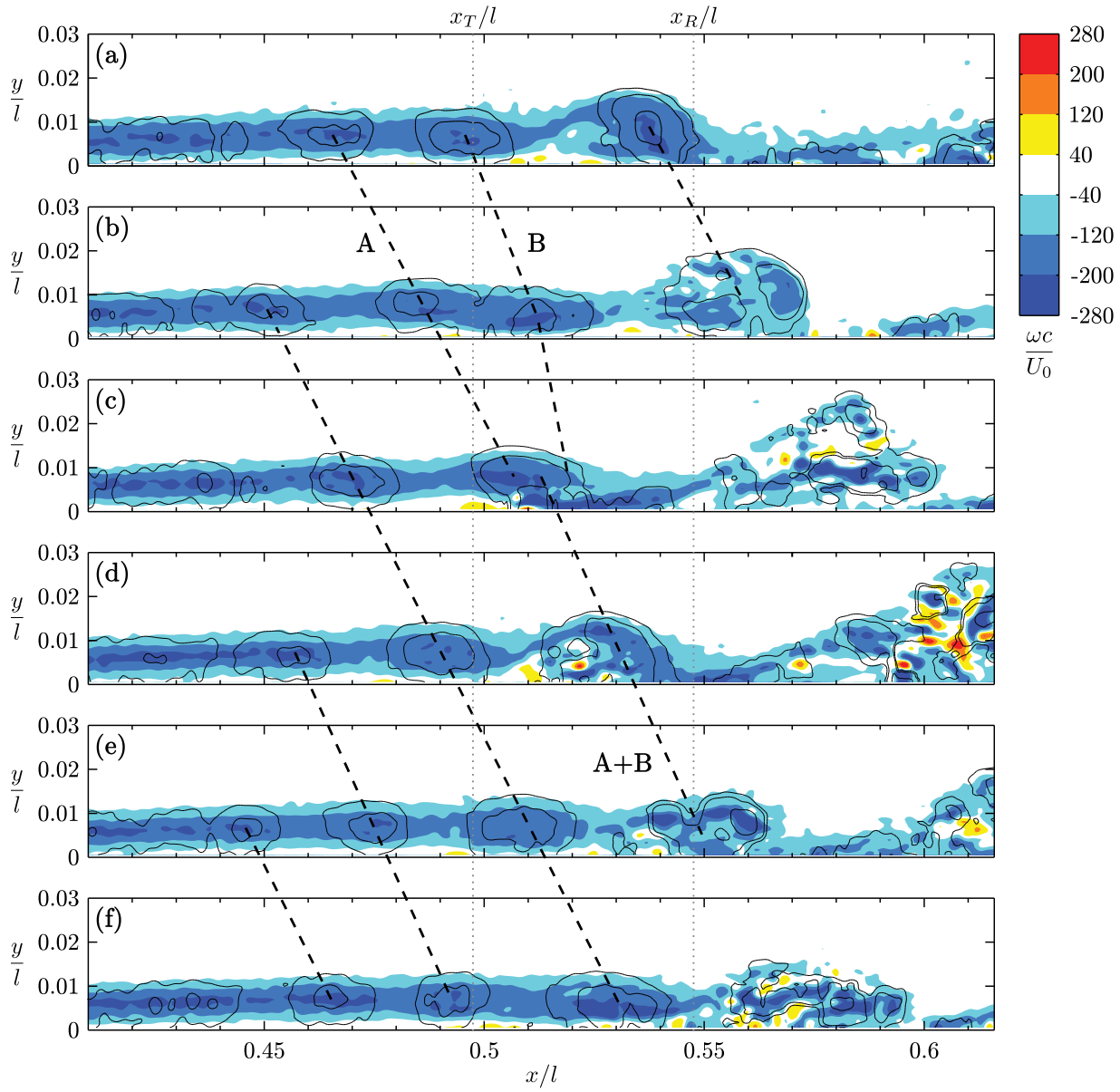

Figure 4.5: Instantaneous contours of spanwise vorticity. Each consecutive frame is separated by $t^* = 3.7 \times 10^{-2}$. Thin black lines indicate λ_2-contours, while black dashed lines trace the same vortices in the sequence.

that the amplification of unstable disturbances within a wave packet leads to shear layer roll-up and shedding of vortices at the frequency matching that of the amplified disturbances, consistent with the findings of previous investigators [7, 8, 16, 145]. The vortex shedding frequency of the separated shear layer is commonly scaled based on the momentum thickness at separation, $\theta_S/l = 0.011 \pm 5.6\%$ from Fig. E.1c, and the separation bubble edge velocity, $U_e = 1.2U_0$ from Fig. 4.2a, i.e. $St_\theta = f\theta_S/U_e$. The result is $St_\theta = 0.0153 \pm 5.6\%$, a value which agrees well with the range, $0.005 \leq St_\theta \leq 0.016$, observed in other experimental and numerical studies of separation bubbles [7, 16, 22, 193, 194], as values near the upper limit have been reported for similar Reynolds numbers and angles of attack [16].

Figure 4.5 shows that the vortices initially have comparable streamwise wavelengths, λ_x, and convective velocities, U_c. For example, consider the three most upstream traces in Figs. 4.5b–f, which correspond to a convective velocity of $U_c/U_e \approx 0.43$ and a streamwise wavelength of $\lambda_x/l \approx 0.032$. To gain insight into the spectrum of wavelengths and frequencies associated with the shedding process, a two-dimensional, wavenumber-frequency spectrum is computed. The result is shown in Fig. 4.6, which is computed by averaging spectra of v within the separated shear layer (i.e. at $y = \delta^*$) using windows of $2^8 \times 2^{10}$ points in space and time, respectively, resulting in wavenumber and frequency resolutions of $\Delta k_x l = 6.8$ and $\Delta St = 0.077$, respectively. Fig. 4.6 shows that spectral energy is concentrated along a line of nearly constant slope, indicated by the red line, which is commonly referred to as the convective ridge, e.g. Ref. [195]. It should be noted that another convective ridge, present at negative wavenumbers, is due to aliasing. Along the true convective ridge, the disturbance wavenumber, $k_x = 2\pi/\lambda_x$, and frequency, f, are related by their convective velocity: $U_c = 2\pi f/k_x = f\lambda_x$. From Fig. 4.6 then, for the frequency of the most amplified disturbances $St = 15.6$ ($f = 750\,\mathrm{Hz}$), the corresponding wavelength and convective velocity are $\lambda_x/l = 0.041$ and $U_c/U_e = 0.55$, respectively. For the latter, good agreement is found with the range $0.3 \lesssim U_c/U_e \lesssim 0.6$, which has been reported in previous investigations [9, 16, 19, 39].

The sequence in Fig. 4.5 reveals that vortex merging can occur, which was observed sporadically throughout the entire recorded sequence. For example, consider the two most upstream structures identified in Fig. 4.5a, labelled as A and B. As the two structures develop downstream, the convective velocity of B decreases in Figs. 4.5b–c, while that of vortex A remains approximately constant. This brings about the coalescence of the two vortices into one structure in Fig. 4.5d, labelled as A+B. The resulting merged vortex is separated from the nearest downstream vortex by an approximately doubled wavelength. The observed merging process is in general agreement with the stages of vortex merging described by Cerretelli and Williamson [196]. After the merge, the structure continues

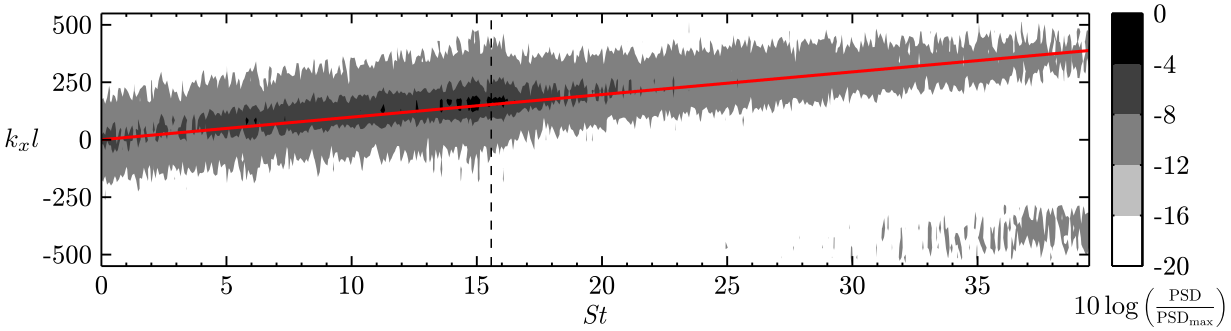

Figure 4.6: Wavenumber-frequency spectrum of wall-normal velocity fluctuations in the separated shear layer. Red line is a linear fit to the locus of energy maxima. Dashed line indicates the frequency of the most amplified disturbances, $St = 15.6$.

to convect downstream (Figs. 4.5d–f), where the well-defined vorticity pattern becomes distorted, which is attributed to vortex breakdown. The sporadic observation of merging, in addition to the absence of pronounced peaks in the velocity spectra in Fig. 4.4a outside the unstable frequency band, suggests that merging is not a strongly periodic phenomenon.

To enable a more in-depth analysis of the convective velocities, wavelengths and merging characteristics of the coherent structures, a tracking algorithm is implemented. Vortex cores are identified as distinct minima in the λ_2-field [192], with a signal-to-noise ratio (SNR) specified such that consistent identification of vortices is achieved upstream of mean reattachment. Each vortex is tracked frame-to-frame using an iterative process, where a search window is advanced downstream using an estimated convective velocity to identify the new vortex position. For the identified vortices, the convective velocity is calculated as the streamwise distance travelled by a core between frames divided by the time separation of the frames, with the position of the velocity recorded as the midpoint between the positions in the two frames. The streamwise wavelength is estimated as the streamwise distance between two neighbouring vortex cores within the same frame, and is associated to a streamwise position at the midpoint between the cores. Further specifics on the vortex tracking algorithm are provided in Appendix F.

Figures 4.7a and 4.7b depict the distributions of all convective velocities and streamwise wavelengths determined by the tracking algorithm. Both histogram are non-symmetric. From Fig. 4.7a, the average convective velocity is $\overline{U_c}/U_e = 0.43$, with a standard deviation of 0.17. This mean value falls within the aforementioned range reported in previous investigations ($0.3 \lesssim U_c/U_e \lesssim 0.6$) [9, 16, 19, 39]; however, it is lower than that predicted by the two-dimensional spectral analysis for disturbances of the most amplified frequency, $U_c/U_e = 0.55$ (Fig. 4.6). This bias to lower convective velocities is attributed to vortex

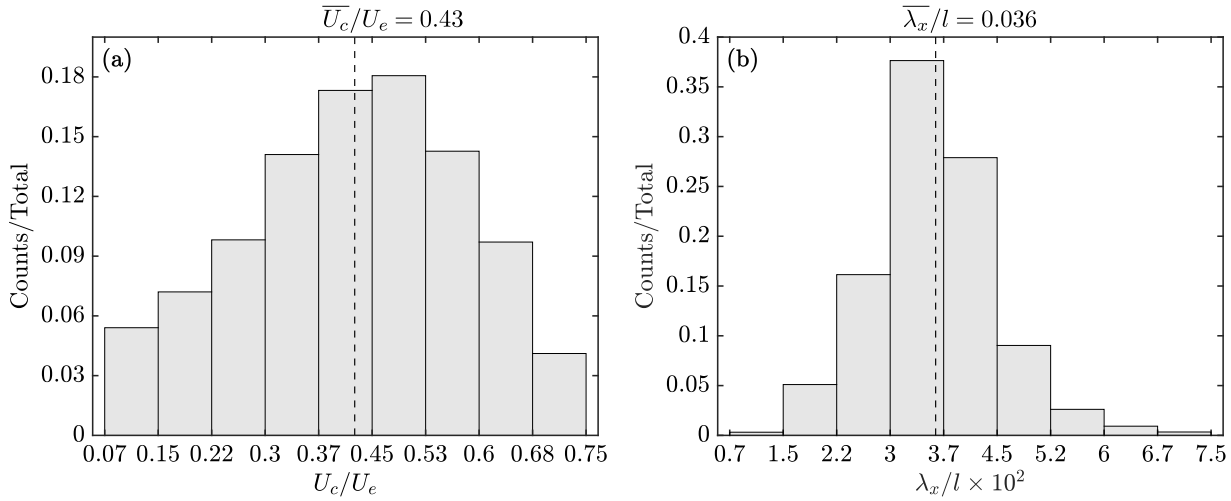

Figure 4.7: Histograms of (a) convective velocity and (b) streamwise wavelength for all tracking algorithm identified shear layer vortices.

merging since, as was observed in Fig. 4.5, the convective velocity of the downstream vortex in a merging pair decreases significantly. Such a phenomenon cannot be captured in the wavenumber-frequency spectral analysis.

From Fig. 4.7b, the average streamwise wavelength of the shear layer vortices within the bubble is $\overline{\lambda_x}/l = 0.036$, which compares move favourably with the results of the two-dimensional spectral analysis ($\lambda_x/l = 0.041$ from Fig. 4.6) than the convective velocity. This is attributed to vortex merging not introducing a similar bias in the wavelength of tracked vortices to that seen for the convective velocity (Fig. 4.7a), since during a merge while the wavelength between the two merging structures does decrease, simultaneously the wavelength between the merged structure and the next vortex downstream increases. This explains the notable excursions to higher wavelengths observed in Fig. 4.7b. In fact, vortex merging is expected to cause the wavelength between the merged paired and the nearest downstream structure to roughly double, which is reflected in Fig. 4.7b. Furthermore, confirming the analysis of the PIV sequence, the result indicate that only a relatively small fraction of vortices undergo merging under the conditions investigated.

The streamwise variation in the convective velocity of the tracked vortices is assessed in Fig. 4.8, where the average convective velocities shown, $\overline{U_{c\text{win}}}$, are computed within a sliding window, $0.04l$ in width, which is advanced downstream with 75% overlap. The error bars shown correspond to two standard deviations of the windowed data. Fig. 4.8 shows that once the roll-up vortices form and are detectable ($x/l > 0.48$), their convective velocity is greater than the average value, however their velocity decreases as the mean

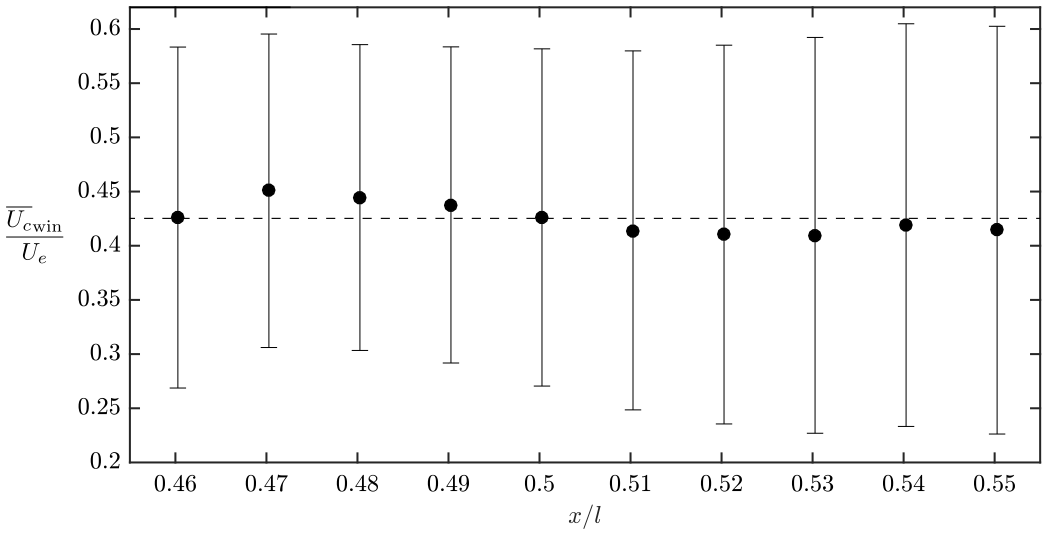

Figure 4.8: Mean convective velocities computed using a sliding window approach. Data points are plotted at the centre of each window. Dashed line indicates the average convective velocity, $\overline{U_c}$. Error bars correspond to twice the standard deviation of $\overline{U_{c\text{win}}}$.

transition point is approached ($x_T/l = 0.50$) and surpassed. This decrease is attributed to the presence of vortex merging as, again, this phenomenon causes a deceleration of the leading vortex in the merging pair (Fig. 4.5). At $x/l = 0.52$, the average convective velocity begins to increase again, indicating that the majority of merges are completed upstream of this station. Downstream of this location, either the merged or unmerged structures continuing to convect at the average convective velocity towards the mean reattachment point ($x_R/l = 0.55$).

Figure 4.9 shows the variation of the window-averaged streamwise wavelength of the vortices, $\overline{\lambda_{x\text{win}}}$, using the same sliding window approach as that employed for $\overline{U_{c\text{win}}}$. Within the region where the average convective velocity of the vortices decreases, $0.48 \leq x/l \leq 0.52$ (Fig. 4.8), the streamwise wavelength also decreases, which is consistent with vortex merging occurring in this region. Furthermore, downstream of $x/l > 0.52$, the average wavelength increases and the spread of values about the mean increase significantly, thus indicating that the excursions to higher wavelengths observed in Fig. 4.7b are most likely occurring within this region, and are due to the increase in distance between a merged pair and the nearest downstream structure.

Figure 4.10 shows the spatial distribution of all vortex cores identified within the separation bubble. The red dashed line indicates the mean vortex trajectory, which corresponds well with the displacement thickness (Fig. 4.2a), and hence the separated shear layer core.

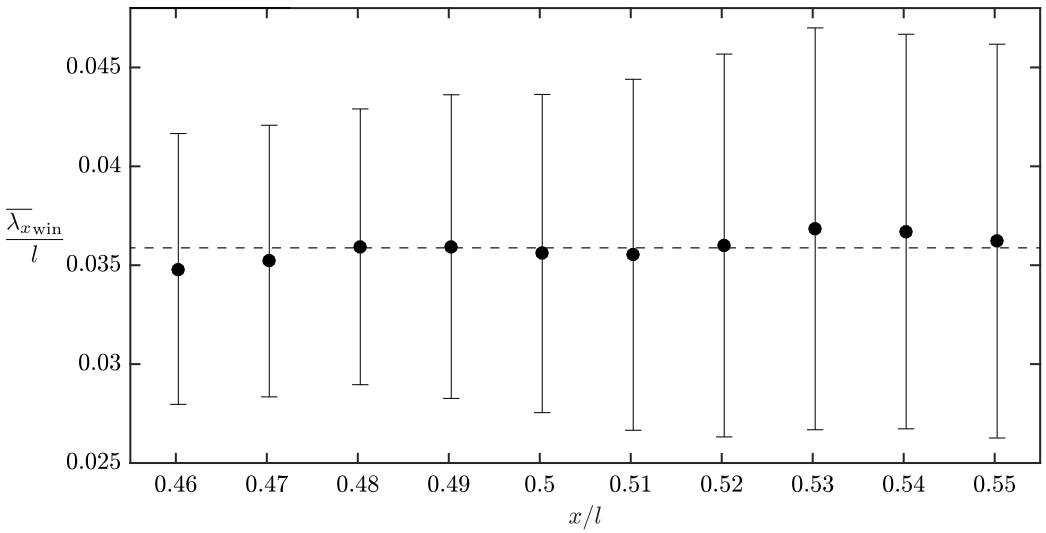

Figure 4.9: Mean streamwise wavelengths computed using a sliding window approach. Data points are plotted at the centre of each window. Dashed line indicates the average streamwise wavelength, $\overline{\lambda_x}$. Error bars correspond to twice the standard deviation of $\overline{\lambda_{x\text{win}}}$.

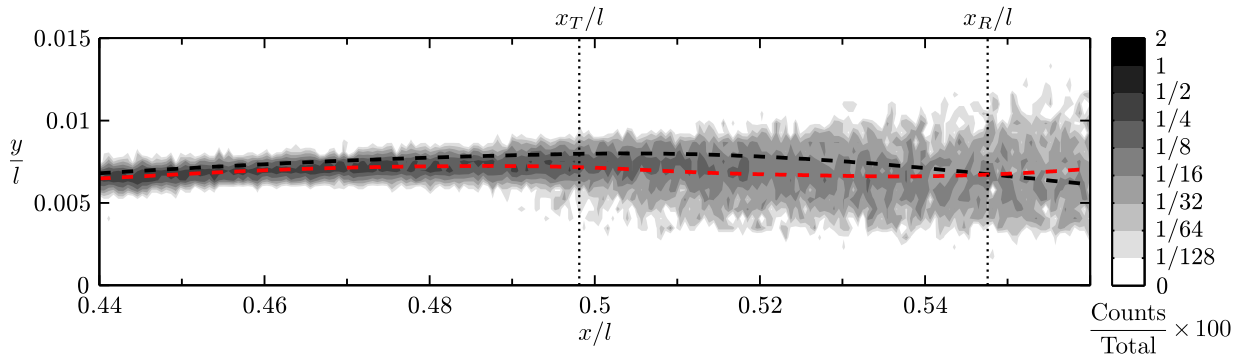

Figure 4.10: Contours of the spatial distribution of vortex core positions within the separation bubble. Red dashed line is a smoothed spline fit and indicates the mean vortex trajectory. Black dashed line indicates displacement thickness (δ^*/l).

Thus, in general, the vortices follow the outer-flow streamlines. This is particularly evident upstream of the mean transition point, where the distribution closely follows the mean trajectory. However, downstream of mean transition, the distribution widens in the wall-normal direction, suggesting increasing deviations of individual vortices away from the mean trajectory. Progressing further downstream, in the vicinity of the mean reattachment point, there are significant departures of vortices away from the wall. The mechanism by which these departures occur will be examined in the next section.

4.2 Spanwise Flow Development

PIV measurements completed in the top-view configuration (Fig. 3.4b) allow for quantitative assessment of both the streamwise and spanwise development of the shear layer vortices. The measurement plane was positioned such that it passed through the top-halves of the roll-up structures, thus allowing their identification as periodic spanwise bands of high streamwise velocity in the planar images, as seen in Fig. 4.11.

Flow is from top-to-bottom in Fig. 4.11, where coherent roll-up structures are first identifiable near the mean transition point, which is consistent with where roll-up is observed in Fig. 4.5. The structures are spanwise uniform at roll-up, which agrees with the results reported in Refs. [21, 23, 157]. However, this observation differs from the experiments of Burgmann and Schröder [16] and Hain *et al.* [18], who did not report formation of spanwise-uniform structures. The discrepancy is attributed to two factors: (i) the relatively high turbulence intensity levels in the employed water tunnels (1% and 0.3% in Refs. [16] and [18], respectively), which is known to have substantial effects on separation bubble development [50, 52, 56, 57], and (ii) limitations of the experimental apparatus, as high spatial resolution and precise laser positioning are essential for detecting relatively small-scale vortical structures at formation.

As seen in Fig. 4.11, the vortices develop spanwise deformations as they convect downstream. For example, the vortex seen at $x/l \approx 0.51$ in Fig. 4.11a (labelled as A), exhibits a spanwise unsteadiness that intensifies as it convects downstream, as seen in Figs. 4.11b–f. The most significant deformations occur near the mean reattachment location ($x_R/l = 0.55$), which lead to the breakup of the structures to smaller scales. From visual inspection of Fig. 4.11, and other sequences, the average wavelength of the spanwise undulations in the vortex filaments, λ_z, is on the order of $0.1l$. The streamwise wavelength of the main rollers in this particular sequence is approximately $0.04l$, a value which is in good agreement with the average streamwise wavelength determined from the PIV side-view measurements (Figs. 4.7b and 4.9).

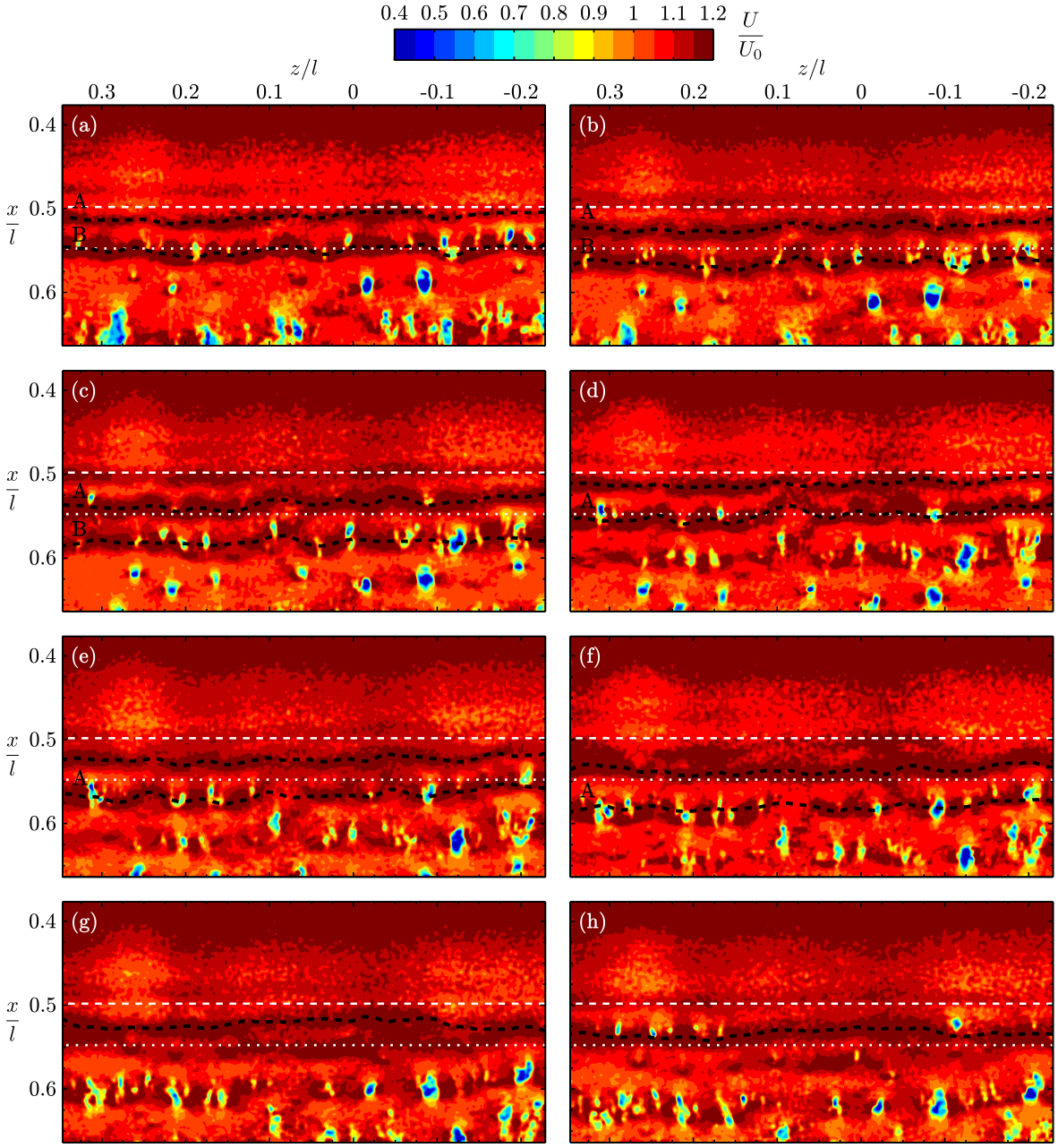

Figure 4.11: Instantaneous contours of streamwise velocity. Each consecutive frame is separated by $t^* = 2.5 \times 10^{-2}$. Dashed black lines indicate smoothed spline fits to the centre of selected structures. Dashed and dotted white lines mark the mean transition and reattachment points, respectively.

To quantify the characteristic wavelength of the spanwise deformations, spectral analysis of the streamwise velocity fluctuations is performed across the FOV at fixed streamwise locations. The results are presented in Fig. 4.12, where each spectrum is the average of spectra computed for each velocity field at the respective streamwise stations and across the entire spanwise extent of the FOV. The resulting maximum resolvable wavelength is $0.6l$. At $x/l = 0.45$ and 0.5 (mean transition), a significant, yet broad, spectral peak is observed at $\lambda_z/l = 0.2$, while a lesser peak is present at the first subharmonic of the dominant peak, $\lambda_z/l = 0.1$. The broadness of the peaks is a consequence of the relatively coarse spectral resolution at these wavelengths, which is directly limited by the spanwise extent of the FOV. Nevertheless, a range of predominant spatial wavelengths, $0.05 \lesssim \lambda_z/l \lesssim 0.3$, can be identified, which is in good agreement with the visualized structures in Fig. 4.11. Furthermore, comparing the mean spanwise and streamwise wavelengths of the structures gives a range of $1 \lesssim \lambda_z/\lambda_x \lesssim 5$, which is consistent with the numerical results of Marxen *et al.* [23], who found the length scale of the spanwise disturbances to be on the order of the streamwise extent of the vortices. Similar to the results of the present study, spanwise deformations of nominally two-dimensional flow disturbances produced by instability waves have been observed to occur as a precursor to the breakdown to turbulence in attached boundary layers [89, 90], and free shear layers [113, 123, 130, 131].

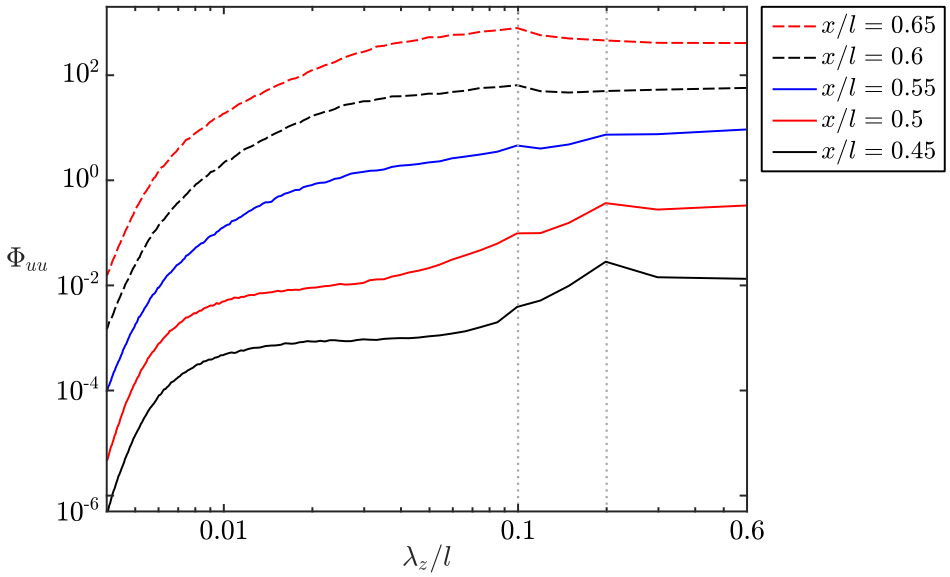

Figure 4.12: Averaged wavelength spectra of streamwise velocity fluctuations across the span. Each spectrum is stepped by one order of magnitude for clarity.

Continuing with Fig. 4.12, the peak at $\lambda_z/l = 0.2$ diminishes, while the peak at $\lambda_z/l = 0.1$ remains identifiable for all streamwise locations. Thus the results indicate that the spanwise deformations tend to persist at the first subharmonic of the roller's initial spanwise wavelength. Such spanwise periodicity is identifiable in Fig. 4.11 near the mean reattachment point, as staggered high and low velocity regions appear across the vortex cores in this region. Thus, the results suggest that the development of spanwise undulations in the shear layer vortices is linked to their breakup. In particular, the staggered high and low velocity regions throughout Fig. 4.11 coincide with the locations of the most significant spanwise deformations. For example, streamwise oriented bulges that develop in vortex A at $z/l \approx 0.2$, 0.15 and -0.1 in Fig. 4.11c are associated with the first signs of local vortex breakup in Figs. 4.11d–e. Similarly, the dominant streamwise bulges in vortex B, seen in Figs. 4.11a–c, coincide with the regions of the most significant breakup.

The breakup of the spanwise shear layer vortices in Fig. 4.11 appears to involve the reorientation of spanwise vorticity as a result of the deformation of the vortex filaments. Fig. 4.13 provides an illustration of the main aspects speculated to be involved in this process. As a spanwise undulation develops in a vortex filament, it produces a bugle in the streamwise direction and thus spanwise vorticity is reoriented into the streamwise direction. This leads to the formation of pairs of counter rotating, streamwise oriented vortex segments, which cause entrainment of high momentum fluid toward the surface and ejection of low momentum fluid away from the surface. As a result, the formation of these structures is marked by alternating regions of high and low streamwise velocity, visible in

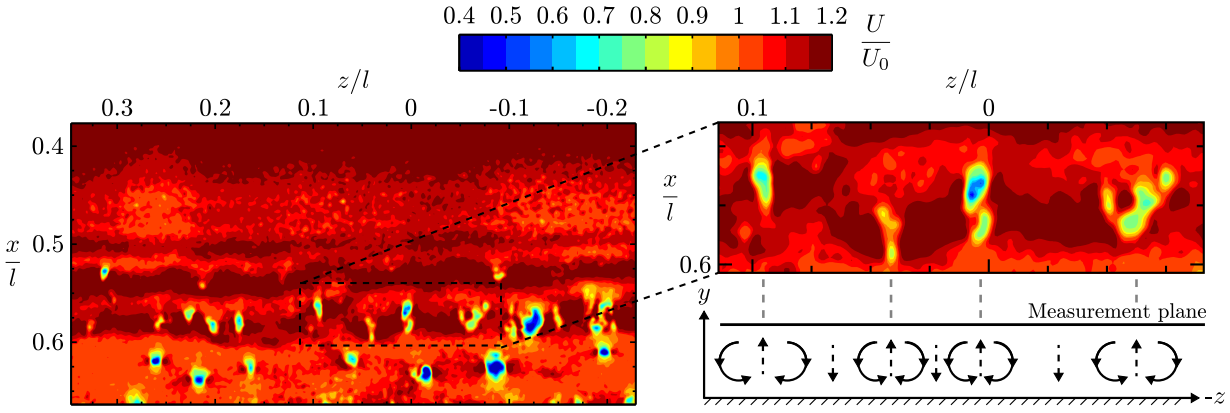

Figure 4.13: Role of streamwise vortices in the breakup of the spanwise shear layer rollers. Streamwise velocity field is reproduced from Fig. 4.11c. Inset image shows the footprints of the streamwise vortex pairs in the x-z plane and the associated flow structure in the y-z plane.

planar velocity fields at the onset of vortex breakdown, as can be seen in the dashed region of Fig. 4.13. In addition, the induced velocity of the streamwise vortex pair is expected to lift the spanwise portion of the shear layer vortex up and away from the wall, agreeing with the earlier discussed vortex lift up seen in the x-y plane measurements (Fig. 4.10) and the associated increase in the convective velocity (Fig. 4.8).

While the onset of vortex breakup appears to be associated with the spanwise deformation of the shear layer vortices and the attendant reorientation of vorticity, regions of localized breakup can be seen spreading rapidly over the entire vortex filaments (Fig. 4.11), with the distinct pattern of bands of high and low magnitude streamwise velocity appearing at wavelengths much less than $0.1l$, for example along structures A and B in Figs. 4.11f and 4.11c, respectively. Although the pattern of alternating high and low velocity streaks is rapidly distorted as the structures break up in the re-developing turbulent boundary, it suggests that the breakup of the spanwise vortex filaments away from the mean streamwise oriented bulges could be linked to the development of streamwise structures within the braid region. Such structures are not detected in the PIV measurements, however, their presence would support the conclusions of Jones *et al.* [21] and Marxen *et al.* [23], as they speculated a secondary instability present in the streamwise braids linking consecutive rollers was one of the mechanisms responsible for vortex breakdown in separation bubbles.

The presented relation between the spanwise deformation of the separated shear layer vortices in the separation and their breakdown to turbulence bears distinct similarities with transition in an attached boundary layer and free shear layer. In the former case, Tollmien-Schlichting waves undergo spanwise deformations leading to the formation of Λ-structures and the subsequent formation of turbulent spots which spread rapidly [63, 64]. In free shear layers, Kelvin-Helmholtz rollers develop significant spanwise deformations as a result of the formation of smaller scale streamwise oriented vortices that wind back and forth between the main rollers [113, 122, 123]. The appearance of such streamwise oriented structures is soon followed by the production of turbulent scales [130, 131]. Thus, the mechanisms of transition in the later stages of a laminar separation bubble involve a combination of phenomena characteristic of boundary layer and free shear layer transition.

To quantitatively relate the spanwise deformation of the shear layer vortices and their streamwise evolution, the spanwise coherence length, ℓ_z, is computed according to

$$\ell_z = \int_0^\infty R_{UU} \mathrm{d}\Delta z \tag{4.1}$$

where R_{UU} is the correlation coefficient function of two $U(t)$ signals measured at two different coordinates along the span, separated by Δz. The difficulty in evaluating ℓ_z from experimental data lies in integrating R_{UU} over a finite span when the function must

asymptotically tend to zero. The most common approach in literature is to apply an exponential curve to the correlation coefficient function [197–199]

$$R_{UU} \approx \exp\left(-\frac{\Delta z}{\ell_z}\right) \tag{4.2}$$

which is convenient since ℓ_z arises as the curve fitting coefficient. A Gaussian curve fit can also be used [200], for example

$$R_{UU} \approx \exp\left(-\frac{\Delta z^2}{A^2}\right) \tag{4.3}$$

where A is the curve fitting coefficient. Eq. 4.3 can provide a more physically consistent model compared to Eq. 4.2 since $\partial R_{UU}/\partial \Delta z = 0$ at $\Delta z = 0$, in addition to $R_{UU} \to 0$ as $\Delta z \to \infty$. In the present analysis both the exponential fit (Eq. 4.2) and the Gaussian fit (Eq. 4.3) are used to evaluate ℓ_z.

The spanwise coherence length along x/l is presented in Fig. 4.14. For both fits employed, a maximum coherence length can be identified, upstream of which the estimates are subject to high uncertainty due to the amplitude of the disturbances falling within the noise level of the measurement. The cutoff point is determined as the streamwise position where, on the average, the streamwise velocity fluctuations rise above two times the random error levels in the PIV measurements (refer to Appendix A and specifically Fig. A.3 for more details). Based on this definition, the cutoff point agrees well with the mean transtion point. Upstream of mean transition, the amplified shear layer disturbances are expected to be strongly two-dimensional [13, 15, 149], which confirms that the trend in ℓ_z upstream of the mean transition is a consequence of the noise level in the PIV measurements and is not a reflection of the flow physics. Downstream of the mean transition point, the exponential and Gaussian fits reach peak values of $\ell_z/c = 0.25$ and 0.22, respectively, at the same streamwise location, $x/l = 0.51$. Following the peak, a rapid decrease in spanwise coherence is observed, and is attributed to the spanwise deformations of the vortex filaments and the subsequent breakup observed in the PIV measurements (Fig. 4.11). The spanwise coherence reaches a minimum value of $\ell_z/c = 0.01$ shortly downstream of mean reattachment, confirming the breakup of the main rollers to smaller turbulent scales.

An evaluation of the appropriateness of the exponential fitting technique versus the Gaussian method is presented in Appendix G. The findings indicate that, in general, the exponential technique provides fits with lower root-mean-squared error for the correlation coefficient functions examined, in addition to being less sensitive to noise in the experimental data. For these reasons, the estimates of the exponential technique are preferred

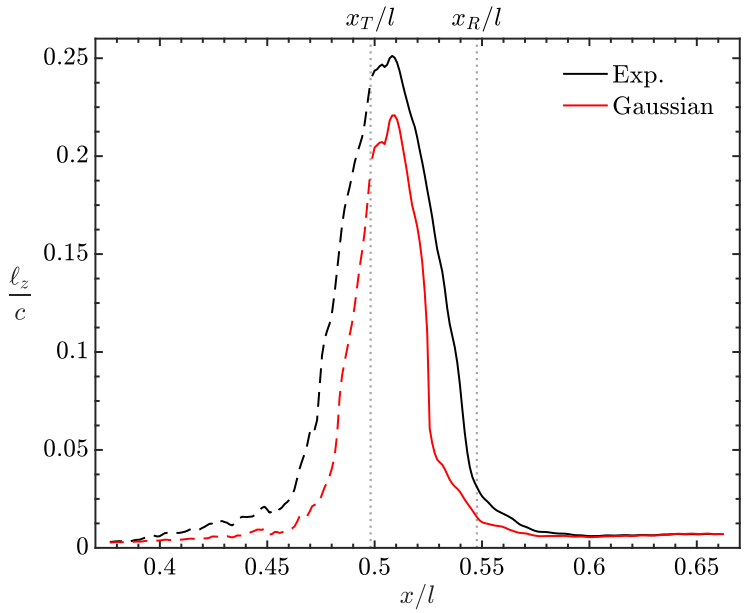

Figure 4.14: Variation of spanwise coherence length with streamwise position. Dashed portions of curves indicate where the results are affected by the measurement uncertainty.

over those of the Gaussian method, and all subsequent coherence length estimates will only employ the exponential curve fitting method.

It is instructive to compare the spanwise coherence lengths to those reported for other vortex-dominated flows. For vortex shedding behind a circular cylinder, Norberg [197] reports maximum coherence lengths of 1 to 10 diameters of the body in the near wake region (see Fig. 3 in Ref. [197]). Since the spanwise coherence length of a vortex train is expected to scale with the mean streamwise wavelength, Norberg's reported range corresponds to approximately $1 \leq \ell_z/\overline{\lambda_x} \leq 10$. In the present study, $\overline{\lambda_x} = 0.036$ (Fig. 4.7b) and so the maximum coherence length, $\ell_z/c = 0.25$, in terms of the mean streamwise wavelength is $\ell_z/\overline{\lambda_x} = 6.9$, which falls within the range given by Norberg. On the other hand, Pröbsting *et al.* [199] report spanwise coherence lengths in turbulent boundary layers on the order of the boundary layer displacement thickness. From Fig. 4.2, the displacement thickness downstream of mean reattachment is approximately $\delta^*/c = 0.005$, which agrees well with the value reached in this region, $\ell_z/c = 0.01$. This confirms that the coherence of the shear layer rollers decreases rapidly due to spanwise deformation, followed by turbulent breakdown, thus reaching values typical for turbulent boundary layers.

Chapter 5

Effect of Controlled Acoustic Excitations

In this chapter, the response of the separation bubble to controlled external acoustic excitations is considered. The flow conditions studied in Chapter 4 are maintained ($Re = 125\,000$ and $\alpha = 4°$), and excitations of three types are considered: (i) harmonic: tonal excitation at the frequency of the most amplified disturbances in the unperturbed flow, i.e. the fundamental frequency, $St = 15.6$ (Fig. 4.4), (ii) subharmonic: tonal excitation at the subharmonic of the fundamental frequency, $St = 7.8$, and (iii) random: white noise band-pass filtered to the unstable frequency band of the unperturbed flow, $10.4 \leq St \leq 20.8$ (Fig. 4.4). Harmonic excitation is studied as it has been shown to be the most effective for improving aerodynamic performance [27–30], and also models the frequency of tonal noise that would be emitted from the trailing edge of an airfoil [35–39]. Subharmonic excitation is considered since subharmonic acoustic forcing has been shown to alter the dynamics of free shear layers significantly, most notably through promoting vortex merging and increasing the shear layer spreading rate [114]. Random excitation provides a spectrum of broadband noise that the separated shear layer is receptive to, and is akin to the spectrum of broadband acoustic emissions created, for example, by a turbulent boundary layer passing over the trailing edge of an airfoil [40, 172].

Spectra of fluctuating surface pressure measured upstream of the natural separation point for all the investigated cases are presented in Fig. 5.1. The natural/unperturbed case (black curves in Fig. 5.1a) is characterized by a sound pressure level (SPL) of 88.9 dB. The natural spectrum is devoid of any significant peaks near the fundamental frequency, therefore ensuring no narrow-band environmental acoustic emissions are influencing the shear layer transition process. Figs. 5.1a and 5.1b show the spectra for the harmonic tone

(blue curves), subharmonic tone (green curve) and random (red curves) excitation cases for the investigated and quiescent flow conditions, respectively, both of which demonstrate that any given excitation is composed of only its intended frequencies. In particular, when the subharmonic excitation is applied (green curve in Fig. 5.1a) the frequencies associated with the standing wave in the test section ($St = 5.9$, refer to Table 3.1) are not excited, which indicates that the subharmonic excitation is sufficiently removed from the resonant test section frequencies for its effects on the transition process to be isolated. For all excitation types investigated, the same excitation amplitudes, in terms of SPL, were investigated: 89.5, 90.4, 97.2 and 94.9 dB. However, due to equipment limitations, only the lowest amplitude considered (89.5 dB) could be reliably studied for the subharmonic case. The cases studied and their characteristic SPLs are summarized Table 5.1.

Table 5.1: Sound pressure levels for the investigated cases.

Case	SPL [dB]				
Natural	88.9	–	–	–	–
Harmonic Tone (H)	–	89.5	90.4	92.7	94.9
Subharmonic Tone (SH)	–	89.5	–	–	–
Random (R)	–	89.5	90.4	92.7	94.9

5.1 Time-Averaged Effects

The time-averaged effects of the acoustic excitations on the separation bubble are first examined via mean surface pressure distributions, shown in Fig. 5.2. The technique illustrated in Fig. 4.1 is again employed to estimate the separation points, which is found to be $x_S/l = 0.36 \pm 0.029$ for all cases. It should be noted that, with the exception of the subharmonic case, there is a small but discernible change in the slope of the pressure plateau due to excitation, visible within $0.35 \leq x/l \leq 0.5$ in the magnified plots of Figs. 5.2a and 5.2b; however, the resultant changes in the separation location fall within the experimental uncertainty. It is in the pressure recovery region, $0.45 \leq x/l \leq 0.69$, where the effect of excitation is most significant. For both the harmonic and random excitation cases, the introduction of excitation and subsequent increase in amplitude causes the mean transition point to shift upstream ($0.49 \leq x/l \leq 0.53$), followed by a decreasing rate of pressure recovery within $0.53 \leq x/l \leq 0.69$. While the results indicate that these excitation cases cause the aft portion of the separation bubble to move upstream, the changes in the transi-

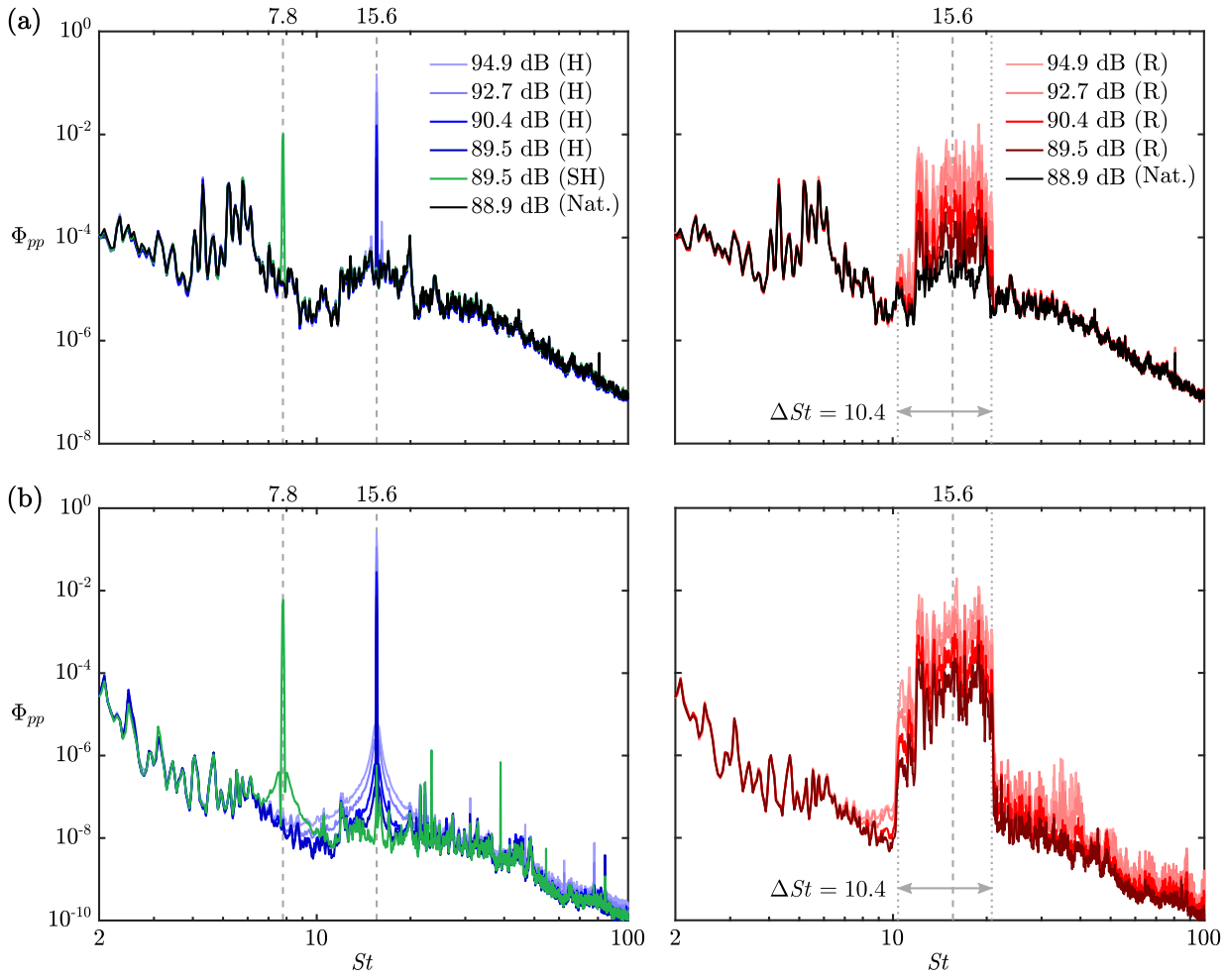

Figure 5.1: Spectra of fluctuating surface pressure measured upstream of the natural separation point for (a) the investigated ($Re = 125\,000$) and (b) quiescent ($Re = 0$) flow conditions.

tion and reattachment points fall within the spatial resolution limits of the measurements and therefore cannot be quantified precisely using this technique. Furthermore, Fig. 5.2a shows that the C_P distribution for the subharmonic case is essentially unchanged compared to that of the natural case, thus the subharmonic excitation does not effect changes that are resolvable by the mean surface pressure measurements.

Figure 5.3 illustrates the effect of excitation on the streamwise time-averaged flow field characteristics of the separation bubble. As per the technique described in Section 4.1 (refer to Fig. 4.2), dividing streamlines are identified for each case and are denoted by the solid lines. In Fig. 5.3a, the natural separation bubble extends from $x_S/l = 0.36 \pm 0.027$ to $x_R/l = 0.55 \pm 0.008$, with its maximum height equal to approximately 1.75% of the bubble's length. When excitation is applied, Fig. 5.3a reveals that the subharmonic excitation does not significantly alter any of the mean topological features of the bubble, with the changes in the x_S and x_R falling within the uncertainty of the estimation technique. For the harmonic and random cases, excitation causes the streamwise extent and height of the bubble to decrease, with the effect becoming more significant with increasing excitation amplitude. In particular, boundary layer separation is delayed, the maximum bubble height reduces and the mean reattachment point advances upstream. These observations are consistent with the behaviour of the displacement thickness (dashed lines in Fig. 5.3), as with increasing excitation amplitude, the dashed line approaches the airfoil surface, thus indicating changes to the trajectory of the separated shear layer. The changes to the mean bubble topology confirm the speculative conclusions made earlier based on the surface pressure measurements.

The rms velocity and Reynolds shear stress contours, Figs. 5.3b–d, indicate that, aside from the subharmonic case, shear layer disturbances reach higher amplitudes at earlier streamwise locations when excitation is applied, with the effect becoming more pronounced at higher excitation amplitudes. Of primary interest is the amplitude of fluctuations reached at the bubble's maximum height location, since it is here where separated shear layer roll-up generally occurs (as detailed in Section 4.1) and the identification of such a value could be related to the critical disturbance amplitude postulated by others to incite non-linear interactions and trigger formation of the roll-up vortices [8, 15, 16, 33, 151]. Examining Figs. 5.3b and 5.3c, reveals that relatively constant values of $u' = v' = 0.06U_0$ are reached at the maximum height locations regardless of excitation type or amplitude. Thus, the results suggest a critical disturbance amplitude, that when reached triggers shear layer roll-up, can be defined, which appears to be 6% of the free-stream velocity for this particular separation bubble.

While the harmonic and random excitations incite higher amplitude disturbances at earlier streamwise locations, the maximum amplitude reached by the disturbances does

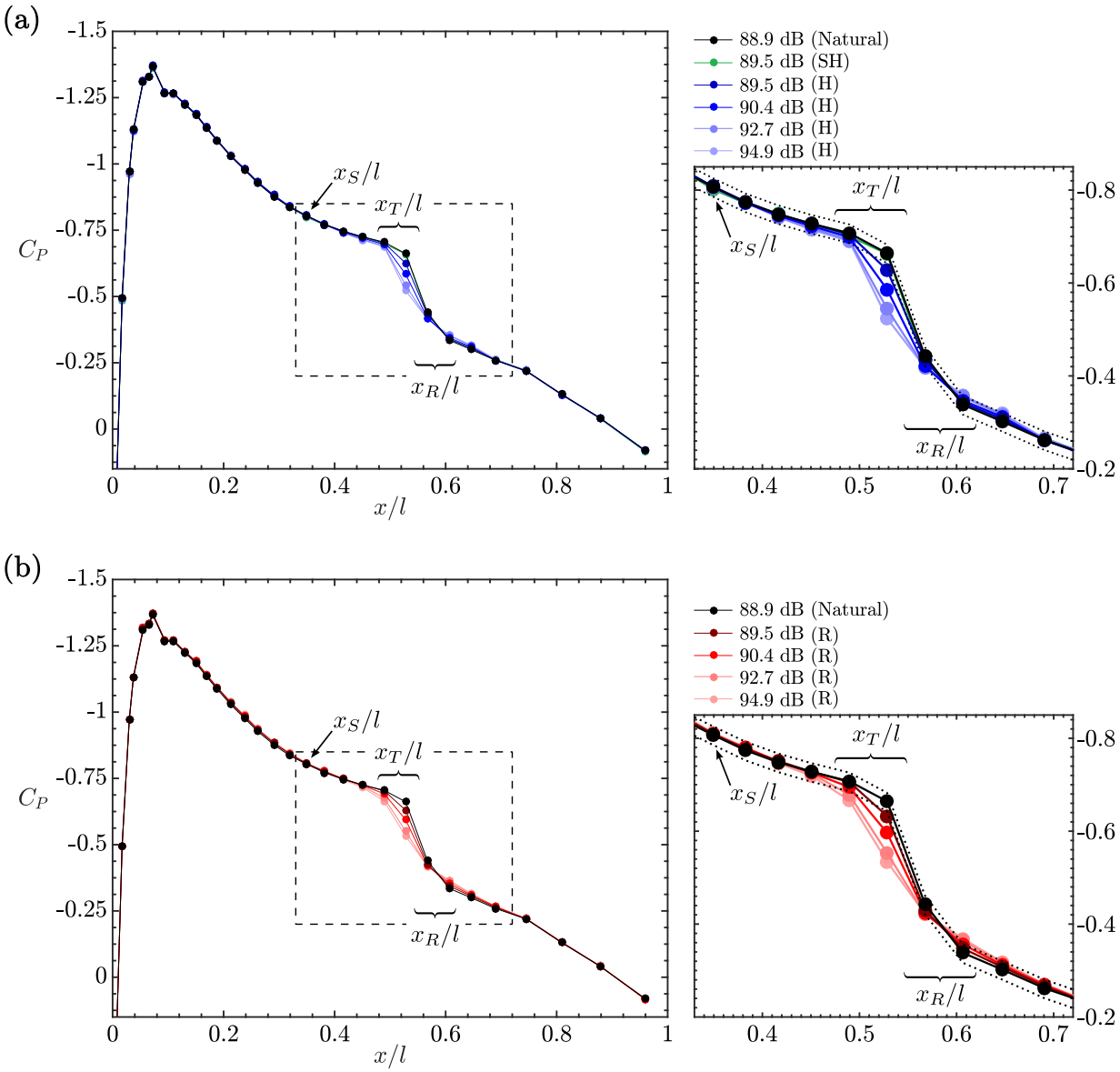

Figure 5.2: Effect of (a) tonal and (b) random excitation on mean suction surface pressure. Black dotted lines indicate uncertainty for the natural case.

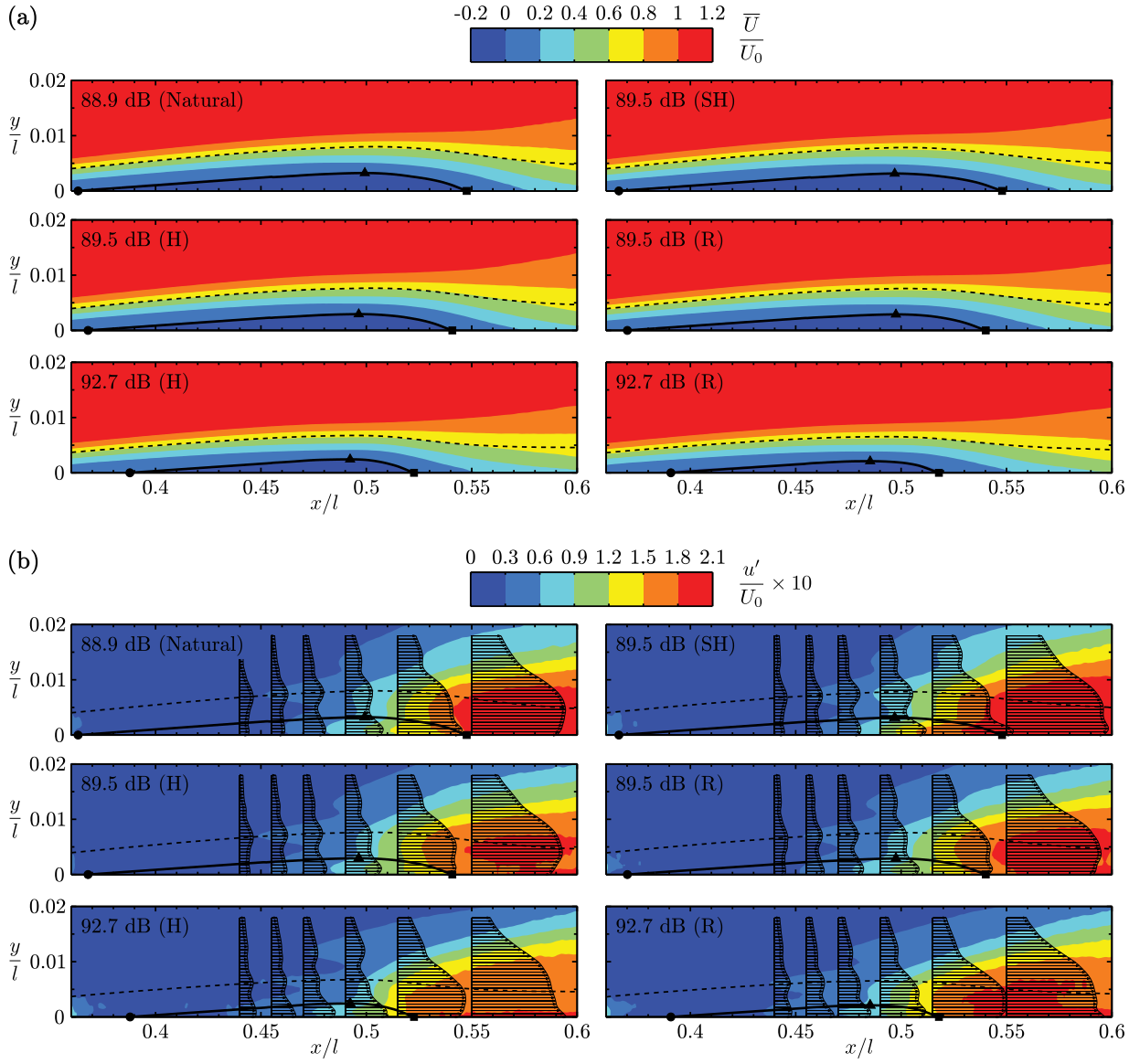

Figure 5.3: (a) Mean streamwise, and (b) streamwise rms velocity contours. Solid lines mark the dividing streamlines. Circle, triangle, and square markers denote mean separation, maximum bubble height, and reattachment points, respectively. Dashed lines indicate displacement thickness (δ^*/l).

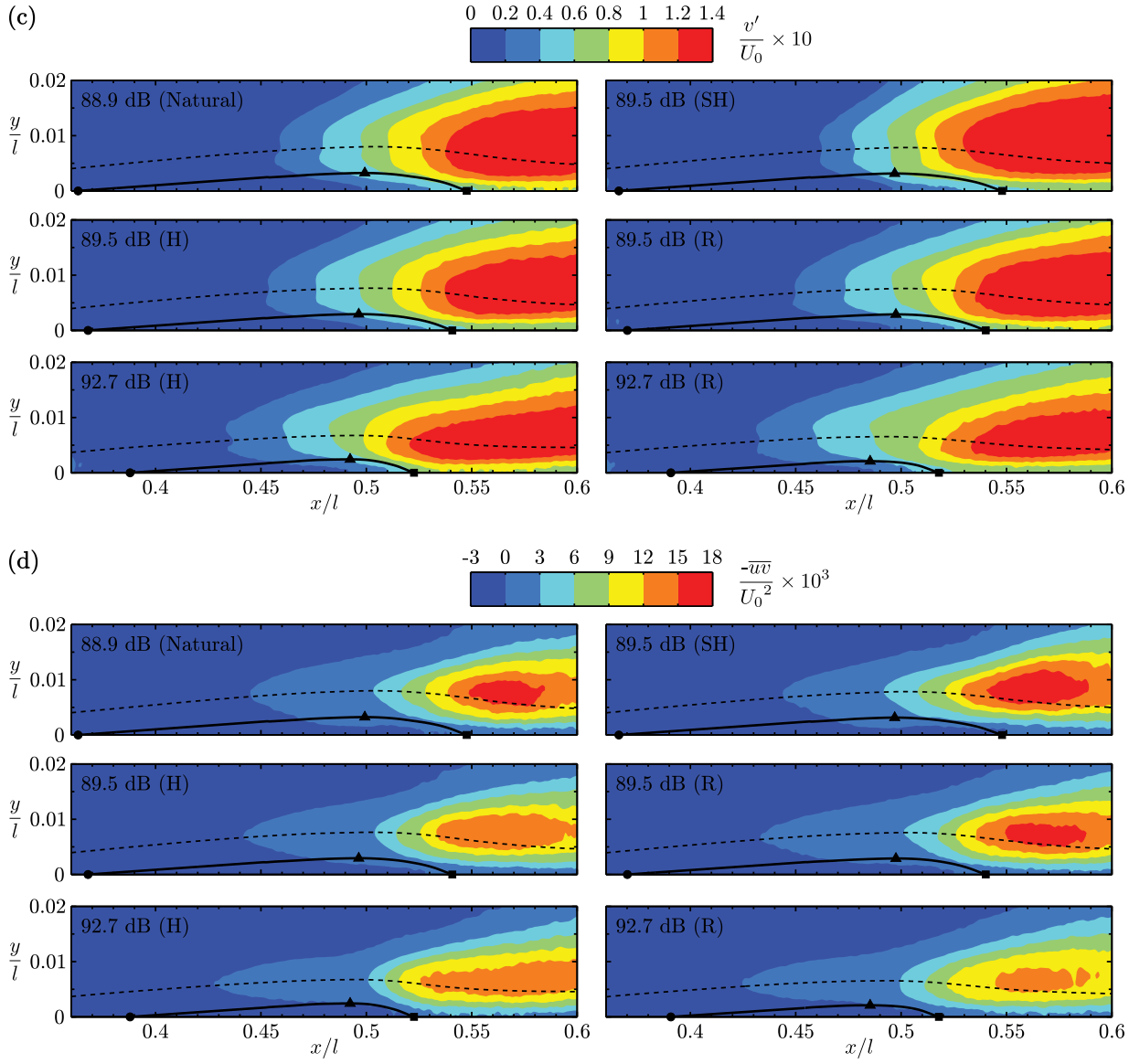

Figure 5.3 (cont.): (c) Wall-normal rms velocity, and (d) Reynolds shear stress contours. Solid lines mark the dividing streamlines. Circle, triangle, and square markers denote mean separation, maximum bubble height, and reattachment points, respectively. Dashed lines indicate displacement thickness (δ^*/l).

not increase, for example, the maximum wall-normal velocity fluctuations stay constant at approximately 14% of U_0 throughout Fig. 5.3c. In fact, Fig. 5.3b indicates that fluctuations of lower magnitude can be attained for higher excitation amplitudes in specific regions, for example, consider the region downstream of reattachment for the harmonic and random cases. This decrease in maximum amplitude is directly related to the reduction in the second u' peak from the wall with increasing excitation amplitude, which is most dramatic when excitation is applied at the fundamental frequency. This effect can be explained by the altered trajectory of the separated shear layer for these excitations cases, as according to Dovgal *et al.* [145] and Boiko *et al.* [151], reductions in the size of a separation bubble leads to an increased influence of the wall on the growth of separated shear layer disturbances. This effect was confirmed in the investigation of Yarusevych and Kotsonis [33], who found that in forcing a separation bubble, in their case via surface mounted plasma actuators, the extent of bubble decreases while maximum disturbance growth rates decrease substantially (e.g., see Figs. 17 and 18 in Ref. [33]). If then disturbance growths rates are expected to decrease and the critical amplitude required to incite shear layer roll-up is fixed, than the implication is that higher amplitude fluctuations are reached at a given streamwise location in the fore portion of the bubble due to an increase in the initial disturbance amplitude as a result of excitation. Overall, when excitation is supplied within the naturally unstable frequency band, the net effect is earlier time-averaged reattachment and a delay in separation through a modification of the mean surface pressure distribution (as seen in Fig. 5.2).

In Section 4.1, estimating the mean transition point by means of the streamwise maximum in shape factor was established as the most appropriate method for the studied flow field (refer to Fig. 4.3), and therefore the same technique is applied here. The streamwise variation in shape factor for all excitation cases is presented in Fig. 5.4 and shows that the subharmonic forcing does not produce any identifiable changes in H, while the harmonic and random excitations reduce the shape factor and shift the maxima upstream. Both of these effects increase with increasing excitation amplitude, and are attributed to the reductions in the bubble's size and the earlier onset of transition. Consistent with the findings presented in Table 4.1, the estimates of x_T from Fig. 5.4 match well with the locations of x_h from Fig. 5.3, as for any particular excitation case, the estimates of x_T and x_h differ by no more than 2%. Thus, the streamwise maximum in H and the mean streamwise location of maximum bubble height can both serve as good indicators of the mean transition location in a separation bubble, even in the presence of external forcing.

The effects of excitation type and amplitude on the mean separation bubble characteristics are summarized in Fig. 5.5. The uncertainty intervals indicated are calculated based on the random error estimates in the PIV measurements and the uncertainty in

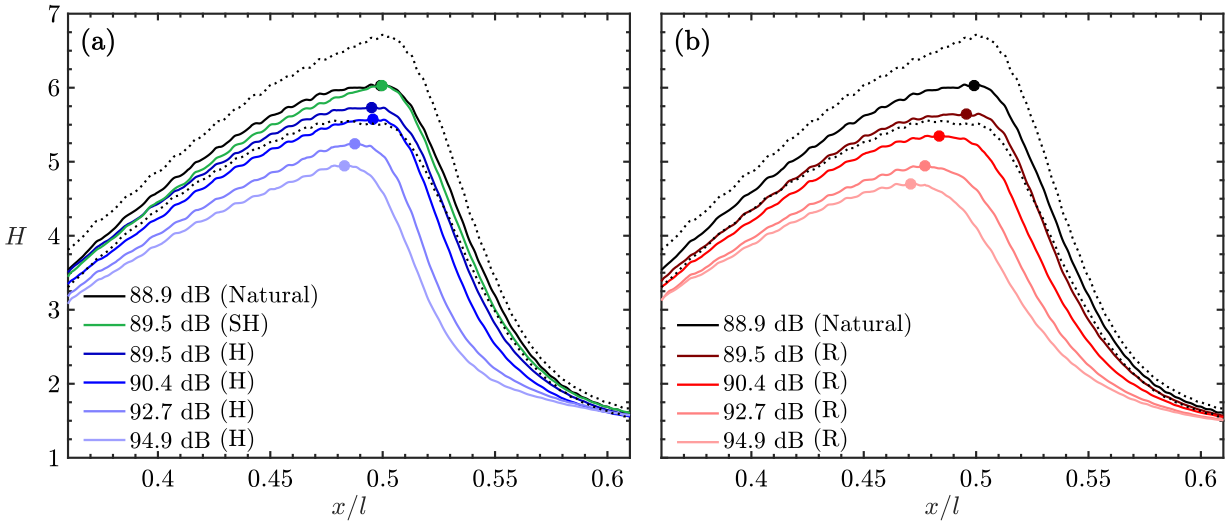

Figure 5.4: Effect of (a) tonal and (b) random excitation on shape factor. Circle markers indicate the streamwise maxima in H, which estimate the mean transition points. Black dotted lines indicate uncertainty for the natural case.

locating the coordinate system origin. For the harmonic and random cases, increasing the excitation amplitude leads to a continuous diminishment in the size of the separation bubble. While the extent of the fore portion of the bubble, i.e. the region between x_S and x_T, is presumed to decrease due to an acceleration of the transition process by providing larger initial amplitude disturbances (Fig. 5.3), the size of the aft portion of the bubble, defined as the region between x_T and x_R, also decreases. In fact, for all cases examined, the extent of the aft portion relative to the total bubble length, $(x_R - x_T) / (x_R - x_S)$, is constant at approximately 25%. Therefore external acoustic excitation supplied within the shear layer's unstable frequency band is effective in proportionally decreasing both the fore and aft portions of the bubble. It is in the aft portion of the bubble where non-linear disturbance interaction [8, 23, 151] and shear layer roll-up occurs (Fig. 4.5). How these phenomena are affected by the forcing and produce the observed mean effects will be examined in detail in Section 5.2.

Comparing the results pertaining to harmonic and random excitation in Fig. 5.5 shows that the uncertainty intervals for estimates of x_T or x_R at equals SPLs generally overlap, thus indicating that these two types of excitations may have equivalent mean effects on the flow field. However, for all SPLs investigated, the random excitations consistently produce larger upstream shifts in x_T and x_R. If these two types of excitation were equivalent, one would expect these variations to be random, rather than the observed trend. Thus the

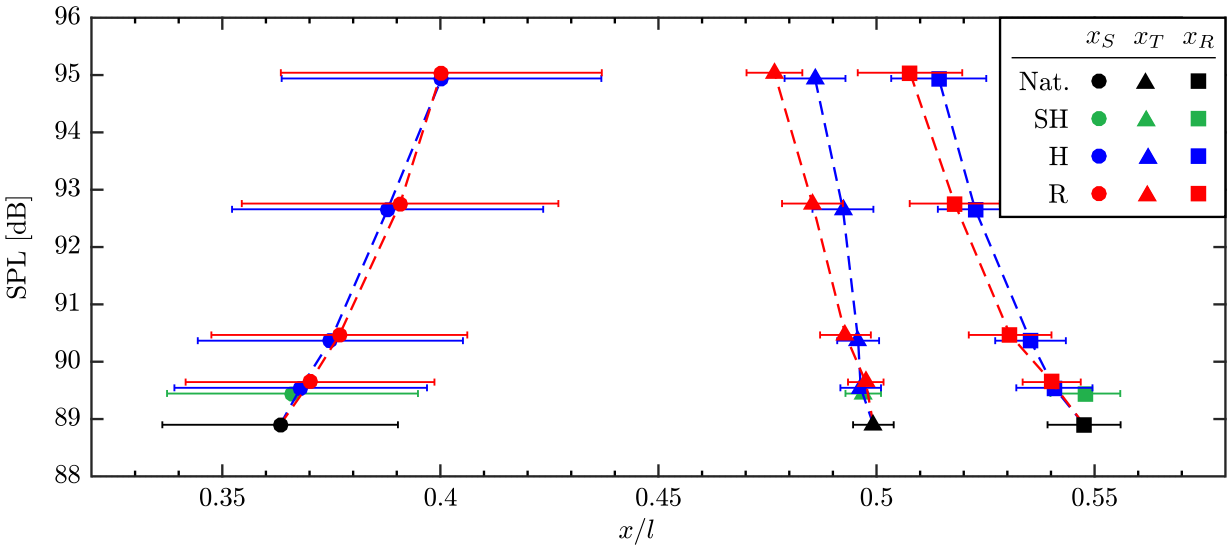

Figure 5.5: Effect of excitation on the mean streamwise locations of separation (x_S), transition (x_T), and reattachment (x_R). Points of equal SPL are offset slightly in the vertical direction for clarity.

random excitations may in fact be more, albeit slightly, impactful on the later stages of transition in the LSB. This assertion will be examined in greater detail in Section 5.3. Furthermore, Fig. 5.5 highlights that, while no distinguishable mean flow field effects have been observed due to the subharmonic forcing, this may be a result of the investigated SPL being limited to a low value and thus unable to produce observable changes in the mean field. Therefore it is left to an examination of the separation bubble dynamics to elucidate any effects of the subharmonic forcing.

5.2 Impact on Separation Bubble Dynamics

5.2.1 Harmonic Tonal Excitation

The streamwise growth of velocity perturbations in the presence of harmonic tonal excitation is analyzed via spectra of the wall-normal velocity fluctuations within the separated shear layer (at $y = \delta^*$) presented in Fig. 5.6. The same approach as that employed in Section 4.1 is used here to compute the spectra, resulting in a frequency resolution of $St = 0.08$. In Fig. 5.6a, the natural band of amplified disturbances is present within $10 \lesssim St \lesssim 20$, and at streamwise locations within the vicinity of the mean transition point

($x_T/l = 0.50$ for the natural case). When the flow is excited at the natural frequency of the most amplified disturbances, $St = 15.6$, the energy content within the unstable band locks to the excitation frequency, with the effect becoming more pronounced with increasing excitation amplitude. For example, consider the spectra at $x/l = 0.4$ and 0.44 in Figs. 5.6a–c. These spectra also reveal that the frequency band of amplified disturbances decreases in width, while the energy content at the most amplified disturbance frequency increases with increasing excitation amplitude. This indicates that higher amplitude fluctuations are reached earlier in the separated shear layer, consistent with the results presented in Fig. 5.3. Furthermore, the excitation also causes the amplified disturbances to persist farther downstream, as substantial peaks are observed in the spectra downstream of mean reattachment in Figs. 5.6b and 5.6c, which are not present for the natural case (Fig. 5.6a). This implies that tonal excitations at the fundamental frequency may delay the breakdown of periodic disturbances, which then persist in the developing turbulent boundary layer.

The effect of harmonic excitation on flow development within the separation bubble is

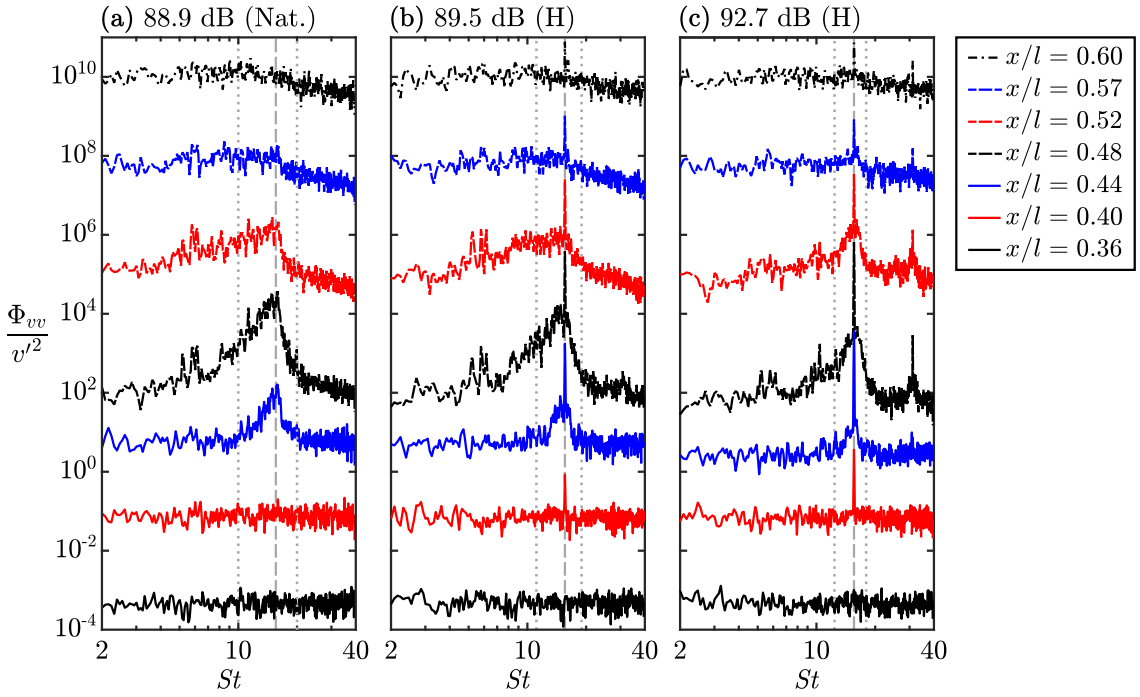

Figure 5.6: Frequency spectra of wall-normal velocity fluctuations within the separated shear layer for the natural and selected harmonic excitation cases. Each spectrum is stepped by two orders of magnitude for clarity. Grey dashed and dotted lines denote the fundamental frequency, $St = 15.6$, and the band of unstable frequencies, respectively.

depicted in Fig. 5.7, which shows sequences of instantaneous spanwise vorticity for the 89.5 and 92.7 dB cases. Contours of the λ_2-criterion [192] are added to aid in identifying vortical structures, in addition to dashed lines which track individual vortices between the frames. Fig. 5.7 demonstrates that, similar to the natural case (Fig. 4.5), the separated shear layer roll ups into periodic vortices upstream of the mean transition point, which then convect downstream, undergo deformation, and eventually begin to break down to smaller scales downstream of mean reattachment. However, in contrast to the natural case, Fig. 5.7 shows that applying excitation at the harmonic frequency leads two distinct changes in the separation bubble flow development; the first being an earlier roll-up of the separated shear layer, i.e., where individual structures are first identifiable via the λ_2-contours in Figs. 5.7a and 5.7b. This upstream advancement of vortex roll-up is consistent with the onset of earlier amplification of disturbances observed in the rms velocity fields (Figs. 5.3b

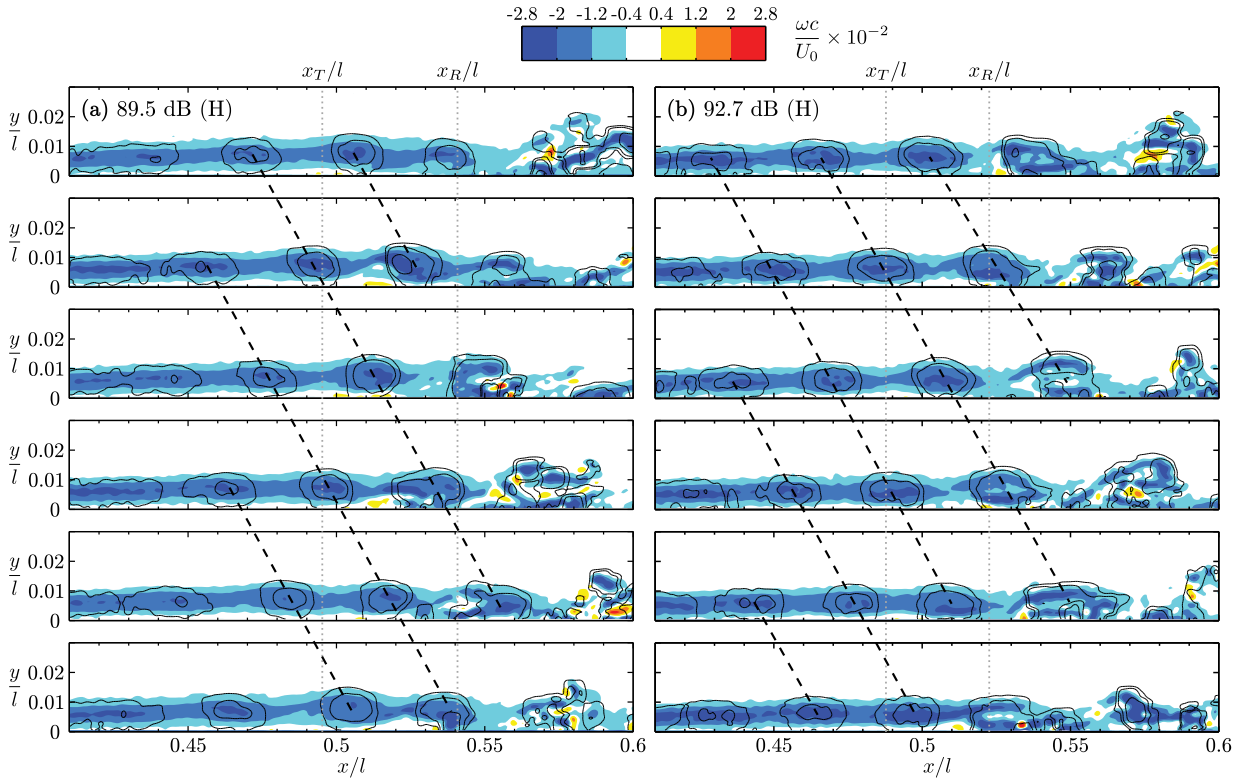

Figure 5.7: Instantaneous contours of spanwise vorticity for the 89.5 dB and 92.7 dB harmonic excitation cases. Consecutive frame are separated by $t^* = 3.7 \times 10^{-2}$. Thin black lines indicate λ_2-contours, while black dashed lines trace the same vortices in the sequence.

and 5.3c) and the upstream movement of the mean transition point (Fig. 5.5).

In Fig. 5.7, the second distinct change in the flow development due to the excitation is the organization of the roll-up process, as there is substantially lower temporal variability in both the convective velocities and streamwise wavelengths in the excited separation bubbles. This is consistent with the reduction in the frequency range of amplified disturbances observed in Fig. 5.6. However, the mean convective velocity and streamwise wavelength of the shear layer vortices identified in Fig. 5.7 are $U_c/U_e = 0.49$ and $\lambda_x/l = 0.036$, which are similar to those for the natural case (Fig. 4.7) and is attributed to matching the excitation and fundamental frequencies. The analysis of these vortex shedding characteristics is further substantiated through the computation of two-dimensional, wavenumber-frequency spectra, which are shown in Fig. 5.8 for the 89.5 and 92.7 dB cases. The spectra are computed using the approach described in Section 4.1. In Fig. 5.8, a dramatic concentration of spectral energy towards the excitation frequency ($St = 15.6$) and its corresponding wavenumber (i.e. the wavenumber at which $St = 15.6$ intersects the convective ridge, $k_x l \approx 170$) is observed, in comparison to the natural case (Fig. 4.6). The effect

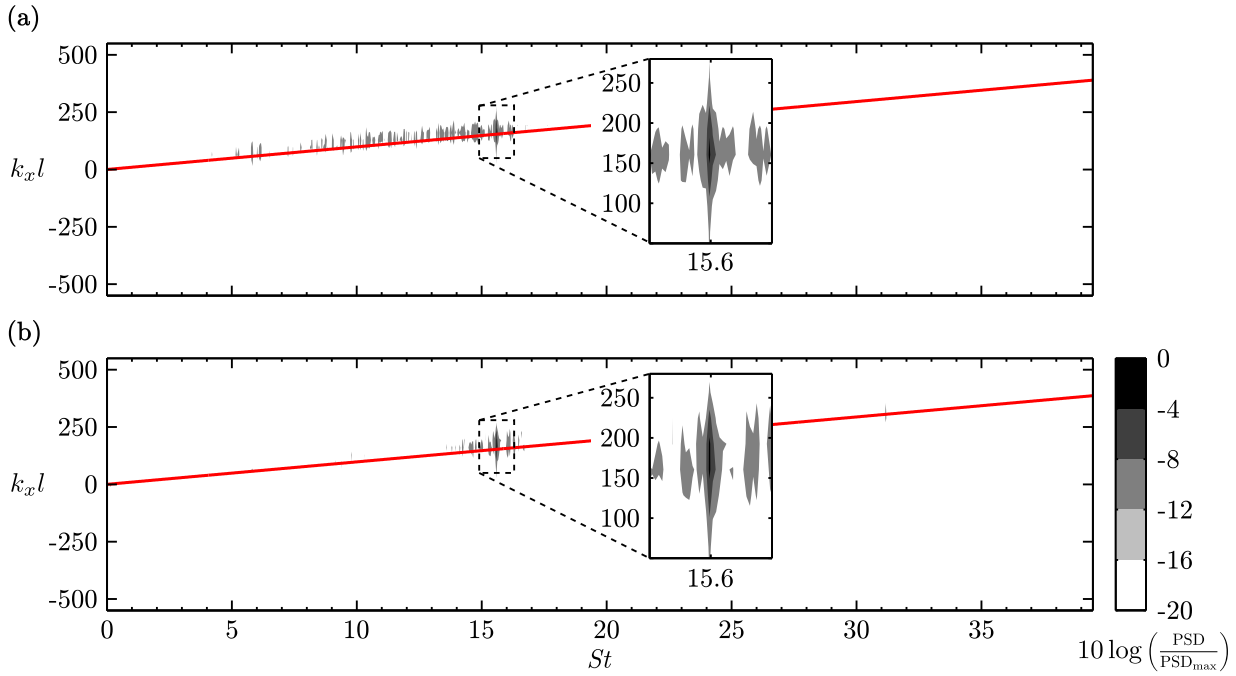

Figure 5.8: Wavenumber-frequency spectra of wall normal-velocity fluctuations in the separated shear layer for the (a) 89.5 dB and (b) 92.7 dB harmonic excitation cases. Red lines are linear fits to the loci of energy maxima.

becomes more pronounced with increasing excitation amplitude, as the range of amplified frequencies about $St = 15.6$ decreases significantly from Fig. 5.8a to Fig. 5.8b. The effect of excitation amplitude on the band of unstable streamwise wavelengths is more difficult to discern visually in Fig. 5.8, since wavenumber is inversely proportional to wavelength. Therefore wavenumber spectra plotted in terms of wavelength are provided for reference in Appendix E (Fig. E.2a), which show continual reductions in the band of amplified streamwise wavelengths with increasing excitation amplitude. Estimating the convective velocity associated with the convective ridge and the fundamental streamwise wavelength produces estimates of $U_c/U_e = 0.55$ and $\lambda_x/l = 0.041$ for both excitation cases presented in Fig. 5.8; values which match those of the natural case.

Vortex merging is not observed throughout the sequences presented in Fig. 5.7, which is characteristic of the flow development for the harmonic excitation cases at higher excitation amplitudes (92.7 and 94.9 dB). This suggests that the sporadic vortex merging observed for the natural case (Fig. 4.5) may result as a consequence of the increased temporal variations in the characteristics of the shear layer vortices. Such is also the case for free shear layers, as when left to develop naturally, vortex merging occurs randomly [111–113]. However, when external acoustic forcing is provided at or near the shedding frequency, the roll-up process is synchronized and vortex pairing is inhibited [102, 103, 114].

Measurements from the top-view PIV configuration (Fig. 3.4b) allow for quantitative assessment of excitation effects on both the streamwise and spanwise development of the shear layer vortices. The measurement plane was positioned in the same fashion as that of the natural case (Fig. 4.11), which again allows for the identification of the roll-up vortices as spanwise bands of high streamwise velocity, as seen in Fig. 5.9. Comparing the harmonic and natural cases, Figs. 5.9 and 4.11, respectively, shows the general features of the flow development are similar. Specifically, in Fig. 5.9 spanwise coherent structures are first identifiable near the mean transition point, consistent with where roll-up is observed in the side-view measurements (Fig. 5.7). Shortly downstream of roll-up, the structures quickly develop spanwise deformations within the vicinity of the mean reattachment point. These deformations intensify as the structures continue to convect downstream, which eventually leads to the emergence of localized vortex breakup 'spots', i.e., the regions of low velocity fluid that appear over the span of the vortex filaments at $x/l \gtrsim 0.55$ throughout Fig. 5.9.

While the general flow development is similar between the natural and harmonic cases, significant differences are observed in Fig. 5.9, which are consistent with the analysis of the side-view results (Fig. 5.7). In particular, applying acoustic harmonic excitation moves shear layer roll-up upstream, organizes the structures in the streamwise direction, and appears to increase their spanwise coherence. Moreover, excitation appears to alter the primary wavelength of the spanwise disturbances that develop in the vortex filaments, as

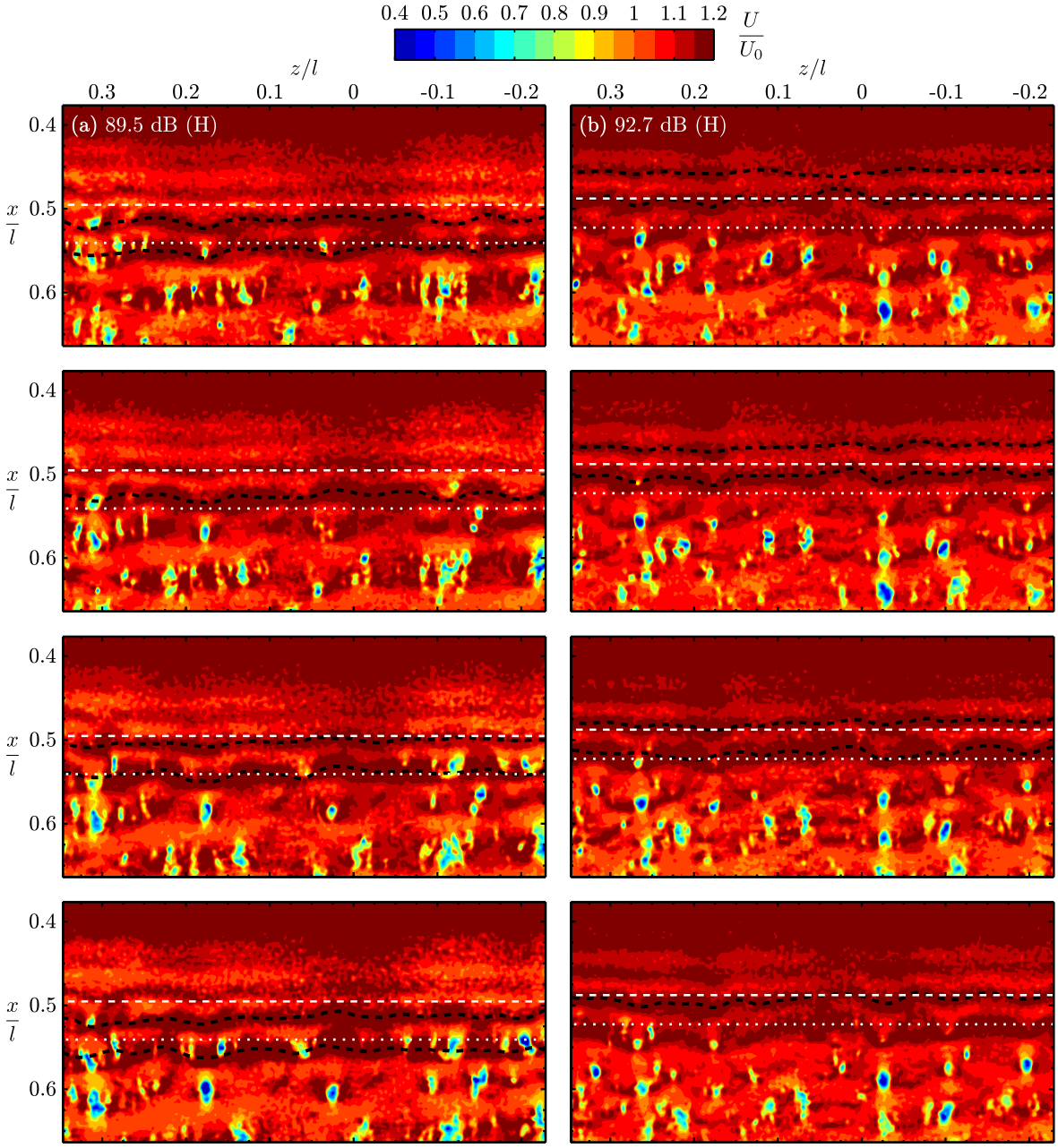

Figure 5.9: Instantaneous contours of streamwise velocity for the 89.5 dB and 92.7 dB harmonic excitation cases. Consecutive frame are separated by $t^* = 2.5 \times 10^{-2}$. Black dashed lines indicate smoothed spline fits to the centre of selected structures. Dashed and dotted white lines mark the mean transition and reattachment points, respectively.

a visual comparison of Fig. 5.9 (harmonic cases) and Fig. 4.11 (natural case) indicates that spanwise disturbances of shorter wavelengths (on the order of $0.1l$) tend to initially develop in Figs. 5.9a and 5.9b, while in the natural flow the initial spanwise wavelengths are on the order of $0.2l$ (Figs. 4.11 and 4.12). To affirm these observations, wavelength spectra are computed using streamwise velocity fluctuations measured across the span at the streamwise location of the mean transition point. The results are presented in Fig. 5.10 for the natural and harmonic cases, where each spectrum is the average of all spectra computed for a given case, and the maximum resolvable spanwise wavelength is $0.6l$.

Figure 5.10 reveals that, for the natural case and harmonic excitations of relatively low amplitude (SPL = 89.5 and 90.4 dB), spanwise disturbances of wavelengths $\lambda_z/l = 0.1$ and 0.2 tend to develop at the mean transition point, with the more pronounced peak at $\lambda_z/l = 0.2$ indicating a preference to this wavelength. Analysis of the natural case, presented in Section 4.2, revealed that, as the structures develop downstream, the breakup to smaller scales is marked by the dispersion of spectral energy to smaller wavelengths and the persistence of the $\lambda_z/l = 0.1$ peak, which was then linked to the physical breakdown mechanism of the vortex filaments (Fig. 4.13). The reader is reminded of this discussion since spectral energy is shifted to $\lambda_z/l = 0.1$ when the flow is subjected to the harmonic

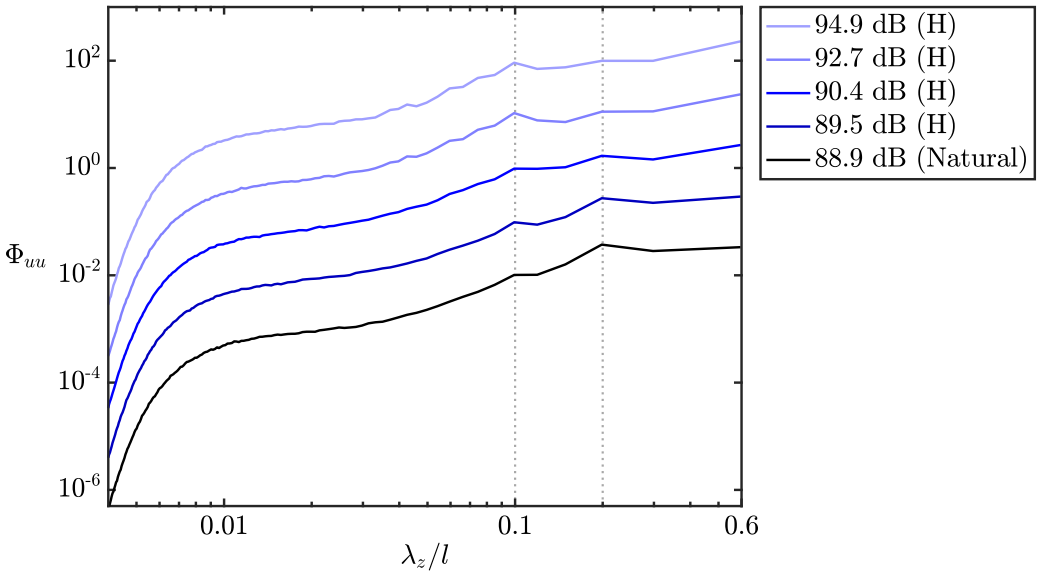

Figure 5.10: Averaged wavelength spectra of streamwise velocity fluctuations across the span at the mean transition point for the natural and harmonic excitation cases. Each spectrum is stepped by one order of magnitude for clarity.

excitations of higher amplitude in Fig. 5.10 (SPL = 92.7 and 94.9 dB). Thus, the results indicate that harmonic excitation promotes the development of spanwise disturbances of a wavelength that are fundamental to the breakdown of the vortex filaments. Similar observations have been made in studying boundary layer transition, as the investigations of Klebanoff *et al.* [89], followed by Saric and Thomas [90], showed that spanwise periodic disturbances of nominally two-dimensional instability waves result when the boundary layer is forced in a periodic fashion, i.e. K- and H-type transition [63, 64].

The flow development in the excited separation bubbles depicted in Fig. 5.9 indicates that excitation modifies the spanwise coherence of the structures, the effects of which can be quantified through computation of the spanwise coherence length using Eqs. 4.1 and 4.2. The streamwise variation in the spanwise coherence length is presented in Fig. 5.11 for the natural and two harmonic excitation cases. The dashed portion of the curves in Fig. 5.11 indicate where the estimates are subject to high uncertainty due to the low amplitude of the disturbances relative to the noise of the measurement, which is discussed in-depth in Section 4.2. For the cases presented in Fig. 5.11, peak values in ℓ_z can be identified; the streamwise locations of which agree well with the locations of shear layer roll-up and mean transition (Figs. 4.5, 5.5, and 5.7). Following roll-up, the spanwise

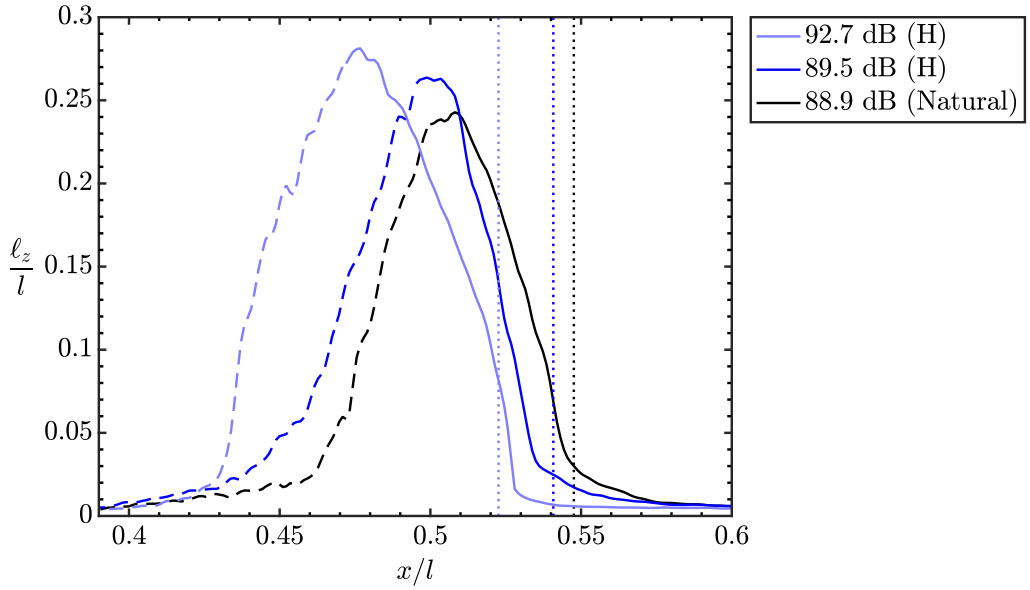

Figure 5.11: Effect of harmonic excitation on spanwise coherence length. Dashed portion of curves indicate where the results are affected by the measurement uncertainty. Dotted lines (coloured according to legend) indicate mean reattachment points.

coherence decreases rapidly, which is attributed to the spanwise deformation of the vortex filaments and the subsequent breakdown to smaller scales (Figs. 4.11 and 5.9). With increasing excitation amplitude, peak values in ℓ_z are attained earlier upstream and reach higher magnitudes. Previous studies [16, 33, 201] have argued that the roll-up vortices are responsible for inducing mean reattachment by entraining high-momentum fluid from the outer-flow and transporting it toward the surface. Based on the present results, it can be argued that acoustic harmonic excitation reduces the size of the separation bubble by advancing shear layer roll-up upstream and enhancing the coherence of the shed structures. While the former results in the upstream movement of the mean transition point, the latter is likely responsible for the reduction in the distance from roll-up (occurring approximately at x_T) to mean reattachment, as shown in Figs. 5.3 and 5.5.

5.2.2 Subharmonic Tonal Excitation

Section 5.1 established that the subharmonic excitation did not produce observable changes in the mean topology of the separation bubble. Whether or not this type of excitation has any effect on the dynamics within the separation bubble is assessed here, which begins by examining spectra of velocity disturbances in the separated shear layer for the natural and subharmonic cases, presented in Fig. 5.12. In comparing Figs. 5.12a and 5.12b, the subharmonic excitation does not alter the natural band of amplified disturbances appreciably; however, significant velocity fluctuations at the subharmonic excitation frequency, $St = 7.8$, appear in the spectra at $x/l = 0.44$. These disturbances are then amplified at the following downstream stations, $x/l = 0.48$ and 0.52. Further downstream ($x/l \geq 0.57$), the subharmonic peaks decay, however, similar to that observed for harmonic excitation (Figs. 5.6b and 5.6c), the peaks at this frequency persist downstream of mean reattachment. Thus, the separated shear layer is receptive to acoustic disturbances at the first subharmonic of the fundamental frequency. This leads to the inception, growth, and subsequent decay of velocity fluctuations at the subharmonic frequency, similar to that observed for free shear layers forced acoustically at the subharmonic frequency of the primary instability [102, 114].

To elucidate subharmonic excitation effects on spatio-temporal flow development within the separation bubble, a sequence of spanwise vorticity is presented in Fig. 5.13, which is to be contrasted with the natural case (Fig. 4.5). The most striking difference between the two is the prevalence of vortex merging for the subharmonic case. In Fig. 5.13, all vortices initially identified near the mean transition point are involved in a pairing process. This observed regular vortex merging is responsible for the spectral peaks at the subharmonic frequency ($St = 7.8$) observed in Fig. 5.12b, as once a merge has occurred, the resulting

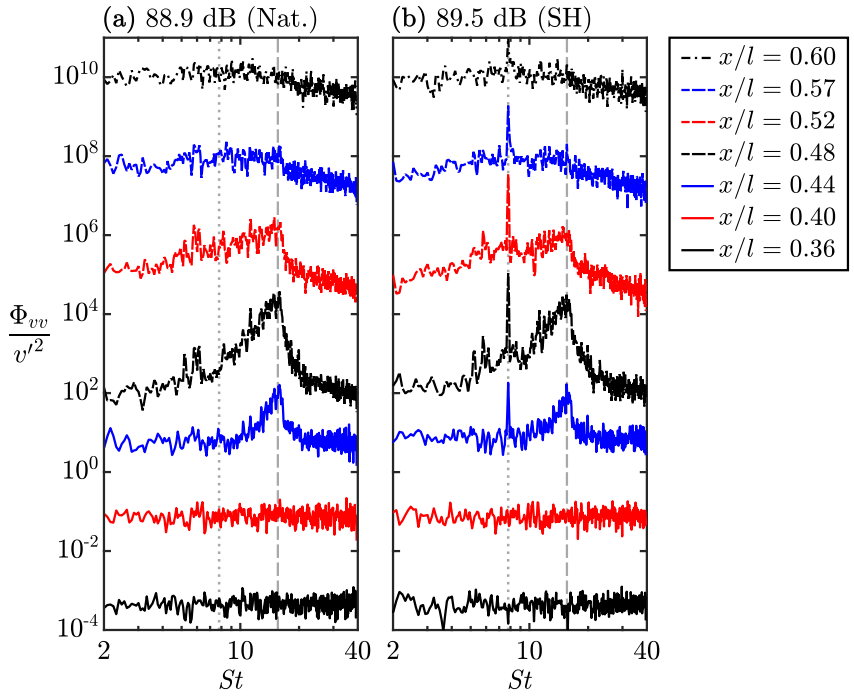

Figure 5.12: Frequency spectra of wall-normal velocity fluctuations within the separated shear layer for the natural and subharmonic excitation cases. Each spectrum is stepped by approximately two orders of magnitude for clarity. Grey dashed and dotted lines denote the fundamental, $St = 15.6$, and subharmonic, $St = 7.8$, frequencies, respectively.

structure is separated from the nearest downstream vortex by an approximately doubled wavelength, as for example in Figs. 5.13c and 5.13f. Thus the characteristic frequency of the vortex train is halved. However, it is important to note that this process must be periodic in order for it to be captured in frequency spectra that are averaged in time (Figs. 4.4 and 5.12). Therefore, the results demonstrate that subharmonic excitation induces periodic vortex merging, that, if left to develop naturally, occurs randomly.

Parallels can be drawn between the present results and the vortex merging characteristics of free shear layers. Ho and Huang [114] showed that acoustic tonal forcing applied at the subharmonic of the vortex shedding frequency promotes periodic vortex pairing. Furthermore, they found that the merging process coincides with the growth of perturbation energy at the subharmonic frequency, which led them to conclude that a secondary subharmonic resonance mechanism [108, 121] was responsible for disturbance growth within this mode. A similar analysis is employed here, where the components of spectral energy associated with the fundamental and subharmonic frequencies are computed and presented in

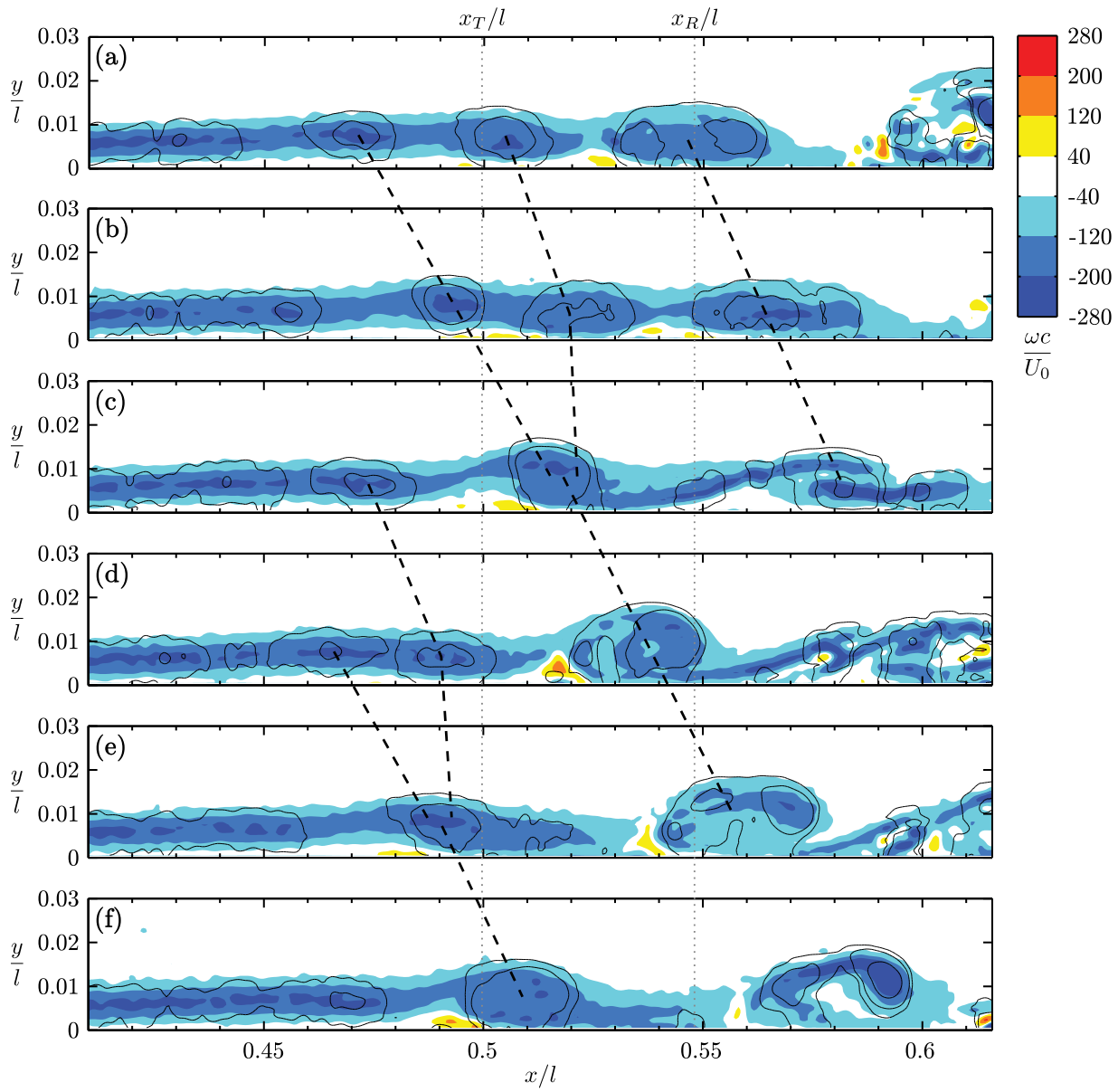

Figure 5.13: Instantaneous contours of spanwise vorticity for the subharmonic excitation case. Consecutive frame are separated by $t^* = 3.7 \times 10^{-2}$. Thin black lines indicate λ_2-contours, while black dashed lines trace the same vortices in the sequence.

Fig. 5.14. When left to develop naturally (Fig. 5.14a), disturbance amplification is detected shortly downstream of separation and only at the fundamental frequency, $St = 15.6$. The growth of the disturbances leads to a saturation of the fundamental mode upstream of mean transition. Further downstream, the fundamental mode decays and the subharmonic mode grows, which is attributed to the redistribution of spectral energy during the last stages of transition. In contrast, in the case of subharmonic tonal excitation (Fig. 5.14b), both the fundamental and subharmonic modes undergo amplification upstream of transition, with both modes sharing approximately equal growth rates in the region $0.4 \leq x/l \leq 0.44$. The fundamental mode then saturates at approximately the same streamwise locations as that of the natural case, while the subharmonic mode continues to grow, reaching its maximum at approximately the mean transition point. The maximum perturbation energy for the subharmonic mode is roughly an order of magnitude larger than that of the fundamental mode.

Re-examining Fig. 5.13 reveals that the identified instances of vortex merging occur near the mean transition point and therefore in the region where the subharmonic mode saturates (Fig. 5.14b), thus supporting the assertions of Ho and Huang [114]. In fact, the trends present in Fig. 5.14b agree well with those reported by Ho and Huang (e.g., consider Figs. 15 and 16 in Ref. [114]), which further reinforces the significance of the role the Kelvin-Helmholtz instability plays in the transition process of separation bubbles, which is discussed at length in Section 2.2.3. However, two important distinction between the present results and free shear layers must be highlighted. The secondary sub-

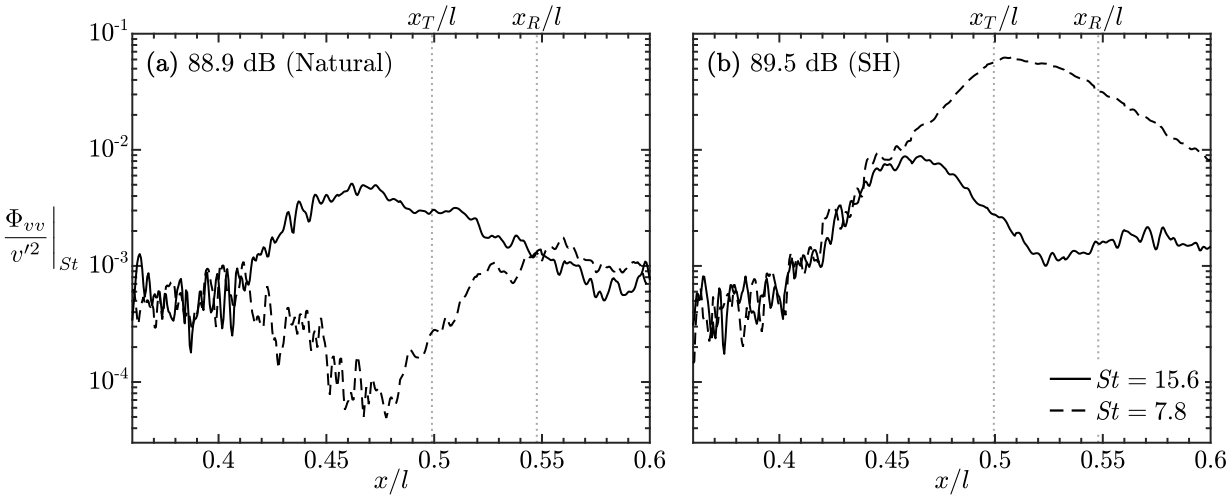

Figure 5.14: Streamwise growth of frequency filtered spectral energy within the separated shear layer for the natural and subharmonic excitation cases.

harmonic resonance mechanism, which has been proposed to be responsible for the growth of the subharmonic mode in free shear layers [108, 114, 121], dictates that the growth of the subharmonic mode must follow the saturation of the fundamental mode, in addition to occurring in both forced and natural free shear layers. In the present results (Fig. 5.14b), growth of the subharmonic mode does not occur in the natural case, and when excited subharmonically, the growth of these two modes occurs concurrently.

The characterization of velocity disturbances within the separated shear layer under subharmonic excitation is furthered through analysis of their wavenumber-frequency spectra, which is presented in Fig. 5.15. Similar to the results for the harmonic excitation cases (Fig. 5.8), the subharmonic acoustic excitations leads to the high concentration of spectral energy towards the excitation frequency, $St = 7.8$, in comparison to the natural case (Fig. 4.6). The convective ridge is identified as a linear fit to the locus of energy maxima, which produces an estimate of the disturbance convective velocity of $U_c/U_e = 0.53$, which is essentially unchanged from the natural case ($U_c/U_e = 0.55$ from Fig. 4.6). Therefore, consistent with the convective velocities that can be ascertained from the vortex traces presented in the Fig. 5.13, the occurrence of period vortex merging does not alter the convective velocity of the disturbances significantly. Along the convective ridge, the wavelength corresponding to the most amplified frequency is $\lambda_x/l = 0.080$ ($k_x l = 79.2$). The result quantifiably confirms that subharmonic excitation promotes velocity fluctuations of half and twice the natural frequency and wavelength, respectively, which are attributed to the merging of the shear layer vortices, as seen in Fig. 5.13.

Figure 5.16 presents a top-view sequence of instantaneous streamwise velocity for the subharmonic case, so that the spanwise behaviour of the structures and the merging phenomena may be examined. The vortex labelled as A in Fig. 5.16a convects downstream

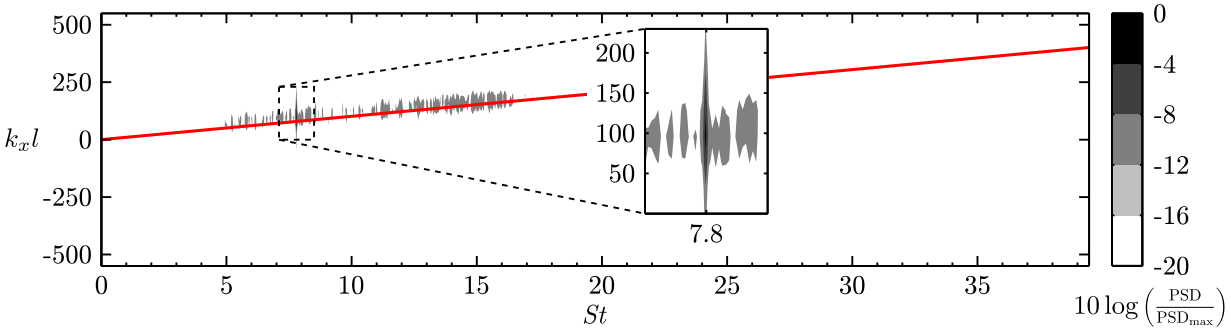

Figure 5.15: Wavenumber-frequency spectra of wall normal-velocity fluctuations in the separated shear layer for the subharmonic excitation case. Red line is a linear fit to the locus of energy maxima.

in Figs. 5.16b and 5.16c, developing spanwise undulations which are most notable at $z/l \approx -0.1$ and 0.3, where forward streamwise bulges form. Concurrently, the following vortex in the shedding process, labelled as B, rolls up at the mean transition point in Fig. 5.13c, and also deforms across the span as it convects downstream to its position in Fig. 5.13d. In Fig. 5.13d, the merging process between A and B begins to take place, as the vortex filaments intertwine within $-0.05 \lesssim z/l \lesssim 0.25$, while the structures do not merge at spanwise locations where the forward streamwise bulges developed in A, and perhaps consequently, where rearward bulges developed in vortex B. The 'merged' structure, labelled as A+B, then continues to convect downstream through Figs. 5.16e–g, while retaining features of the original vortices at some spanwise segments, e.g. at $z/l \approx -0.1$ and 0.3, where the initial streamwise bulges that developed in A and B are still identifiable in A+B. The next merge in the sequence then occurs between vortices C and A+B in Figs. 5.16g and 5.16h. Similar to the previous instance, the merge that occurs between vortices C and A+B is spanwise non-uniform. As discussed in Section 4.2, the spanwise deformations of the vortex filaments was shown to be fundamental to their breakdown process (Fig. 4.13), while here they are shown to play an intrinsic role in the merging process of the shear layer vortices.

To finalize the characterization of the shear layer velocity disturbances when subjected to subharmonic excitation, the predominant spanwise wavenumbers and spanwise coherence length are assessed via Figs. 5.17 and 5.18, respectively. In Fig. 5.17, the averaged wavenumber spectra for the natural and subharmonic cases are practically identical at both the mean transition and reattachment locations. This indicates that, despite the prevalence of vortex merging in the subharmonic case, the characteristics of the spanwise deformations, as they initially develop and evolve with downstream convection, are unaltered from the natural case. Thus the breakup mechanism of the spanwise rollers, and the role the spanwise deformations play in this process, discussed in Section 4.2 (refer to Figs. 4.12 and 4.13) applies to the subharmonic excitation case, which is consistent with the development of the structures as they breakup in Fig. 5.16.

Figure 5.18 shows that subharmonic excitation has a significant effect on the measured spanwise coherence of the shear layer vortices, as the maximum coherence length for the subharmonic case is 25% higher than that of the natural case. One might argue that this higher coherence length is an artifact of the estimation technique and the fixed noise level in the measurement, since as a result of a vortex merge, the merged structure would contain the sum of the circulation of the two vortices involved in the process. This 'stronger' merged vortex could then induce a higher tangential velocity, which would be captured in the planar PIV measurements. This would result in an increase in the mean of the signal used in computing the spanwise coherence while the noise level is fixed, and so a

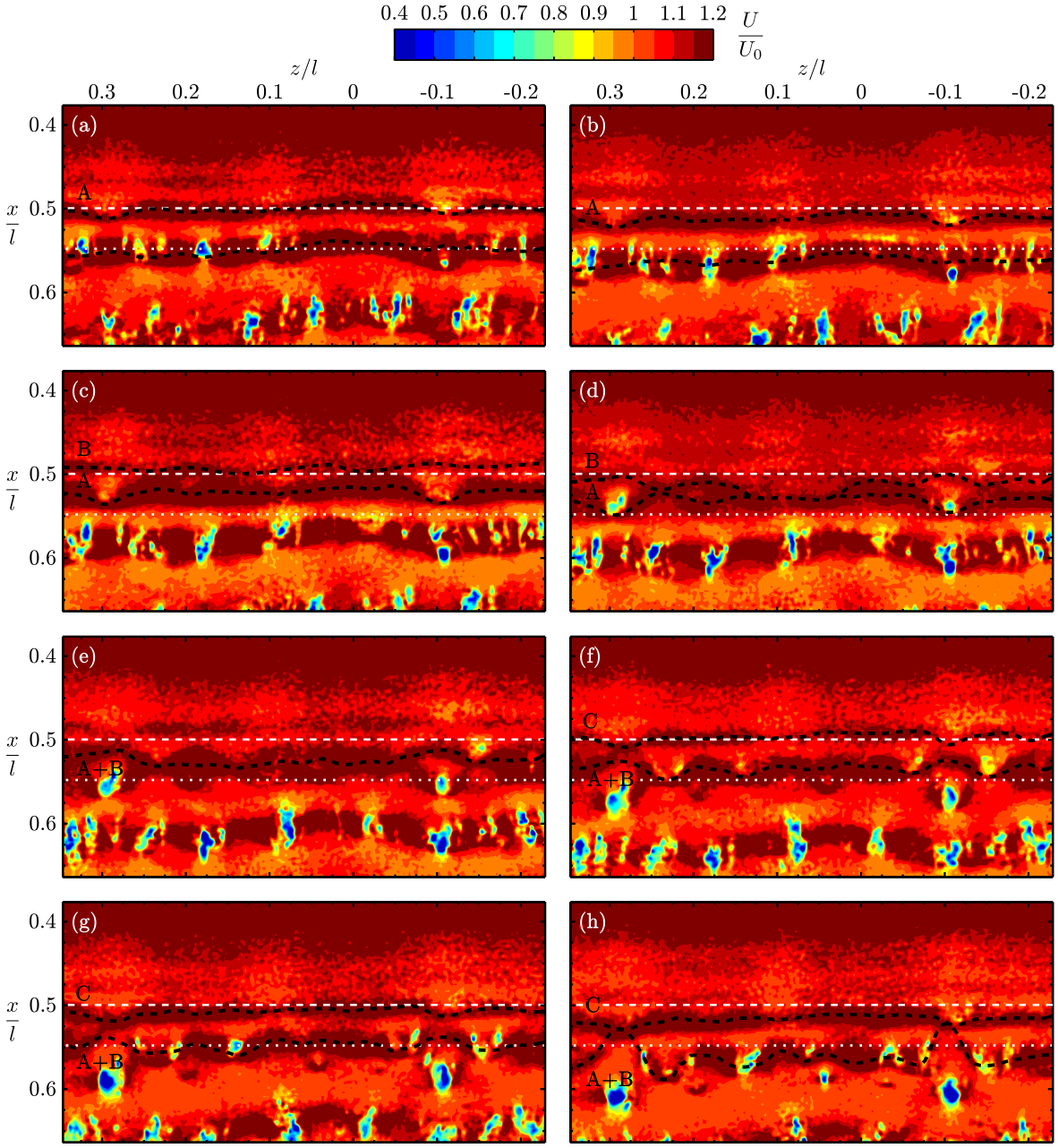

Figure 5.16: Instantaneous contours of streamwise velocity for the subharmonic excitation case. Consecutive frame are separated by $t^* = 2.5 \times 10^{-2}$. Black dashed lines indicate smoothed spline fits to the centre of selected structures. Dashed and dotted white lines mark the mean transition and reattachment points, respectively.

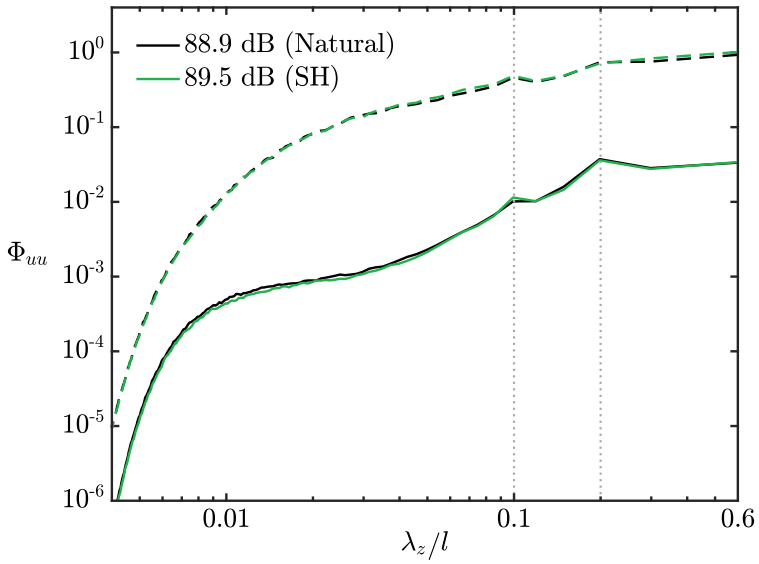

Figure 5.17: Averaged wavelength spectra of streamwise velocity fluctuations across the span for the natural and subharmonic excitation cases. Solid and dashed curves (coloured according to legend and stepped by one order of magnitude for clarity) are computed at the mean transition and reattachment points, respectively.

perceived increase in coherence would result, as demonstrated by the analysis performed in Appendix G. However, such an increase in the velocity of the structures is not observed, as the mean streamwise velocity across the span of vortex A+B is $U/U_0 \approx 1.2$ throughout Fig. 5.16, while in comparison, the mean streamwise velocity across vortex A in the natural case (Fig. 4.11) is also $U/U_0 \approx 1.2$. Furthermore, based on the sensitivity analysis presented in Appendix G, given the typical random errors in the top-view PIV measurements (Appendix A), the mean streamwise velocity would need to be doubled in order to produce a perceived increase in the spanwise coherence length of 25%. Therefore the increase in spanwise coherence due to the subharmonic excitation observed in Fig. 5.18 can be taken as a reflection of the flow physics, and is presumably due to vortex merging.

In Section 5.2.1 it was argued that the increased spanwise coherence of the shear layer vortices, due to the harmonic excitations, was responsible for inducing earlier time-averaged reattachment. An increase in spanwise coherence results from subharmonic excitation, however, the mean topology in the aft portion of the bubble is unchanged, as the mean transition and reattachment points are essentially equal for the natural and subharmonic cases (Figs. 5.3 and 5.5). Thus, in summarizing the effects, subharmonic excitation leads to periodic vortex merging, which increases the spanwise coherence of the structures relative

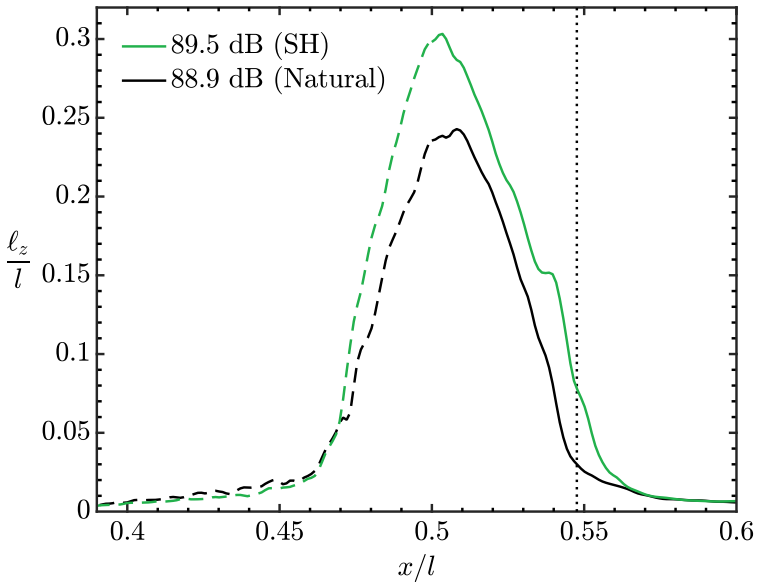

Figure 5.18: Effect of subharmonic excitation on spanwise coherence length. Dashed portion of curves indicate where the results are affected by the measurement uncertainty. Dotted line indicates mean reattachment points for both cases.

to the natural case (Fig. 5.18). These structures occur at half the fundamental frequency (Figs. 5.12 and 5.13), and so it is speculated that the time-averaged flux of high-momentum fluid from the outer-flow to the airfoil surface is approximately equal to that of the natural case, resulting in equal mean reattachment estimates (Figs. 5.3 and 5.5).

5.2.3 Random Excitation

Analysis of the random excitation's impact on flow development within the separation bubble begins with an examination of the spectra of wall-normal velocity fluctuations within the separated shear layer, presented in Fig. 5.19. As discussed previously, the spectra of the natural flow (Fig. 5.19a) show the convective amplification of flow disturbances within an unstable band of frequencies, $10 \lesssim St \lesssim 20$, followed by the decay of these velocity perturbations. As indicated in Fig. 5.1, the energy content of the random excitation is entirely contained within and approximately constant across the naturally unstable frequency band. When the excitation is applied (Figs. 5.19b and 5.19c), the shear layer shows preferential amplification of disturbances at the fundamental frequency, $St = 15.6$, although the peak energy content shifts to lower frequencies within the band compared to the natural case. This shift to slightly lower frequencies of the most amplified disturbances is similar

to the LST results of Yarusevych and Kotsonis [33], and will be examined in more detail in Section 5.3. When randomly excited, earlier amplification is detected within the shear layer, as indicated by the spectra at $x/l = 0.4$ for all cases. This effect is also reflected in the rms velocity contours (Figs. 5.3b and 5.3c) and consequently the upstream movement of the mean transition point with increasing excitation amplitude, as seen in Fig. 5.5, which was also shown to occur for harmonic excitation. As discussed in Section 5.1, the increase in fluctuation amplitude at a given streamwise location due to excitation is attributed to an increase in the initial disturbance amplitude of the transition process.

Examining the spectra at $x/l = 0.44$ and 0.48 in Fig. 5.19 reveals that, when excited randomly (Figs. 5.19b and 5.19c), the range of significantly amplified frequencies within the unstable frequency band increases, since the input energy provided by random excitation is approximately equal across all frequencies to which the shear layer is receptive. This is in contrast to harmonic excitation, where the excitation energy is concentrated within a narrow band (Fig. 5.6). As the randomly excited disturbances progress downstream

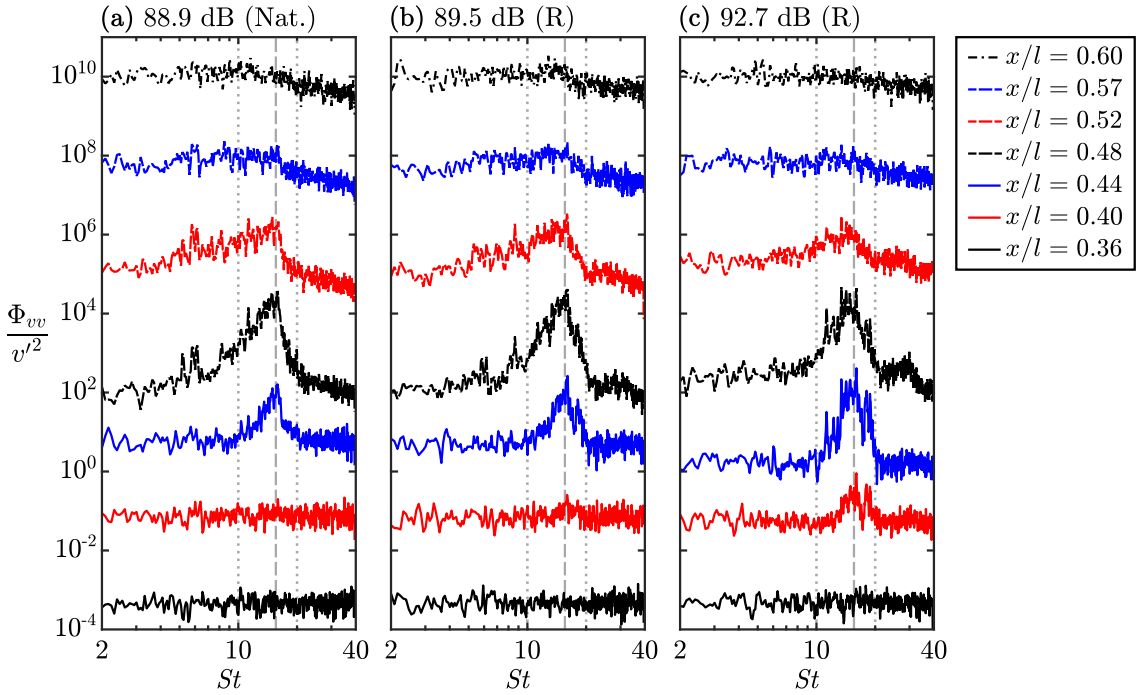

Figure 5.19: Frequency spectra of wall-normal velocity fluctuations within the separated shear layer for the natural and selected random excitation cases. Each spectrum is stepped by approximately two orders of magnitude for clarity. Grey dashed and dotted lines denote the fundamental frequency, $St = 15.6$, and the band of unstable frequencies, respectively.

($x/l = 0.52$ and 0.57), a rapid redistribution of energy to frequencies outside of the unstable band occurs, most notably for the 92.7 dB case (Fig. 5.19c) where the spectral energy is more broadband than in the natural case (Fig. 5.19a). Thus, the results from Fig. 5.19 indicate that random excitation promote the decay of the velocity fluctuations in the aft portion of the bubble.

Sequences of spanwise vorticity contours for the 89.5 and 92.7 dB random excitation cases are presented in Fig. 5.20. Considering the 89.5 dB case (Fig. 5.20a), the first three frames in the sequence show similar flow development to the natural case (Fig. 4.5), namely, the shedding of shear layer vortices of approximately constant convective velocity and streamwise wavelength. Tracing the progression of vortices A and B in Fig. 5.20a reveals that these structures begin to breakdown to smaller scales in the aft portion of the bubble, i.e., between mean transition and reattachment, which is consistent with the natural case. When the excitation amplitude is increased to 92.7 dB (Fig. 5.20b), a stark change in the flow development is observed, as coherent roll-up vortices can only be identified upstream of the mean transition point, for example, structures C and D in the first three frames of Fig. 5.20b. Tracing these structures as they convect downstream reveals that they begin to breakdown near the mean transition point, creating a disorganized flow state in the aft portion of the bubble. This early breakdown has not been observed for the natural case, as well-defined coherent structures could be identified in the aft portion of the bubble throughout the entire recorded sequence. It should be noted that, while the particular sequence presented in Fig. 5.20b demonstrates this disorganized flow state, these events are not ubiquitous. In particular, the shedding process alternates between periods of shedding where coherent structures persist downstream of mean reattachment (similar to the natural case), followed by periods with earlier onset of vortex breakup, similar to that presented in Fig. 5.20. These observations lend to the random nature of the excitation that is influencing the flow development, as it is speculated that the shear layer instability locks onto frequencies near or at the fundamental frequency for some period of time, while at others the excitation promotes this different behaviour.

The characteristics of the shear layer disturbances when subjected to random excitation are further examined through their wavenumber-frequency spectra, which are presented in Fig. 5.21. The spectra for the random excitation cases reveal similar features to the natural case (Fig. 4.6), as estimates of the disturbance convective velocity and streamwise wavelength are found to be $U_c/U_e = 0.55$ and $\lambda_x/l = 0.041$ for both Figs. 5.21a and 5.21b; values which are equal to those of the natural case. However, the random excitation cases show signs of the increased randomization of the shear layer shedding process, as energy levels show a greater spread about both the convective ridge and frequency of the most amplified disturbances. This indicates that at higher excitation amplitudes, convective

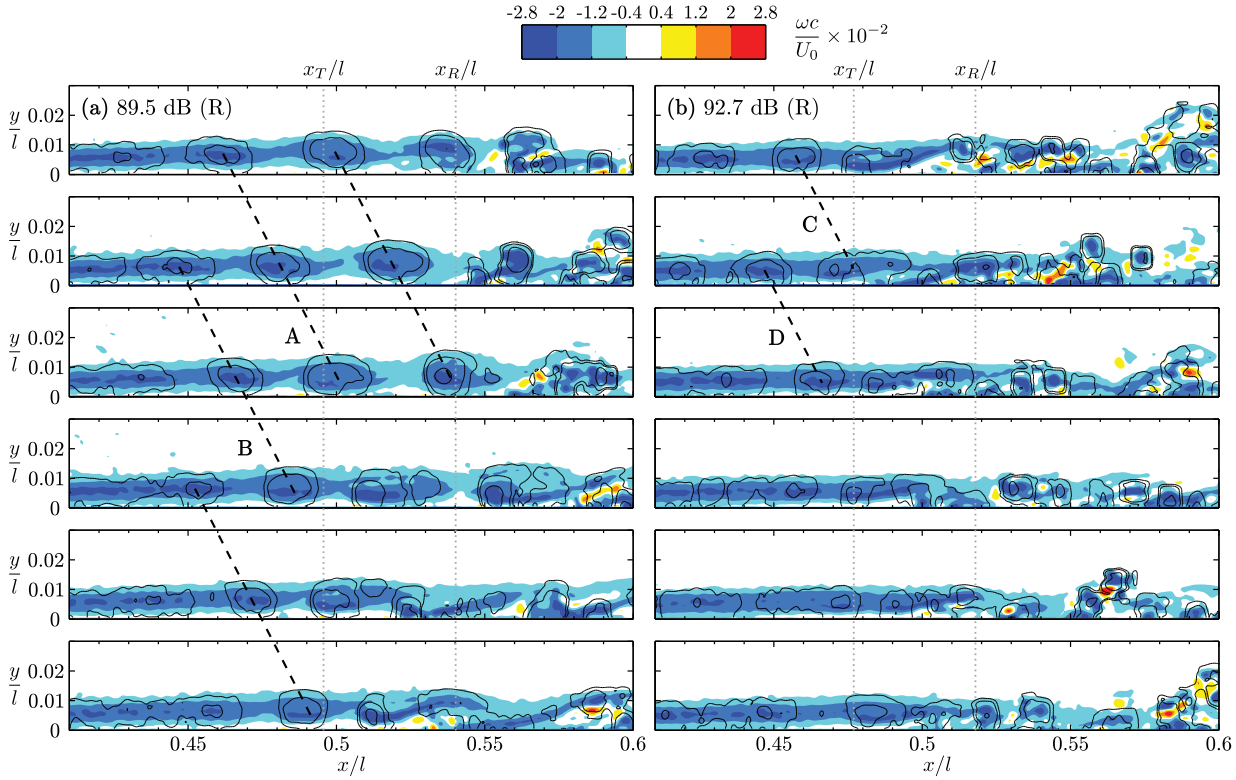

Figure 5.20: Instantaneous contours of spanwise vorticity for the 89.5 dB and 92.7 dB random excitation cases. Consecutive frame are separated by $t^* = 3.7 \times 10^{-2}$. Thin black lines indicate λ_2-contours, while black dashed lines trace the same vortices in the sequence.

disturbances are prevalent over a wider range of wavenumbers and frequencies, which even extend outside of the shear layer's unstable bands ($10 \lesssim St \lesssim 20$ and $100 \lesssim k_x l \lesssim 200$). This is indicative of the relatively large wavelength and low frequency shear layer disturbances breaking down to smaller length scales and higher frequencies, which is consistent with the periods of disorganized flow in the aft portion of the bubble observed in Fig. 5.20b.

The spanwise evolution of the shear layer vortices when subjected to random excitation is assessed in Fig. 5.22, which presents sequences of instantaneous streamwise velocity measured using the top-view PIV configuration (Fig. 3.4b). Analysis of the side-view results (Figs. 5.19–21) established that random excitation can invoke two different states of flow development in the aft portion of the bubble; either one similar to the natural case where the shed structures preserve their coherence and eventually breakdown beyond the mean reattachment point, or where the vortices breakdown earlier and produce a more chaotic state in the aft portion of the bubble. These two flow states have also been observed

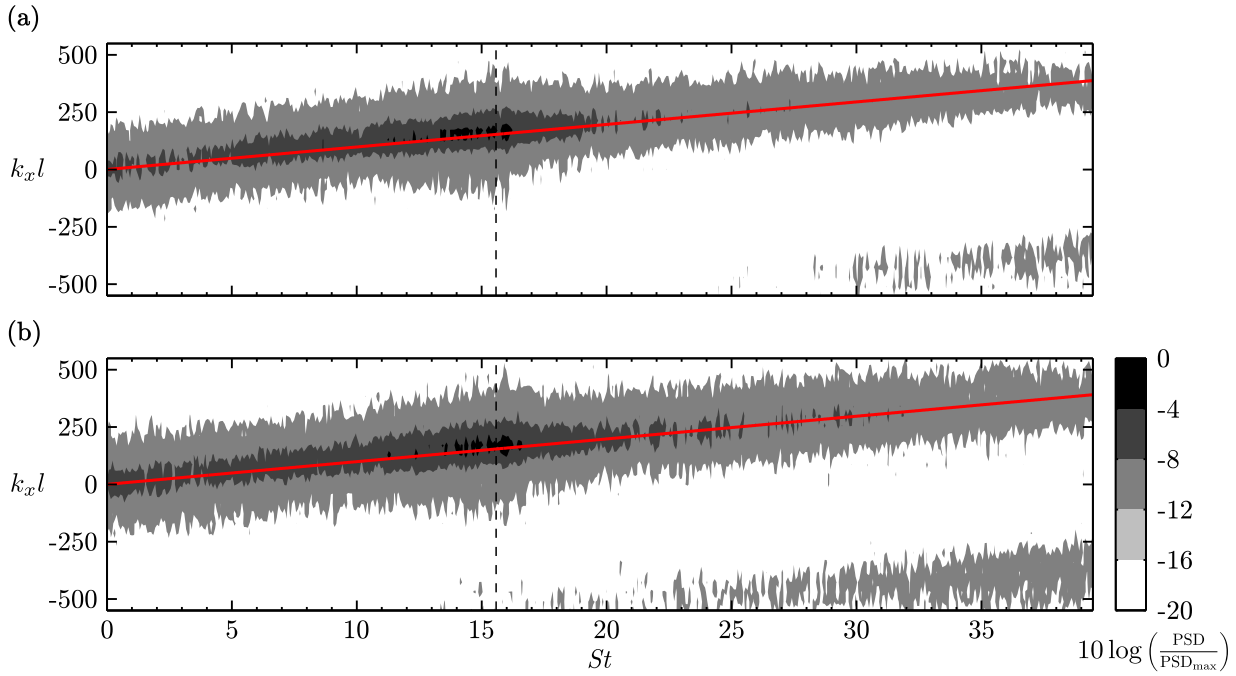

Figure 5.21: Wavenumber-frequency spectra of wall normal-velocity fluctuations in the separated shear layer for the (a) 89.5 dB and (b) 92.7 dB random excitation cases. Red lines are linear fits to the loci of energy maxima. Dashed lines indicate the frequency of the most amplified disturbances, $St = 15.6$.

in the top-view results. The case of earlier vortex breakdown is capture in Fig. 5.22, with the delayed breakdown being similar to the natural flow development results presented in Section 4.2.

Figure 5.22a shows the flow development sequence for the 89.5 dB random excitation case, which depicts a highly disorganized state in the aft portion of the bubble, as the spanwise structures identifiable between the mean transition and reattachment points are significantly deformed due to spanwise undulations and/or spanwise non-uniform merging. For example, consider the region downstream of mean transition in the first frame, where only structures that have undergone significant spanwise deformation are seen. Furthermore, the absence of a uniform vortex filament at $x/l \approx 0.57$ across the entire span indicates that a spanwise non-uniform merge occurred. It is instructive to trace vortex A, identified in the first frame of Figure 5.22a. As the vortex convects downstream through the first to third frames in the sequence, it develops significant spanwise deformations. This results in a highly deformed and weakly coherent structure in the fourth frame, that appears to be

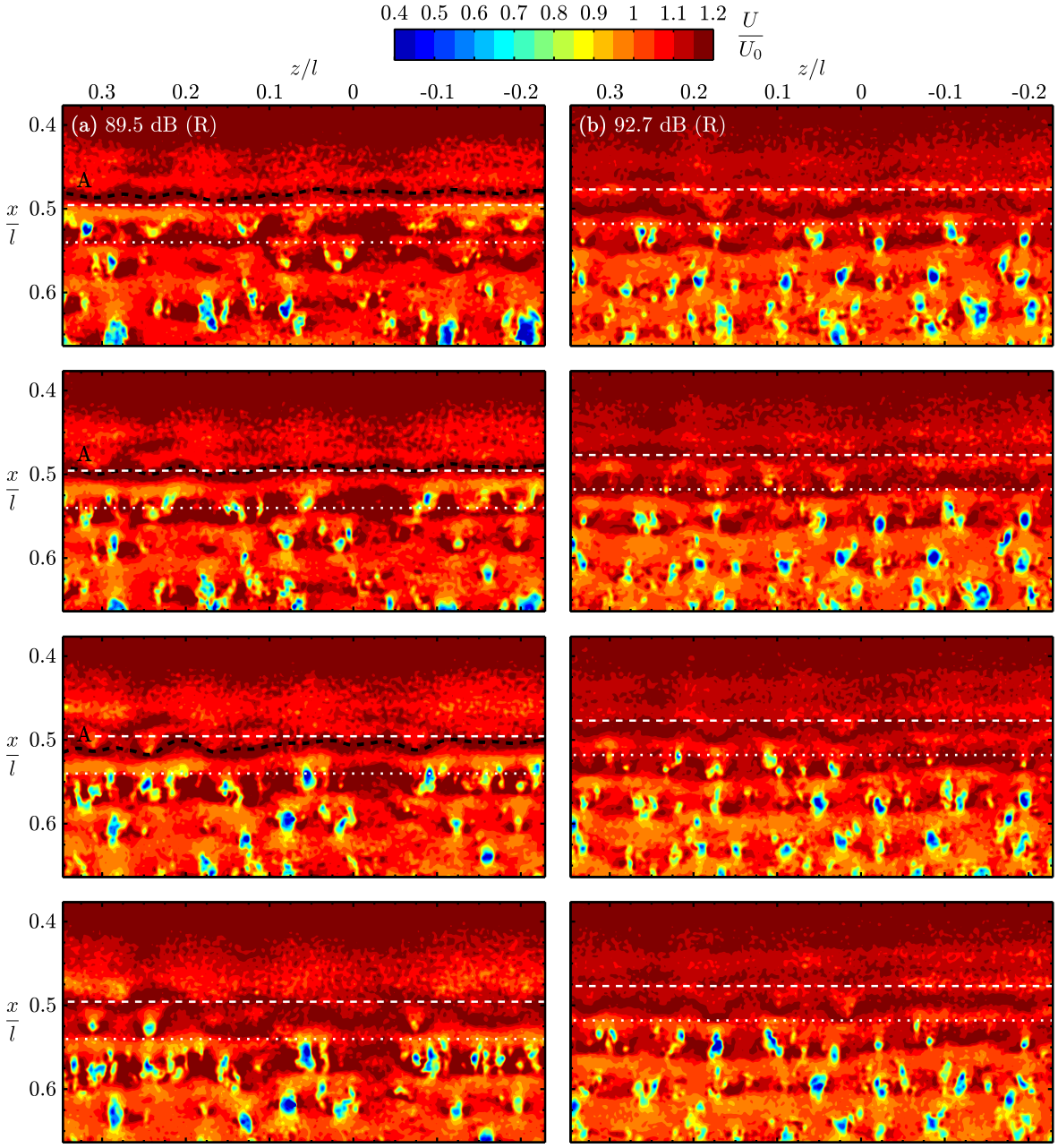

Figure 5.22: Instantaneous contours of streamwise velocity for the 89.5 dB and 92.7 dB random excitation cases. Consecutive frame are separated by $t^* = 2.5 \times 10^{-2}$. Black dashed lines indicate smoothed spline fits to the centre of selected structures. Dashed and dotted white lines mark the mean transition and reattachment points, respectively.

undergoing local merging with the following vortex. Similar observations can be made for the higher excitation amplitude case, shown in Fig. 5.22b. Throughout the sequence, the structures identified at the mean transition point exhibit significant spanwise deformations and appear much less coherent than those observed for the natural and random excitation case of lower amplitude, Figs. 4.11 and 5.22a, respectively. As the structures convect downstream in Fig. 5.22b, the spanwise deformations intensify and lead to localized breakup across the span of the filaments, which occurs in a similar fashion to that observed for the natural case. The hypothesized process by which the localized breakdown of the vortex filaments occurs is discussed in Section 4.2 (see Fig. 4.13). However, no vortex merging is captured in Fig. 5.22b, which indicates that vortex merging is not a necessary condition to incite the disorganized flow state in the aft portion of the bubble.

The characteristic wavelength(s) of the spanwise deformations in the vortex filaments are quantified through spectral analysis of the streamwise velocity fluctuations across the span at the mean transition point. The results for the natural and all random excitation cases are presented in Fig. 5.23. The spectra at low excitation amplitudes (89.5 and 90.4 dB) are similar to that of the natural case, indicating no significant change in the predominant spanwise wavelengths. However, as the excitation amplitude is increased to 92.7 and 94.9 dB, the spectral peak at $\lambda_z/l = 0.2$ diminishes while the peak at $\lambda_z/l = 0.1$ grows, similar to that observed for harmonic excitation when the excitation amplitude is increased (Fig. 5.10). The result is significant, since disturbances with a wavelength of $\lambda_z/l = 0.1$ are associated with deformations that lead to the breakup of the main rollers (as discussed in Section 4.2). This supports the earlier analysis of the flow development presented for Fig. 5.22, showing that increasing amplitudes of random excitation lead to an intensification of the vortex filament deformations. Furthermore, the spectral peaks present at $\lambda_z/l = 0.1$ for the 92.7 and 94.9 dB cases in Fig. 5.23 are more broad, especially towards the smaller wavelengths, than for those of the natural case (Fig. 4.12), as well as the comparable harmonic cases (Fig. 5.10). This implies that random excitation shifts the spanwise deformations to smaller wavelengths, which is speculated to be linked to earlier breakdown of the structures.

Figure 5.24 presents the spanwise coherence lengths, evaluated using Eqs. 4.1 and 4.2, along x/l for selected random excitation cases and the natural case. With increasing excitation amplitude, the peak value in ℓ_z shifts upstream, which is consistent with the upstream movement of the roll-up location and mean transition point, observed in Figs. 5.20 and 5.5, respectively. This was also found to be the case for the harmonic excitations (Fig. 5.11). However, random excitation does not increase the maximum coherence length, as the peak values for the cases presented in Fig. 5.24 are approximately equal. This is different from the harmonic excitation case, where coherence length increased with increasing excitation

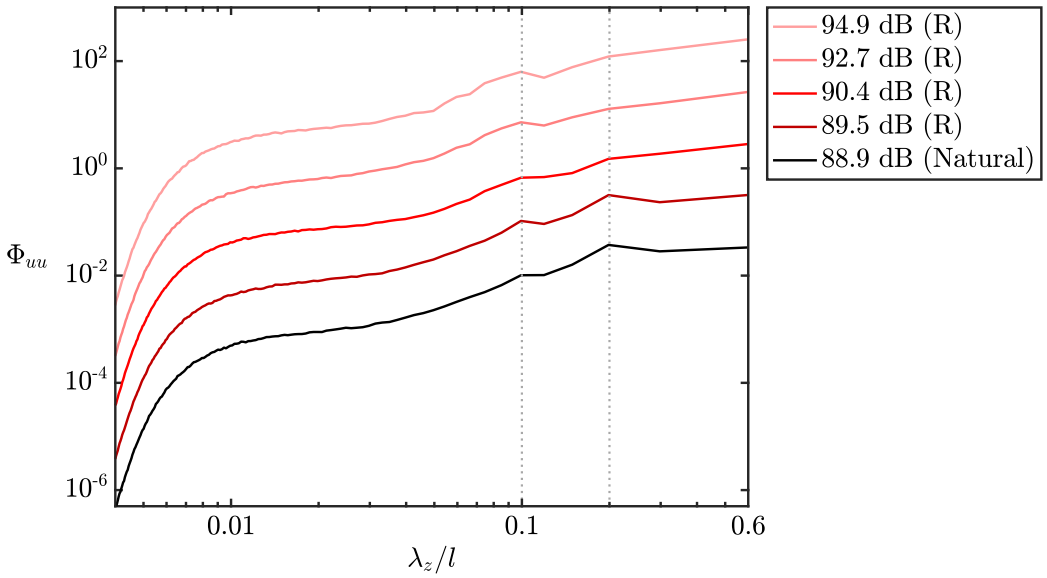

Figure 5.23: Averaged wavelength spectra of streamwise velocity fluctuations across the span at the mean transition point for the natural and random excitation cases. Each spectrum is stepped by one order of magnitude for clarity.

amplitude (Fig. 5.11). While in the case of random excitation, the shedding frequency is forced to vary (Fig. 5.19) and strongly periodic shedding of vortices can be suppressed (as seen in Fig. 5.20). The implication here being that such variability in the shedding process is associated with a decreased coherence of the rollers.

5.3 Discussion

To facilitate a cross-examination of the different excitation types and their effects on the transition process within the studied separation bubble, key characteristics of the most amplified velocity disturbances for all cases examined are summarized in Table 5.2. Subharmonic excitation was shown to produce velocity disturbances in the shear layer of half and twice the fundamental frequency and wavelength, respectively. These disturbances resulted due to a promotion of periodic merging of the shear layer vortices, as shown in Figs. 5.13 and 5.16. Harmonic excitation was applied at the frequency of the most amplified disturbances in the natural flow, which caused the shear layer instability to lock to this frequency, thus reducing both the unstable frequency and wavelength bands (Figs. 5.6 and 5.8); a trend that continued with increasing excitation amplitude, as shown in Ta-

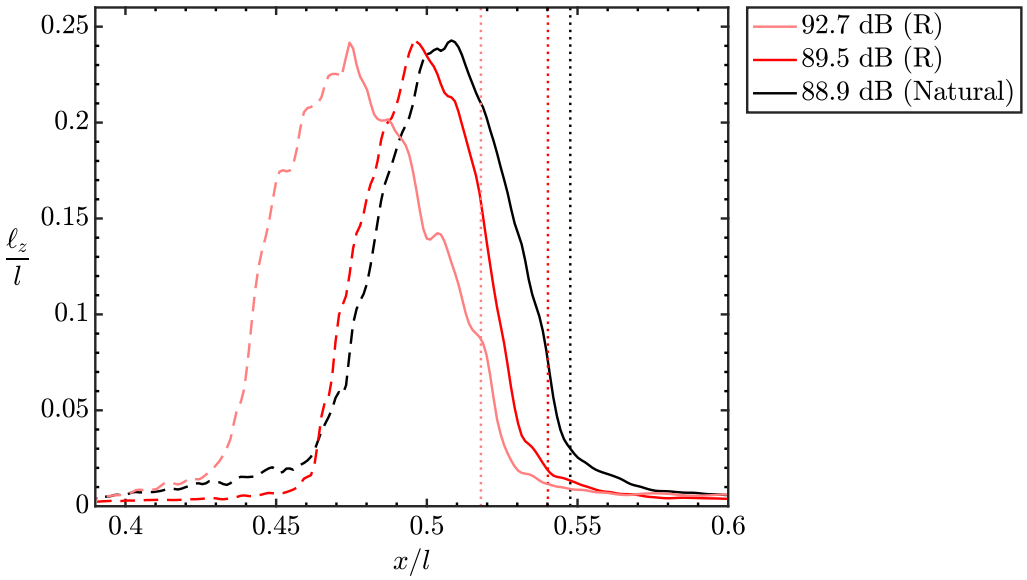

Figure 5.24: Effect of random excitation on spanwise coherence length. Dashed portion of curves indicate where the results are affected by the measurement uncertainty. Dotted lines (coloured according to legend) indicate mean reattachment points.

ble 5.2. These changes in the shear layer's transition process resulted in a more organized flow development in the aft portion of the bubble in both a streamwise and spanwise sense, as shown in Figs. 5.7 and 5.9, respectively. On the other hand, random excitation promoted amplification at all frequencies within the unstable band, which is reflected in Table 5.2 by the width of the unstable frequency and wavelength bands remaining relatively constant with increasing excitation amplitude. The subsequent effect on flow development within the separation bubble was the alternating of the shedding process between two flow distinct flow states, as seen in Fig. 5.7, whereby the random nature of the excitation is speculated to cause the flow to randomly alternate between periods of more and less organized vortex shedding.

With respect to the amplification of disturbances in the separated shear layer, an important distinction must be drawn between the frequency of the most amplified disturbances (as reported in Table 5.2) and the most unstable frequency, as the former was determined in an approximate manner from spectra of velocity fluctuations in the separated shear layer (i.e., Figs. 5.6, 5.12, and 5.19), while the latter is determined through LST analysis of the mean flow, which was not considered in the present investigation. As discussed in Section 2.2.3, the development of unstable disturbances in the fore portion of separation bubbles has been shown to be well-modelled by LST (e.g., Refs. [9, 11–14]), and so the most

Table 5.2: Characteristics of the most amplified velocity disturbances in the separated shear layer.

Case	Parameter*	SPL [dB]				
		88.9	89.5	90.4	92.7	94.9
Nat.	St	$15.6 \pm 33\%$				
	U_c/U_e	0.55				
	λ_x/l	$0.041 \pm 25\%$				
SH	St		$7.8 \pm 8\%$			
	U_c/U_e		0.53			
	λ_x/l		0.080			
H	St		$15.6 \pm 25\%$	$15.6 \pm 22\%$	$15.6 \pm 19\%$	$15.6 \pm 17\%$
	U_c/U_e		0.55	0.55	0.55	0.56
	λ_x/l		$0.041 \pm 23\%$	$0.041 \pm 22\%$	$0.041 \pm 20\%$	$0.043 \pm 19\%$
R	$St^\dagger$		$15.6 \pm 33\%$	$15.6 \pm 33\%$	$15.6 \pm 33\%$	$15.6 \pm 33\%$
	U_c/U_e		0.55	0.55	0.55	0.55
	λ_x/l		$0.041 \pm 23\%$	$0.041 \pm 22\%$	$0.041 \pm 22\%$	$0.041 \pm 22\%$

* Intervals for St and λ_x are estimates of the bands of the amplified frequencies and wavelengths, respectively.
† Value is approximated as the central frequency of the amplified band.

unstable disturbance frequencies can be predicted from experimentally measured mean flow fields. In fact, in the investigation of Yarusevych and Kotsonis [33], the authors showed that the reduction in size of the separation bubble resulting from flow control alters stability characteristics. Specifically, they report that a reduction in bubble length by 30% leads to a reduction in the most amplified frequency by approximately 10% (e.g., see Figs. 17 and 20 in Ref. [33]) as a result of the mean flow deformation. In the present investigation, the separation bubble decreases in length by as much 25% when excited harmonically or randomly (Fig. 5.5). Therefore this effect is expected to occur in the present investigation for these excitation types, which is supported by the more significant amplification of disturbance at frequencies slightly less than fundamental frequency, observed in the spectra of the randomly excited flow (Fig. 5.19). Furthermore, this can explain why earlier roll-up, and hence earlier mean transition, are observed for random excitation in comparison to harmonic excitation, as seen in Figs. 5.3 and 5.5. Prior to excitation, the separated shear layer is most unstable to a particular frequency, which is initially provided by both harmonic and random excitation. However, as the mean topology of the separation bubble changes as a result of the excitation, the most unstable frequency shifts away from the natural

value. This results in a reduction of the effectiveness of the harmonic excitation, while the broadband nature of the random excitation provide excitation at the new most unstable frequency. It can be speculated that, while the disturbances are initiated at lower initial amplitude by random excitation, compared to the harmonic case, the higher growth rate they experience at the continually shifting most unstable frequency allows disturbances to reach critical amplitudes earlier, leading to earlier shear layer roll-up. In future work, LST analysis should be performed on the present results to determine if such a shift in the most unstable frequency can lead to reductions in the effectiveness of harmonic excitation, such that earlier transition is predicted for the comparable random excitation case.

Analyses of the vortex dynamics, presented throughout Section 5.2, demonstrated that both harmonic and random excitation lead to earlier roll-up of the separated shear layer, which correlates with decreases to the overall bubble length. Thus, shear layer roll-up and the production of coherent vortices is the primary cause of reattachment. Similar arguments has been put forward by previous investigators examining reattachment in separation bubbles [16, 33, 201], in addition to results from free shear layer studies, where the Kelvin-Helmholtz rollers are suggested to be the primary mechanism by which momentum is exchanged across the layer [102, 114, 116, 119, 132].

The results presented in Section 5.2.1 established that harmonic excitation organizes the shedding process and leads to more coherent roll-up structures, while random excitation, examined in Section 5.2.3, tends to disorganize the shedding process, leading to a decrease in the coherence of the structures. These different effects on the dynamics within the separation bubble must now be reconciled with the changes in the mean reattachment point, observed in Figs. 5.3 and 5.5. In Section 5.2.1 it was argued that the increased spanwise coherence due to harmonic excitation was responsible for inducing earlier time-averaged reattachment, as the more coherent structures should be more effective at entraining high-momentum fluid from the outer-flow towards the airfoil surface. However, such a conclusion appears to be in contradiction with the results presented in Fig. 5.5 since, for a given SPL (i.e. equal excitation energy input), random excitation produces structures of significantly lower coherence, seen in comparing Figs. 5.11 and 5.24, while still inducing earlier time-averaged reattachment compared to the harmonic case. However, several studies involving separation bubbles formed over airfoils have shown, either directly or indirectly, that highly disorganized and turbulent structures are effective at inducing mean reattachment. For example, consider the relatively small separation bubbles that form on airfoils at high angles of attack [16, 17, 144, 155] or when subjected to three-dimensional forcing [15, 21]. Further examples can be found when separation bubbles form on flat plates with large adverse pressure gradients imposed [11, 148]. In these cases, the development of the shear layer vortices has been described as almost instantly becoming

three-dimensional and turbulent following roll-up [11, 15, 21, 144, 148, 155]. Therefore, in these cases, reattachment is induced by the entertainment of momentum from the outer-flow by structures with turbulent-like scales, rather than the relatively large and initially coherent roll-up vortices. Therefore, the results of this investigation propose that reattachment in a separation bubble is a result of momentum exchange between the outer flow and the near wall region, which can be facilitated by either large scale, coherent shear layer roll-up vortices or smaller scale, turbulent structures that result from the breakup of the shear layer rollers, with the latter proving to be more effective.

Chapter 6

Conclusions

Flow development, the laminar-to-turbulent transition process, and the attendant changes due to controlled acoustic excitation were investigated experimentally within a separation bubble formed on a NACA 0018 airfoil at a chord Reynolds number of 125 000 and an angle of attack of 4°. The flow field was assessed in a series of wind tunnel tests carried out using a combination of surface pressure measurements, and time-resolved, planar, two-component PIV. The PIV measurements were performed in two different configurations, allowing for analysis of both the streamwise and spanwise flow development. Three types of external acoustic excitation were investigated: (i) harmonic: excitation at the frequency of the most amplified disturbances in the unperturbed flow, (ii) subharmonic: excitation at the first subharmonic frequency, and (iii) random: white noise excitation band-pass filtered to the unstable frequency band of the unperturbed flow. A range of excitation amplitudes were considered for the harmonic and random excitation types.

6.1 Natural Separation Bubble Flow Development

For the studied flow conditions, a separation bubble formed on the suction side of the airfoil in the presence of natural disturbances, i.e., without controlled acoustic excitations applied. The mean topological features of the bubble were characterized using both the mean surface pressure distribution and the mean streamwise velocity field. Excellent agreement was found in the estimates produced by these two methodologies. This afforded the opportunity to assess several different approaches proposed in literature [15, 16, 18, 47, 48, 50] for estimating the mean transition point from the mean streamwise velocity. For the studied flow conditions, the streamwise location of the maximum boundary layer shape factor was found to be most appropriate.

In examining the transition process within the separation bubble, the results showed the amplification of disturbances in the fore portion of the bubble led to the roll-up of the separated shear layer and the periodic shedding of vortices. Roll-up occurred in the vicinity of the mean transition point, and the shedding of these structures induced flow reattachment in the mean sense, which was associated with rapid pressure recovery in the aft portion of the bubble. The roll-up vortices were shown to shed within a band of frequencies matching that of the amplified disturbances in the separated shear layer.

The roll-up vortices were characterized by an average convective velocity of $U_c/U_e = 0.55$ and streamwise wavelength of $\lambda_x/l = 0.041$, however, substantial cycle-to-cycle variations in these parameters, as well as the shedding frequency, were observed. The results showed that some of the shed vortices merged. The merging occurred due to the gradual reduction of the convective velocity of the leading vortex in the merging pair, which allowed the two vortices to approach and coalesce. As a result, the streamwise wavelength separating the merged pair and the next downstream vortex approximately doubled.

The newly formed shear layer vortices were characterized by a relatively high spanwise coherence length, $\ell_z/l = 0.25$. However, they underwent rapid spanwise deformations and broke down to smaller structures in the vicinity of the mean reattachment point, marking the last stage in the transition to turbulence. Just downstream of mean reattachment, the spanwise coherence length was shown to decrease to the levels expected for a turbulent boundary layer, indicating that no strongly coherent structures persisted in the redeveloping turbulent boundary layer.

The breakup of the spanwise structures was linked to spanwise deformations of the vortex filaments. Spanwise undulations developed within a range of spanwise wavelengths, $0.05 \lesssim \lambda_z/l \lesssim 0.3$, that corresponds to one to five times that of the mean streamwise wavelength. The development of undulations of wavelength $\lambda_z/l = 0.1$ was shown to be fundamental to the breakdown process, as streamwise bulges in the vortex filaments developed primarily at this wavelength. This lead to the reorientation of spanwise vorticity in the streamwise direction, producing pairs of counter rotating vortices and localized breakup spots, with the general flow structure bearing similarities to Λ-vortices observed in K and H-type transition in attached boundary layers [63, 64, 89, 90]. The local breakup then rapidly spread over the entire spanwise extent of the deformed vortex filament.

6.2 Effect of Acoustic Excitation

Through examination of the mean flow field, applying harmonic or random excitation was found to delay separation, reduce the maximum height of the bubble, and shift mean

transition and reattachment upstream, with the changes becoming more pronounced with increasing excitation amplitude. These trends were attributed to the earlier onset of vortex roll-up in the separated shear layer, which was linked to the excitation providing higher initial amplitude flow perturbations for amplification. The results demonstrated that shear layer roll-up was triggered when velocity fluctuations in the separated shear layer reached a critical amplitude, which was found to be approximately 6% of the free-stream for all cases examined.

A single and relatively low excitation amplitude was investigated for the subharmonic excitation case, which did not produce any significant changes in the mean bubble topology. However, the separated shear layer was found to be receptive to these acoustic disturbances, which led to the inception, growth and decay of velocity fluctuations in the shear layer at the subharmonic frequency, similar to that observed in free shear layers [102, 114]. These velocity disturbances were shown to manifest through periodic vortex merging, that otherwise occurred randomly. Assessment of the spanwise behaviour of the vortex merging process revealed that structures merge in a spanwise non-uniform manner, with localized merging occurring where forward and rearward streamwise-oriented bulges developed in the downstream and upstream vortices, respectively. Therefore, in addition to their fundamental role played in the breakdown process of the shear layer vortices, the spanwise deformations were found to be intrinsic to the vortex merging process.

Spatio-temporal analysis of the flow development within the separation bubble was employed to contrast the effects of the harmonic and random excitation types. Both types of excitation were shown to advance shear layer roll-up upstream, while promoting the development of spanwise deformations in the vortex filaments with a wavelength of $\lambda_z/l = 0.1$, which was previously linked to the breakdown of the structures. However, harmonic excitation was shown to organize the shedding process in the streamwise direction, locking it to the excitation frequency, which led to an increase in spanwise coherence and reductions in the shear layer's unstable frequency and wavelength bands; trends that continued with increasing excitation amplitude. In contrast, random excitation was found to promote periods of disorganized flow development in the aft portion of the bubble, which was associated with decreased spanwise coherence and more evenly distributed spectral energy within the unstable band.

The changes observed in the transition process due to harmonic and random excitation were reconciled with the trends observed in the mean bubble topology. Both excitation types lead to earlier shear layer roll-up, and hence earlier mean transition, in addition to a reduction in the overall bubble length. Therefore, the roll-up of separated shear layer and the production of coherent vortices is the primary cause of mean reattachment. However, random excitation produced earlier mean transition points in comparison the harmonic

case, which was speculated to be caused by changes in the shear layer's most unstable disturbance frequency as a result of the excitation changing the mean topology of the separation bubble. Increased harmonic excitation amplitudes were found to increase the spanwise coherence of the roll-up structures and cause earlier time-averaged reattachment; with the two effects linked, as one would expect a more coherent structure to be more effective at entraining high-momentum fluid from the outer-flow and transporting it to the airfoil surface. Conversely, for a given sound pressure level, random excitation was shown to induce earlier mean reattachment, whose structures were shown to be less coherent than the comparable harmonic case. However, highly disorganized and turbulent structures have been shown to be effective in inducing mean reattachment, for example, in the case of separation bubbles formed on airfoils or flat plates in the presence of large adverse pressure gradients [11, 144, 148, 155] or three-dimensional forcing [15, 154]. Therefore, this investigation proposes that reattachment in a separation bubble is a result of momentum exchange between the outer flow and the near wall region, which can be facilitated by either large scale, coherent shear layer vortices or smaller scale, turbulent structures that result from the breakup of the shear layer rollers, with the latter proving to be more effective.

Chapter 7

Recommendations

The following recommendations are made based on the findings of this thesis:

1) The streamwise oriented vortices speculated to be involved in the breakdown process of the main rollers should be experimentally investigated. Many authors have speculated that such structures are instrumental to the breakdown of spanwise vortices, in both separation bubbles and free shear layers, and so confirmation of their presence would serve to advance the understanding of the later stages of transition. Care should be taken in attempting to identify these structures, as they are not temporally periodic, and therefore would not be captured by phase-averaged measurements.
2) The vortex tracking algorithm employed in this thesis should be improved. The algorithm was only employed for the natural case since it required a significant amount of tuning in order to reliably identify and track the shear layer vortices, to the point where it was unfeasible to implement it for all the excitations cases. Alternatives to vortex identification based on the λ_2-criterion should be assessed, as they may prove to be more robust. Furthermore, the algorithm would benefit from improvements to its logic in identifying vortex merging and breakdown, as currently these two phenomena are not being explicitly identified.
3) Stochastic estimation techniques can be employed to enable robust vortex identification using the airfoil's surface embedded microphone array. Lambert [182], as part of his thesis, developed a vortex tracking algorithm based on high-speed flow visualizations and fluctuating surface pressure signals. Lambert's vortex tracking algorithm and the one developed here should be combined and used to analyze synchronous PIV and surface pressure measurements. In this way, vortex identification from the pressure signals can be made more accurate, which would allow for more robust flow sensing that could be used in a closed-loop flow control system.

4) Stability analysis should be conducted using the base flows measured in this thesis. LST analysis should be performed to determine if the changes to the mean flow invoked by harmonic and random excitation change the most unstable disturbance frequency. Such analysis can examine if such changes in the most unstable frequency lead to reductions in the effectiveness of harmonic excitation, such that earlier transition is predicted for comparable random excitation cases.

5) Stability analysis should also be conducted using the Parabolized Stability Equations (PSE) [202]. PSE analysis is well suited for the results of this investigation as it requires two-component velocity data and can account for non-parallel flow and non-linear interaction effects. Furthermore, secondary instability analysis [63] should be employed, as this tool may be able to provide analytical predictions for the secondary disturbances that develop in the shear layer vortices.

6) The effect of forcing the separated shear layer via spanwise modulated disturbances should be investigated. The results of this investigation indicated that when the shear layer is excited by disturbances with no apparent spanwise wavelength, secondary disturbances develop in the vortex filaments of a fixed spanwise wavelength, the origin of which is unknown. If the spanwise wavelength of the input disturbances can be varied, insight can be gained into the process by which the shear layer selects spanwise disturbances for amplification. Such an experiment could be conducted using the classical vibrating ribbon technique of Klebanoff *et al.* [89] or DBD plasma actuators.

7) The effect of increased excitation amplitude for subharmonic tonal acoustic excitation should be investigated. The results of this study showed significant changes in the dynamics of the separation bubble when subharmonic excitation was supplied; however, these changes did not result in appreciable modifications to the mean bubble topology. This investigation was limited to a single and relatively low excitation amplitude for this case, and therefore it remains unclear if changes in the mean flow field could be produced by higher amplitude subharmonic excitations.

8) Coherence lengths estimates of the structures studied in this thesis would benefit greatly from tomographic PIV measurements, as the coherence for different excitation cases could be calculated at the same positions within and along the separated shear layer with a higher degree of confidence. In the present investigation, the accuracy of the estimates greatly depends on the positioning of the laser sheet with respect to the separated shear layer, which changes in curvature and moves closer to the surface with increasing excitation amplitude.

Permissions

UNIVERSITY OF WATERLOO
200 University Avenue West, Waterloo, ON, Canada N2L 3G1
519-888-4567 | uwaterloo.ca

August 11, 2016

Dear John Kurelek,

This letter serves as a permission for you to publish content from the following papers, in full or in part, in your MASc thesis:

[1] J. W. Kurelek, A. Lambert, and S. Yarusevych, "Development of coherent structures within the laminar separation bubble of a NACA0018 airfoil," in *45th AIAA Fluid Dynamics Conference and Exhibit*, 2015.

[2] J. W. Kurelek, A. R. Lambert, and S. Yarusevych, "Coherent Structures in the Transition Process of a Laminar Separation Bubble," *AIAA J.*, pp. 1–15, May 2016.

[3] J. W. Kurelek and S. Yarusevych, "The effect of acoustic excitation on the later stages of transition in a laminar separation bubble," in *46th AIAA Fluid Dynamics Conference*, 2016.

Sincerely yours,

Serhiy Yarusevych, Ph.D., P.Eng.,

Associate Professor
Department of Mechanical and Mechatronics Engineering
University of Waterloo
200 University Avenue West
Waterloo, On, Canada, N2L 3G1
Phone: (519) 888-4567 x35442
Fax: (519) 885-5862
E-mail: syarus@uwaterloo.ca
Web: http://www.fmrl.uwaterloo.ca

References

[1] P. B. S. Lissaman. Low-Reynolds-Number Airfoils. *Annu. Rev. Fluid Mech.*, 15(1):223–239, 1983. DOI. ↩

[2] B. H. Carmichael. Low Reynolds Number Airfoil Survey. Technical report. NASA Contract Report No. 165803, 1981. URL. ↩

[3] T. J. Mueller and J. D. DeLaurier. Aerodynamics of Small Vehicles. *Annu. Rev. Fluid Mech.*, 35(1):89–111, 2003. DOI. ↩

[4] I. Tani. Low-speed flows involving bubble separations. *Prog. Aerosp. Sci.*, 5:70–103, January 1964. DOI. ↩

[5] M. Gaster. The Structure and Behaviour of Laminar Separation Bubbles. *Aeronaut. Res. Counc.*, RM 3595, 1967. URL. ↩

[6] H. P. Horton. Laminar separation bubbles in two and three dimensional incompressible flow. PhD thesis. Queen Mary College, University of London, 1968. URL. ↩

[7] L. L. Pauley, P. Moin, and W. C. Reynolds. The structure of two-dimensional separation. *J. Fluid Mech.*, 220:397–441, April 1990. DOI. ↩

[8] J. H. Watmuff. Evolution of a wave packet into vortex loops in a laminar separation bubble. *J. Fluid Mech.*, 31:119–169, October 1999. DOI. ↩

[9] M. S. H. Boutilier and S. Yarusevych. Separated shear layer transition over an airfoil at a low Reynolds number. *Phys. Fluids*, 24(8):084105, 2012. DOI. ↩

[10] U. Rist, U. Maucher, and S. Wagner. Direct numerical simulation of some fundamental problems related to transition in laminar separation bubbles. In J.-A. Désidér, C. Hirsch, P. La Tallec, M. Pandolfi, and J. Périaux, editors, *Comput. Fluid Dyn. 96*, pages 319–325. Wiley, 1996. ↩

[11] M. Alam and N. D. Sandham. Direct numerical simulation of 'short' laminar separation bubbles with turbulent reattachment. *J. Fluid Mech.*, 403:223–250, January 2000. DOI. ↩

[12] U. Rist and U. Maucher. Investigations of time-growing instabilities in laminar separation bubbles. *Eur. J. Mech. - B/Fluids*, 21(5):495–509, 2002. DOI. ↩

[13] O. Marxen, M. Lang, U. Rist, and S. Wagner. A Combined Experimental/Numerical Study of Unsteady Phenomena in a Laminar Separation Bubble. *Flow, Turbul. Combust.*, 71(1-4):133–146, 2003. DOI. ↩

[14] S. S. Diwan and O. N. Ramesh. On the origin of the inflectional instability of a laminar separation bubble. *J. Fluid Mech.*, 629:263–298, June 2009. DOI. ↩

[15] M. Lang, U. Rist, and S. Wagner. Investigations on controlled transition development in a laminar separation bubble by means of LDA and PIV. *Exp. Fluids*, 36(1):43–52, 2004. DOI. ↩

[16] S. Burgmann and W. Schröder. Investigation of the vortex induced unsteadiness of a separation bubble via time-resolved and scanning PIV measurements. *Exp. Fluids*, 45(4):675–691, 2008. DOI. ↩

[17] W. Zhang, R. Hain, and C. J. Kähler. Scanning PIV investigation of the laminar separation bubble on a SD7003 airfoil. *Exp. Fluids*, 45(4):725–743, 2008. DOI. ↩

[18] R. Hain, C. J. Kähler, and R. Radespiel. Dynamics of laminar separation bubbles at low-Reynolds-number aerofoils. *J. Fluid Mech.*, 630:129–153, July 2009. DOI. ↩

[19] S. Yarusevych, P. E. Sullivan, and J. G. Kawall. On vortex shedding from an airfoil in low-Reynolds-number flows. *J. Fluid Mech.*, 632:245–271, August 2009. DOI. ↩

[20] E. Wolf, C. J. Kähler, D. R. Troolin, C. Kykal, and W. Lai. Time-resolved volumetric particle tracking velocimetry of large-scale vortex structures from the reattachment region of a laminar separation bubble to the wake. *Exp. Fluids*, 50(4):977–988, 2011. DOI. ↩

[21] L. E. Jones, R. D. Sandberg, and N. D. Sandham. Direct numerical simulations of forced and unforced separation bubbles on an airfoil at incidence. *J. Fluid Mech.*, 602:175–207, May 2008. DOI. ↩

[22] J. R. Brinkerhoff and M. I. Yaras. Interaction of viscous and inviscid instability modes in separation–bubble transition. *Phys. Fluids*, 23(12):124102, 2011. DOI. ↩

[23] O. Marxen, M. Lang, and U. Rist. Vortex Formation and Vortex Breakup in a Laminar Separation Bubble. *J. Fluid Mech.*, 728:58–90, August 2013. DOI. ↩

[24] J.-C. Robinet. Instabilities in laminar separation bubbles. *J. Fluid Mech.*, 732:1–4, October 2013. DOI. ↩

[25] M. Gad-el-Hak. Control of low-speed airfoil aerodynamics. *AIAA J.*, 28(9):1537–1552, 1990. DOI. ↩

[26] D. Greenblatt and I. J. Wygnanski. The control of flow separation by periodic excitation. *Prog. Aerosp. Sci.*, 36(7):487–545, 2000. DOI. ↩

[27] K. K. Ahuja and R. H. Burrin. Control of flow separation by sound. In *9th AIAA Aeroacoustics Conf.* Williamsburg, VA, USA, 1984. DOI. ↩

[28] M. Nishioka, M. Asai, and S. Yoshida. Control of flow separation by acoustic excitation. *AIAA J.*, 28(11):1909–1915, 1990. DOI. ↩

[29] K. B. M. Q. Zaman and D. J. McKinzie. Control of laminar separation over airfoils by acoustic excitation. *AIAA J.*, 29(7):1075–1083, 1991. DOI. ↩

[30] S. Yarusevych, P. E. Sullivan, and J. G. Kawall. Effect of Acoustic Excitation Amplitude on Airfoil Boundary Layer and Wake Development. *AIAA J.*, 45(4):760–771, 2007. DOI. ↩

[31] A. Glezer and M. Amitay. Synthetic Jets. *Annu. Rev. Fluid Mech.*, 34(1):503–529, 2002. DOI. ↩

[32] T. C. Corke, C. L. Enloe, and S. P. Wilkinson. Dielectric Barrier Discharge Plasma Actuators for Flow Control. *Annu. Rev. Fluid Mech.*, 42(1):505–529, 2010. DOI. ↩

[33] S. Yarusevych and M. Kotsonis. Effect of Local DBD Plasma Actuation on Transition in a Laminar Separation Bubble. *Flow, Turbul. Combust.*, 2016 (In Press). DOI. ↩

[34] R. W. Paterson, P. G. Vogt, M. R. Fink, and C. L. Munch. Vortex Noise of Isolated Airfoils. *J. Aircr.*, 10(5):296–302, 1973. DOI. ↩

[35] E. C. Nash, M. V. Lowson, and A. McAlpine. Boundary-layer instability noise on aerofoils. *J. Fluid Mech.*, 382:22–61, March 1999. DOI. ↩

[36] G. Desquesnes, M. Terracol, and P. Sagaut. Numerical investigation of the tone noise mechanism over laminar airfoils. *J. Fluid Mech.*, 591:155–182, November 2007. DOI. ↩

[37] L. E. Jones and R. D. Sandberg. Numerical analysis of tonal airfoil self-noise and acoustic feedback-loops. *J. Sound Vib.*, 330(25):6137–6152, 2011. DOI. ↩

[38] S. Pröbsting, J. Serpieri, and F. Scarano. Experimental investigation of aerofoil tonal noise generation. *J. Fluid Mech.*, 747:656–687, May 2014. DOI. ↩

[39] S. Pröbsting and S. Yarusevych. Laminar separation bubble development on an airfoil emitting tonal noise. *J. Fluid Mech.*, 780:167–191, October 2015. DOI. ↩

[40] R. K. Amiet. Noise due to turbulent flow past a trailing edge. *J. Sound Vib.*, 47(3):387–393, 1976. DOI. ↩

[41] H. Arbey and J. Bataille. Noise generated by airfoil profiles placed in a uniform laminar flow. *J. Fluid Mech.*, 134:33–47, September 1983. DOI. ↩

[42] M. Fosas de Pando, P. J. Schmid, and D. Sipp. A global analysis of tonal noise in flows around aerofoils. *J. Fluid Mech.*, 754:5–38, September 2014. DOI. ↩

[43] P. R. Owen and L. Klanfer. On the Laminar Boundary Layer Separation from the Leading Edge of a Thin Aerofoil. Technical report. R.A.E. Report No. Aero 2508, 1953. URL. ↩

[44] E. J. Fitzgerald and T. J. Mueller. Measurements in a separation bubble on an airfoil using laser velocimetry. *AIAA J.*, 28(4):584–592, 1990. DOI. ↩

[45] M. O'Meara and T. J. Mueller. Laminar separation bubble characteristics on an airfoil at low Reynolds numbers. *AIAA J.*, 25(8):1033–1041, 1987. DOI. ↩

[46] M. S. H. Boutilier and S. Yarusevych. Parametric study of separation and transition characteristics over an airfoil at low Reynolds numbers. *Exp. Fluids*, 52(6):1491–1506, 2012. DOI. ↩

[47] M. Brendel and T. J. Mueller. Boundary-layer measurements on an airfoil at low Reynolds numbers. *J. Aircr.*, 25(7):612–617, 1988. DOI. ↩

[48] B. R. McAuliffe and M. I. Yaras. Separation-Bubble-Transition Measurements on a Low-Re Airfoil Using Particle Image Velocimetry. In *Vol. 3 Turbo Expo 2005, Parts A B*. ASME, Reno, NV, USA, 2005, pages 1029–1038. DOI. ↩

[49] B. R. McAuliffe and M. I. Yaras. Transition Mechanisms in Separation Bubbles Under Low- and Elevated-Freestream Turbulence. *J. Turbomach.*, 132(1):011004, 2010. DOI. ↩

[50] M. V. Ol, B. R. McCauliffe, E. S. Hanff, U. Scholz, and C. Kähler. Comparison of Laminar Separation Bubble Measurements on a Low Reynolds Number Airfoil in Three Facilities. In *35th AIAA Fluid Dyn. Conf. Exhib.* Toronto, ON, Canada, 2005. DOI. ↩

[51] S. Burgmann, J. Dannemann, and W. Schröder. Time-resolved and volumetric PIV measurements of a transitional separation bubble on an SD7003 airfoil. *Exp. Fluids*, 44(4):609–622, 2008. DOI. ↩

[52] J. F. Marchman. Aerodynamic testing at low Reynolds numbers. *J. Aircr.*, 24(2):107–114, 1987. DOI. ↩

[53] E. V. Laitone. Wind tunnel tests of wings at Reynolds numbers below 70 000. *Exp. Fluids*, 23(5):405–409, 1997. DOI. ↩

[54] A. Pelletier and T. J. Mueller. Low Reynolds Number Aerodynamics of Low-Aspect-Ratio, Thin/Flat/Cambered-Plate Wings. *J. Aircr.*, 37(5):825–832, 2000. DOI. ↩

[55] R. Gerakopulos, M. S. H. Boutilier, and S. Yarusevych. Aerodynamic Characterization of a NACA 0018 Airfoil at Low Reynolds Numbers. In *40th AIAA Fluid Dyn. Conf. Exhib.* Chicago, IL, USA, 2010. DOI. ↩

[56] T. J. Mueller. Low Reynolds Number Vehicles. Technical report. AGARDograph No. 288, 1985. ISBN. ↩

[57] T. J. Mueller, L. J. Pohlen, P. E. Conigliaro, and B. J. Jansen. The influence of free-stream disturbances on low Reynolds number airfoil experiments. *Exp. Fluids*, 1(1):3–14, 1983. DOI. ↩

[58] T. J. Mueller. The influence of laminar separation and transition on low Reynolds number airfoil hysteresis. *J. Aircr.*, 22(9):763–770, 1985. DOI. ↩

[59] D. A. Olson, A. W. Katz, A. M. Naguib, M. M. Koochesfahani, D. P. Rizzetta, and M. R. Visbal. On the challenges in experimental characterization of flow separation over airfoils at low Reynolds number. *Exp. Fluids*, 54(2):1470, 2013. DOI. ↩

[60] M. S. Istvan, J. W. Kurelek, and S. Yarusevych. The effect of free-stream turbulence on the structure of laminar separation bubbles. In *46th AIAA Fluid Dyn. Conf.* Washington, DC, USA, June 2016. DOI. ↩

[61] T. Kirk and S. Yarusevych. Later Stages of Transition over a NACA 0018 Airfoil at Low Reynolds Numbers. In *31st AIAA Appl. Aerodyn. Conf.* San Diego, CA, USA, 2013. DOI. ↩

[62] M. S. H. Boutilier and S. Yarusevych. Effects of End Plates and Blockage on Low-Reynolds-Number Flows Over Airfoils. *AIAA J.*, 50(7):1547–1559, 2012. DOI. ↩

[63] T. Herbert. Secondary Instability Of Boundary Layers. *Annu. Rev. Fluid Mech.*, 20(1):487–526, 1988. DOI. ↩

[64] Y. S. Kachanov. Physical Mechanisms of Laminar-Boundary-Layer Transition. *Annu. Rev. Fluid Mech.*, 26(1):411–482, 1994. DOI. ↩

[65] H. L. Reed, W. S. Saric, and D. Arnal. Linear Stability Theory Applied to Boundary Layers. *Annu. Rev. Fluid Mech.*, 28(1):389–428, 1996. DOI. ↩

[66] W. S. Saric, H. L. Reed, and E. J. Kerschen. Boundary-Layer Receptivity to Freestream Disturbances. *Annu. Rev. Fluid Mech.*, 34(1):291–319, 2002. DOI. ↩

[67] W. S. Saric, H. L. Reed, and E. B. White. Stability and Transition of Three-Dimensional Boundary Layers. *Annu. Rev. Fluid Mech.*, 35(1):413–440, 2003. DOI. ↩

[68] M. V. Morkovin, E. Reshotko, and T. Herbert. Transition in open flow systems - a reassessment. *Bull. Am. Phys. Soc.*, 39:1882, 1994. ↩

[69] M. V. Morkovin. On the Many Faces of Transition. In C. S. Wells, editor, *Viscous Drag Reduct.* Pages 1–31. Springer US, Boston, MA, 1969. DOI. ↩

[70] M. Gaster. Growth of Disturbances in Both Space and Time. *Phys. Fluids*, 11(4):723–727, 1968. DOI. ↩

[71] P. Huerre and P. A. Monkewitz. Local and Global Instabilities in Spatially Developing Flows. *Annu. Rev. Fluid Mech.*, 22(1):473–537, 1990. DOI. ↩

[72] P. Andersson, M. Berggren, and D. S. Henningson. Optimal disturbances and bypass transition in boundary layers. *Phys. Fluids*, 11(1):134–150, 1999. DOI. ↩

[73] E. Reshotko. Transient growth: A factor in bypass transition. *Phys. Fluids*, 13(5):1067–1075, 2001. DOI. ↩

[74] F. M. White. *Viscous Fluid Flow*. McGraw Hill, 3rd edition, 2006. ISBN. ↩

[75] H. Schlichting and K. Gersten. *Boundary-Layer Theory*. Springer-Verlag, 8th edition, 2000. ISBN. ↩

[76] W. M. Orr. The Stability or Instability of the Steady Motions of a Perfect Liquid and of a Viscous Liquid. *Proc. R. Irish Acad. Sect. A Math. Phys. Sci.*, 27:9–138, 1907. URL. ↩

[77] A. Sommerfeld. Ein beitrag zur hydrodynamischen erklaerung der turbulenten fluessigkeitsbewegungen. In *Proc. 4th Int. Congr. Math. III*. Rome, Italy, 1908, pages 116–124. URL. ↩

[78] R. Betchov and W. O. Criminale. *Stability of Parallel Flows*. F. N. Frenkiel and G. Temple, editors. Academic Press, 1967. ISBN. ↩

[79] P. G. Drazin and W. H. Reid. *Hydrodynamic Stability*. G. K. Batchelor and J. W. Miles, editors. Cambridge University Press, 2nd edition, 1981. ISBN. ↩

[80] W. Tollmien. Über die Entstehung der Turbulenz. In, *Vor. aus dem Gebiete der Aerodyn. und verwandter Gebiete*, pages 18–21. Springer Berlin Heidelberg, Berlin, Heidelberg, 1930. [translated in NACA Technical Memo. 609]. DOI. ↩

[81] H. Schlichting. Zur Entstehung der Turbulenz bei der Plattenströmung. *Nachrichten von der Gesellschaft der Wissenschaften zu Göttingen, Math. Klasse*:182–208, 1933. URL. ↩

[82] G. Schubauer and H. Skramstad. Laminar boundary-layer oscillations and transition on a flat plate. *J. Res. Natl. Bur. Stand. (1934).*, 38(2):251, 1947. [see also NACA Report No. 909]. DOI. ↩

[83] D. Arnal, J. C. Julien, and R. Michel. Analyse experimentale et calcul de l'apparition et du developpement de la transition de la couche limit. In *AGARD Conf. Proc. 224*, 1977, 13–1 to 13–7. ↩

[84] J. A. Ross, F. H. Barnes, J. G. Burns, and M. A. S. Ross. The flat plate boundary layer. Part 3. Comparison of theory with experiment. *J. Fluid Mech.*, 43(04):819–832, 1970. DOI. ↩

[85] A. J. Strazisar, E. Reshotko, and J. M. Prahl. Experimental study of the stability of heated laminar boundary layers in water. *J. Fluid Mech.*, 83(02):225–247, 1977. DOI. ↩

[86] W. S. Saric. Low-Speed Experiments: Requirements for Stability Measurements. In M. Y. Hussaini and R. G. Voigt, editors, *Instab. Transition; Proc. Work. Hampton, VA, USA, 1989*, pages 162–174. Springer, 1990. DOI. ↩

[87] F. P. Bertolotti, T. Herbert, and P. R. Spalart. Linear and nonlinear stability of the Blasius boundary layer. *J. Fluid Mech.*, 242:441–474, September 1992. DOI. ↩

[88] D. E. Ashpis and E. Reshotko. The vibrating ribbon problem revisited. *J. Fluid Mech.*, 213:531–547, 1990. DOI. ↩

[89] P. S. Klebanoff, K. D. Tidstrom, and L. M. Sargent. The three-dimensional nature of boundary-layer instability. *J. Fluid Mech.*, 12(01):1–34, 1962. DOI. ↩

[90] W. S. Saric and A. S. W. Thomas. Experiments on the subharmonic route to turbulence in boundary layers. In *Turbul. choatic Phenom. fluids; Proc. Int. Symp. Kyoto, Japan, 1983*. T. Tatsumi, editor. Elsevier, 1984, pages 117–122. URL. ↩

[91] Y. S. Kachanov and V. Y. Levchenko. The resonant interaction of disturbances at laminar-turbulent transition in a boundary layer. *J. Fluid Mech.*, 138:209, January 1984. DOI. ↩

[92] S. A. Orszag and L. C. Kells. Transition to turbulence in plane Poiseuille and plane Couette flow. *J. Fluid Mech.*, 96(01):159–205, 1980. DOI. ↩

[93] S. A. Orszag and A. T. Patera. Secondary instability of wall-bounded shear flows. *J. Fluid Mech.*, 128:347–385, March 1983. DOI. ↩

[94] A. Wray and M. Y. Hussaini. Numerical Experiments in Boundary-Layer Stability. *Proc. R. Soc. London, Ser. A*, 392(1803):373–389, 1984. URL. ↩

[95] P. R. Spalart and K.-S. Yang. Numerical study of ribbon-induced transition in Blasius flow. *J. Fluid Mech.*, 178:345–365, May 1987. DOI. ↩

[96] E. Laurien and L. Kleiser. Numerical simulation of boundary-layer transition and transition control. *J. Fluid Mech.*, 199:403–440, February 1989. DOI. ↩

[97] M. M. Rai and P. Moin. Direct Numerical Simulation of Transition and Turbulence in a Spatially Evolving Boundary Layer. *J. Comput. Phys.*, 109(2):169–192, 1993. DOI. ↩

[98] R. D. Joslin, C. L. Streett, and C.-L. Chang. Spatial direct numerical simulation of boundary-layer transition mechanisms: Validation of PSE theory. *Theor. Comput. Fluid Dyn.*, 4(6):271–288, 1993. DOI. ↩

[99] U. Rist and H. Fasel. Direct numerical simulation of controlled transition in a flat-plate boundary layer. *J. Fluid Mech.*, 298:211, September 1995. DOI. ↩

[100] P. Moin and K. Mahesh. Direct Numerical Simulation: A Tool in Turbulence Research. *Annu. Rev. Fluid Mech.*, 30(1):539–578, 1998. DOI. ↩

[101] Lord Kelvin (Sir W. Thomson). Hydrokinetic solutions and observations. *Philos. Mag. Ser. 4*, 42(281):362–377, 1871. URL. ↩

[102] C.-M. Ho. Perturbed Free Shear Layers. *Annu. Rev. Fluid Mech.*, 16(1):365–424, 1984. DOI. ↩

[103] P. Huerre. Open Shear Flow Instabilities. In G. K. Batchelor, H. K. Moffatt, and M. G. Worster, editors, *Perspect. Fluid Dyn. A Collect. Introd. to Curr. Res.* Pages 159–229. Cambridge University Press, 2000. ISBN. ↩

[104] P. Huerre and P. A. Monkewitz. Absolute and convective instabilities in free shear layers. *J. Fluid Mech.*, 159:151–168, October 1985. DOI. ↩

[105] P. J. Strykowski and D. L. Niccum. The stability of countercurrent mixing layers in circular jets. *J. Fluid Mech.*, 227:309–343, June 1991. DOI. ↩

[106] A. Michalke. On spatially growing disturbances in an inviscid shear layer. *J. Fluid Mech.*, 23(03):521–544, 1965. DOI. ↩

[107] C.-M. Ho. Local and Global Dynamics of Free Shear Layers. In T. Cebeci, editor, *Numer. Phys. Asp. Aerodyn. Flows*, pages 521–533. Springer Berlin Heidelberg, Berlin, Heidelberg, 1982. DOI. ↩

[108] P. A. Monkewitz. Influence of the velocity ratio on the spatial instability of mixing layers. *Phys. Fluids*, 25(7):1137–1143, 1982. DOI. ↩

[109] A. Michalke. On the inviscid instability of the hyperbolictangent velocity profile. *J. Fluid Mech.*, 19(04):543–556, 1964. DOI. ↩

[110] H. Sato. Experimental Investigation on the Transition of Laminar Separated Layer. *J. Phys. Soc. Japan*, 11(6):702–709, 1956. DOI. ↩

[111] F. K. Browand. An experimental investigation of the instability of an incompressible, separated shear layer. *J. Fluid Mech.*, 26(02):281–307, 1966. DOI. ↩

[112] P. Freymuth. On transition in a separated laminar boundary layer. *J. Fluid Mech.*, 25(04):683–704, 1966. DOI. ↩

[113] R. W. Miksad. Experiments on the nonlinear stages of free-shear-layer transition. *J. Fluid Mech.*, 56(04):695, 1972. DOI. ↩

[114] C.-M. Ho and L.-S. Huang. Subharmonics and vortex merging in mixing layers. *J. Fluid Mech.*, 119:443–473, June 1982. DOI. ↩

[115] A. Michalke. A note on spatially growing three-dimensional disturbances in a free shear layer. *J. Fluid Mech.*, 38(04):765–767, 1969. DOI. ↩

[116] C. D. Winant and F. K. Browand. Vortex pairing: the mechanism of turbulent mixing-layer growth at moderate Reynolds number. *J. Fluid Mech.*, 63(02):237–255, 1974. DOI. ↩

[117] F. A. Roberts, P. E. Dimotakis, and A. Roshko. Kelvin-Helmholtz instability of superposed streams. In M. Van Dyke, editor, *An Album Fluid Motion*, page 85. Parabolic, Standford, CA, 1982. URL. ↩

[118] J. C. Lasheras and H. Choi. Three-dimensional instability of a plane free shear layer: an experimental study of the formation and evolution of streamwise vortices. *J. Fluid Mech.*, 189:53, April 1988. DOI. ↩

[119] G. L. Brown and A. Roshko. On density effects and large structure in turbulent mixing layers. *J. Fluid Mech.*, 64(04):775–816, 1974. DOI. ↩

[120] F. K. Browand and P. D. Weidman. Large scales in the developing mixing layer. *J. Fluid Mech.*, 76(01):127–144, 1976. DOI. ↩

[121] R. E. Kelly. On the stability of an inviscid shear layer which is periodic in space and time. *J. Fluid Mech.*, 27(04):657–689, 1967. DOI. ↩

[122] J. H. Konrad. An experimental investigation of mixing in two-dimensional turbulent shear flows with applications to diffusion-limited chemical reactions. PhD thesis. California Institute of Technology, 1977. URL. ↩

[123] L. P. Bernal and A. Roshko. Streamwise vortex structure in plane mixing layers. *J. Fluid Mech.*, 170:499–525, September 1986. DOI. ↩

[124] A. K. M. F. Hussain. Coherent structures and incoherent turbulence. In *Turbul. chaotic Phenom. fluids; Proc. Int. Symp. Kyoto, Japan, 1983*. T. Tatsumi, editor. Elsevier, 1984, pages 453–460. ISBN. ↩

[125] J. Jimenez. A spanwise structure in the plane shear layer. *J. Fluid Mech.*, 132:319–336, July 1983. DOI. ↩

[126] J. H. Bell and R. D. Mehta. Measurements of the streamwise vortical structures in a plane mixing layer. *J. Fluid Mech.*, 239:213–248, June 1992. DOI. ↩

[127] R. W. Metcalfe, S. A. Orszag, M. E. Brachet, S. Menon, and J. J. Riley. Secondary instability of a temporally growing mixing layer. *J. Fluid Mech.*, 184:207–243, November 1987. DOI. ↩

[128] W. T. Ashurst and E. Meiburg. Three-dimensional shear layers via vortex dynamics. *J. Fluid Mech.*, 189:87–116, 1988. DOI. ↩

[129] M. M. Rogers and R. D. Moser. The three-dimensional evolution of a plane mixing layer: the Kelvin–Helmholtz rollup. *J. Fluid Mech.*, 243:183–226, October 1992. DOI. ↩

[130] L.-S. Huang and C.-M. Ho. Small-scale transition in a plane mixing layer. *J. Fluid Mech.*, 210:475–500, January 1990. DOI. ↩

[131] K. J. Nygaard and A. Glezer. Evolution of stream wise vortices and generation of small-scale motion in a plane mixing layer. *J. Fluid Mech.*, 231:257–301, October 1991. DOI. ↩

[132] P. E. Dimotakis and G. L. Brown. The mixing layer at high Reynolds number: large-structure dynamics and entrainment. *J. Fluid Mech.*, 78(03):535–560, 1976. DOI. ↩

[133] J. T. Stuart. On finite amplitude oscillations in laminar mixing layers. *J. Fluid Mech.*, 29(03):417–440, 1967. DOI. ↩

[134] R. T. Pierrehumbert and S. E. Widnall. The two- and three-dimensional instabilities of a spatially periodic shear layer. *J. Fluid Mech.*, 114:59–82, January 1982. DOI. ↩

[135] R. T. Pierrehumbert. Universal Short-Wave Instability of Two-Dimensional Eddies in an Inviscid Fluid. *Phys. Rev. Lett.*, 57(17):2157–2159, 1986. DOI. ↩

[136] B. J. Bayly. Three-Dimensional Instability of Elliptical Flow. *Phys. Rev. Lett.*, 57(17):2160–2163, 1986. DOI. ↩

[137] R. R. Kerswell. Elliptical Instability. *Annu. Rev. Fluid Mech.*, 34(1):83–113, 2002. DOI. ↩

[138] G. P. Klaassen and W. R. Peltier. The onset of turbulence in finite-amplitude Kelvin–Helmholtz billows. *J. Fluid Mech.*, 155:1–35, June 1985. DOI. ↩

[139] C. P. Caulfield and R. R. Kerswell. The nonlinear development of three-dimensional disturbances at hyperbolic stagnation points: A model of the braid region in mixing layers. *Phys. Fluids*, 12(5):1032, 2000. DOI. ↩

[140] R. R. Lagnado, N. Phan-Thien, and L. G. Leal. The stability of two-dimensional linear flows. *Phys. Fluids*, 27(5):1094–1101, 1984. DOI. ↩

[141] A. D. D. Craik and W. O. Criminale. Evolution of Wavelike Disturbances in Shear Flows: A Class of Exact Solutions of the Navier-Stokes Equations. *Proc. R. Soc. A Math. Phys. Eng. Sci.*, 406(1830):13–26, 1986. DOI. ↩

[142] T. M. Kirk. The Later Stages of Transition over a NACA0018 Airfoil at a Low Reynolds Number. MASc. Thesis. University of Waterloo, 2014. URL. ↩

[143] J. Serna and B. J. Lázaro. The final stages of transition and the reattachment region in transitional separation bubbles. *Exp. Fluids*, 55(4):1695, 2014. DOI. ↩

[144] A. R. Lambert and S. Yarusevych. Analyzing Vortex Dynamics in the Laminar Separation Bubble via Surface Pressure Measurements. In *45th AIAA Fluid Dyn. Conf. Exhib.* Dallas, TX, USA, 2015. DOI. ↩

[145] A. Dovgal, V. Kozlov, and A. Michalke. Laminar boundary layer separation: Instability and associated phenomena. *Prog. Aerosp. Sci.*, 30(1):61–94, 1994. DOI. ↩

[146] P. LeBlanc, R. Blackwelder, and R. Liebeck. A Comparison Between Boundary Layer Measurements in a Laminar Separation Bubble Flow and Linear Stability Theory Calculations. In T. J. Mueller, editor, *Low Reynolds Number Aerodyn.* Pages 189–205. Spinger Berlin Heidelberg, 1989. DOI. ↩

[147] E. Malkiel and R. E. Mayle. Transition in a Separation Bubble. *J. Turbomach.*, 118(4):752, 1996. DOI. ↩

[148] P. R. Spalart and M. K. Strelets. Mechanisms of transition and heat transfer in a separation bubble. *J. Fluid Mech.*, 403:329–349, January 2000. DOI. ↩

[149] O. Marxen, U. Rist, and S. Wagner. Effect of Spanwise-Modulated Disturbances on Transition in a Separated Boundary Layer. *AIAA J.*, 42(5):937–944, 2004. DOI. ↩

[150] R. Gerakopulos and S. Yarusevych. Novel Time-Resolved Pressure Measurements on an Airfoil at a Low Reynolds Number. *AIAA J.*, 50(5):1189–1200, 2012. DOI. ↩

[151] A. V. Boiko, G. R. Grek, A. V. Dovgal, and V. V. Kozlov. *The Origin of Turbulence in Near-Wall Flows*. Springer, 2002. ISBN. ↩

[152] D. Lengani, D. Simoni, M. Ubaldi, and P. Zunino. POD analysis of the unsteady behavior of a laminar separation bubble. *Exp. Therm. Fluid Sci.*, 58:70–79, October 2014. DOI. ↩

[153] J. C. M. Lin and L. L. Pauley. Low-Reynolds-number separation on an airfoil. *AIAA J.*, 34(8):1570–1577, 1996. DOI. ↩

[154] L. E. Jones, R. D. Sandberg, and N. D. Sandham. Stability and Receptivity Characteristics of a Laminar Separation Bubble on an Aerofoil. *J. Fluid Mech.*, 648:257–296, April 2010. DOI. ↩

[155] W. Balzer and H. F. Fasel. Direct Numerical Simulation of Laminar Boundary-Layer Separation and Separation Control on the Suction Side of an Airfoil at Low Reynolds Number Conditions. In *40th AIAA Fluid Dyn. Conf. Exhib.* Chicago, IL, USA, 2010. DOI. ↩

[156] R. Wahidi, W. Lai, J. P. Hubner, and A. Lang. Time-averaged and time-resolved volumetric velocimetry measurements of a laminar separation bubble on an airfoil. *Eur. J. Mech. - B/Fluids*, 41:46–59, September 2013. DOI. ↩

[157] A. Nati, R. de Kat, F. Scarano, and B. W. van Oudheusden. Dynamic pitching effect on a laminar separation bubble. *Exp. Fluids*, 56(9):172, 2015. DOI. ↩

[158] C. Willert and M. Gharib. Three-dimensional particle imaging with a single camera. *Exp. Fluids*, 12(6):353–358, 1992. DOI. ↩

[159] F. Pereira, M. Gharib, D. Dabiri, and D. Modarress. Defocusing digital particle image velocimetry: a 3-component 3-dimensional DPIV measurement technique. Application to bubbly flows. *Exp. Fluids*, 29(7):S078–S084, 2000. DOI. ↩

[160] T. F. Brooks, D. S. Pope, and M. A. Marcolini. Airfoil Self-Noise and Prediction. Technical report. NASA Ref. Pub. 1218, 1989. URL. ↩

[161] F. G. Collins and J. Zelenevitz. Influence of Sound upon Separated Flow over Wings. *AIAA J.*, 13(3):408–410, 1975. DOI. ↩

[162] K. B. M. Q. Zaman, A. Bar-Sever, and S. M. Mangalam. Effect of acoustic excitation on the flow over a low- Re airfoil. *J. Fluid Mech.*, 182:127–148, September 1987. DOI. ↩

[163] K. B. M. Q. Zaman. Effect of acoustic excitation on stalled flows over an airfoil. *AIAA J.*, 30(6):1492–1499, 1992. DOI. ↩

[164] S. Yarusevych, J. G. Kawall, and P. E. Sullivan. Airfoil Performance at Low Reynolds Numbers in the Presence of Periodic Disturbances. *J. Fluids Eng.*, 128(3):587, 2006. DOI. ↩

[165] L. S. Huang, L. Maestrello, and T. D. Bryant. Separation control over an airfoil at high angles of attack by sound emanating from the surface. In *19th AIAA Fluid Dyn. Plasma Dyn. Lasers Conf.* Honolulu, HI, USA, 1987. DOI. ↩

[166] R. C. Chang, F.-B. Hsiao, and R.-N. Shyu. Forcing level effects of internal acoustic excitation on the improvement of airfoil performance. *J. Aircr.*, 29(5):823–829, 1992. DOI. ↩

[167] F.-B. Hsiao, J.-J. Jih, and R.-N. Shyu. The effect of acoustics on flow passing a high-AOA airfoil. *J. Sound Vib.*, 199(2):177–188, 1997. DOI. ↩

[168] L. N. Cattafesta and M. Sheplak. Actuators for Active Flow Control. *Annu. Rev. Fluid Mech.*, 43(1):247–272, 2011. DOI. ↩

[169] M. Amitay and A. Glezer. Role of Actuation Frequency in Controlled Flow Reattachment over a Stalled Airfoil. *AIAA J.*, 40(2):209–216, 2002. DOI. ↩

[170] A. Glezer, M. Amitay, and A. M. Honohan. Aspects of Low- and High-Frequency Actuation for Aerodynamic Flow Control. *AIAA J.*, 43(7):1501–1511, 2005. DOI. ↩

[171] S. Pröbsting, F. Scarano, and S. C. Morris. Regimes of tonal noise on an airfoil at moderate Reynolds number. *J. Fluid Mech.*, 780:407–438, October 2015. DOI. ↩

[172] T. Brooks and T. Hodgson. Trailing edge noise prediction from measured surface pressures. *J. Sound Vib.*, 78(1):69–117, 1981. DOI. ↩

[173] T. P. Chong and P. Joseph. "Ladder" structure in tonal noise generated by laminar flow around an airfoil. *J. Acoust. Soc. Am.*, 131(6):EL461–EL467, 2012. DOI. ↩

[174] C. K. W. Tam. Discrete tones of isolated airfoils. *J. Acoust. Soc. Am.*, 55(6):1173, 1974. DOI. ↩

[175] H. Atassi. Feedback in separated flows over symmetric airfoils. In *9th AIAA Aeroacoustics Conf.* Williamsburg, VA, USA, October 1984. DOI. ↩

[176] S. Takagi and Y. Konishi. Frequency Selection Mechanism of Airfoil Trailing-Edge Noise. *J. Aircr.*, 47(4):1111–1116, 2010. DOI. ↩

[177] B. Plogmann, A. Herrig, and W. Würz. Experimental investigations of a trailing edge noise feedback mechanism on a NACA 0012 airfoil. *Exp. Fluids*, 54(5):1480, 2013. DOI. ↩

[178] K. L. Schumacher, C. J. Doolan, and R. M. Kelso. The effect of a cavity on airfoil tones. *J. Sound Vib.*, 333(7):1913–1931, 2014. DOI. ↩

[179] M. J. Kingan and J. R. Pearse. Laminar boundary layer instability noise produced by an aerofoil. *J. Sound Vib.*, 322(4-5):808–828, 2009. DOI. ↩

[180] R. J. Gerakopulos. Investigating Flow over an Airfoil at Low Reynolds Numbers Using Novel Time-Resolved Surface Pressure Measurements. MASc. Thesis. University of Waterloo, 2011. URL. ↩

[181] M. S. H. Boutilier. Experimental Investigation of Transition over a NACA 0018 Airfoil at a Low Reynolds Number. MASc. Thesis. University of Waterloo, 2011. URL. ↩

[182] A. R. Lambert. Vortex Dynamics within the Laminar Separation Bubble over a NACA 0018 Airfoil at Low Reynolds Numbers. MASc. Thesis. University of Waterloo, 2015. URL. ↩

[183] J. B. Barlow, W. H. Rae, and A. Pope. *Low-speed wind tunnel testing*. Wiley, 3rd edition, 1999. ISBN. ↩

[184] R. Parker. Resonance effects in wake shedding from parallel plates: Some experimental observations. *J. Sound Vib.*, 4(1):62–72, 1966. DOI. ↩

[185] R. Parker. Resonance effects in wake shedding from parallel plates: Calculation of resonant frequencies. *J. Sound Vib.*, 5(2):330–343, 1967. DOI. ↩

[186] T. Atobe, M. Tuinstra, and S. Takagi. Airfoil Tonal Noise Generation in Resonant Environments. *Trans. Japan Soc. Aero. Sp. Sci.*, 52(176):74–80, 2009. DOI. ↩

[187] C. Tropea, A. Yarin, and J. F. Foss, editors. *Springer Handbook of Experimental Fluid Mechanics*. Springer-Verlag, 2007. ISBN. ↩

[188] P. Welch. The use of fast Fourier transform for the estimation of power spectra: A method based on time averaging over short, modified periodograms. *IEEE Trans. Audio Electroacoust.*, 15(2):70–73, 1967. DOI. ↩

[189] A. Sciacchitano, B. Wieneke, and F. Scarano. PIV uncertainty quantification by image matching. *Meas. Sci. Technol.*, 24(4):045302, 2013. DOI. ↩

[190] A. Sciacchitano, D. R. Neal, B. L. Smith, S. O. Warner, P. P. Vlachos, B. Wieneke, and F. Scarano. Collaborative framework for PIV uncertainty quantification: comparative assessment of methods. *Meas. Sci. Technol.*, 26(7):074004, 2015. DOI. ↩

[191] J. Westerweel and F. Scarano. Universal outlier detection for PIV data. *Exp. Fluids*, 39(6):1096–1100, 2005. DOI. ↩

[192] J. Jeong and F. Hussain. On the identification of a vortex. *J. Fluid Mech.*, 285:69–94, February 1995. DOI. ↩

[193] Z. Yang and P. R. Voke. Large-eddy simulation of boundary-layer separation and transition at a change of surface curvature. *J. Fluid Mech.*, 439:305–333, July 2001. DOI. ↩

[194] M. Talan and J. Hourmouziadis. Characteristic Regimes of Transitional Separation Bubbles in Unsteady Flow. *Flow, Turbul. Combust.*, 69(3-4):207–227, 2002. DOI. ↩

[195] M. S. Howe. *Acoustics of Fluid-Structure Interactions*. G. K. Batchelor, L. B. Freund, S. Leibovich, and V. Tvergaard, editors. Cambridge University Press, 1998. ISBN. ↩

[196] C. Cerretelli and C. Williamson. The physical mechanism for vortex merging. *J. Fluid Mech.*, 475:41–77, January 2003. DOI. ↩

[197] C. Norberg. Fluctuating lift on a circular cylinder: review and new measurements. *J. Fluids Struct.*, 17(1):57–96, 2003. DOI. ↩

[198] D. Palumbo. Determining correlation and coherence lengths in turbulent boundary layer flight data. *J. Sound Vib.*, 331(16):3721–3737, 2012. DOI. ↩

[199] S. Pröbsting, F. Scarano, M. Bernardini, and S. Pirozzoli. On the estimation of wall pressure coherence using time-resolved tomographic PIV. *Exp. Fluids*, 54(7):1567, 2013. DOI. ↩

[200] M. Roger, S. Moreau, and A. Guédel. Vortex-Shedding Noise and Potential-Interaction Noise Modeling by a Reversed Sears' Problem. In *12th AIAA/CEAS Aeroacoustics Conf. Exhib.* Cambridge, MA, USA, 2006. DOI. ↩

[201] O. Marxen and D. S. Henningson. The effect of small-amplitude convective disturbances on the size and bursting of a laminar separation bubble. *J. Fluid Mech.*, 671:1–33, March 2011. DOI. ↩

[202] T. Herbert. Parabolized Stability Equations. *Annu. Rev. Fluid Mech.*, 29:245–283, January 1997. DOI. ↩

[203] R. J. Moffat. Contributions to the Theory of Single-Sample Uncertainty Analysis. *J. Fluids Eng.*, 104(2):250–258, 1982. DOI. ↩

[204] R. J. Moffat. Using Uncertainty Analysis in the Planning of an Experiment. *J. Fluids Eng.*, 107(2):173, 1985. DOI. ↩

[205] R. J. Moffat. Describing the uncertainties in experimental results. *Exp. Therm. Fluid Sci.*, 1(1):3–17, 1988. DOI. ↩

[206] M. Raffel, C. Willert, S. Wereley, and J. Kompenhans. *Particle Image Velocimetry: A Practical Guide*. Springer, 2nd edition, 2007. DOI. ↩

[207] R. J. Adrian. Particle-Imaging Techniques for Experimental Fluid Mechanics. *Annu. Rev. Fluid Mech.*, 23(1):261–304, 1991. DOI. ↩

[208] J. Westerweel. Fundamentals of digital particle image velocimetry. *Meas. Sci. Technol.*, 8(12):1379–1392, 1997. DOI. ↩

[209] J. Westerweel. Theoretical analysis of the measurement precision in particle image velocimetry. *Exp. Fluids*, 29(7):S003–S012, 2000. DOI. ↩

[210] R. D. Keane and R. J. Adrian. Theory of cross-correlation analysis of PIV images. *Appl. Sci. Res.*, 49(3):191–215, 1992. DOI. ↩

[211] J. S. Bendat and A. G. Piersol. *Random Data - Analysis and Measurement Procedures*. Wiley, 4th edition, 2010. ISBN. ↩

[212] S. Chue. Pressure probes for fluid measurement. *Prog. Aerosp. Sci.*, 16(2):147–223, 1975. DOI. ↩

[213] F. M. White. *Fluid Mechanics*. McGraw Hill, 6th edition, 2008. ISBN. ↩

[214] S. B. Pope. *Turbulent Flows*. Cambridge University Press, 2000. ISBN. ↩

[215] S. Tavoularis. *Measurement in Fluid Mechanics*. Cambridge University Press, 2005. ISBN. ↩

[216] Y. Kubo, M. Miyazaki, and K. Kato. Effects of end plates and blockage of structural members on drag forces. *J. Wind Eng. Ind. Aerodyn.*, 32(3):329–342, 1989. DOI. ↩

[217] G. S. West and C. J. Apelt. The effects of tunnel blockage and aspect ratio on the mean flow past a circular cylinder with Reynolds numbers between 10^4 and 10^5. *J. Fluid Mech.*, 114:361–377, January 1982. DOI. ↩

[218] T. A. Fox and G. S. West. On the use of end plates with circular cylinders. *Exp. Fluids*, 9(4):237–239, 1990. DOI. ↩

[219] Brüel and Kjær. Microphone Handbook - Vol. 1: Theory. Technical report. 1999. URL. ↩

Appendices

Appendix A

Experimental Uncertainties

Table A.1 summarizes the uncertainty estimates for the principle results presented in this thesis. All uncertainties presented as part of this work are determined using the n^{th} order uncertainty methodology of Moffat [203–205], where the uncertainty in a particular quantity β is the result of the n sources of error in the measurement, with the total uncertainty, ψ_β, estimated as the root-sum-square of all the error estimates:

$$\psi_\beta = \pm \left(\sum_{i=1}^{n} {\psi_i}^2 \right)^{1/2} \tag{A.1}$$

Inevitably, the investigator is unable to account for all n source of error in the measurement, and so it is their responsibility to evaluate the major contributors to the total uncertainty, such that the observations and conclusions drawn from the measurement are unambiguous.

Often in experiments a desired quantity is measured indirectly, e.g. measuring the dynamic pressure captured by a pitot-static tube and then converting this to a velocity estimate using Bernoulli's principle. In these cases, when the relationship between the desired, β, and all measurement quantities, ϵ_i, is known, i.e. $\beta = g\left(\epsilon_1, \epsilon_2, \ldots \epsilon_n\right)$, then the uncertainty in β can be determined using a root-sum-square approach:

$$\psi_\beta = \left[\left(\frac{\partial g}{\partial \epsilon_1} \psi_{\epsilon_1} \right)^2 + \left(\frac{\partial g}{\partial \epsilon_2} \psi_{\epsilon_2} \right)^2 + \ldots \left(\frac{\partial g}{\partial \epsilon_n} \psi_{\epsilon_n} \right)^2 \right]^{1/2} \tag{A.2}$$

where the partial derivatives represent the sensitivities of the desired quantity to the measured values. The use of Eq. A.2 is straight forward when the function g is known and its derivatives can be evaluated. In this investigation this is not always the case, as desired

Table A.1: Measurement uncertainty estimates.

Quantity	Condition	Uncertainty*	Applies To
C_P		± 0.008	Figs. 4.1 and 5.2
H		$[\pm 3.3\%, \pm 10.9\%]$	Figs. 4.3 and 5.4
Re		$\pm 2.90\%$	
St		± 0.04	Figs. 4.4a, 5.6, 5.12, and 5.19 and Table 5.2
$k_x l$	along convective ridge	± 0.26	Figs. 4.6, 5.8, 5.15, and 5.21
ℓ_z		$\pm 5\%$	Figs. 4.14, 5.11, 5.18, and 5.24
SPL		$\pm 0.2\,\mathrm{dB}$	Fig. 5.1 and Table 5.1
U/U_0	from side-view PIV	$[\pm 0.014, \pm 0.07]$	Figs. 4.2a and 5.3a
U/U_0	from top-view PIV	$[\pm 0.015, \pm 0.08]$	Figs. 4.11, 5.9, 5.16, and 5.22
U_c		$[\pm 15.2\%, \pm 18.5\%]$	Figs. 4.6, 5.8, 5.15, and 5.21 and Table 5.2
u'		$\pm 2.17\%$	Figs. 4.2b and 5.3b
v'		$\pm 2.33\%$	Figs. 4.2c and 5.3c
x_h	from dividing streamline	$[\pm 0.82\%, \pm 1.4\%]$	Figs. 4.2 and 5.3
x_R	from dividing streamline	$[\pm 1.2\%, \pm 2.4\%]$	Figs. 4.2, 5.3, and 5.5 and Table 4.1
x_R	from C_P		
x_S	from dividing streamline	$[\pm 7.4\%, \pm 9.3\%]$	Figs. 4.2, 5.3, and 5.5 and Table 4.1
x_S	from C_P		
x_T	from H	$[\pm 0.82\%, \pm 1.8\%]$	Table 4.1 and Fig. 5.5
x_T	from C_P		
α		$\pm 4.0\%$	
δ		$[\pm 0.01\%, \pm 4.7\%]$	Fig. E.1a
δ^*		$[\pm 1.6\%, \pm 8.2\%]$	Figs. 4.2, 4.10, 5.3, and E.1b
θ		$[\pm 0.04\%, \pm 8.3\%]$	Fig. E.1c
λ_x/l	along convective ridge	$\pm 1.05 \times 10^{-4}$	Figs. 4.6, 5.8, 5.15, and 5.21 and Table 5.2
λ_z/l		$[\pm 15\%, \pm 50\%]$	Figs. 4.12, 5.10, 5.17, and 5.23

* All uncertainty estimates are associated with a 95% confidence interval.

results are often derived from numerical approximations (e.g. of derivatives or integrations) that must be employed due to the discrete nature of the data. In these instances a 'propagation of uncertainties' approach is taken, where the known uncertainty of the measured quantity is applied to the data before being put through the analysis procedure. The result with the uncertainty embedded within is then compared to that without. In this sense, the uncertainty is propagated through the analysis technique to give an estimate of its impact on the desired result given the particular analysis employed. This uncertainty estimate can then be combined with others using the root-sum-square approach (Eq. A.1).

The remaining sections of this appendix detail how the uncertainty estimates presented in Table A.1 were determined.

A.1 Experimental Conditions

The chord-based Reynolds number depends on three measured quantities: free-stream velocity, U_0, airfoil chord length, c, and fluid kinematic viscosity, ν. The airfoil chord length is known to a high degree of precision and therefore does not contribute to the uncertainty of Re, i.e. $\psi_c \approx 0$. The dynamic viscosity was measured indirectly via measurement of the ambient temperature and pressure, which are associated with uncertainties of $\pm 0.2\%$ and $\pm 0.01\%$, respectively. Combining these estimates results in $\psi_\nu = \pm 0.2\%$. The free-stream velocity was determined by measuring the pressure drop across the wind tunnel's contraction, relating this to a free-stream dynamic pressure through a calibration relationship, and then calculating U_0 using Bernoulli's principle (see Appendix B). The contraction pressure drop was measured using a Setra Model 239 differential pressure transducer with a full range of 500 Pa, resulting in an uncertainty of $\pm 0.3\%$, which takes into account the innate accuracy of the device and temporal fluctuations in the measurement. This uncertainty in the contraction pressure drop is converted to that of the free-stream dynamic pressure using Eq. A.2 and the calibration relationship (Eq. B.2), resulting in an uncertainty on P_{dyn} of $\pm 5.76\%$, with the major contributor being the quality of the calibration fit. Then, the uncertainty on P_{dyn} is converted to that on U_0 according to Bernoulli's principle, which is also root-sum-squared with the fluid density uncertainty ($\pm 0.2\%$) to give a final estimate of the free-stream velocity uncertainty of $\psi_{U_0} = \pm 2.89\%$. The uncertainty on the Reynolds number is then calculated using Eq. A.2, with the uncertainty estimates for the free-stream velocity and the dynamic viscosity as inputs, resulting in $\psi_{Re} = \pm 2.90\%$.

The angle of attack was set using a digital protractor with an angular resolution of $0.1°$, however, the uncertainty in α is also influenced by a possible bias error introduced when determining the aerodynamic zero angle of attack. This angle was determined by

measuring lift coefficients, via the model's static pressure taps, over a range of negative and positive angles within which the lift slope is linear. By fitting a linear trend line to these data and finding the angle that gives zero lift via interpolation, the uncertainty in the aerodynamic zero angle of attack is estimated to be $\pm 0.15°$. The combined uncertainty on the angle of attack is then $\psi_\alpha = \pm 0.16°$, or approximately 4% of the investigated value (4°).

The sound pressure level due to acoustic excitation was measured at the natural separation point, approximately 5 mm from the airfoil surface using a Brüel and Kjær 4192 condenser microphone. The manufacturer reports the accuracy of the device is ± 0.2 dB for a frequency range of 40 to 1000 Hz ($0.8 \leq St \leq 20.8$), which the frequency content of all excitation types was kept within. For any given excitation case, the SPL was verified to be uniform, within the uncertainty of the device, over the span of the model. Therefore the uncertainty in the excitation SPLs measured at the streamwise location of natural separation is estimated to be ± 0.2 dB.

A.2 PIV Measurements

Uncertainty estimation from PIV measurements is challenging, as the complexity of the measurement system lends to a multitude of error sources, some of which cannot be quantified [206]. Furthermore, while the research community has put forward a variety of approaches to quantify PIV uncertainty [190, 206–209], a generally accepted methodology has yet to be established [189]. That being said, the quantifiable sources of uncertainty in PIV measurements can generally be divided into two categories: (i) bias errors arising from the calibration procedure, and (ii) random errors that propagate through, and may be introduced by, the cross-correlation analysis of the particle images.

The uncertainty that arises due to the calibration procedure can be quantified. For both the side (Fig. 3.4a) and top-view (Fig. 3.4b) PIV configurations, calibration was carried out by imaging a calibration target consisting of marks on a 5×5 mm grid placed within the laser sheet. The spacing between the calibration marks was measured to be accurate within ± 0.05 mm ($\pm 1\%$). A third order polynomial calibration relationship, which relates the image space to physical space, was then computed based on the grid of calibration marks captured in the images. The use of a third order polynomial allows for the calibration relationship to correct for lens distortion near the edge of the field of view and small misalignment between the sensor and image planes. For both PIV configurations, these calibration fits were found to deviate from the calibration images by no more than 0.4 px at any location. The uncertainty associated with these deviations are derived based on

the distance between the calibration marks in pixels, which are, on average, 150 and 83 pixels for the side and top-views, respectively; resulting in uncertainty estimates of $\pm 0.27\%$ and $\pm 0.48\%$, respectively. Thus, adding in the uncertainty associated with spacing of the calibration marks ($\pm 1\%$), the combined uncertainties due to the calibration procedure are $\pm 1.03\%$ and $\pm 1.11\%$ for the side and top-view configurations, respectively.

The random errors that occur in PIV measurements are more difficult to quantify, as they can stem from many different sources. Some examples that can significantly undermine a measurement include: (i) the change in particle intensity between the first and second exposures, which can be caused by the complete or partial loss of particles due to out-of-place motions, (ii) fluctuating background intensity and camera noise levels, (iii) high velocity gradients, and (iv) improper selection of interrogation window parameters, including those related to size, deformation and weighting. Some studies have attempted to address how these effects contribute to PIV uncertainty through Monte Carlo-type simulations, finding that random error contributions generally fall within ± 0.04 to ± 0.1 px [206, 209, 210]. Based on the edge velocity outside of the investigated separation bubble, $U_e = 1.2U_0 = 11.6\,\mathrm{m\,s^{-1}}$, and the frame separation times employed for the side and top-views, 40 and 60 µs, the particle displacements in the outer flow region are 17 and 9 px, respectively. This leads to random error estimates of $\pm 0.23\% \leq \psi_U \leq \pm 0.59\%$ and $\pm 0.5\% \leq \psi_U \leq \pm 1.25\%$ for the side and top-views, respectively. However, this approach has several shortcomings, some of which include: (i) errornously high random errors in areas with low velocity, (ii) erroneously low random errors in areas with large velocity gradients (i.e. near the wall and in the separated shear layer), and (iii) the inability to account for the use of state-of-the-art methods, such as iterative window deformation, which are less prone to random errors [189].

A more comprehensive evaluation of the random errors in PIV measurements can be done using the particle disparity method of Sciacchitano *et al.* [189, 190], which can estimate local and instantaneous velocity uncertainties. The methodology involves applying *a posteriori* displacements to the interrogation windows of a particle image based on the determined velocity field. An inevitable disparity is found between the displaced window and its counterpart in the second exposure, which is used to estimate the local random error. This method addresses all the aforementioned shortcomings of the 0.1 px 'rule-of-thumb' approach, in addition to providing the ability to assess the uncertainty in the instantaneous, mean and rms velocity fields.

The random error estimates in the streamwise, and rms velocity fields for the side-view PIV configuration and the natural case are presented in Fig. A.1. For the streamwise velocity field, Fig. A.1a shows that, as expected, the highest random errors (7% of U_0) are present near the airfoil surface, while within the separated shear (where most of the

analysis of this thesis is performed) the random errors are much less, i.e. 2% to 3% of U_0. In the free-stream, the random error levels produced by the particle disparity method match well with those predicted by the 0.1 px rule-of-thumb. Using Eq. A.1 to combine the random errors in the streamwise velocity field with the uncertainty contribution from the calibration produce produces a total uncertainty estimate of $\pm 0.014 \leq \psi_U/U_0 \leq \pm 0.07$, which is reported in Table A.1.

As previously mentioned, one of the benefits of the particle disparity method is the ability to estimate the random uncertainty in the rms velocity fields, which are shown in Figs. A.1b and A.1c. Overall, the uncertainties in the rms fields, normalized by their respective maximum values, are less than the random errors in the streamwise velocity field, which is attributed to reducing random errors through temporal averaging. The maxima in $\psi_{u'}$ and $\psi_{v'}$ share similar values of $\pm 2.3\%$ and $\pm 2.2\%$, respectively, in addition to both their spatial distributions resembling that of their respective rms fields (Figs. 4.2b and 4.2c). Thus, the random errors in the u' and v' fields, if normalized by their local rms

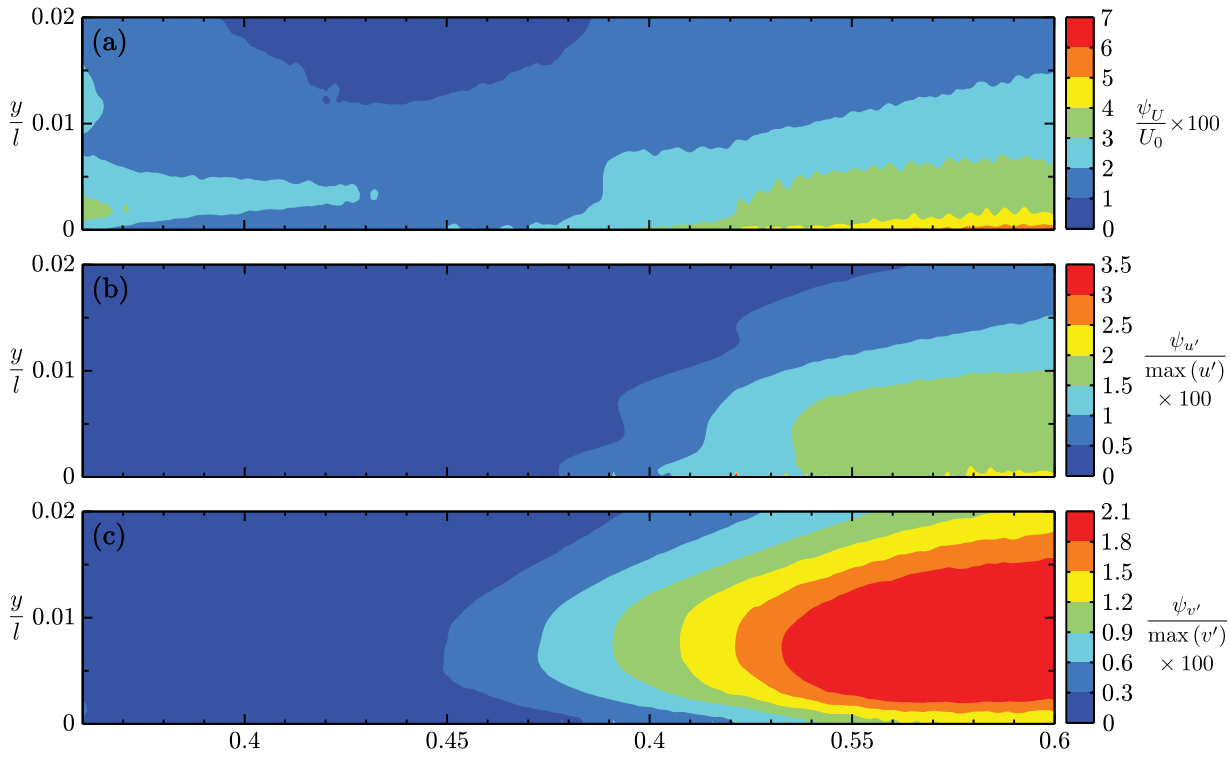

Figure A.1: Side-view PIV random error estimates for the natural case. Estimates are made using the particle disparity method [189, 190].

values, are approximately constant at ±2.3% and ±2.2%, respectively.

Figure A.2 shows the uncertainty in the streamwise velocity measurements from the top-view PIV configuration for the natural case. Similar to the spectrum of random errors for the side-view measurements, the estimated random errors for the top-view setup fall within 1% to 8% of U_0. Combining these estimates with the uncertainty contribution from the calibration produce produces a total uncertainty estimate of $\pm 0.015 \leq \psi_U/U_0 \leq \pm 0.08$, which is reported in Table A.1. The distribution of the random errors in Fig. A.2 is noticeably different for the regions $z/l > 0.08$ and $z/l < 0.08$, which is attributed to fitting one of the cameras with a Scheimpflug adapter (see Fig. 3.4b). The use of the Scheimpflug adapter degraded the quality of the measurement for $z/l < 0.08$, as it restricted the passage of light though the aperture of the camera, resulting in a lower SNR compared to the camera without an adapter ($z/l > 0.08$).

A.2.1 PIV Derived Quantities

Boundary layer thickness parameters (δ, δ^*, θ, and H) were computed from the mean streamwise velocity fields measured using the side-view PIV configuration. Therefore, these estimates are susceptible to the uncertainty present in the PIV measurements. To assess

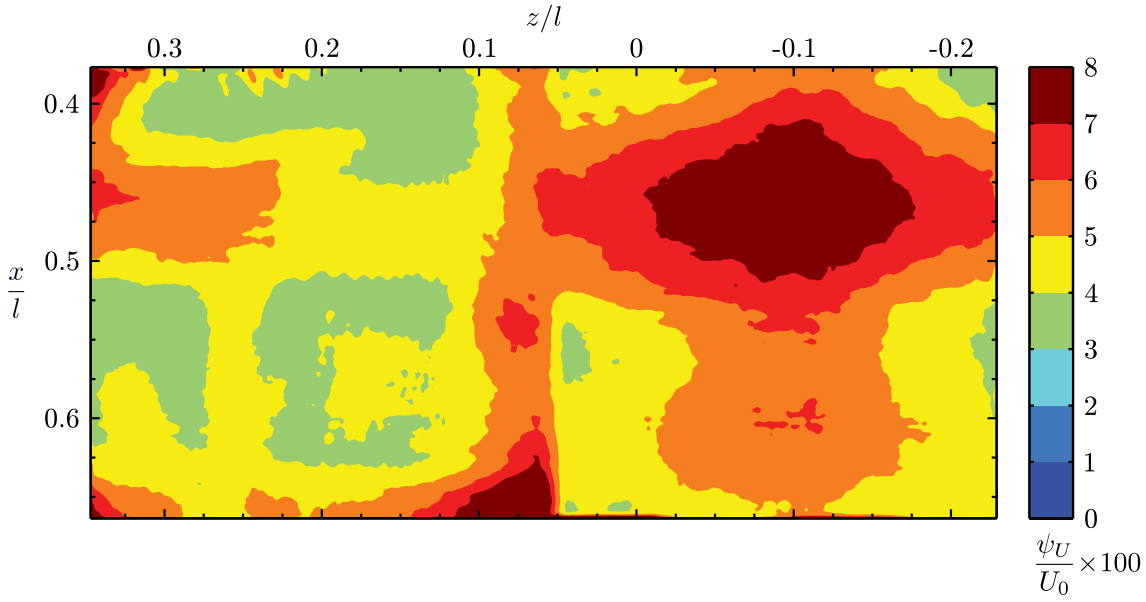

Figure A.2: Top-view PIV random error estimates for the natural case. Estimates are made using the particle disparity method [189, 190].

their impact the propagation of uncertainty technique was employed, where the estimated random errors in the PIV measurements were superposed onto the mean field and the boundary layer parameters were re-computed. Doing so for the natural case produced the uncertainty intervals presented in Figs. 5.4 and E.1. The range of uncertainty intervals for all the investigated boundary layer parameters are summarized in Table A.1. Furthermore, the streamwise location in the maximum shape factor was used in estimating the mean transition point. Therefore the uncertainty in x_T when using this method was determined by the change in the location of maximum H due to propagating the PIV random errors through the computation of H. A range of uncertainties for x_T derived from H is given in Table A.1 since the estimates varied slightly depending on the excitation case.

The separation bubble's dividing streamline was determined from the mean streamwise velocity fields measured using the side-view PIV configuration. The dividing streamline was then used to identify the mean separation, maximum bubble height and reattachment points, respectively, and so these estimates are subject to the uncertainty in the PIV measurements. Furthermore, since determining x_S and x_R involves finding the points where the dividing streamline intersects the airfoil surface, the accuracy to which the airfoil surface can be identified comes into play. The airfoil surface was located in particle images that were taken with the tunnel off and the laser on. Due to the very thin reflection of the laser on the airfoil, the surface could be identified in the images within $\pm 4\,\mathrm{px}$, resulting in uncertainties of $\pm 0.25\,\mathrm{mm}$ in locating the airfoil surface in both x and y. Therefore, in order to determine the uncertainties on x_S, x_h, and x_R, the random errors in the PIV measurements were propagated through the estimation of the dividing streamlines and the resulting uncertainties were combined with the uncertainty in locating the airfoil surface. Uncertainty estimates in the dividing streamline for the natural case are depicted in Fig. 4.2a and all values are summarized in Table A.1.

Quite often spectral analysis of the PIV measurements was employed to identify dominant disturbance frequencies, wavelengths and convective velocities. All spectra were computed using Welch's method [188]; however, depending on the situation different signal widths and overlap were employed, which affects the resolution of the spectra and therefore the accuracy to which a particular result can be determined. All one-dimensional frequency spectra (Figs. 4.4a, 5.6, 5.12, and 5.19) were computed by dividing the velocity signals into equal windows of 2^{10} points with 75% overlap, resulting in a frequency resolution of $St = 0.08$. Therefore the uncertainty associated with identifying any particular frequency using this technique is $\psi_{St} = \pm 0.04$.

In performing two-dimensional, wavenumber-frequency spectral analysis, the velocity signals were divided into windows of $2^8 \times 2^{10}$ points in space and time, respectively, so that the wavenumber resolution was $k_x l = 6.8$ and the frequency resolution was maintained

from the one-dimensional analysis ($St = 0.08$). The nominal uncertainty in determining streamwise wavenumbers from the 2D spectra is half of the wavenumber frequency, however, this value was improved by limiting wavenumber estimations to only those along the convective ridge at a given frequency, as the frequency resolution is much finer than that of the wavenumbers. Therefore the uncertainty in determining a particular streamwise wavenumber along the convective ridge is $\psi_{k_x l} = \pm 0.26$, which translates to an uncertainty on the fundamental streamwise wavelength of $\psi_{\lambda_x/l} = \pm 1.05 \times 10^{-4}$. The uncertainty in determining the convective velocity at the fundamental frequency is a function of the frequency resolution of the 2D spectra and the quality of the linear fit used to determine the convective ridge (evaluated using the fit's root-mean-squared error). The frequency resolution ($St = 0.08$) results in uncertainty on the fundamental convective velocity of $\pm 0.26\%$ while the contribution due to the quality of the fit varied between $\pm 15.2\%$ and $\pm 18.5\%$, depending on the excitation case. Therefore the total uncertainty is $\pm 15.2\% \leq \psi_{U_c} \leq 18.5\%$.

Spectral analysis was also performed on the streamwise velocity signals from the top-view PIV measurements in order to determine the dominant spanwise wavenumbers across the span of the vortex filaments. In order to maximize the wavenumber resolution, these spectra were computed without dividing the signal into windows and so the number of points used in a spectrum was 2^9, which resulted in a wavenumber resolution of $k_z l = 10.5$. For the spanwise wavelengths of interest ($0.08 \leq \lambda_z/l \leq 0.3$), this equates to uncertainties of $\pm 15\% \leq \psi_{\lambda_z/l} \leq \pm 50\%$.

The top-view PIV measurements were used to evaluate the spanwise coherence length of the shear layer vortices. The methodology involved computing the correlation coefficient function (R_{UU} in Eq. 4.1) of $U(t)$ separated by increasing spanwise distances. The correlation functions were then fit with an exponential function (Eq. 4.2) and the coherence length, ℓ_z, was evaluated by integrating the fit. Based on the repeated measurements and error analysis of Bendat and Piersol [211], the estimated uncertainty in the correlation coefficients is ± 0.02 (± 0.01 for correlation levels higher than 0.8). This results in a typical uncertainty on the coherence lengths reported of $\pm 5\%$. Furthermore, as discussed in Section 4.2, the spanwise coherence length estimates were subject to high uncertainty when the amplitude of the disturbances fell within the noise level of the top-view PIV measurements. This is illustated in Fig. A.3 for the natural case, which shows the streamwise rms velocity field relative to the estimated random errors in the measurement (from Fig. A.2). At the mean transition point ($x_T/l = 0.5$), the signal-to-noise ratio between the velocity fluctuations and the random error level is generally above two, downstream of which much higher SNRs are achieved. This analysis was repeated for all excitation cases, and found that the SNR consistently rose above two near the mean transition point. Therefore this cut-off criterion was deemed acceptable and applied for all excitation cases.

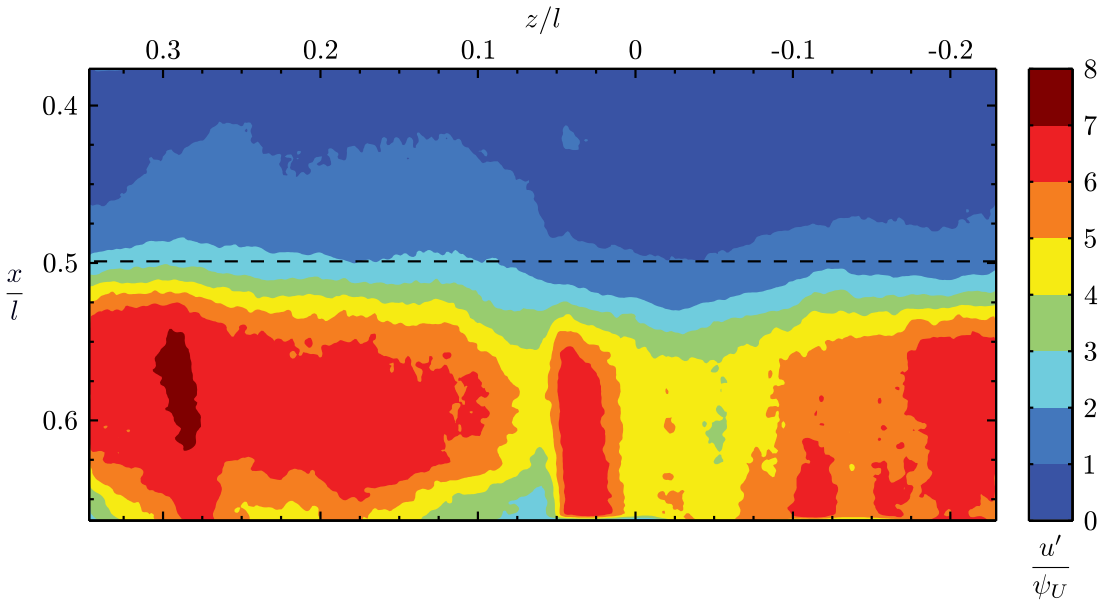

Figure A.3: Streamwise velocity fluctuations relative to the top-view PIV random error estimates for the natural case. Uncertainty estimates are made using the particle disparity method [189, 190]. Dashed line indicates the mean transition point.

A.3 Mean Pressure Measurements

All mean surface pressure measurements were made using Setra Model 239 high accuracy differential pressure transducers with full ranges of 500 Pa. The accuracy of the device is quoted as 0.14% of full-scale (which accounts for hysteresis, non-linearity and non-repeatability effects), and so the associated uncertainty is ±0.7 Pa. Each device was calibrated by applying constant and known pressures using a Druck DPI 610 LP pressure calibrator and recording output voltages. A total of ten pressures, spanning the operating range of the transducer, were evaluated. A linear regression fit was applied to the data and used to interpolate mean pressures from measured transducer voltages. The uncertainty in the calibration procedure is quantified through the root-mean-squared error of the fit from the calibration data points, and results in a value of ±0.12 Pa.

Pressure transducers are sensitive to temperature [187], as changes in the ambient temperature relative to the temperature at which calibration was conducted cause the zero-pressure voltage to shift. For the transducer employed, the zero-point shifts by 5 Pa per 50 °C changes in temperature. This effect was accounted for by determining a new zero-pressure voltage prior to each experiment. However, the ambient temperature varied during

measurements, as the measurement sequence for the ninety-five airfoil static pressure taps take approximately one hour. Therefore, the ambient temperature was monitored and a particular measurement was abandoned if the temperature varied by more than 2 °C. Thus, uncertainty due to ambient temperature changes during measurements is estimated to be ±0.2 Pa.

Static pressure tap geometry can affect the measurement, as the tap geometry can cause a small local change in streamline curvature above the tap. This effect can either increase the measured pressure, or if a small separated flow region is produced, decrease the measured pressure [212]. According to the results of Chue [212], the estimated uncertainty due to static pressure tap geometry in this study is ±0.14 Pa.

Combining the uncertainty estimates discussed throughout this section using Eq. A.1 produces a total uncertainty of ±0.75 Pa, or equivalently ±0.8% of the free-stream dynamic pressure, for all mean pressure measurements presented throughout this thesis.

Appendix B

Facility Characterization

The closed-loop wind tunnel facility employed for all experimental measurements presented in this thesis was first brought online at the beginning of the year 2015, and therefore required detailed characterization prior to any experimental campaigns, the results of which are presented and discussed in this appendix.

A calibration relationship was required that would allow for the test section velocity to be set in a reliable and repeatable manner, regardless of the model installed for a particular experimental campaign or the ambient conditions. Such a relationship was determined between the static pressure drop measured across the wind tunnel contraction, ΔP_{con}, and the free-stream dynamic pressure, P_{dyn}, measured in the empty test section via a pitot-static tube. A schematic of the experimental configuration used is provided in Fig. B.1. The contraction inlet free-stream static pressure was measured by mechanically averaging the pressures from four static pressure taps installed within and flush with the four walls of the contraction. The same approached was used for the contraction outlet pressure, which when measured relative to the inlet gives ΔP_{con}.

The theoretical relationship between the contraction pressure drop and the free-stream dynamic pressure can be derived using Bernoulli's principle. If the contraction outlet velocity is assumed to be the test section free-stream velocity, U_0, and the contraction inlet velocity, U_i, is related to U_0 through conservation of mass, then

$$\begin{aligned}
\Delta P_{\text{con}} &= {}^{1}\!/_{2}\rho\left({U_0}^2 - {U_i}^2\right) \\
\Delta P_{\text{con}} &= \left[1 - \left({}^{1}\!/_{9}\right)^2\right] {}^{1}\!/_{2}\rho {U_0}^2 \\
\Delta P_{\text{con}} &= {}^{80}\!/_{81} P_{\text{dyn}} \\
P_{\text{dyn}} &= 1.0125 \Delta P_{\text{con}}
\end{aligned} \tag{B.1}$$

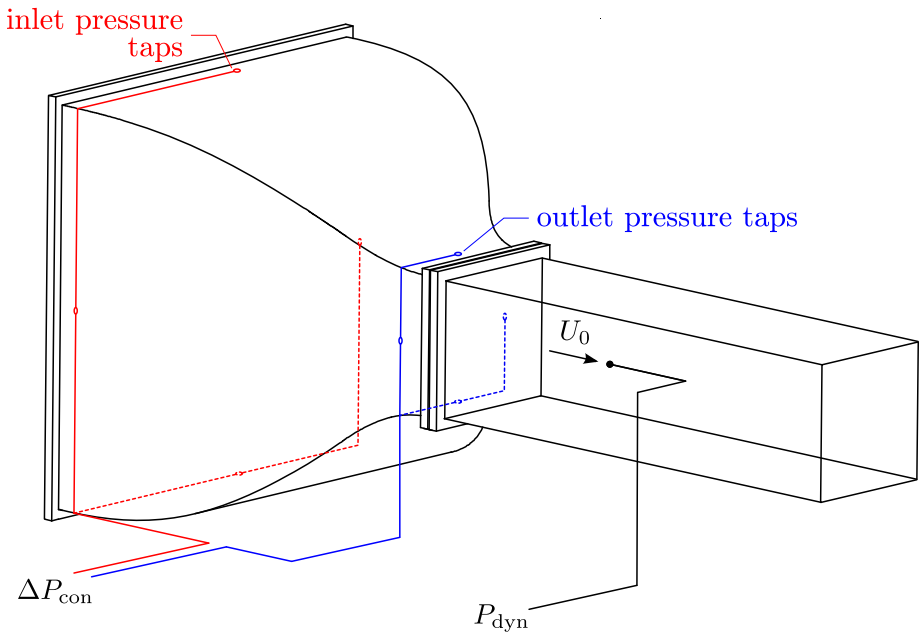

Figure B.1: Schematic of experimental configuration used to calibrate the test section free-stream velocity.

The free-stream dynamic pressure measured in the empty test section over the operating range of the wind tunnel is plotted against the measured contraction pressure drop in Fig. B.2. The maximum free-stream dynamic pressure is approximately 608 Pa and results from running the wind tunnel fan at full speed. The corresponding maximum free-stream velocity is approximately $32\,\mathrm{m\,s^{-1}}$. The minimum free-stream dynamic pressure presented in Fig. B.2 corresponds to the minimum speed at which the fan can be operated without producing significant temporal fluctuations in the free-stream velocity. This defines the minimum operable test section velocity, which is approximately $2\,\mathrm{m\,s^{-1}}$. The experimental calibration relationship between the contraction pressure drop and the free-stream dynamic pressure is determined by a least-squares linear fit to the data in Fig. B.2, and gives the following expression:

$$P_{\text{dyn}} = 0.9176 \Delta P_{\text{con}} \tag{B.2}$$

whose associated root-mean-squared error is 1.83 Pa. Comparing Eq. B.2 with the theoretical prediction (Eq. B.1) gives an indication of the effectiveness of the contraction, as the coefficient from Eq. B.1 should be recovered in Eq. B.2 in ideal conditions. The ratio of the experimentally determined and theoretical coefficients is $0.9176/1.0125 = 0.91$, which is typical for a well designed contraction [183, 213].

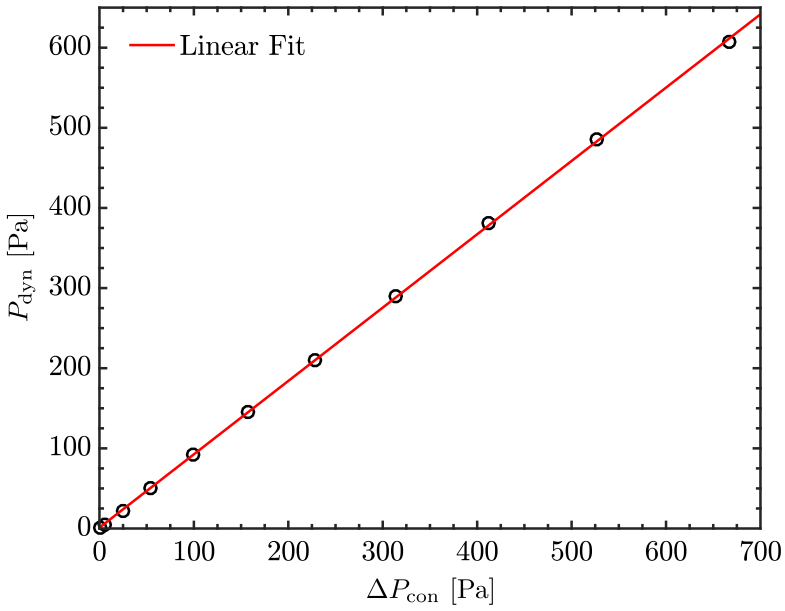

Figure B.2: Measured free-stream dynamic pressure in the empty test section as a function of the measured contraction pressure drop. Equation of linear fit given in Eq. B.2.

The disturbance environment of the empty test section was characterized at the operating conditions studied in this thesis, $Re = 125\,000$, which corresponds to a nominal free-stream velocity of $U_0 = 9.6\,\mathrm{m\,s^{-1}}$. Free-stream velocity fluctuations were assessed using a single, normal hot-wire probe in the empty test section. The results are presented in Fig. B.3, where the spectrum of free-stream streamwise velocity fluctuations from the hot-wire measurements are compared to a velocity spectrum obtained in the separated shear layer from the PIV measurements. The spectrum pertaining to the empty test section shows no significant energy content within the frequency range of interest to this investigation, $2 \leq St \leq 42$ ($100 \leq f \leq 2000\,\mathrm{Hz}$), with the free-stream velocity fluctuations within this range orders of magnitude less than the fluctuations measured in the separated shear layer. There are moderate spectral peaks corresponding to the fan blade passage frequency at $St = 0.58$ and 1.16 ($f = 28$ and $56\,\mathrm{Hz}$), however, these are outside of the frequency range of interest. The turbulence intensity for a low-pass filtered velocity signal at $St = 208$ ($10\,\mathrm{kHz}$) is 0.1%. When the free-stream measurements are band-pass filtered within $2 \leq St \leq 42$, the turbulence intensity decreases to 0.01%.

The autocorrelation function (ACF) of the free-stream velocity is shown in Fig. B.4. The integral time scale is estimated by applying an exponential curve fit to the result and integrating the fit from zero to infinity. The resulting time scale is $t^* = 0.21$. The integral

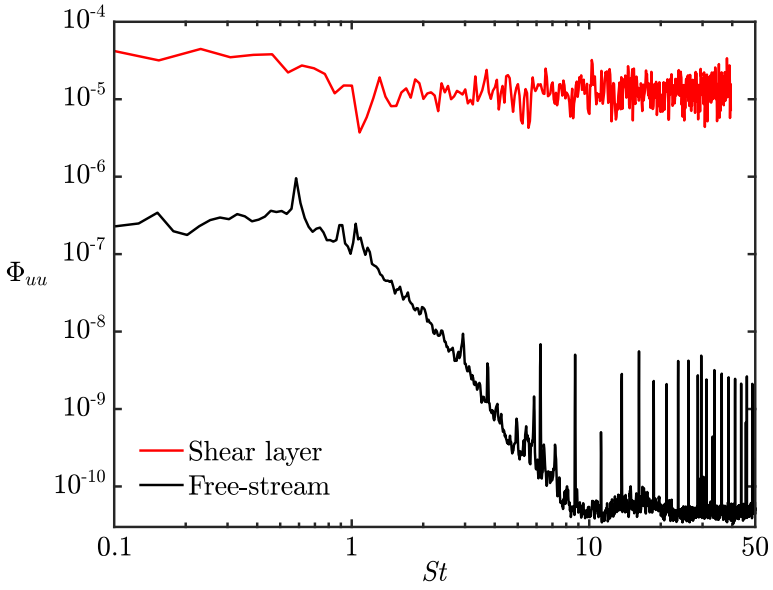

Figure B.3: Spectra of streamwise velocity fluctuations. Free-stream measurements are shown in black while separated shear layer spectrum within the bubble is shown in red.

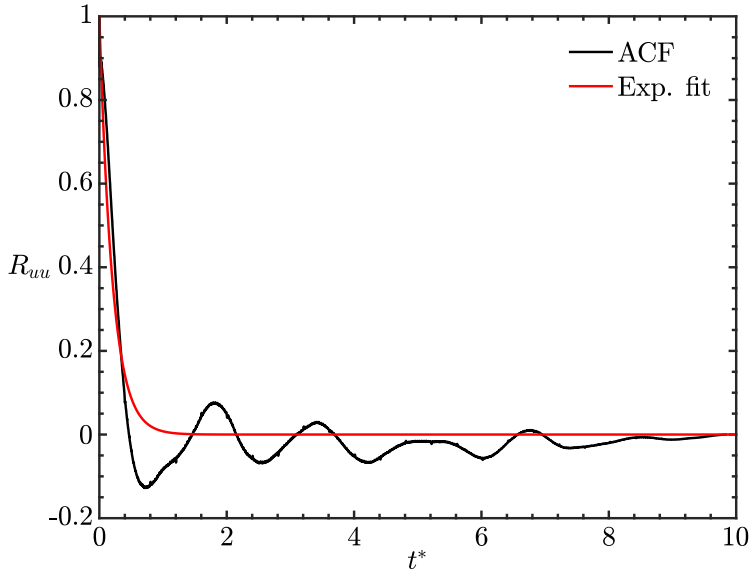

Figure B.4: Autocorrelation function of streamwise velocity fluctuations in the free-stream. Exponential curve fit to the data is shown in red.

length scale is estimated from the integral time scale using Taylor's frozen turbulence hypothesis (e.g. see Pope [214]), and results in a value of $0.20c$.

The uniformity of the free-stream velocity was assessed in the empty test section via Laser Doppler Velocimetry (LDV) measurements. The measurements were performed at a nominal free-stream velocity of $6.7\,\mathrm{m\,s^{-1}}$ using a Measurement Sciences Enterprise MiniLDV-5GL probe and glycol-water based fog with a mean particle diameter of $4\,\mu\mathrm{m}$. Based on the inherent accuracy of the measurement device, the temporal fluctuations in the measured signals, and the velocity bias error [215], the uncertainty in the LDV measurements of the free-stream velocity is estimated to be $\pm 1.05\%$.

Figure B.5 presents the variation in the free-stream velocity in the y-coordinate direction, measured in the empty test section at streamwise locations $0.4c$ upstream and $3c$ downstream of the airfoil leading edge position. Similar measurements, showing the free-stream uniformity in the z-direction, are presented in Fig. B.6. The results show that there is minimal variation in the free-stream velocity in both the y and z directions, as the velocity does not deviates from the mean value, $\overline{U_0}$, by more than 0.5% at any particular location. The variability of the experimental data is characterized by standard deviations values equal to 0.20% and 0.11% of $\overline{U_0}$ for the y and z directions, respectively (denoted by the dashed lines in Figs. B.5 and B.6). For both the y and z directions, the standard deviation is not appreciably different between the streamwise locations. Therefore, taking twice the maximum standard deviation (0.20%), it can be conservatively stated that the free-stream uniformity is within $\pm 0.4\%$ in any direction.

The LDV measurements can also provide an estimate of the streamwise pressure gradient, $\partial P/\partial x$, present within the empty test section. Such a pressure gradient is expected due to the growth of the boundary layers on the test section walls, thus reducing the effective cross-sectional area of the test section. From the measurements presented in Figs. B.5 and B.6, the average free-stream velocity increased from $\overline{U_0} = 6.714\,\mathrm{m\,s^{-1}}$ to $6.767\,\mathrm{m\,s^{-1}}$ between the two investigated streamwise locations, which are separated by a streamwise distance of $3.4c$ (0.68 m). The dynamic pressure associated with the measured increase in the free-stream velocity is 0.41 Pa, which when divided by the streamwise distance gives an estimate of $\partial P/\partial x = 0.60\,\mathrm{Pa\,m^{-1}}$. Over the chord length of the airfoil this favourable pressure gradient is approximately equal to 0.23% of the free-stream dynamic pressure, and therefore its effect on the investigated flow fields can be safely considered negligible.

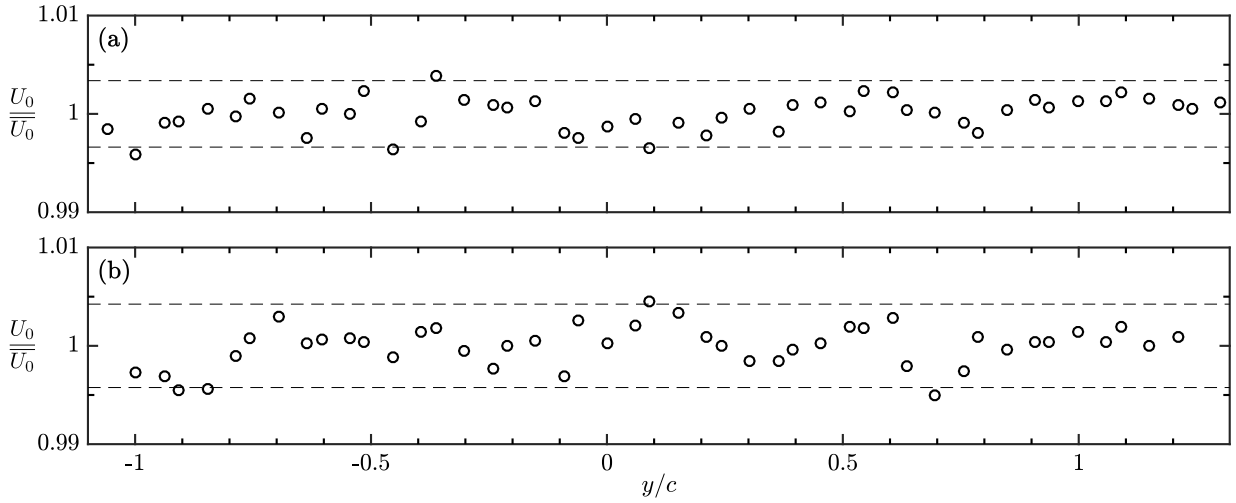

Figure B.5: Free-stream velocity uniformity in the y-direction in the empty test section measured (a) $0.4c$ upstream and (b) $3c$ downstream of the airfoil leading edge position. Dashed lines indicate two times the standard deviation from the mean ($\overline{U_0}$).

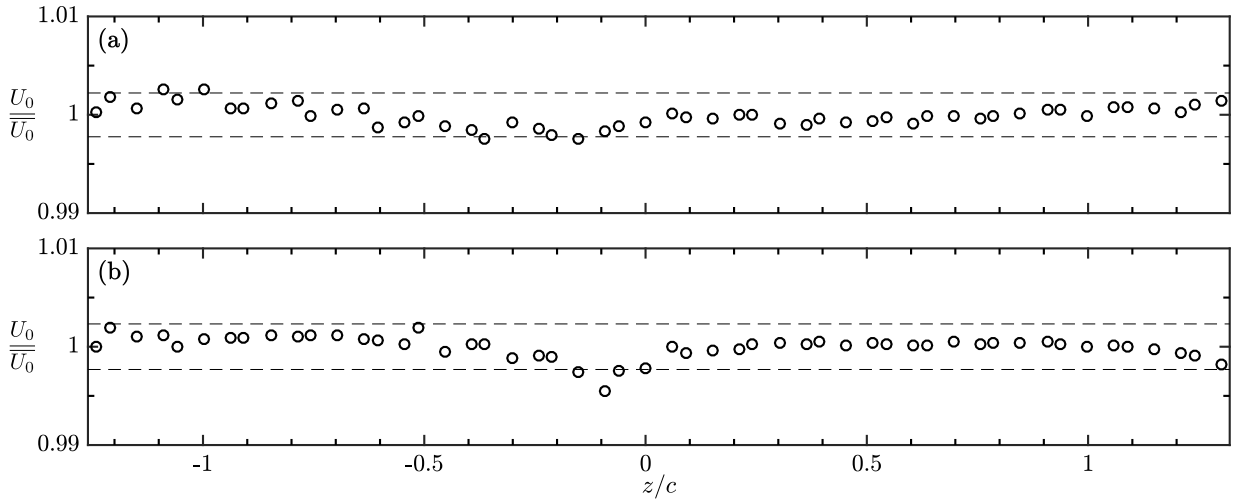

Figure B.6: Free-stream velocity uniformity in the z-direction in the empty test section measured (a) $0.4c$ upstream and (b) $3c$ downstream of the airfoil leading edge position. Dashed lines indicate two times the standard deviation from the mean ($\overline{U_0}$).

Appendix C

Assessment of End Effects

Three-dimensional flows created by the ends of an aerodynamic model, i.e. end effects, can have a substantial effect on flow development for low-aspect ratio models, and as such end plates are commonly employed to mitigate these effects [216]. In the present study, the airfoil model spanned the entire width of tunnel, with the ends sealed to the test section walls using end caps (refer to Fig. 3.2). In addition, the boundary layer thickness on the side-walls of the test section is less than 10 mm at the model location, corresponding to approximately 3% of the spanwise dimension of the test section, and hence the model span. Nevertheless, according to the recommendations of West *et al.* [217, 218], end plates should be employed when the length-to-diameter ratio of the model is less than 30, so that the flow at the center-plane is similar to that over a wide-span model. In the present investigation the ratio between the model height projected onto a streamwise normal plane and the span is approximately 16 and therefore a careful evaluation of any possible end effects was assessed via mean surface pressure measurements with and without end plates installed. The measurements were performed for the flow conditions investigated throughout this thesis, $Re = 125\,000$ and $\alpha = 4°$.

Figure C.1 presents spanwise mean surface pressure distributions on the airfoil suction side measured at three streamwise locations using the model's spanwise rows of static pressure taps (Fig. 3.2). Without end plates the model aspect ratio (b/c) is equal to 3, while the end plates were installed 0.4 m apart resulting in an aspect ratio of 2, as per the recommendation of Boutilier and Yarusevych [62]. The results in Fig. C.1 show that adding end plates does not have any appreciable effect on the spanwise flow uniformity, while added solid blockage leads to a slight increase in suction. These observation are consistent with the findings of Boutilier and Yarusevych [62], who found that, given negligible boundary layer thickness and the absence of a gap between the model and the side wall, adding

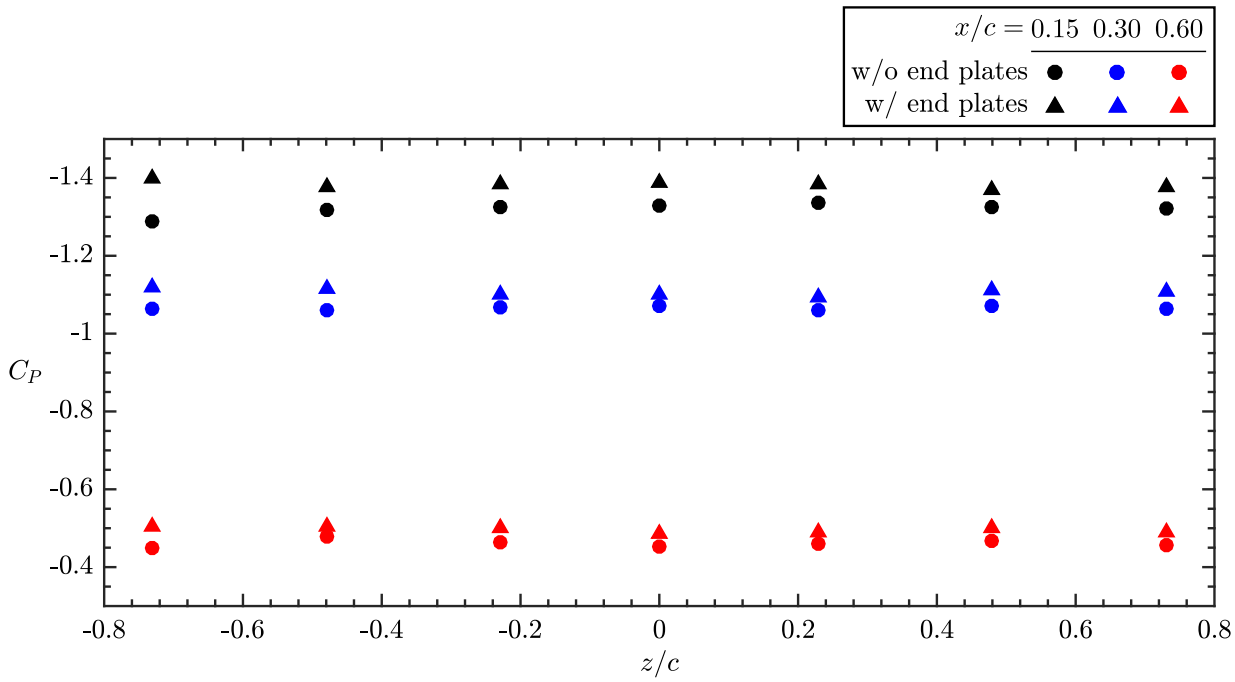

Figure C.1: Suction surface spanwise mean pressure distributions with and without end plates. End plates were installed at an aspect ratio of 2. Black, blue, and red markers show pressure coefficients at $x/c = 0.15$, 0.30, and 0.6, respectively.

end plates has only a minor effect on the position of the separation bubble, except close to the bursting conditions, which was not examined in this thesis. These changes in the mean separation bubble topology fall within the experimental uncertainty of the present investigation, and therefore are not deemed significant. On the other hand, adding end plates negatively impacted the quality of the PIV images, and therefore it was decided to perform all tests without end plates.

Appendix D

Airfoil Microphone Re-calibration

The airfoil model was manufactured and its surface embedded microphones were calibrated over five years ago by Gerakopulos [180], and as a result, some drift from the original calibration relationships is expected to have occurred since. Therefore a re-calibration of the airfoil microphones was required prior to any experimental campaign. The calibration was carried out in an *in situ* manner, as the microphones were left installed in the airfoil. Due to the unavailability of an anechoic facility, the calibration was carried out in a large open space (approximately $50 \times 50\,\text{ft}$), with the airfoil installed on a small table far removed from any acoustically reflective surfaces. Each airfoil microphone was individually calibrated relative to a Bruël and Kjær 4192 condenser microphone, which was placed facing towards an airfoil microphone, separated by approximately 5 mm. Excitation was driven by a Fender Super Champ XD Type PR 737 amplifier, with the excitation signal supplied by an NI USB-6259 DAQ. The voltage signals from the reference and airfoil microphone were recorded simultaneously at a sampling frequency 40 kHz using an NI PCI-4472 DAQ. Twenty calibration points were used within the frequency range of $75 \leq f \leq 5200\,\text{Hz}$ ($1.6 \leq St \leq 108$), with $1/8^{\text{th}}$ octave increments used between calibration points. This frequency range was selected as it encompasses the frequency range of interest to this investigation ($2 \leq St \leq 42$). For all calibration points, the amplitude of the excitation was held approximately constant at an SPL of 90 dB. Furthermore, the calibration results were verified to be insensitive to changes in the calibration excitation amplitude.

The relative response curves of the eight microphones that were re-calibrated are shown in Fig. D.1. The naming convention of the microphones (S03, S04, etc...) is respected from the works of Gerakopulos [180]. The relative response at a particular frequency is defined according to the convention described by Brüel and Kjær [219], where the RMS of the recorded pressure signal is taken relative to an equivalent measurement at a chosen

reference frequency. For the present results the reference response is chosen at a frequency of 225 Hz. The results in Fig. D.1 show that the response of all microphones is relatively flat within the frequency range of $100 \leq f \leq 2500$ Hz ($2 \leq St \leq 52$). To characterize microphone response flatness, the standard deviation of response values within this range is calculated for each microphone. For all the re-calibration microphones, averaging twice the standard deviation yields ± 0.9 dB. Gerakopulos [180] reported a similar value of ± 1 dB, which covered all the airfoil microphones. As responses are flat within $100 \leq f \leq 2500$ Hz, sensitivity values, in terms of mV Pa^{-1}, are calculated using the average responses within this range. These sensitivity values are summarized in Table D.1, which are compared to those from the original calibration [180]. Overall, the sensitivity values determined in the present study differ from those of Gerakopulos by, on average, 9%, thus highlighting the merit of the re-calibration process.

Table D.1: Microphone sensitivity values

Microphone	Location $[x/c]$	Sensitivity [mV Pa^{-1}]		% Difference
		Gerakopulos [180]	Present Study	
S03	0.60	205.47	184.54	−10.2
S04	0.56	193.85	178.69	−7.8
S05	0.51	189.61	159.37	−15.9
S06	0.47	197.68	185.74	−6.0
S07	0.43	167.91	142.83	−14.9
S09	0.39	193.55	206.79	6.8
S10	0.36	173.39	187.71	8.3
S11	0.34	159.45	152.47	−4.4

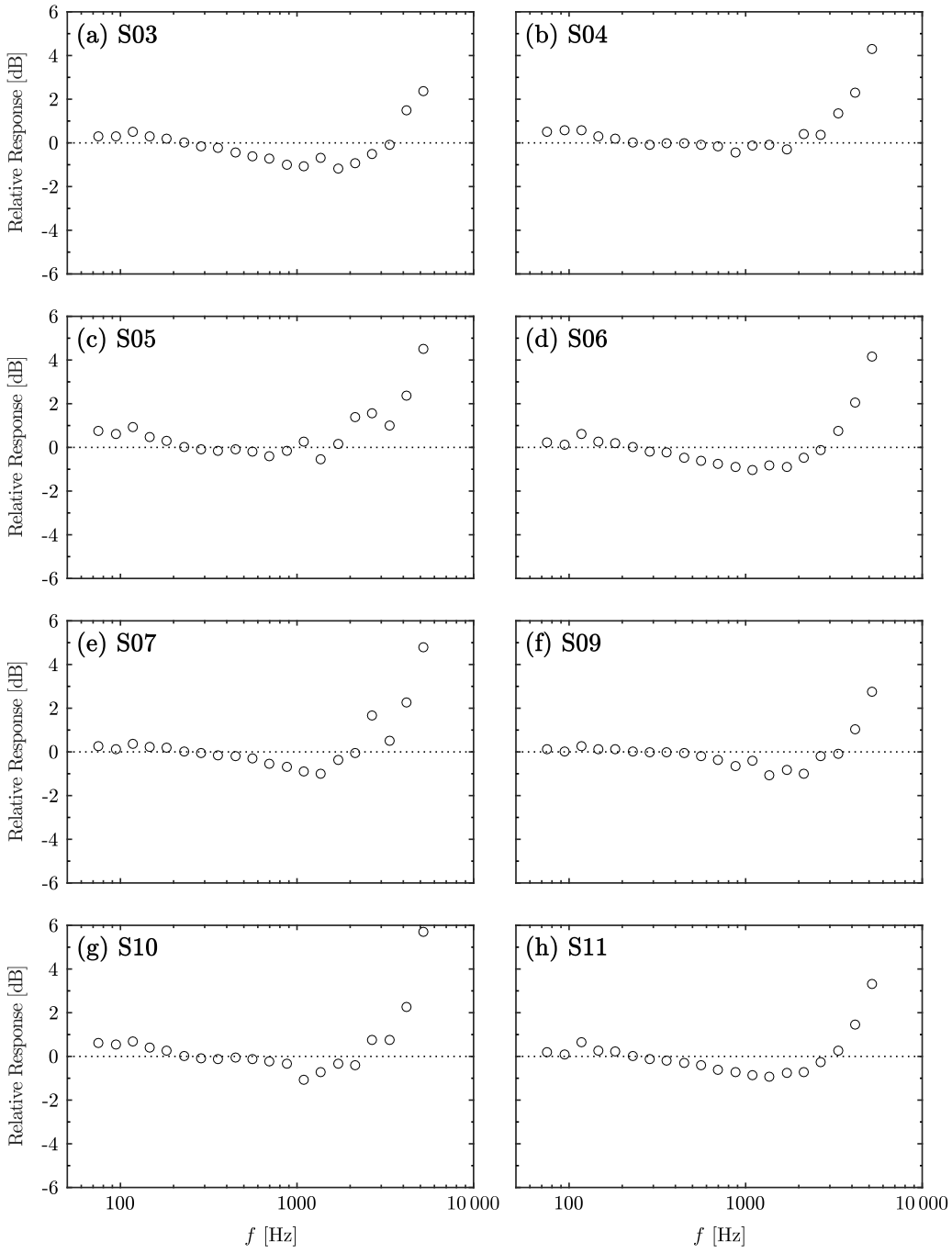

Figure D.1: Relative frequency response of airfoil microphones. Response at 225 Hz is taken as reference.

Appendix E

Supplementary Results

Through the works of this thesis a multitude of experimental data was collected, the entirety of which could not be cohesively included in Chapters 4 and 5. As such, it is the purpose of this appendix to provide the results which where referenced throughout the aforementioned chapters, but were not presented. In addition, it is the author's hope that including these supplementary results helps a future researcher who may find this data useful.

Throughout both Chapters 4 and 5, integral boundary layer/shear layer parameters were employed to aid in characterizing the mean topology of the separation bubble. For example, the displacement thickness, δ^*, was used extensively to approximate the trajectory of the separated shear layer, while the momentum thickness, θ, was used to non-dimensionalize the natural vortex frequency in Section 4.1. Furthermore, the boundary layer shape factor, H, was used in estimating the mean transition locations, and while the shape factor distributions were presented in Fig. 5.4, H is calculated directly from δ^* and θ. Therefore, for the sake of completeness, integral boundary layer parameters (boundary layer thickness, displacement thickness, and momentum thickness) are presented in Fig. E.1 for all cases examined in this thesis. Each parameter is computed according to their respective equation provided in the Nomenclature. It is important to note that all these parameters are computed using their local edge velocity, U_e, and not the free-stream velocity.

In Figs. 4.6, 5.8, 5.15, and 5.21 frequency-wavenumber spectra were presented to aid in characterizing the shear layer perturbations. These spectra were plotted in terms of the disturbance streamwise wavenumber, k_x, as this allowed for the slope of the convective ridge to be directly related to the disturbance convective velocity, U_c. However, for the harmonic excitation cases (Fig. 5.8), increasing the excitation amplitude increasingly concentrated

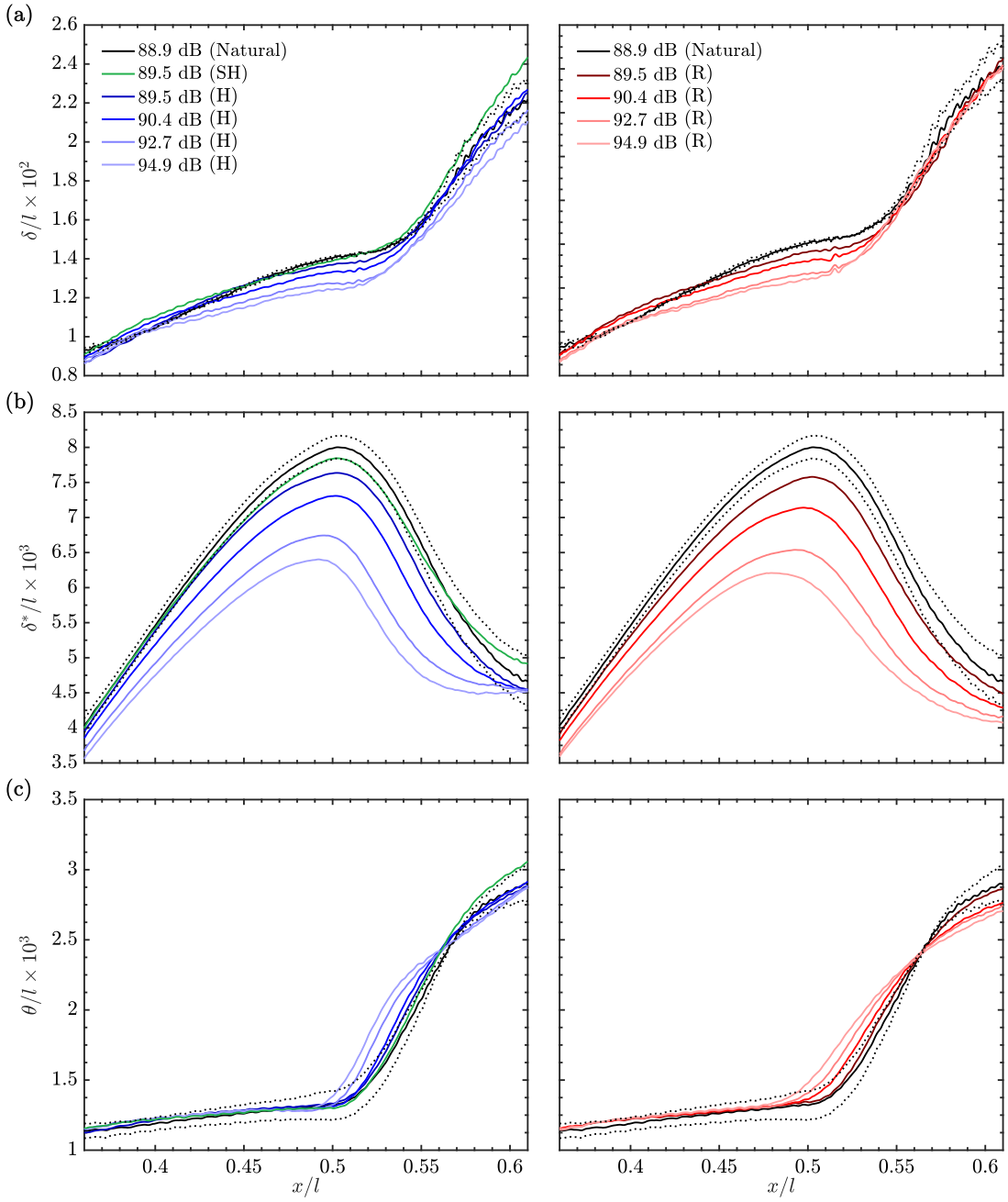

Figure E.1: Boundary/shear layer parameters: (a) thickness, (b) displacement thickness, and (c) momentum thickness. Black dotted lines indicate uncertainty for the natural case.

spectral energy at the fundamental disturbance wavelength, however, this trend is difficult to discern since wavelength is inversely proportional to wavenumber. Therefore, to show this trend more clearly, one-dimensional wavenumber spectra are computed for the natural and harmonic excitation cases and are presented in Fig. E.2. For completeness, spectra for the subharmonic and random excitation cases are also included. Each spectrum is computed by first extracting the wall-normal velocity fluctuations in the separated shear layer (approximated as where $y = \delta^*$), and then computing the wavelength spectrum using the full streamwise extent of the FOV. This process is repeated for all instantaneous fields in the recorded sequence, and then all spectra are averaged. As a result, the maximum resolvable streamwise wavelength is $\lambda_x/l = 0.25$.

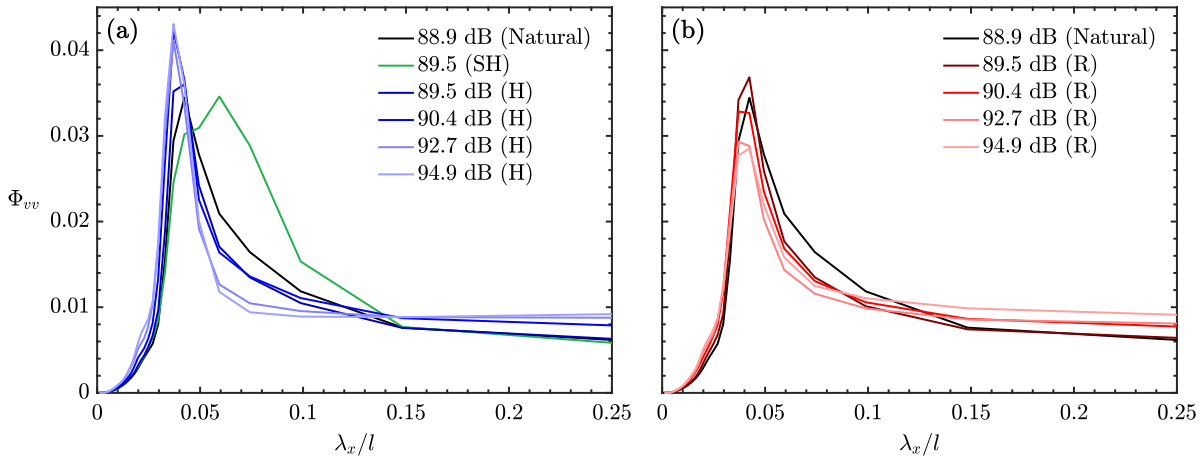

Figure E.2: Averaged wavelength spectra of wall-normal velocity fluctuations within the separated shear layer for the (a) tonal and (b) random excitations cases.

Appendix F

Vortex Tracking Algorithm

In Chapter 4, results of the vortex tracking algorithm implemented using the side-view PIV data were presented (Figs. 4.7–10). This appendix describes the methodology used in implementing this tracking algorithm. The algorithm was written in the MATLAB programming language, the source code of which is available in Section F.1.

An illustration of the algorithm applied to an arbitrary sequence is provided in Fig. F.1. In general terms, the algorithm operates by identifying vortex cores in a velocity field via the λ_2 vortex identification method [192], and then tracing these cores as they convect downstream in the subsequent velocity fields. The λ_2-criterion defines a vortex core at the location of a local pressure minimum due to vortical motion, and as such can be identified by the local minima in the negative second eigenvalues of $\mathbf{S}^2 + \mathbf{\Omega}^2$, where $\mathbf{S}$ and $\mathbf{\Omega}$ are the rate-of-strain and rate-of-rotation tensors, respectively. Refer to the works of Jeong and Hussain [192] for further details on this methodology. For a two-dimensional velocity field, such as those studied here, the strain and rotation tensors are formulated as

$$\mathbf{S} = \begin{bmatrix} \dfrac{\partial U}{\partial x} & \dfrac{1}{2}\left(\dfrac{\partial U}{\partial y} + \dfrac{\partial V}{\partial x}\right) \\ \dfrac{1}{2}\left(\dfrac{\partial U}{\partial y} + \dfrac{\partial V}{\partial x}\right) & \dfrac{\partial V}{\partial y} \end{bmatrix} \tag{F.1}$$

$$\mathbf{\Omega} = \begin{bmatrix} 0 & \dfrac{1}{2}\left(\dfrac{\partial U}{\partial y} - \dfrac{\partial V}{\partial x}\right) \\ \dfrac{1}{2}\left(\dfrac{\partial V}{\partial x} - \dfrac{\partial U}{\partial y}\right) & 0 \end{bmatrix} \tag{F.2}$$

and so the $\mathbf{S}^2 + \mathbf{\Omega}^2$ matrix is completely determined from the spatial gradients of the

two-dimensional velocity field, which can be computed from the PIV measurements. The determination of the λ_2-field is implemented in lines 29–43 in Section F.1.2, where the velocity derivatives are approximated using second order central differences.

Following computation of the λ_2-field, the field is smoothed using an 5×5 spatial averaging filter and MATLAB's peak detection algorithm is run to identify all locally distinct minima (lines 48–55 in Section F.1.2). Several criteria are then evaluated to determine if the detected minima should be deemed vortex cores (lines 58–67). Namely, the minima must be: (i) above a user specified signal-to-noise ratio, which is evaluated relative to the mean of the field, and (ii) within a user specified region. For this investigation, detections were limited to a region beginning downstream of separation, ending upstream of reattachment, and away from the surface. Within this region, a signal-to-noise ratio of 7.5 was found to provide reliable detection of λ_2-minima. The resulting minima are indicated in Fig. F.1 by the red dots, where it is clear that in some instances a single λ_2-minima can correspond well with a vortex core (black dots), e.g. the two most upstream detections in Fig. F.1e. However, quite often, a number of minima are detected within the vicinity of a vortex core, which is attributed to the imperfect nature of experimental data. Therefore a grouping procedure is applied (lines 70–108), where a search radius is defined, and all neighbouring minima within that radius are grouped into what is termed a 'neighbourhood'. The grouping procedure is run iteratively, i.e. an initial neighbourhood is established by searching with respect to a particular minima, and then the search is repeated by searching with respect to all new additions to the neighbourhood. Once the search is completed, a vortex core is then defined as the centroid of all the minima included within the neighbourhood. A search radius of $0.0135c$ was employed for this investigation. The vortex cores resulting from the grouping procedure are indicated by the black dots in Fig. F.1.

The tracking portion of the algorithm, whose source code is provided in Section F.1.1, begins with loading two consecutive velocity fields, and determining all vortex cores within the two (lines 65–99). For each vortex identified in the first field, a trace is initialized. Then, for each of these individuals cores, a set of convective velocities is calculated based on the position of the core in the first field, all identified vortex core positions in the second field, and the time separation between the two (line 106). This set is then filtered based on user defined convective velocity limits (line 108). Through a trial-and-error process, convective velocity limits of $0 < U_c/U_0 < 0.9$ were found to produce reliable results for this investigation. It it worth nothing that this process of estimating where a vortex core has convected to in a subsequent frame through the evaluation of all possible convective velocities against limiting velocities is identical to defining a physical search window, advancing this window downstream and evaluating if any cores fall within this

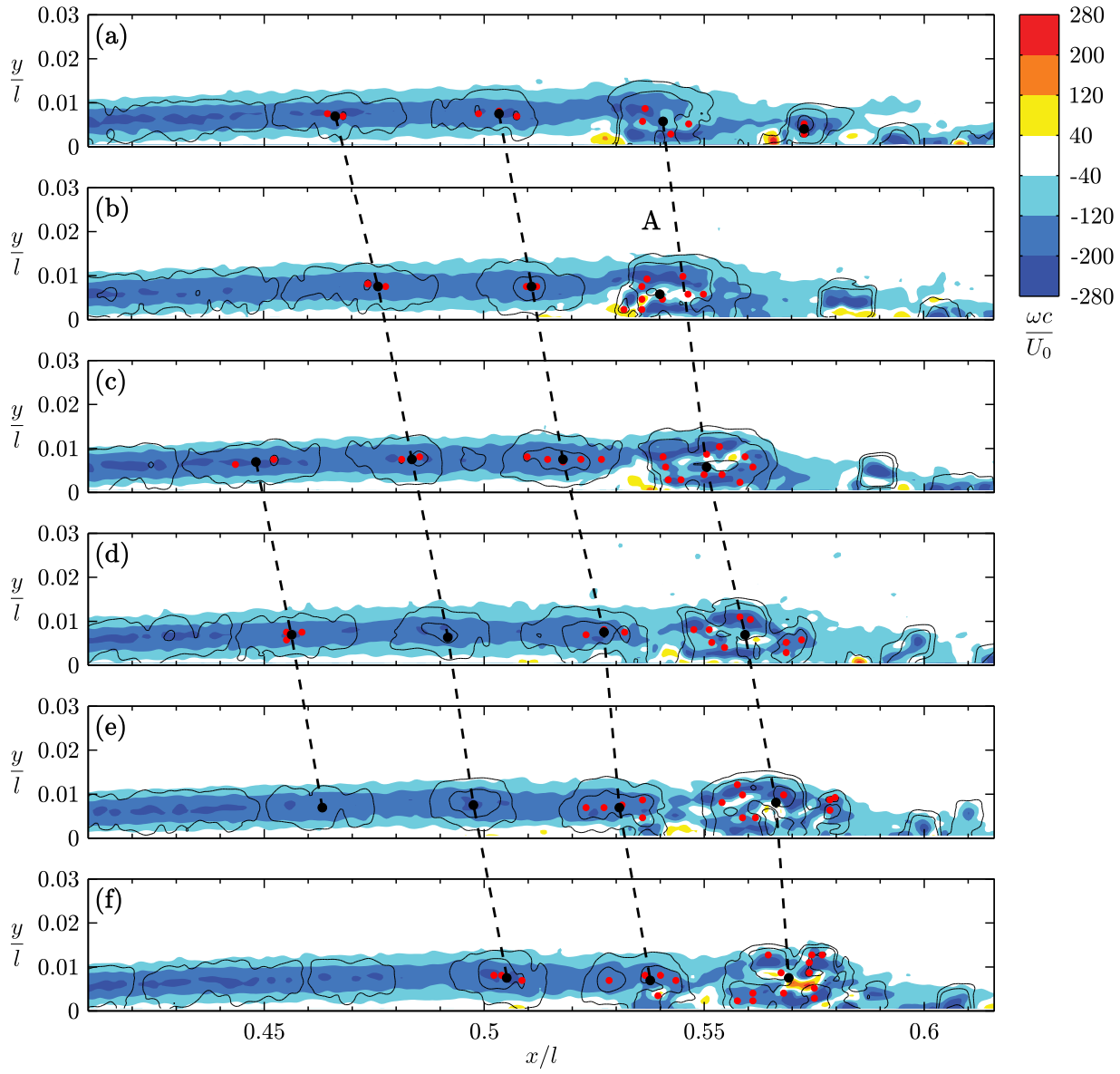

Figure F.1: Vortex tracking algorithm applied to a time-resolved, side-view PIV sequence. λ_2-minima (red circles) are grouped into representative vortex cores (black circles), which are then traced throughout the sequence (dashed lines). Thin black lines indicates λ_2-contours.

window in subsequent frames.

The next set of steps taken by the tracking algorithm depends on the number of valid convective velocities determined in the previously described steps. If only a single valid instance is found, then the vortex core is assumed to have convected to the associated position in the second frame. As such, the new position is added to trace and the convective velocity is recorded, in addition to several housekeeping items. These steps are performed by lines 110–120 in Section F.1.1. If any number of valid convective velocities other than one are detected, then, first, the 'effective search window' is checked against the downstream limit of the region within which cores can be identified (line 121). If the search window is beyond this limit, then the trace is 'retired', i.e. its cores are no longer included in the tracing process. If the search window has not reached the downstream limit, then the trace is not retired and a vortex core is searched for in the next frame (i.e. the third velocity field, in the present example). This allows a trace to withstand an 'erroneous' vortex core detection in a particular frame, as long as a more representative core is detected in the following frames. An example of this is presented in Fig. F.1, where trace A 'skips' the core detected in Fig. F.1b due to the calculated convective velocity being negative, and continues the trace in Figs. F.1c–f.

The algorithm continues by creating new traces for any cores identified in the second frame that were not added to an existing trace (lines 152–162), and then loading subsequent velocity fields and repeating the tracing procedure described above. Once the end of the measurement sequence is reached the algorithm is finished, whose output includes all vortex core positions in time and space, the traces linking them, and all convective velocities. In addition, streamwise wavelengths between all neighbouring vortex cores in the same frame are determined and recorded (lines 168–176). The wavelengths are determined by computing the streamwise distances separating all detected vortex cores in a frame, and then eliminating wavelengths which fall outside a user defined range. A limiting range of $0.01 < \lambda_x/l < 0.12$ was employed for this investigation, which was estimated according to the nominal convective velocity and shedding frequency of the disturbances. With one pass of the tracking algorithm completed, the user has the option of running the algorithm again while employing the output of the first pass to improve on the results. For this investigation, the entire set of convective velocities and wavelengths determined from the first pass were analyzed and the limits for the second pass were set to two standard deviations above and below the mean values from the first pass.

It should be noted that the tracking algorithm described herein does not explicitly address two important features of the flow, namely, vortex breakdown and vortex merging. In the case of the first, vortex breakdown is ignored completely. The structures are never discarded based on some evaluation of their state (i.e. whether or not they've 'broken down'),

instead they are not considered only once they have convected beyond the downstream limit of the tracking algorithm. In the case of vortex merging, merges can be (and are) detected by the tracking algorithm, as once a core is included in a trace, it is not excluded from possible inclusion in another trace. Therefore, searching for cores that belong to multiple traces could lead to identifying possible vortex merges. However, the author did not scrutinize such results to a degree that would allow for confident conclusion that these instance are in fact merges (and are not due to some other phenomena). Furthermore, it is the author's belief that some sort of quantifiable criteria should support an assertion that a merge has occurred between two structures. No such criteria was defined for this investigation, and so no attempt was made to explicitly identify vortex merging from the results of the tracking algorithm.

F.1 MATLAB Code

F.1.1 Vortex Tracking Routine

```
%--------------------------------------------------------------------------
%% Pre
%--------------------------------------------------------------------------
clear
clc
set(0,'defaultTextInterpreter','latex');

%--------------------------------------------------------------------------
% Parameters
%--------------------------------------------------------------------------
basePath = 'E:\Experiments\01 MASc\2015-08 LSB Side\';
load([basePath 'cases.mat']);
nCase = 1; % case number
name = cases.name{nCase}; % case name
s = cases.s; % chord arc length [mm]
c = cases.c; % chord length [mm]
U = cases.U; % freestream velocity [m/s]
dt = cases.dt; % time separation between measurements [s]

% Load
loadPath = [basePath 'Data\Re125k_AOA4'];
load([loadPath name '\PIV\XY.mat']);

% Normalize
xx = xx./s;
```

```
yy = yy./s;

% Build mask
xLim = [0.439 0.58];
mask = find(yy < yy(4,1) | xx < xLim(1) | xx > xLim(2));

%-------------------------------------------------------------------------
%% Loop
%-------------------------------------------------------------------------
%#ok<*SAGROW>

% Files
files = 1:5000;

% Core identification criteria
smooth = [5 5];
SNR = 7.5;
r = 0.0135;

% Tracking limits
Uc_LL = 0;
Uc_UL = 0.9;
lambda_LL = 0.01;
lambda_UL = Uc_UL*U/350/c*1000; % 350 is lowest reasonable shedding
    frequency

% Initialize
oTraces = cell(1,2);
traces = cell(1,1);
Uc = traces;
Uc_x = Uc;
T = Uc;
oT = Uc;
cores = cell(length(files),1);
lambda = cores;
lambda_x = cores;

for i=1:length(files)-1
    if i==1
        % Load first field
        load([loadPath name '\PIV\V' sprintf('%05d',files(i)) '.mat']);
        u = u./U;
        v = v./U;

        % Find cores
```

```
70          [~,~,cores1] = findVortexCores(xx,yy,u,v,SNR,mask,r,smooth);
71          cores{i} = cores1;
72
73          % Compute wavelengths
74          x = xx(cores1);
75          lambda1 = diff(x);
76          % Find valid wavelengths
77          idx = find(lambda1 > lambda_LL & lambda1 < lambda_UL);
78          % Store
79          for j=1:numel(idx)
80              lambda{i} = [lambda{i}; lambda1(idx(j))];
81              lambda_x{i} = [lambda_x{i}; mean([x(idx(j)) x(idx(j)+1)])];
82          end
83
84          % Tracing
85          for j=1:length(cores1)
86             oTraces{j,1} = cores1(j);
87             oTraces{j,2} = 1; % per trace dt multiplier
88             oT{j,1} = 0; % time tracker
89          end
90          oUc = cell(size(oTraces,1),1);
91          oUc_x = oUc;
92      end
93
94      % Load second field
95      load([loadPath name '\PIV\V' sprintf('%05d',files(i+1)) '.mat']);
96      u = u./U;
97      v = v./U;
98      % Find cores
99      [~,~,cores2] = findVortexCores(xx,yy,u,v,SNR,mask,r,smooth);
100
101     % Tracing
102     used = [];
103     remove = [];
104     for j=1:size(oTraces,1)
105         % Compute convective velocities
106         Uc2 = (xx(cores2) - xx(oTraces{j,1}(end)))*s/1000/(dt*oTraces{j
                ,2})/U;
107         % Find valid velocities
108         idx = find(Uc2 > Uc_LL & Uc2 < Uc_UL);
109
110         if numel(idx) == 1 % structure convected
111             oTraces{j,1} = [oTraces{j,1}; cores2(idx)];
112             oUc{j} = [oUc{j}; Uc2(idx)];
113             oUc_x{j} = [oUc_x{j}; mean([xx(oTraces{j,1}(end)) xx(oTraces{
```

```
                j,1}(end-1))])];
114             oT{j} = [oT{j}; i];
115             if isempty(used)
116                 used = idx;
117             else
118                 used(end+1) = idx;
119             end
120             oTraces{j,2} = 1; % Reset dt multiplier
121         elseif xx(oTraces{j}(end))+0.6*U*(dt*oTraces{j,2})/(s/1000) >
                xLim(2) % check if near AOI edge
122             % Retire trace
123             if isempty(traces{1})
124                 traces(end,1) = oTraces(j,1);
125                 Uc(end,1) = oUc(j);
126                 Uc_x(end,1) = oUc_x(j);
127                 T(end,1) = oT(j);
128             else
129                 traces(end+1,1) = oTraces(j,1);
130                 Uc(end+1,1) = oUc(j);
131                 Uc_x(end+1,1) = oUc_x(j);
132                 T(end+1,1) = oT(j);
133             end
134             % Mark trace for removal
135             if isempty(remove)
136                 remove = j;
137             else
138                 remove(end+1) = j;
139             end
140         else % we'll check the next frame
141             oTraces{j,2} = oTraces{j,2}+1;
142         end
143     end
144
145     % Remove retired traces
146     oTraces(remove,:) = [];
147     oUc(remove) = [];
148     oUc_x(remove) = [];
149     oT(remove) = [];
150
151     % New traces for new cores
152     unused = setxor(1:length(cores2),used);
153     removeCores = zeros(size(unused));
154     for j=1:length(unused)
155         if xx(cores2(unused(j))) < xLim(1)+0.02 % core is new
156             oTraces{end+1,1} = cores2(unused(j));
```

```
            oTraces{end,2} = 1;
            oUc{end+1,1} = [];
            oUc_x{end+1,1} = [];
            oT{end+1,1} = [];
        end
    end

    % Record cores
    cores{i+1} = cores2;

    % Compute wavelengths
    x = xx(cores2);
    lambda2 = diff(x);
    % Find valid wavelengths
    idx = find(lambda2 > lambda_LL & lambda2 < lambda_UL);
    % Store
    for j=1:numel(idx)
        lambda{i+1} = [lambda{i+1}; lambda2(idx(j))];
        lambda_x{i+1} = [lambda_x{i+1}; mean([x(idx(j)) x(idx(j)+1)])];
    end
end

%-------------------------------------------------------------------------
%% Post
%-------------------------------------------------------------------------
% Add in unfinished traces
for i=1:size(oTraces,1)
    traces(end+1,1) = oTraces(i,1);
    Uc(end+1,1) = oUc(i);
    Uc_x(end+1,1) = oUc_x(i);
    T(end+1,1) = oT(i);
end
```

F.1.2 Vortex Core Identification Subroutine

```
function [lambda,cores,peaks] = findVortexCores(xx,yy,u,v,SNR,mask,r,
    smooth)
%-------------------------------------------------------------------------
% Finds vortex cores in a velocity field using the lambda2 criterion
%-------------------------------------------------------------------------
% Inputs:
% xx, yy = meshgrids of location data
% u,v = velocity fields
% SNR = lambda value must be greater than SNR times average value of the
    field to be considered a valid peak
```

```
% mask = linear indices of locations that are not allowed to be peaks (i.
    e. near surfaces and edge of FOV)
% r = search radius. All neighbouring peaks found within a search radius
    are combined into one 'core' by finding the centroid of the '
    neighbourhood'
% smooth = width and height of rectangle (in pts.) used for mean
    filtering of lambda. If smooth = [], no smoothing is applied
%-------------------------------------------------------------------------
% Output:
% lambda = lambda2 field in meshgrid form
% cores = linear indices of identified cores
% peaks = linear indices of identified peaks organized into cells (by
    nbhds) in the same order as the cores
%-------------------------------------------------------------------------
% Initialize
lambda = NaN(size(u,1),size(u,2));

for i = 2:size(u,2)-1
    for j = 2:size(u,1)-1
        % Check if we'll try to use masked region
        if(sum(isnan([u(j+1,i) u(j-1,i)  u(j,i+1) u(j,i-1)])))
            break;
        end

        % Calculate derivatives
        dudx = (u(j,i+1)-u(j,i-1))/(xx(j,i+1)-xx(j,i-1));
        dudy = (u(j-1,i)-u(j+1,i))/(yy(j-1,i)-yy(j+1,i));
        dvdx = (v(j,i+1)-v(j,i-1))/(xx(j,i+1)-xx(j,i-1));
        dvdy = (v(j-1,i)-v(j+1,i))/(yy(j-1,i)-yy(j+1,i));

        % Strain matrix
        S = [dudx, 0.5*(dudy+dvdx);
             0.5*(dvdx+dudy), dvdy];

        % Rotation matrix
        R = [0, 0.5*(dudy-dvdx);
             0.5*(dvdx-dudy), 0];

        % Solve for eigenvalues
        lambda(j,i) = min(eig(S^2+R^2));
    end
end

% Apply smoothing
if ~isempty(smooth)
```

```
49      lambda = smooth2a(lambda,smooth(2),smooth(1));
50  end
51
52  avg = nanmean(nanmean(lambda));
53
54  % Find local minima in lambda
55  [~,~,lpeak,peaks] = extrema2(lambda);
56
57  % Remove peaks that are < SNR*avg
58  for i=1:size(peaks)
59      if (lpeak(i) > SNR*avg)
60          peaks(i:end) = [];
61          break;
62      end
63  end
64
65  % Remove peaks that are within the mask
66  peaks = peaks.*(~ismember(peaks,mask));
67  peaks(peaks == 0) = [];
68
69  % Searching and combining. In neighbourhood matrix (nbhd), columns rep.
        eventual 'cores' with each row containing a peak within the search
        radius
70  nbhd = zeros(size(peaks,1),size(peaks,1));
71  cores = NaN(size(peaks,1),1);
72  t = 1;
73
74  for i=1:length(peaks)
75      if ~ismember(peaks(i),nbhd) % Check if peak is already part of a
            neighbourhood
76          % Find neighbouring peaks
77          k = 1;
78          for j=1:length(peaks)
79              if sqrt((xx(peaks(i))-xx(peaks(j)))^2+(yy(peaks(i))-yy(peaks(j)
                    ))^2) < r
80                  nbhd(k,i) = peaks(j);
81                  k = k + 1;
82              end
83          end
84          % Add to neighbourhood by searching wrt to all newly added peaks
85          j = 1;
86          while j < k
87              for q=1:length(peaks)
88                  if ~ismember(peaks(q),nbhd(:,i)) && sqrt((xx(nbhd(j,i))-xx
                        (peaks(q)))^2+(yy(nbhd(j,i))-yy(peaks(q)))^2) < r
```

```
                    nbhd(k,i) = peaks(q);
                    k = k + 1;
                end
            end
            j = j + 1;
        end
        % Find centroid of neighbourhood
        if k == 2
            cores(t) = nbhd(k-1,i);
            t = t + 1;
        else
            cX = sum(xx(nbhd(1:k-1,i)))/(k-1);
            cY = sum(yy(nbhd(1:k-1,i)))/(k-1);
            % Convert centroid coordinates to closest linear index
            temp = intersect(find(abs(xx-cX)==min(min(abs(xx-cX)))),find(
               abs(yy-cY)==min(min(abs(yy-cY)))));
            cores(t) = temp(1);
            t = t + 1;
        end
    end
end
cores(isnan(cores)) = [];

end
```

Appendix G

Coherence Length Estimates

G.1 Curve Fitting Techniques

As described in Section 4.2, the spanwise coherence length, ℓ_z, is computed by integrating the correlation coefficient function, R_{UU}, from zero to infinity in the spanwise direction (refer to Eq. 4.1). These limits of integration are required as the correlation coefficient function must asymptotically tend to zero. Herein lies the difficulty in evaluating spanwise coherence lengths from experimental data, as the investigator is always restricted to a finite observation space and so direct integration of the data suffers from convergence issues. To subvert this issue, a function can be fit to the data and ℓ_z is evaluated from integration of the function. In the current investigation, both exponential (Eq. 4.2) and Gaussian (Eq. 4.3) fits were employed in evaluating coherence lengths for the natural case (Fig. 4.14). It the purpose of this section to evaluate these two fitting techniques, with the aim of identifying which method is superior.

Figure G.1 shows correlation coefficient functions evaluated at four streamwise locations (x/l = 0.45, 0.5, 0.55, and 0.6) and the resulting exponential and Gaussian curve fits. The root-mean-squared errors (RMSE), calculated by square rooting and averaging all squared deviations of the experimental data from the fit, are also indicated. A lower RMSE indicates a more representative fit, and so the exponential fits outperform their Gaussian counterparts for the cases presented in Fig. G.1. A mean RMSE value can also be calculated for each type fit, which is the average of all RMSE values for all fits of a particular type evaluated at the streamwise locations downstream of mean transition. The results are 0.091 and 0.113 for the exponential and Gaussian fitting techniques, respectively, which further supports the superiority of the exponential method.

It is worth noting that downstream of mean reattachment (Fig. G.1d), the flow is

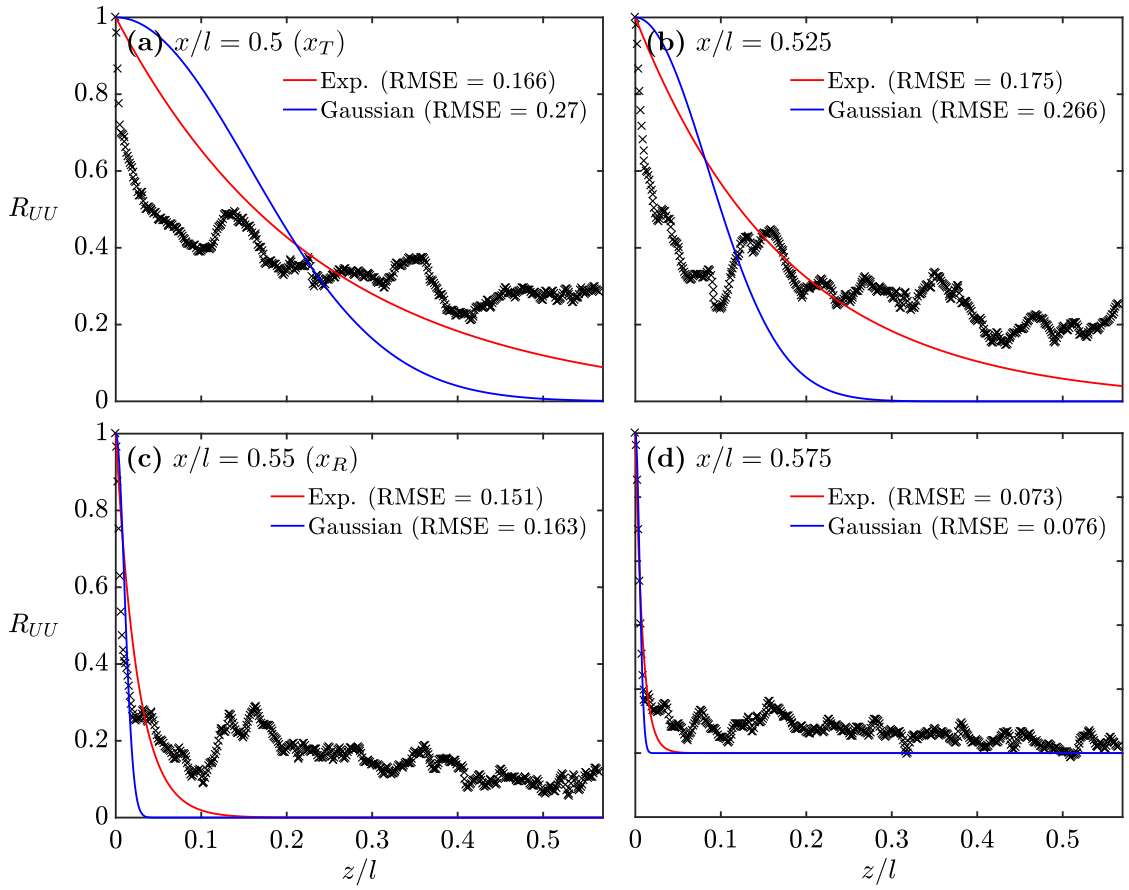

Figure G.1: Evaluation of exponential and Gaussian fits to correlation coefficient functions at various streamwise locations for the natural case.

relatively uncorrelated, as R_{UU} quickly decays to zero, and so both fitting techniques perform well, as both their RMSE values are on the order of 10^{-2}. In the region $x_T \leq x \leq x_R$, where the flow is much more correlated due to the presence of the roll-up vortices, while the exponential method does provide better fits with respect to the Gaussian method, neither provide especially good fits, as for both the RMSE values increase by an order of magnitude. This can be attributed to the relative inflexibility of the two curve fitting methods, as both only allow for one curve fitting parameter. Theory has firmly established that the exponential and Gaussian functions satisfy the end conditions for any general correlation coefficient function [197, 198], namely that $R_{UU}|_{z=0} = 1$ and $R_{UU} \to 0$ as $z \to \infty$. However, the results of this investigation seem to indicate that for highly correlated flow regions, such as those along the filament of a coherent vortex, a different fitting

technique may be required. This technique should still respect the aforementioned end conditions, however, it should allow for added flexibility between these end conditions.

G.2 Random Error Effects

The effect of random errors on the estimation of coherence lengths from the PIV data is assessed in this section, since in Section 5.2.2 it was postulated that a change in the SNR between the mean flow and random error level (as a consequence of vortex merging) could result in a perceived change in the coherence of the studied structures. To examine if such effects are possible, an analysis is conducted on the velocity data from the natural case, where the sensitivity of the computed coherence length to increased levels of random noise is assessed. Ideally, one would examine the effect of decreased levels of random noise, however, decreasing the embedded noise within the measured signal is not possible, and so the effects of increased noise will have to be examined and the findings extrapolated.

Figure G.2 depicts samples of the streamwise velocity data from the top-view PIV measurements for the natural case used to compute the coherence length. The 5% added noise signal (black curve in Fig. G.2) corresponds to the unaltered measured signal used in the process of computing ℓ_z, as presented in Fig. 5.18. The noise level of this case is estimated from the random errors estimates in the top-view PIV data, as discussed in Section A.2. Synthetic random noise of varied amplitudes are then added to the measured signal, producing the coloured curves presented in Fig. G.2. The noise levels are characterized by their RMS values as a percentage of the mean, for which levels of 5%, 5.1%, 6%, 10%, 15%, and 100% are examined, with the last not depicted in Fig. G.2. Computation of the coherence length for all the signals is then carried out using the same procedure as that described in Section 5.2.2.

The coherence lengths computed from the signals depicted in Fig. G.2 are presented in Table G.1. The results demonstrate that as the level of added random noise increases, the estimate of the coherence length decreases. Conversely, this can be viewed as decreases in the random noise level resulting in higher coherence length estimates, and so the assertion made in Section 5.2.2, that an increase in the SNR due to vortex merging could lead to higher perceived spanwise coherence, is correct. In the case of subharmonic excitation, ℓ_z increased by approximately 25% over that of the natural case. Similarly, in the results presented in Table G.1, the coherence length increases by approximately 25% when the noise RMS level is decreased from 10% to 5%. This is equivalent to the SNR being reduced by a factor of one half, which can also be achieved by doubling the mean of the signal. Therefore, from the results of this sensitivity analysis, it can be inferred that in order for

the coherence length estimates produced from the PIV data of this thesis to increase by 25% as a result of changes to the SNR, the mean streamwise velocity would have to be approximately doubled.

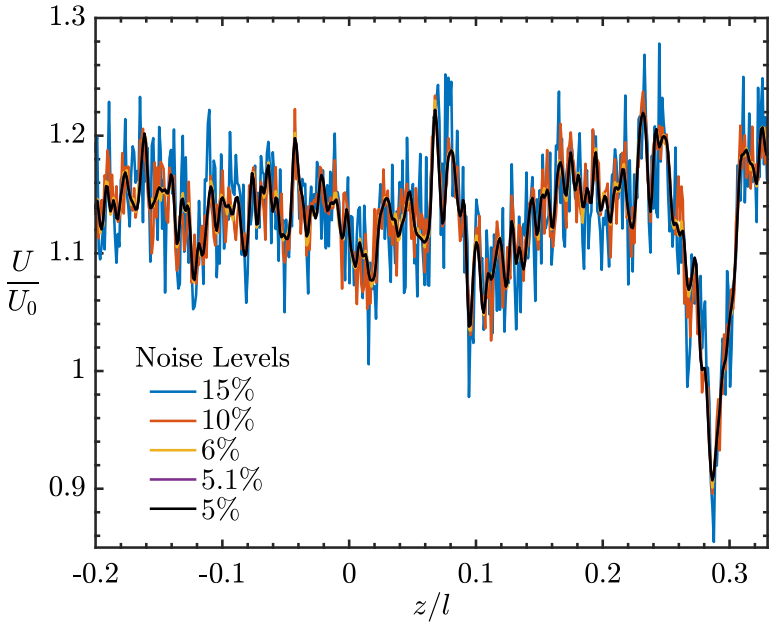

Figure G.2: Sample of streamwise velocity signals with varied levels of random noise used to compute coherence length estimates. Signal is taken from the natural case at x_T. Noise levels are characterized by their RMS value as a percentage of the mean.

Table G.1: Effect of Random Error on Coherence Length Estimates.

	Noise RMS Level [% of Mean]					
	5	5.1	6	10	15	100
ℓ_z/l	0.236	0.236	0.232	0.188	0.088	0.001